

New Linkers for Organic-Inorganic Hybrid Materials

Dissertation zur Erlangung
des Doktorgrades der Naturwissenschaften (Dr. rer. nat.)
genehmigt vom Fachbereich Chemie
der Technischen Universität Kaiserslautern
(D 386)

vorgelegt von
M. Sc. Ezgi Keceli

Betreuer der Arbeit: Prof. Dr. W. R. Thiel
Tag der wissenschaftlichen Aussprache: 20.09.2012

Kaiserslautern 2012

Tag der wissenschaftlichen Aussprache: 20.09.2012

Dekan:

Prof. Dr.-Ing. J. Hartung

Vorsitzender der Prüfungskommission:

Junprof. Dr. M. Esselen

1. Berichterstatter:

Prof. Dr. W. R. Thiel

2. Berichterstatter:

Prof. Dr. H. Sitzmann

Die vorliegende Arbeit wurde in der Zeit von September 2008 bis Juni 2012 im Arbeitskreis von Professor Dr. W. R. Thiel im Fachbereich Anorganische Chemie der Technischen Universität Kaiserslautern angefertigt.

To my family and all loved ones...

Research is what I`m doing when I don`t know what I`m doing.

Wernher Von Braun

Table of Contents

Table of Contents.....	I
List of Figures	VI
List of Schemes	X
Abbreviations.....	XI
1. Organic-Inorganic Hybrid Materials.....	1
2. Metal Organic Frameworks.....	4
2.1 Isoreticular Metal Organic Frameworks (IRMOFs)	10
2.2 Synthesis of the –Br, –NO ₂ and –NH ₂ Functionalized BPDC Linkers	11
2.2.1 Synthesis of the Br-BPDC Linker	11
2.2.2 Synthesis of the NO ₂ -BPDC Linker	16
2.2.3 Synthesis of the NH ₂ -BPDC Linker	19
2.3 Synthesis of the –Br, –NO ₂ and –NH ₂ Functionalized BPDC MOFs; ZnBrBPDC, ZnNO ₂ BPDC and ZnNH ₂ BPDC	24
2.3.1 Characterization of ZnBrBPDC, ZnNO ₂ BPDC and ZnNH ₂ BPDC	26
2.3.1.1 Single Crystal X-Ray Diffraction Measurements of ZnBrBPDC, ZnNO ₂ BPDC and ZnNH ₂ BPDC	26
2.3.1.2 Powder X-Ray Diffraction (PXRD) Measurements of ZnBrBPDC, ZnNO ₂ BPDC and ZnNH ₂ BPDC	30
2.3.1.3 Thermogravimetric Analysis (TGA) of ZnBrBPDC, ZnNO ₂ BPDC and ZnNH ₂ BPDC	32
2.3.1.4 ¹³ C CP-MAS NMR Measurements of ZnBrBPDC, ZnNO ₂ BPDC and ZnNH ₂ BPDC	36
2.3.1.5 IR Measurements of ZnBrBPDC, ZnNO ₂ BPDC and ZnNH ₂ BPDC.....	39
2.3.1.6 N ₂ Adsorption Measurements of ZnBrBPDC, ZnNO ₂ BPDC and ZnNH ₂ BPDC	40
2.3.2 Adsorption of Light Alkanes (C ₁ – C ₄) at Different Temperatures.....	42
2.4 Amide Functionalized BPDC Linkers	47
2.5 Synthesis of the Amide Functionalized BPDC MOFs; ZnAcBPDC, ZnPrBPDC, ZnBuBPDC and ZnPeBPDC.....	54
2.5.1 Characterization of ZnAcBPDC, ZnPrBPDC, ZnBuBPDC and ZnPeBPDC	59
2.5.1.1 Single Crystal X-Ray Diffraction Measurements of ZnAcBPDC, ZnPrBPDC, ZnBuBPDC and ZnPeBPDC.....	59
2.5.2.2 Powder X-Ray Diffraction (PXRD) Measurements of ZnAcBPDC, ZnPrBPDC, ZnBuBPDC and ZnPeBPDC.....	61

2.5.2.3 X-ray Absorption Spectroscopy of ZnAcBPDC, ZnPrBPDC, ZnBuBPDC and ZnPeBPDC	66
2.5.2.4 Thermogravimetric Analysis (TGA) of ZnAcBPDC, ZnPrBPDC, ZnBuBPDC and ZnPeBPDC	70
2.5.2.5 IR Measurements of ZnAcBPDC, ZnPrBPDC, ZnBuBPDC and ZnPeBPDC.....	74
2.5.2.6 ¹³ C CP-MAS NMR Measurements of ZnAcBPDC, ZnPrBPDC, ZnBuBPDC and ZnPeBPDC	75
2.5.2.7 N ₂ Adsorption Measurements of ZnAcBPDC, ZnPrBPDC, ZnBuBPDC and ZnPeBPDC	77
2.5.3 Alkane and Alkene Adsorptions of ZnAcBPDC and ZnBuBPDC	83
2.5.4 CO ₂ Adsorptions of ZnAcBPDC and ZnBuBPDC	88
2.5.5 Dye Adsorption of ZnAcBPDC, ZnPrBPDC, ZnBuBPDC and ZnPeBPDC.....	90
2.6 The Thiophene Linkers	91
2.7 MOF Synthesis using the Thiophene Linkers.....	101
2.8 Zirconium-MOFs with linkers 7 and 9; ZrNH ₂ BPDC and ZrAcBPDC	108
2.8.1 Characterization of ZrNH ₂ BPDC and ZrAcBPDC	110
2.8.1.1 Powder X-Ray Diffraction (PXRD) Measurements of ZrNH ₂ BPDC and ZrAcBPDC	110
2.8.2 Thermogravimetric Analysis (TGA) of ZrNH ₂ BPDC and ZrAcBPDC	113
3. Surface Modification of the Metal Oxides Using Phosphonates as Coupling Molecules..	115
3.1 Synthesis of the Coupling Molecules.....	117
3.1.1 Reduction of the Esters to Alcohols.....	117
3.1.2 Chlorination of the Alcohols	121
3.1.3 Synthesis of the Phosphonates.....	124
3.2 Surface Modification of the Metal Oxides; TiO ₂ , Al ₂ O ₃ , ZrO ₂	128
3.3 Characterization of the Immobilized Surfaces	129
3.3.1 Characterization of the Modified ZrO ₂ Surface	129
3.3.2 Characterization of the Modified TiO ₂ Surface.....	131
3.3.3 Characterization of the Modified Al ₂ O ₃ Surface	133
3.3.4 IR Measurements of the Modified Surfaces	135
3.3.5 ³¹ P CP MAS NMR of the Modified Surfaces	136
3.3.6 TGA Measurements of 38@Al ₂ O ₃ , 38@TiO ₂ and 38@ZrO ₂	137
3.4 Fluorescence Data of the modified TiO ₂ , Al ₂ O ₃ , ZrO ₂ Surfaces	138

5.3.15 Synthesis of Dimethyl-2,2'-bis(2,2,2-trifluoroacetamido)-(1,1'-biphenyl)-4,4'-dicarboxylate (16).....	160
5.3.16 Synthesis of Dibutyl-5,5'-(1,4-phenylene)bis(thiophene-2-carboxylate) (20)	161
5.3.17 Synthesis of Dibutyl-5,5'-(2,5-dimethyl-1,4-phenylene)bis(thiophene-2-carboxylate) (21).....	162
5.3.18 Synthesis of Tributyl 5,5',5''-(nitrilotris(benzene-4,1-diyl))tris(thiophene-2-carboxylate) (22).....	163
5.3.19 Synthesis of 5,5'-(1,4-Phenylene)bis(thiophene-2-carboxylic acid) (23)	164
5.3.20 Synthesis of 5,5'-(2,5-Dimethyl-1,4-phenylene)bis(thiophene-2-carboxylic acid) (24)	164
5.3.21 Synthesis of 5,5',5''-(Nitrilotris(benzene-4,1-diyl))tris(thiophene-2-carboxylic acid) (25).....	165
5.3.22 Synthesis of 1,4-Dichloro-2,5-bis(dibromomethyl)benzene (27)	166
5.3.23 Synthesis of 2,5-Dichloroterephthalaldehyde (28).....	167
5.3.24 Synthesis of 5,5'-(1,4-Phenylene)bis(thiophene-5,2-diyl))dimethanol (32)	168
5.3.25 Synthesis of 5,5'-(2,5-Dimethyl-1,4-phenylene)bis(thiophene-5,2-diyl))dimethanol (33)	169
5.3.26 Synthesis of 5,5',5''-(Nitrilotris(benzene-4,1-diyl))tris(thiophene-5,2-diyl))trimethanol (34)	170
5.3.27 Synthesis of 1,4-Bis(5-chloromethyl)thiophen-2-yl)benzene (35).....	171
5.3.28 Synthesis of 5,5'-(2,5-Dimethyl-1,4-phenylene)bis(2-(chloromethyl)thiophene) (36)	172
5.3.29 Synthesis of Tris(4-(5-(chloromethyl)thiophen-2-yl)phenyl)amine (37).....	173
5.3.30 Synthesis of Tetraethyl-((5,5'-(1,4-phenylene)bis(thiophene-5,2-diyl))bis(methylene))bis(phosphonate) (38).....	174
5.3.31 Synthesis of Tetraethyl-((5,5'-(2,5-dimethyl-1,4-phenylene)bis(thiophene-5,2-diyl))bis(methylene))bis(phosphonate) (39).....	175
5.3.32 Synthesis of Hexaethyl ((5,5',5''-(nitrilotris(benzene-4,1-diyl))tris(thiophene-5,2-diyl))tris(methylene)tris(phosphonate) (40).....	176
5.4 Synthesis of the MOFs.....	177
5.4.1 Synthesis of ZnBrBPDC.....	177
5.4.2 Synthesis of ZnNO ₂ BPDC.....	177
5.4.3 Synthesis of ZnNH ₂ BPDC.....	178
5.4.4 Synthesis of ZnAcBPDC	178
5.4.5 Synthesis of ZnPrBPDC.....	178

5.4.6 Synthesis of ZnBuBPDC	179
5.4.7 Synthesis of ZnPeBPDC	179
5.5 Immobilization of Phosphonate Derivatives on ZrO_2 , TiO_2 and Al_2O_3	180
5.5.1 General Procedure for the immobilization of 38 and 39	180
5.5.2 General Procedure for the immobilization of 40	181
6. References	184
Appendix	198
Acknowledgement	203
Curriculum Vitae	206
Selbstständigkeitserklärung	207

List of Figures

Figure 1.1 Schematic representation of the generation of hybrid materials and the possibilities offered by them.	3
Figure 2.1 Schematic representation of the MOF formation.....	4
Figure 2.2 Secondary building units (SBUs) from some carboxylate MOFs..	6
Figure 2.3 Crystal structure of MOF-210.	8
Figure 2.4 Representation of the non-catenated and catenated frameworks.	9
Figure 2.5 Comparison of MOF building units	9
Figure 2.6 A series of IRMOFs based on MOF-5 topology.	11
Figure 2.7 Crystal structure of 2.....	13
Figure 2.8 ^1H and ^{13}C NMR spectra of 2	14
Figure 2.9 ^1H NMR spectrum of 3	15
Figure 2.10 ^{13}C NMR spectrum of 3	16
Figure 2.11 Crystal structure of 4.....	17
Figure 2.12 ^1H NMR spectrum of 4	18
Figure 2.13 ^{13}C NMR spectrum of 4	19
Figure 2.14 Comparison of the ^1H and ^{13}C NMR spectra of 4 and $\text{C}_{14}\text{H}_{12}\text{N}_2\text{O}_4\cdot\text{HCl}$	21
Figure 2.15 Crystal structure of 6.....	22
Figure 2.16 ^1H NMR spectrum of 6	23
Figure 2.17 ^{13}C NMR spectrum of 6	24
Figure 2.18 SEM pictures of the MOF crystals synthesized with linker 3, linker 5 and linker 7	25
Figure 2.19 Linkers 3, 5 and 7 used for the synthesis of ZnBrBPDC , ZnNO_2BPDC and ZnNH_2BPDC	25
Figure 2.20 Crystal structure of ZnBrBPDC	27
Figure 2.21 Crystal structure of ZnBrBPDC	28
Figure 2.22 Crystal structure of ZnNO_2BPDC	29
Figure 2.23 PXRD patterns of ZnBrBPDC	30
Figure 2.24 PXRD patterns ZnNO_2BPDC	31
Figure 2.25 PXRD pattern of ZnNH_2BPDC	32
Figure 2.26 TGA of evacuated ZnBrBPDC	33
Figure 2.27 TGA of evacuated ZnNO_2BPDC	34
Figure 2.28 TGA of evacuated ZnNH_2BPDC	35
Figure 2.29 ^{13}C CP-MAS NMR spectrum of ZnBrBPDC and high resolution ^{13}C NMR spectrum of the linker 3.....	37
Figure 2.30 ^{13}C CP-MAS NMR spectrum of ZnNO_2BPDC and high resolution ^{13}C NMR spectrum of the linker 5	38
Figure 2.31 ^{13}C CP-MAS NMR spectrum of ZnNH_2BPDC and high resolution ^{13}C NMR spectrum of the linker 7.....	39
Figure 2.32 IR spectra of ZnBrBPDC , ZnNO_2BPDC and ZnNH_2BDC and their linkers 3, 5 and 7.	40

Figure 2.33 N ₂ adsorption and desorption isotherms of ZnBrBPDC, ZnNO ₂ BPDC and ZnNH ₂ BPDC	41
Figure 2.34 Adsorption isotherms of ZnBrBPDC, ZnNO ₂ BPDC and ZnNH ₂ BPDC for the gases CH ₄ , C ₂ H ₆ , C ₃ H ₈ , <i>n</i> -C ₄ H ₁₀ at T= 273 K.	44
Figure 2.35 Adsorption isotherms of ZnBrBPDC, ZnNO ₂ BPDC and ZnNH ₂ BPDC for the gases CH ₄ , C ₂ H ₆ , C ₃ H ₈ , <i>n</i> -C ₄ H ₁₀ at T= 293 K.	45
Figure 2.36 Adsorption isotherms of ZnBrBPDC, ZnNO ₂ BPDC and ZnNH ₂ BPDC for the gases CH ₄ , C ₂ H ₆ , C ₃ H ₈ , <i>n</i> -C ₄ H ₁₀ at T= 313 K.	46
Figure 2.37 ¹ H NMR spectra of 8,10, 12 and 14.....	48
Figure 2.38 ¹ H NMR spectrum of 10.	49
Figure 2.39 ¹³ C NMR spectra of 8,10, 12 and 14.....	50
Figure 2.40 Crystal structures of 8 and 10..	51
Figure 2.41 ¹ H NMR spectra of 9, 11, 13 and 15.....	52
Figure 2.42 ¹³ C NMR spectra of 9, 11, 13 and 15.	53
Figure 2.43 SEM pictures of the MOF crystals synthesized with linker 9 and 13.....	56
Figure 2.44 SEM pictures of the MOF crystals synthesized with linker 11 and 15.....	58
Figure 2.45 Linkers used for the synthesis of ZnAcBPDC, ZnPrBPDC, ZnBuBPDC and ZnPeBPDC.	58
Figure 2.46 The framework connectivity of ZnPrBPDC with the zinc coordination sphere	60
Figure 2.47 Crystal structure of ZnBuBPDC.....	60
Figure 2.48 PXRD patterns of ZnPrBPDC.....	62
Figure 2.49 PXRD patterns of ZnBuBPDC	63
Figure 2.50 PXRD patterns of ZnPeBPDC..	64
Figure 2.51 The simulated PXRD pattern of IRMOF-9 and patterns of ZnPrBPDC.	65
Figure 2.52 XANES spectra of the samples ZnAcBPDC, ZnPrBPDC, ZnBuBPDC and ZnPeBPDC.	67
Figure 2.53 Experimental and fitted Fourier transformed EXAFS spectra of the samples ZnAcBPDC, ZnPrBPDC, ZnBuBPDC and ZnPeBPDC.	67
Figure 2.54 Experimental and fitted Fourier transformed EXAFS spectra of the sample ZnAcBPDC in the dry state and before and after CO ₂ absorption in DMF.	69
Figure 2.55 TGA of the as-synthesized ZnAcBPDC sample.....	70
Figure 2.56 TGA of the as-synthesized ZnPrBPDC sample.	71
Figure 2.57 TGA of the as-synthesized ZnBuBPDC sample.	72
Figure 2.58 TGA analysis of as-synthesized ZnPeBPDC sample.	73
Figure 2.59 IR spectra of ZnAcBPDC, ZnPrBPDC, ZnBuBPDC and ZnPeBPDC and their linkers 9, 11, 13 and 15	75
Figure 2.60 ¹³ C CP-MAS NMR spectra of ZnAcBPDC, ZnPrBPDC, ZnBuBPDC and ZnPeBPDC and high resolution ¹³ C NMR spectra of their linkers 9, 11, 13 and 15.....	76
Figure 2.61 Temperature dependent ¹³ C CP-MAS NMR spectra of ZnPeBPDC.....	77
Figure 2.62 N ₂ adsorption and desorption isotherms of ZnAcBPDC.	78
Figure 2.63 N ₂ adsorption and desorption isotherms of the acetone exchanged and evacuated ZnPrBPDC sample.	80

Figure 2.64 N ₂ adsorption and desorption isotherms of the acetone exchanged and evacuated ZnBuBPDC sample.	81
Figure 2.65 N ₂ adsorption and desorption isotherms of acetone exchanged and evacuated ZnPeBPDC sample.	82
Figure 2.66 Alkane adsorptions of ZnAcBPDC at 273, 293 and 313 K.	84
Figure 2.67 Alkene adsorptions of ZnAcBPDC at 273, 293 and 313 K.	85
Figure 2.68 Alkane adsorptions of ZnBuBPDC at 273, 293 and 313 K.	87
Figure 2.69 Alkene adsorptions of ZnBuBPDC at 273, 293 and 313 K.	88
Figure 2.70 CO ₂ adsorption of ZnAcBPDC and ZnBuBPDC.	89
Figure 2.71 Adsorption of para red. ZnAcBPDC , ZnPrBPDC, ZnBuBPDC and ZnPeBPDC.	91
Figure 2.72 Precursors for the thiophene linkers.	92
Figure 2.73 Esters 20, 21 and 22.	94
Figure 2.74 ¹ H spectrum of 20	95
Figure 2.75 ¹³ C NMR spectrum of 20	96
Figure 2.76 ¹ H and ¹³ C NMR spectra of 21	97
Figure 2.77 ¹ H spectrum of 22	98
Figure 2.78 ¹³ C NMR spectrum of 22	99
Figure 2.79 Crystal structure of 20.	99
Figure 2.80 Crystal structure of 21.	100
Figure 2.81 Carboxylic acid derivatives 23, 24 and 25.	101
Figure 2.82 Representation of the non-linear carboxylic acid groups in 23, 24 and the linear carboxylic acid groups in 30.	103
Figure 2.83 ¹ H and spectrum of 27	105
Figure 2.84 ¹³ C NMR spectrum of 27	106
Figure 2.85 ¹ H NMR and ¹³ C NMR spectra of 27	107
Figure 2.86 The framework connectivity of UiO-67 with the zirconium coordination sphere	108
Figure 2.87 SEM pictures of ZrNH ₂ BPDC and ZrAcBPDC	110
Figure 2.88 PXRD patterns of the synthesized MOFs and UiO-67.	111
Figure 2.89 PXRD patterns of UiO-67 and ZrNH ₂ BPDC MOFs prepared with different amounts of benzoic acid.	112
Figure 2.90 PXRD patterns of UiO-67 and ZrAcBPDC MOFs prepared with different amounts of benzoic acid	113
Figure 2.91 TGA of ZrNH ₂ BPDC and ZrAcBPDC.	114
Figure 3.1 Preparation of the surfaces by the surface modification and the sol-gel method	115
Figure 3.2 Schematic representation of the anchoring of phosphonic acid on the metal oxide surface	116
Figure 3.3 Schematic representation of the anchoring of diethylphosphonate on the metal oxide surface.	117
Figure 3.4 Alcohol derivatives 32, 33 and 34.	118
Figure 3.5 ¹ H NMR spectrum of 33	119

Figure 3.6 ^1H NMR spectrum of 33	120
Figure 3.7 ^{13}C NMR spectrum of 33	121
Figure 3.8 Chloro derivatives 35, 36 and 37.	122
Figure 3.9 ^1H NMR spectrum of 36	123
Figure 3.10 ^{13}C NMR spectrum of 36	124
Figure 3.11 The Phosphonates 38, 39 and 40.	125
Figure 3.12 ^1H NMR spectrum of 39	126
Figure 3.13 ^{13}C and ^{31}P NMR spectra of 39	127
Figure 3.14 Modified ZrO_2 surfaces.	129
Figure 3.15 N_2 adsorption isotherms of 38@ ZrO_2 , 39@ ZrO_2 and 40@ ZrO_2	131
Figure 3.16 Modified TiO_2 surfaces.	131
Figure 3.17 N_2 adsorption isotherms of 38@ TiO_2 , 39@ TiO_2 and 40@ TiO_2	133
Figure 3.18 Modified Al_2O_3 surfaces.	133
Figure 3.19 N_2 adsorption isotherms of 38@ Al_2O_3 , 39@ Al_2O_3) and 40@ Al_2O_3	135
Figure 3.20 IR spectra of the metal oxides before and after surface modification.	136
Figure 3.21 ^{31}P CP MAS NMR spectrum of 40@ ZrO_2	137
Figure 3.22 TGA of 38 on Al_2O_3 , TiO_2 , ZrO_2	138
Figure 3.23 Emission spectra of 38@ Al_2O_3 , 38@ ZrO_2 , 38@ TiO_2 , 39@ Al_2O_3 , 39@ ZrO_2 , 39@ TiO_2 and 40@ Al_2O_3 , 40@ ZrO_2 , 40@ TiO_2	139
Figure 5.1 Scheme of the adsorption apparatus.	145

List of Schemes

Scheme 2.1 Overall reaction for the synthesis of linker 3.	11
Scheme 2.2 Reaction mechanism for the bromination reaction.	12
Scheme 2.3 Overall reaction for the synthesis of the linker 5.	16
Scheme 2.4 Reaction mechanism for the nitration reaction.	17
Scheme 2.5 Reduction of the nitro group.....	19
Scheme 2.6 Overall reaction for the synthesis of linker 7.	22
Scheme 2.7 Overall reaction for the synthesis of linkers 9, 11, 13 and 15.	47
Scheme 2.8 Mechanism for the amide formation.	48
Scheme 2.9 Synthesis route for the trifluoromethyl amide functionalized linker.....	54
Scheme 2.10 Mechanism for the palladium catalyzed carboalkylation.....	93
Scheme 2.11 Carboalkylation reaction of 17, 18 and 19.	94
Scheme 2.12 Overall reaction for the synthesis of linker 30.	104
Scheme 2.13 Bromination of 26.	104
Scheme 3.1 Reaction scheme for the synthesis of phosphonates starting from the corresponding esters.	117
Scheme 3.2 Reaction scheme for the alcohol synthesis.	118
Scheme 3.3 Reaction scheme for the chlorination of the alcohols.	122
Scheme 3.4 Reaction scheme for the synthesis of the phosphates.....	124

Abbreviations

ATR-IR	Attenuated total reflection infrared
BPDC	Biphenyl-4,4'-dicarboxylic acid
BET	Brunauer-Emmett-Teller
DMF	<i>N,N</i> -Dimethyl Formamide
DEF	<i>N,N</i> -Diethyl Formamide
DMSO-d ₆	Deuterated dimethyl sulfoxide
EXAFS	Extended X-ray Absorption Fine Structure
FT-IR	Fourier Transform Infrared
HMBC	Heteronuclear Multiple Bond Correlation
HMQC	Heteronuclear Multiple-Quantum Correlation
IR	Infrared
IRMOF	Isorecticular Metal Organic Framework
KOH	Potassium Hydroxide
MAS	Magic Angle Spinning
MeOH	Methanol
MOF	Metal Organic Framework
NMR	Nuclear magnetic resonance
NMP	<i>N</i> -methyl-2pyrrolidone
SBU	Secondary Building Unit
PXRD	Powder X-Ray Diffraction
TGA	Thermogravimetric Analysis
THF	Tetrahydrofuran
SEM	Scanning Electron Microscope
SCD	Supercritical Carbondioxide Drying
XAS	X-ray Absorption Spectroscopy
XANES	X-ray Absorption Near Edge Structure

1. Organic-Inorganic Hybrid Materials

Organic-inorganic hybrid materials are one of the outstanding fields in material science. These materials can simply be defined as a composition of organic and inorganic parts in which the mechanical, the thermal or the structural stabilities are provided by the inorganic whereas the functionality of the material is provided by the organic constituents.¹ The history of these materials goes back to 1950s with the manufacturing of commercial inorganic-organic polymers.² Although the first studies on hybrid materials reach back for a quite long time, the most promising time for them started in the 1990s with the discovery of the two new classes: periodically formed mesoporous materials synthesized by applying the sol-gel method in the presence of templating molecules³⁻⁵ and Metal Organic Frameworks (MOFs)^{6,7} which can be defined as hybrid coordination polymers.⁸ Nowadays, these advanced materials attract lots of interest due to their possible applications arising from new demands.

Such hybrids can be either homogeneous or heterogeneous, whereby the homogeneity originates from the monomers and miscible organic-inorganic components and the heterogeneity arises from the components which have dimensions between a few angstroms and some nanometers.⁹⁻¹¹ According to their origin, organic-inorganic hybrid materials are divided into two classes.¹² Class I covers the organic and inorganic compounds which are encapsulated and their interactions are based on weak bonds such as hydrogen bondings, van der Waals forces or ionic bonds. In Class II hybrids; linking of the components is afforded by strong chemical bonds like covalent or ionic-covalent bonds.^{13,14} However, some class II materials may also reveal weak bonding.¹³

The inorganic parts of the hybrid materials mainly consist of metal-oxo polymers and metal oxides and they are obtained by condensing metal organic precursors or metal salts. These reactions are defined as sol-gel polymerization reactions and can occur hydrolytic or non-hydrolytic.⁸ In a hydrolytic sol-gel reaction, metal-oxo oligomers and polymers are formed by hydrolysis and polycondensation via M–O–M and/or M–OH–M bridges, whereas in a non-hydrolytic sol-gel process, condensation of halide and alkoxide groups,¹⁰ thermal

decomposition of metal alkoxides¹⁵⁻¹⁹ or reactions of carbonyl compounds and metal oxides²⁰ lead to the formation of the M–O–M bridges. Using sol-gel process, it is possible to obtain known materials, but also materials with novel compositions and properties. Moreover, it makes the idea of designing inorganic materials possible.^{12,13,21-29}

With the usage of network modifiers, the organic units can be brought into the inorganic networks.^{30,31} Principally, two procedures are followed for the applications of modifiers. In the first method, already synthesized macromonomers are chemically grafted or they are introduced through an inorganic network which is forming in a solvent. In the second method, modifiers can be obtained *in situ*. The methods given in the literature for *in situ* formation are photo or thermally induced polyadditions using a radical initiator, atomic transfer radical polymerization, polycondensation and chemically or electrochemically supported oxidative polymerization.⁸

The special properties of hybrid materials combining the physical and the chemical features of both inorganic and organic compounds provide lots of applications in various fields. A study by Sanchez et al. summarizes the generation of hybrid materials and the possibilities offered by them via three routes (Figure 1.1): Route A represents sol-gel chemistry, bridged and polyfunctional precursors and hydrothermal synthesis, Route B shows the hybridization of nanobuilding blocks and Route C reveals the self assembly of amphiphilic molecules or polymers coupled with sol–gel polymerisation.³²

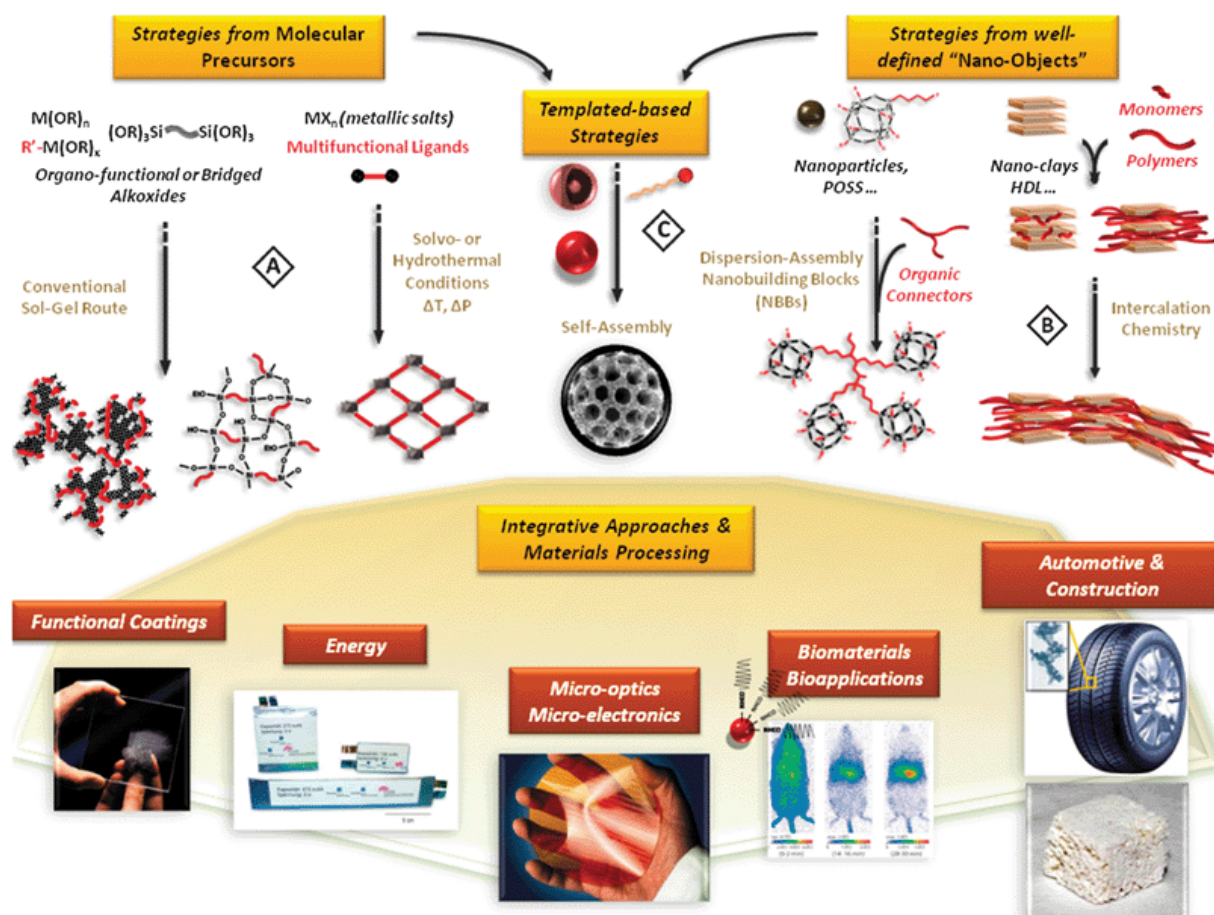


Figure 1.1 Schematic representation of the generation of hybrid materials and the possibilities offered by them.³²

In this study, two outstanding subgroups of organic-inorganic hybrid materials are presented. The first part covers the design, synthesis, characterization and applications of nine novel Metal Organic Frameworks. In the second part, surface modification of metal oxides ZrO_2 , TiO_2 and Al_2O_3 using phosphonate derivatives is reported.

2. Metal Organic Frameworks

Metal Organic Frameworks (MOFs) are one of the unique groups of coordination polymers which are formed by the coordination of metal centers to multidentate organic molecules that results in a three dimensional network (Figure 2.1).³³ Although these materials took interest mainly in 1990s, in reality their history goes back to 1950s. For instance, in 1959, Kinoshita et al. reported a three dimensional network built by the transition metal complex $[\text{Cu}(\text{adiponitrile})_2]$ and nitrate ions.³⁴ There were also other studies reported on such materials in 1960.^{35,36} However the importance of these coordination polymers became known only after the synthesis of MOF-5 by Yaghi *et al.* in 1999.^{6,7} Nowadays many researches work on the synthesis, characterization and design of these promising, highly porous materials.

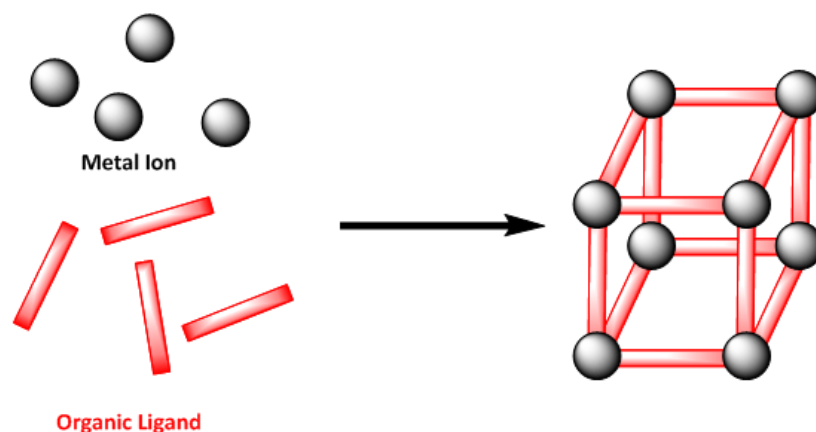


Figure 2.1 Schematic representation of the MOF formation.

The interest in porous materials results from their unique properties and their possible applications. Generally, porous materials are sorted by their pore sizes as microporous (< 2 nm), mesoporous (2 – 50 nm) and macroporous (> 50 nm).³⁷ Zeolites are one of the important classes of these porous materials. They are crystalline aluminosilicates with high surface areas and ordered micropores which makes them suitable for many applications.³⁸ Like MOFs, zeolites are also connected in a way to form frameworks with channels and cavities.^{39,40} However, the topologies of zeolites are limited, since they are built up by tetrahedral Al and Si units. Moreover zeolites do not show high porosity.⁴¹ Therefore, the tunable structures of MOFs give rise to a broader variation of geometries and sizes compared to zeolites.

MOFs are crystalline and porous materials having strong metal-ligand interactions.⁴² These strong interactions give stability to the structure which is also even preserved without any structure collapse after the complete removal of the solvents.⁴³

The solvothermal reaction is the most common method to synthesize MOFs. Its identity can be described as a Lewis-acid/base reaction wherein the metal ions act as Lewis-acids and the linkers act as Lewis-bases.⁴⁴ Generally, it is carried out by simply mixing the metal salts, the ligands, and the solvents and heating to elevated temperatures. Recently, the so-called modulator strategy (Section 2.7 and 2.8) was developed in order to control the reaction rates in the synthesis of MOFs. However, if the aim is high yields instead of high crystal quality, the reaction times are decreased by using high reactant concentrations or employing agitation.^{42,45} DMF, DEF, DMSO, methanol and ethanol are the typical solvents in these synthesis. They are used either alone or as mixtures with other solvents.^{46,47} The temperatures applied in the reactions can change from room temperature to 250 °C depending on the solvents used.⁴²

Besides the conventional solvothermal synthesis, different further methods are applied in order to improve the MOF synthesis. For instance, Forster *et al.* showed that using the hydrothermal synthesis with non-miscible solvents, high quality single crystals can be obtained at the interface.⁴⁸ Moreover electrochemical synthesis⁴⁹ and microwave synthesis⁵⁰⁻⁵² were also found to be effective methods for the MOF synthesis in order to reduce the time for the crystal formation.

Without doubt, the most important point in the MOF chemistry is the production of highly specific and functional materials.⁵³⁻⁵⁵ The choice of the organic linker is one of the key points to achieve rigid, functional MOFs. The linkers should have appropriate functional groups to coordinate the metal ions. Carboxylic acids,⁵⁶⁻⁶¹ phosphonic acids,⁶²⁻⁶⁷ phosphonates,⁶⁸ *N*-heterocyclics,⁶⁹⁻⁷² and cyanides^{73,74} are the most viewed linkers used in the MOF synthesis in which the functional groups build up a polyhedra by coordinating to the metal ions. When these polyhedras link to each other they form linked clusters in which each cluster is named as Secondary Building Unit (SBU).⁵³ Figure 2.2 shows some SBU examples of carboxylate MOFs.

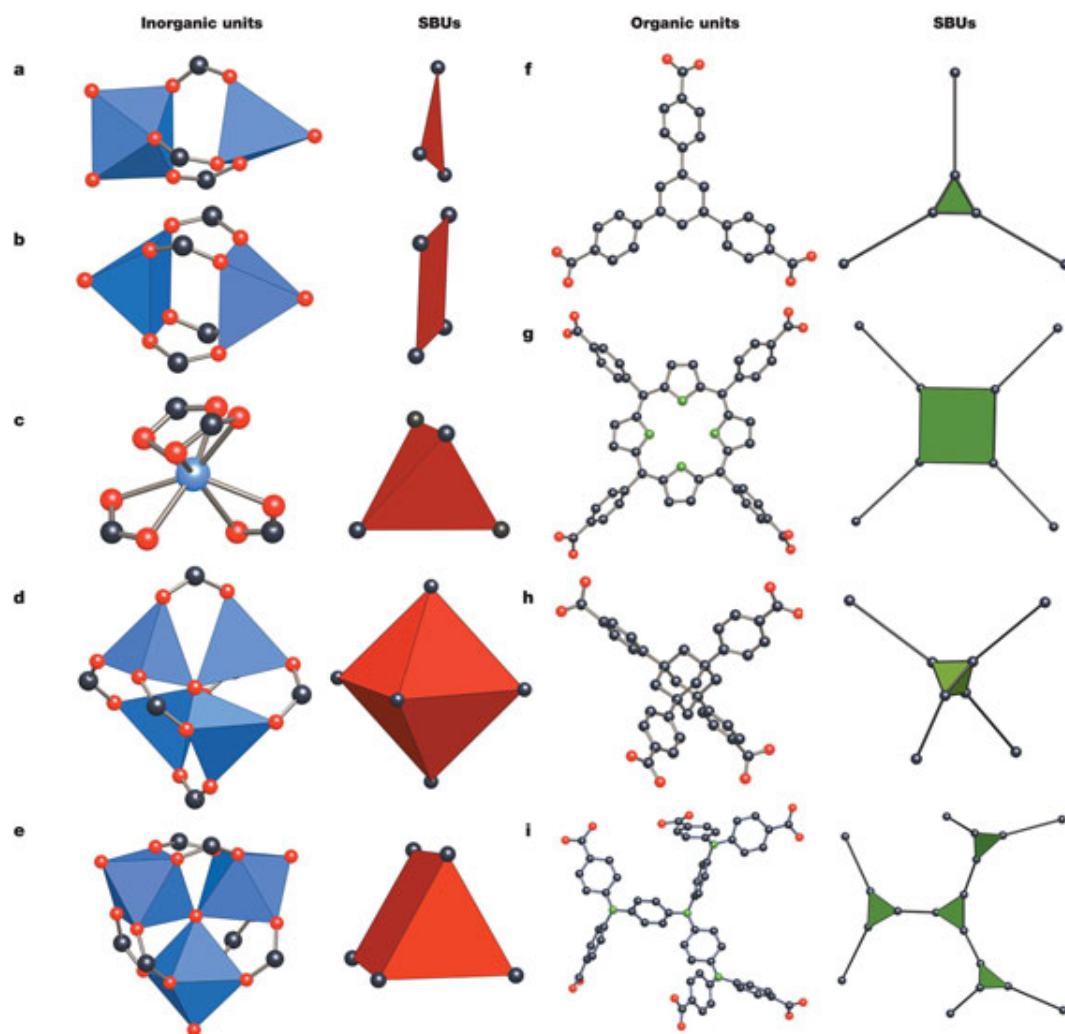


Figure 2.2 Secondary building units (SBUs) from some carboxylate MOFs. In inorganic units metal-oxygen polyhedra are blue, and the polygons or polyhedrons defined by carboxylate carbon atoms (SBUs) are red.⁵³

Generally the character of the solids obtained by the traditional methods cannot be controlled since the precursors do not preserve their structure during the reaction and give rise to a poor correlation between reactants and products.⁵³ However a network can be designed by using well-defined and rigid molecular building blocks via reticular chemistry which is defined as the linking of molecular building blocks into predefined structures wherein the units are repeated and bound strongly.⁷⁵

According to the reticular synthesis approach it can be said that the synthesis of the desired MOFs are done by firstly designing the primary building units which are the metallic centers and the organic linkers. The organic linkers used in the MOFs research are often

commercially available. On the other hand, preparation or design of new organic linker is also carried out. *In situ* synthesis can be performed by modification of the organic linkers which are already in the secondary building blocks or the conventional synthesis can be applied which may cover several syntheses before building up the network.⁷⁶

As already mentioned, the functionality of the MOF structure mainly depends on the organic linker used. The linker selected for the structure should have special features to obtain the most promising materials suitable for applications. Different functional groups on the linker may modulate the adsorbent-adsorbate interactions during the adsorption processes⁷⁷ or they may act as molecular sieves⁷⁸ and may reveal shape selective properties.⁷⁹

The pore sizes and the BET surface areas can be also tuned by the organic linker. There are several studies⁸⁰⁻⁸³ based on the synthesis of MOFs using this approach which resulted in large surface areas. One of the most common methods viewed recently is introducing metal-carboxylates as building units with large linkers.⁸⁴ Using this approach, highly porous MOFs showing different cavities were obtained. DUT-6,⁸⁵ NOTT-116,⁸⁶ NU-100,⁶¹ UMCM-1,⁸³ PCN-610⁸⁷ and MOF-210⁸⁸ are the examples for such MOFs. Up to date, the largest BET surface area (6.240 m²/g) was reported for MOF-210 which has 4,4',4''-[benzene-1,3,5-triyl-tris(ethyne-2,1-diyl)]tribenzoate (BTE) and biphenyl-4,4'-dicarboxylate (BPDC) as linkers (Figure 2.3).^{84,88}

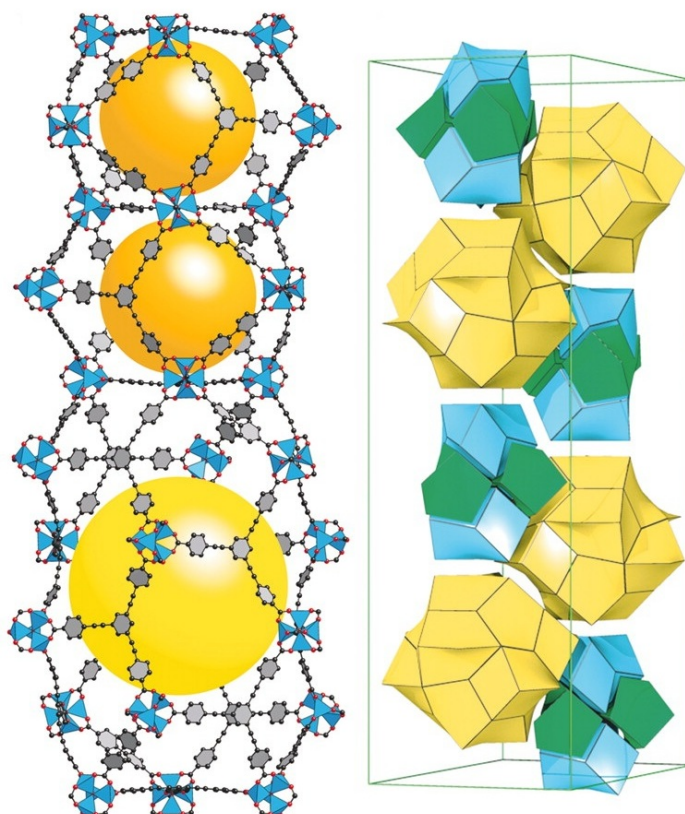


Figure 2.3 Crystal structure of MOF-210. The yellow and orange balls indicate the space in the cage. Zn, blue, tetrahedral; O, red; and C, black. Hydrogen atoms are omitted for clarity.⁸⁸

However, using longer linkers may lead to catenation instead of porosity (Section 2.3.1.1). In a catenated structure two or more identical frameworks intergrow and located in the same space (Figure 2.4).⁸⁹ It is shown in the literature that it is possible to control the catenation by varying the temperature and the concentrations in the synthesis^{90,91} or by applying organic patterns containing liquid-phase epitaxy.⁸⁹

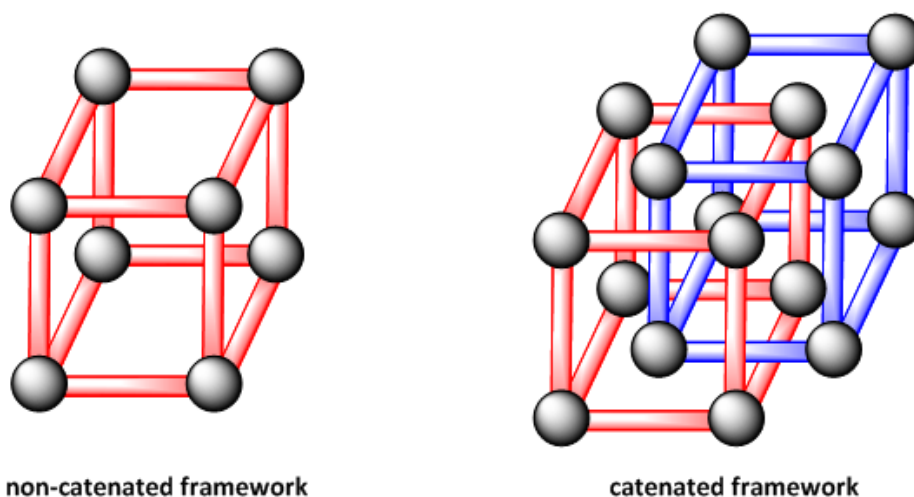


Figure 2.4 Representation of the non-catenated and catenated frameworks.

Alternative to long linkers, recent studies prove that it is also possible to reach high porosity by using larger metal-cluster vertices.⁹²⁻⁹⁶ A study by An *et al.* showed that using large zinc-adeninate vertices an highly porous material bio-MOF-100 could be synthesized which has the largest MOF pore volume reported to date ($4.3 \text{ cm}^3/\text{g}$) (Figure 2.5).⁸⁴ Moreover, other metal atoms such as alkaline-earth, transition metals, main group metals and rare-earth elements have also been used in the MOF synthesis.⁴³

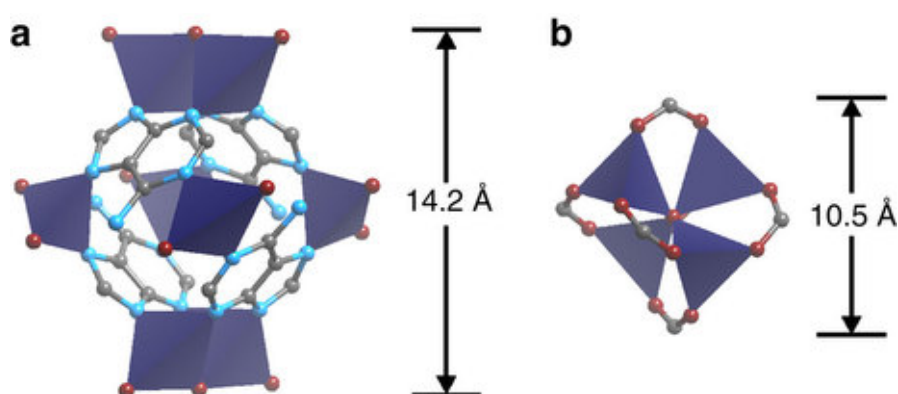


Figure 2.5 Comparison of MOF building units, zinc-adeninate building unit (ZABU) (a) compared with the basic zinc-carboxylate building unit (b) (Zn^{2+} , dark blue tetrahedra; C, grey spheres; O, red spheres; N, blue spheres; H, omitted for clarity).⁸⁴

Characterization of these crystalline and porous materials is very important. To check the porosity and crystallinity of the material, the most frequently used method is powder X-ray diffraction (PXRD) which is correlated with thermogravimetric analysis (TGA) in order to determine the stability. However these methods should be supported by Infrared (IR) and/or nuclear magnetic resonance (NMR) spectroscopy, as well as elemental analysis for complete structural analysis. Moreover nitrogen adsorption at 77 K or argon uptake at 87 K are applied to determine the Langmuir and Brunauer-Emmett-Teller (BET) surface areas.⁴²

As mentioned above, the reticular chemistry approach allows the tuning of pore size and functionality, thus it leads to MOFs applicable for a wide range of applications. This highly porous and functional frameworks are particularly useful for applications like gas adsorption,⁹⁷⁻¹⁰¹ separation¹⁰² and catalysis,^{103,104} as well as drug delivery.¹⁰⁵⁻¹⁰⁷

2.1 Isorecticular Metal Organic Frameworks (IRMOFs)

Isorecticular metal organic frameworks (IRMOFs) were firstly discovered by Yaghi *et. al* starting with the synthesis of MOF-5 which is also named as IRMOF-1.⁶ It was obtained by formally linking $[Zn_4O]^{6+}$ clusters possessing six octahedrally arranged free coordination sites for carboxylates with 1,4-benzenedicarboxylic acid as the organic linker. A series of these materials having the identical topology with MOF-5 were synthesized which have a cubic framework structure with different length and functionality.⁶⁰ This is an excellent example of adjusting and designing frameworks, in other words reticular chemistry which results in materials differing in pore properties (size and volume), surface area and chemical features (Figure 2.6).

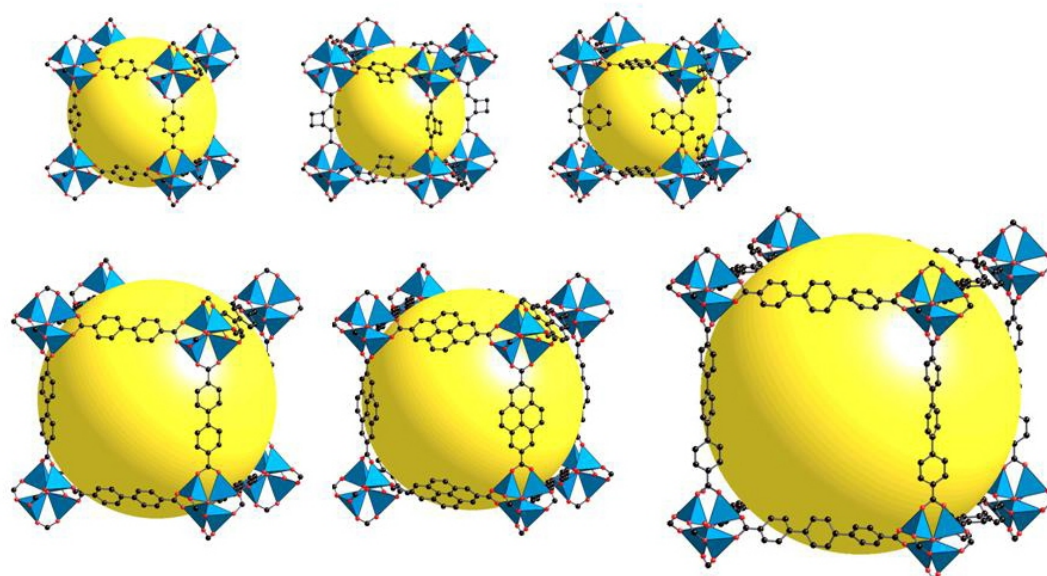


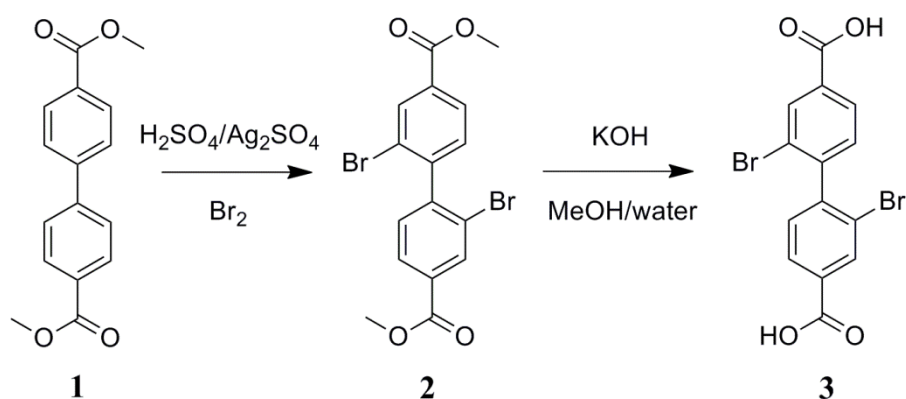
Figure 2.6 A series of IRMOFs based on MOF-5 topology.⁶⁰

In the following sections, the synthesis, characterization and applications of seven functionalized linkers leading to IRMOF structures shall be presented. A common feature of them is that functionalized 4,4'-biphenyldicarboxylic acids were introduced as the organic linkers.

2.2 Synthesis of the –Br, –NO₂ and –NH₂ Functionalized BPDC Linkers

2.2.1 Synthesis of the Br-BPDC Linker

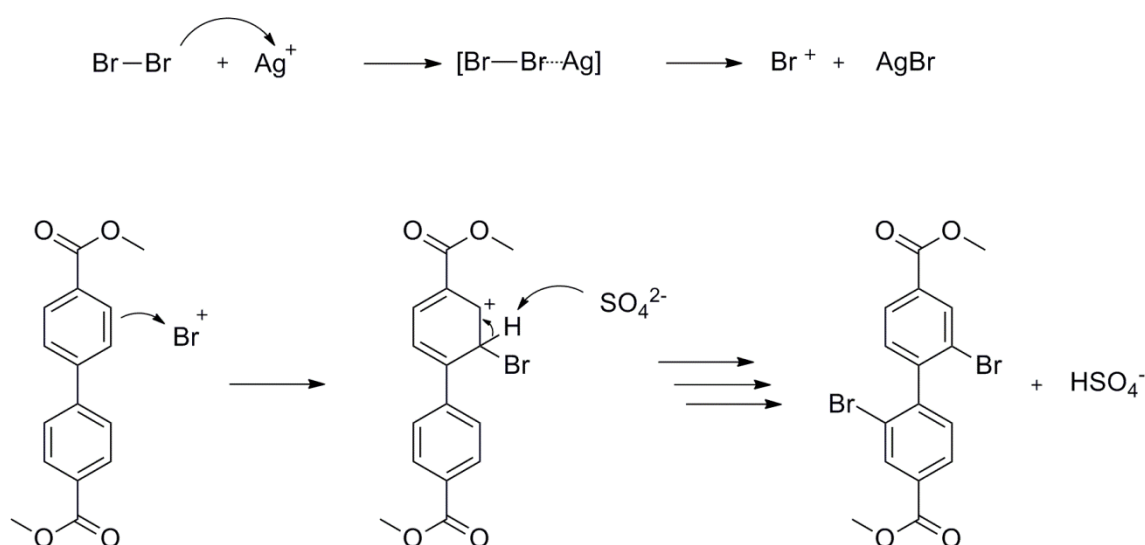
To synthesize the bromo functionalized biphenyl carboxylate linker **3**, dimethyl biphenyl-4,4'-dicarboxylate (**1**) was reacted in the presence of silver sulphate and sulphuric acid according to a published procedure (Scheme 2.1).¹⁰⁸



Scheme 2.1 Overall reaction for the synthesis of linker **3**.

Electrophilic aromatic brominations are generally possible for electron poor aromatic compounds having an electron withdrawing group such as $-\text{COOCH}_3$. This leads to the *meta* substitutions, that was desired in this study. Lewis acid catalysts such as FeBr_3 , AlCl_3 , Ag_2SO_4 ¹⁰⁹ are required in this situation. The Lewis acid forms an intermediate complex with bromine that polarizes the Br-Br bond and increases the electrophilicity of the reagent.¹¹⁰

In the presence of Ag_2SO_4 , bromonium cations are formed and even deactivated aromatics can be easily brominated.¹¹¹ For this reason, silver sulphate was decided to be used instead of FeBr_3 , AlCl_3 . In the first step of the reaction, bromine forms a complex with Ag^+ which then dissociates to generate the bromonium cation. The electrophilic attack of the bromonium cation to the aromatic ring forms an arenium ion. Then the proton is removed by the sulphate anion giving the brominated compound, bromosulfonate and silver bromide (Scheme 2.2).¹¹⁰



Scheme 2.2 Reaction mechanism for the bromination reaction.

After the reaction, the obtained green precipitate was Soxhlet-extracted with EtOH over night to separate **2** from AgBr completely. **2** was obtained as white solid. Recrystallization from ethanol yielded white crystals suitable for an X-ray structure analysis (Figure 2.7).

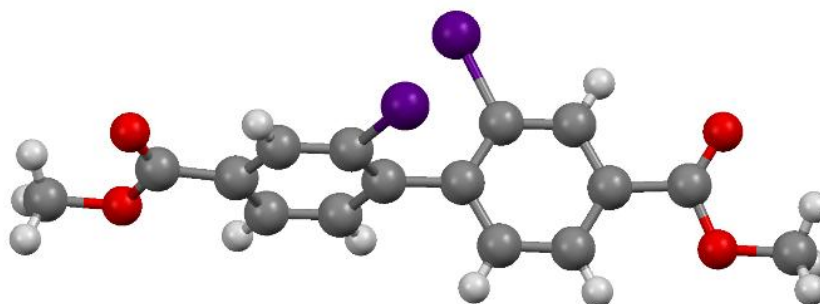


Figure 2.7 Crystal structure of **2**. Atom colors: C grey, O red, H white, Br purple.

The structural elucidation of **2** was accomplished by ^1H NMR and ^{13}C NMR spectroscopy (Figure 2.8). The ^1H NMR spectrum shows three peaks in the aromatic region. Two aromatic protons appear at 8.04 and 7.30 ppm as a doublet of doublet and a doublet with coupling constants of 8.0 and 0.8 Hz and 8.0 Hz respectively, the proton neighboring the bromine substituent shows a doublet at 8.33 ppm with a coupling constant of 0.8 Hz. A characteristic singlet peak at 3.94 ppm belongs to the methoxy groups of the compound. The ^{13}C NMR spectrum reveals resonances of eight different carbon atoms (as expected) confirming the substitution of each phenyl ring (Figure 2.8). For a final assignment of carbon resonances, the HMBC technique (showing longer coupling interactions) was used.

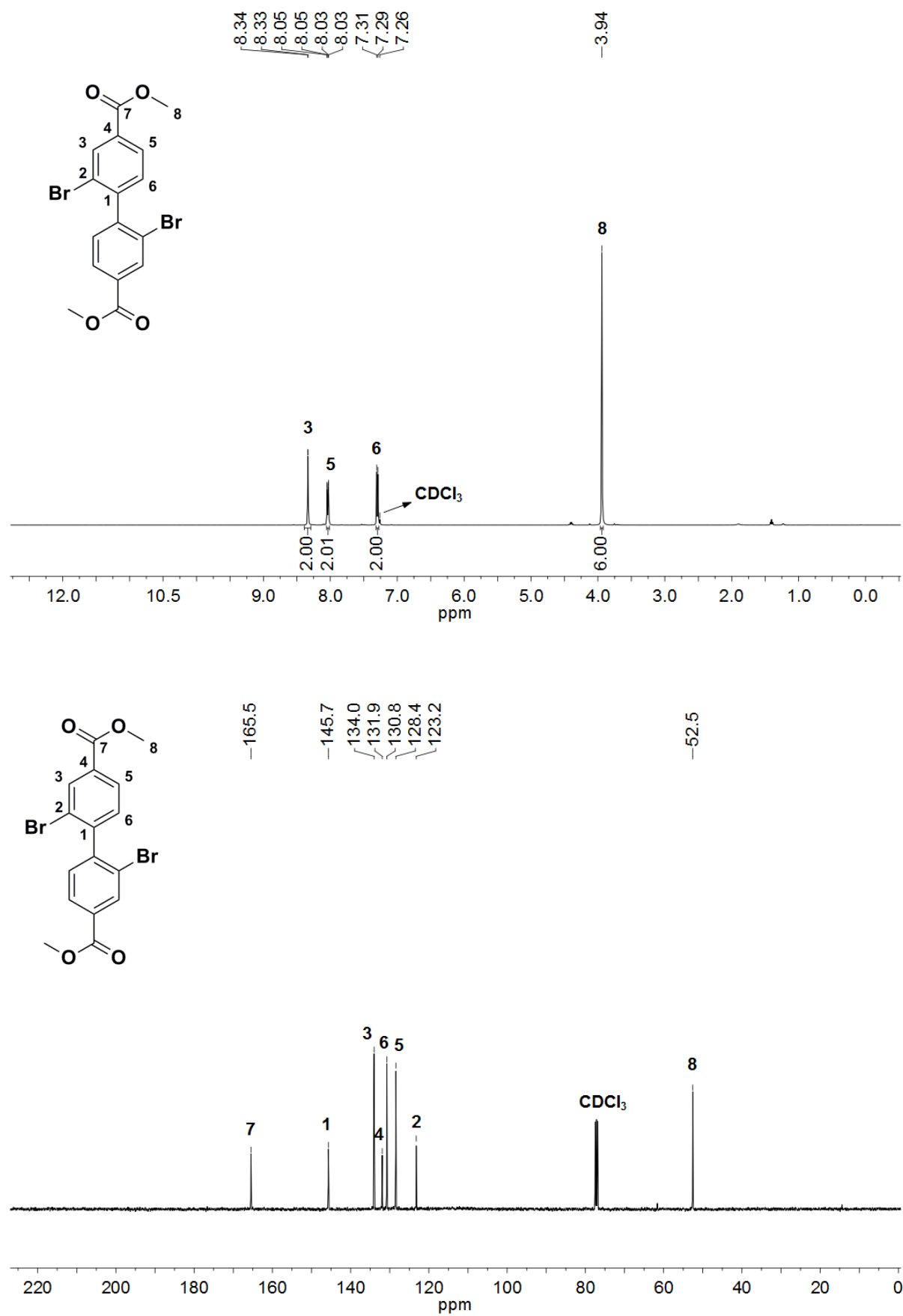


Figure 2.8 ^1H and ^{13}C NMR spectra of **2** recorded in CDCl_3 .

Compound **2** was hydrolyzed using KOH in a 1:1 methanol/water mixture ¹¹² to obtain the target carboxylic acid derivative **3** for the MOF synthesis. The disappearance of the methyl resonances in both the ¹H and the ¹³C NMR spectrum indicates the formation of this compound (Figure 2.9 and 2.10).

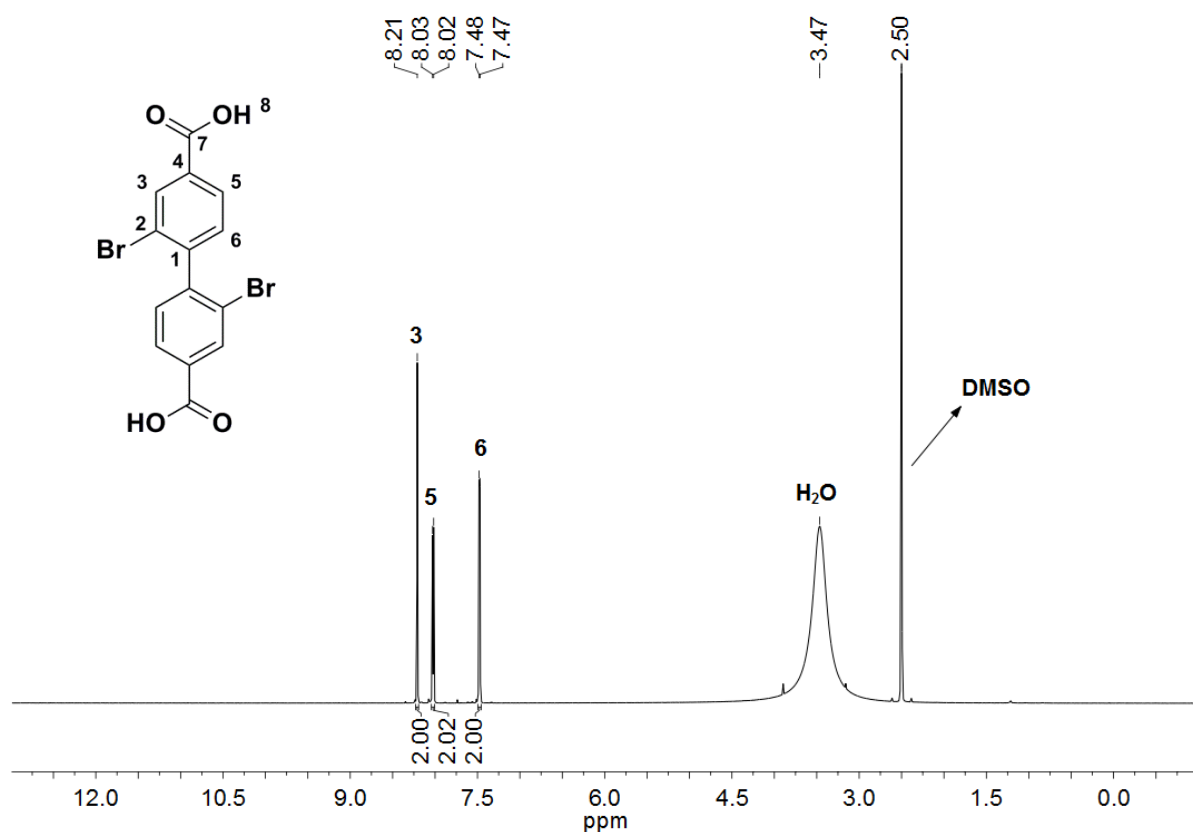


Figure 2.9 ¹H NMR spectrum of **3** recorded in DMSO-d₆.

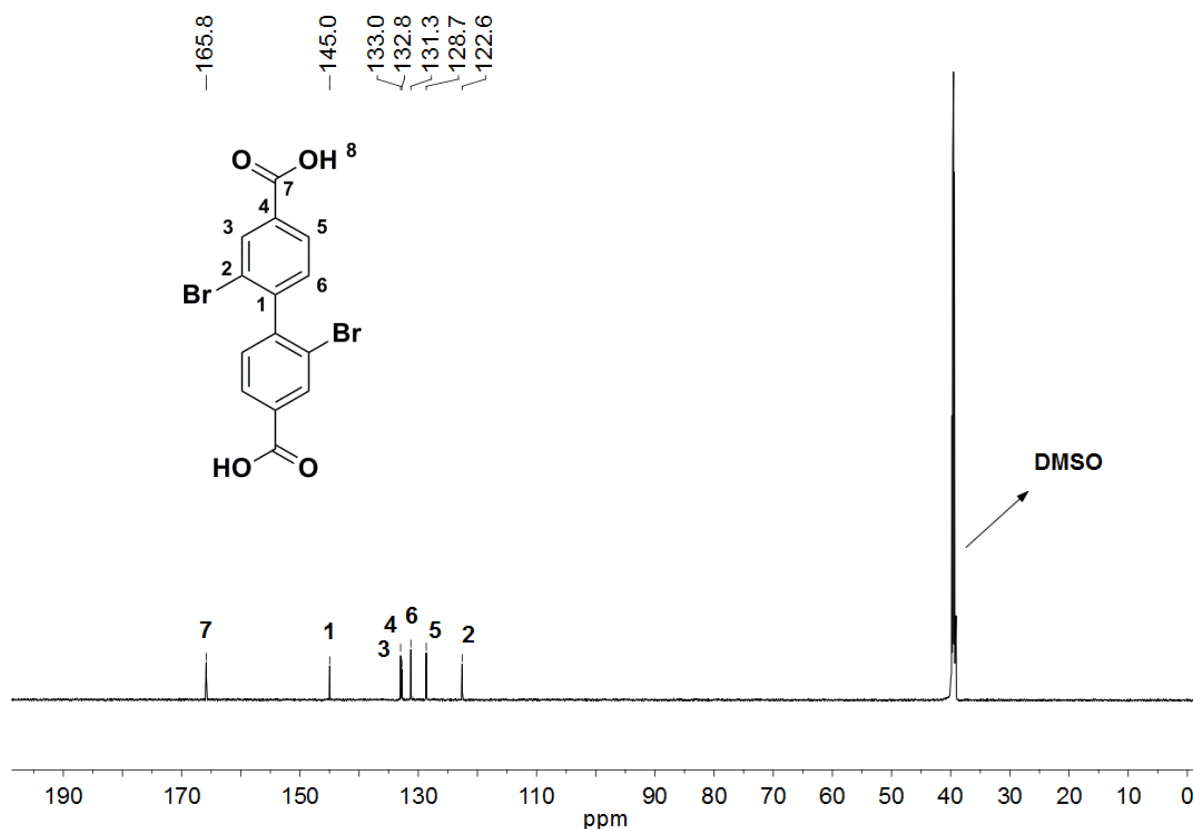
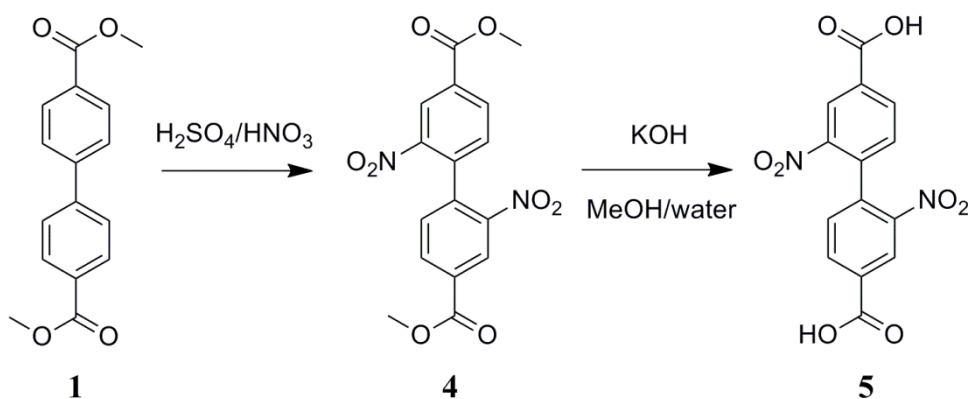


Figure 2.10 ^{13}C NMR spectrum of **3** recorded in DMSO- d_6 .

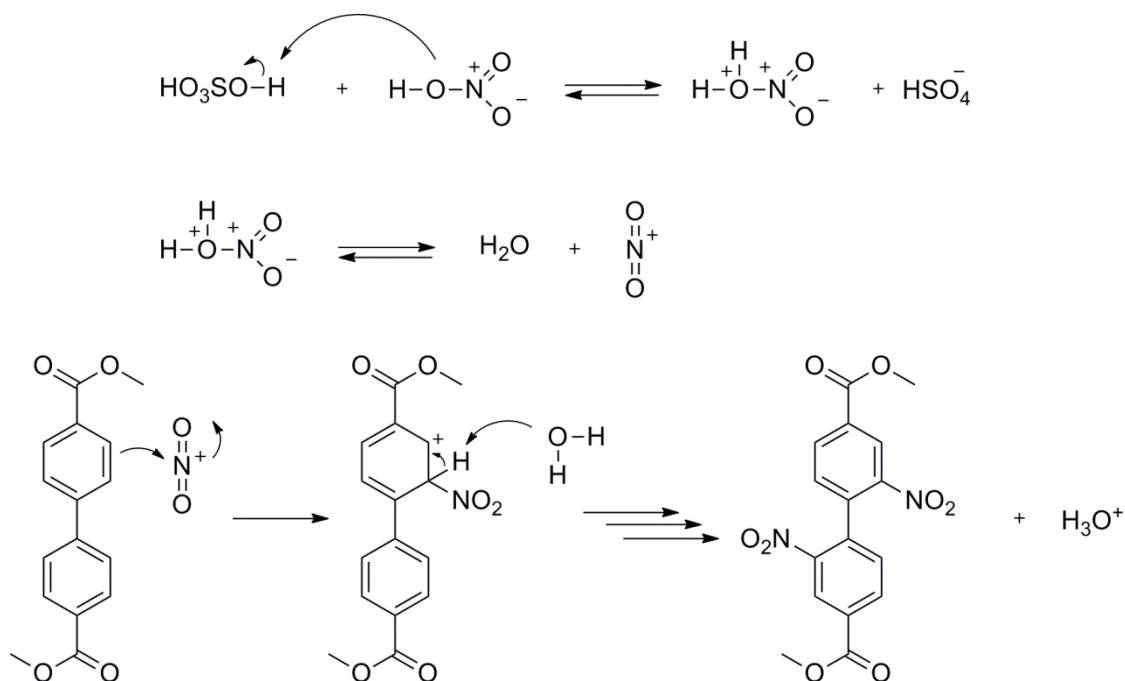
2.2.2 Synthesis of the NO_2 -BPDC Linker

To change the substitution pattern on the phenyl rings of the biphenyl dicarboxylate to $-\text{NO}_2$, an electrophilic aromatic nitration was carried out. In this study the nitration of **1** was performed using fuming nitric acid and concentrated sulfuric acid according to a published procedure (Scheme 2.3).¹¹³



Scheme 2.3 Overall synthesis of the linker **5**.

For the nitration, a sufficiently high concentration of nitronium ion is required which being provided by the addition of concentrated sulfuric acid (Scheme 2.4).¹¹⁴ The nitronium ions formed act as electrophiles and react readily with the phenyl rings. Nitro functionalized target ester forms by the loose of protons.



Scheme 2.4 Reaction mechanism for the nitration reaction.

Excess amounts of acids were used to favor the substitution of both phenyl rings. The acids HNO_3 and H_2SO_4 were previously mixed and afterwards the starting material was added in small portions until all solid dissolved completely to prevent the formation of undesirable by products. The obtained pale yellow product was recrystallized from methanol yielding crystals suitable for an X-ray structure analysis (Figure 2.11).

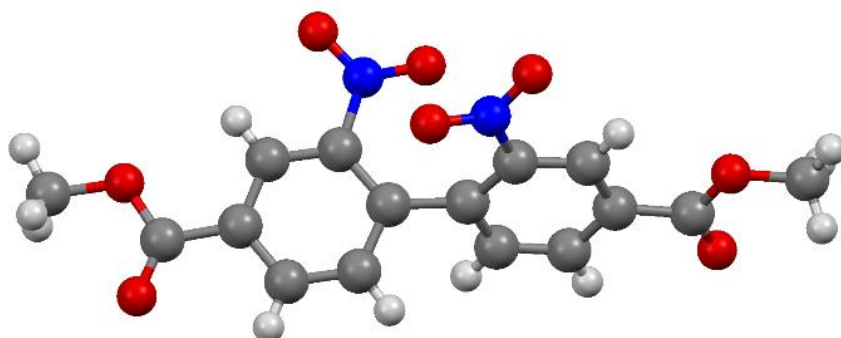


Figure 2.11 Crystal structure of **4**. Atom colors: C grey, O red, H white, N blue.

The ^1H NMR spectrum of **4** reveals three peaks in the aromatic and one resonance in the aliphatic region (Figure 2.12). A doublet in the aromatic region at 8.69 ppm ($J = 1.2$ Hz) belongs to the proton neighboring the $-\text{NO}_2$ group. Two further aromatic protons appear at 8.37 and 7.71 ppm as a doublet of doublet ($J = 8.0$ Hz, 1.2 Hz) and a doublet ($J = 8.0$ Hz) respectively. A singlet peak at 3.96 ppm is assigned to the $-\text{OCH}_3$ group. As expected, the ^{13}C NMR spectrum shows eight peaks, the carbon resonances were assigned by an HMBC spectrum. When the spectrum is compared with the bromine functionalized ester's ^{13}C NMR data, the effect of the different groups on the phenyl ring can easily be observed. The electron withdrawing $-\text{NO}_2$ group shifts the resonance of the C2 carbon atoms to low field. They appear at 146.6 ppm, while they appear at 123.2 ppm for **2** (Figure 2.13).

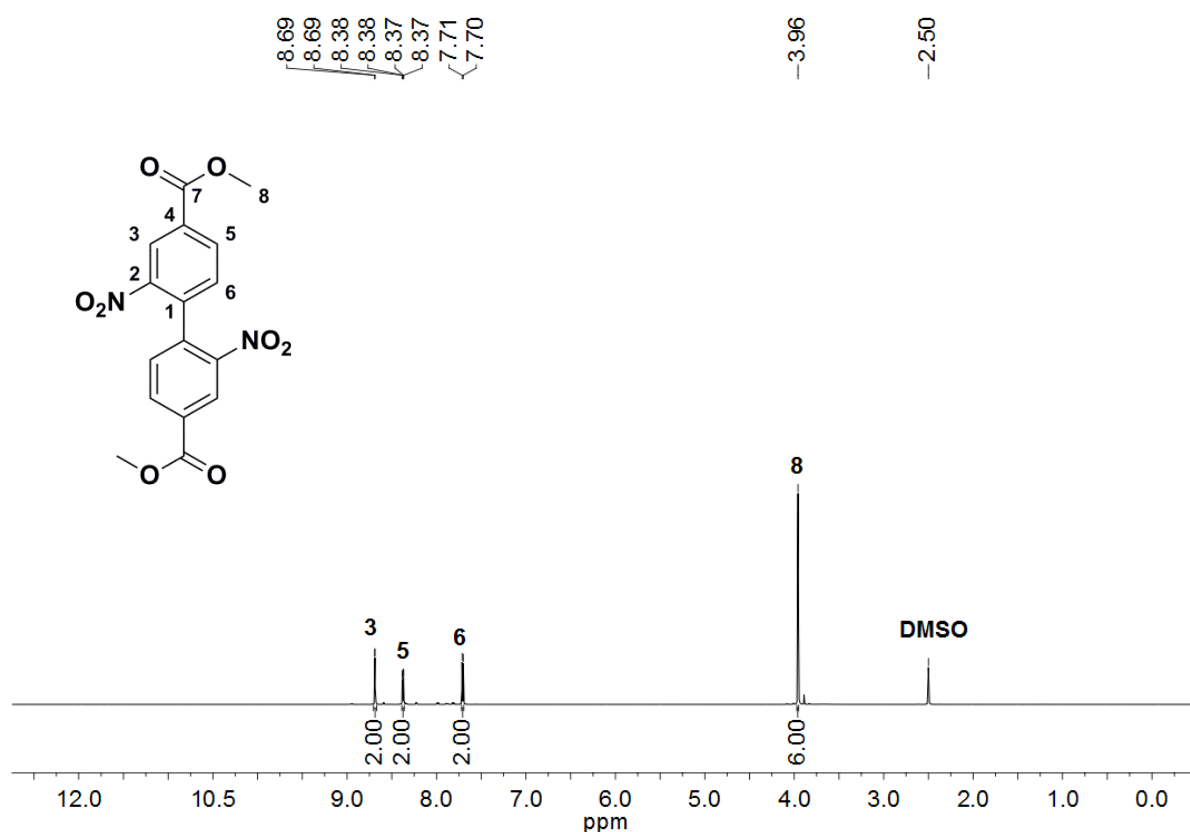


Figure 2.12 ^1H NMR spectrum of **4** recorded in DMSO-d_6 .

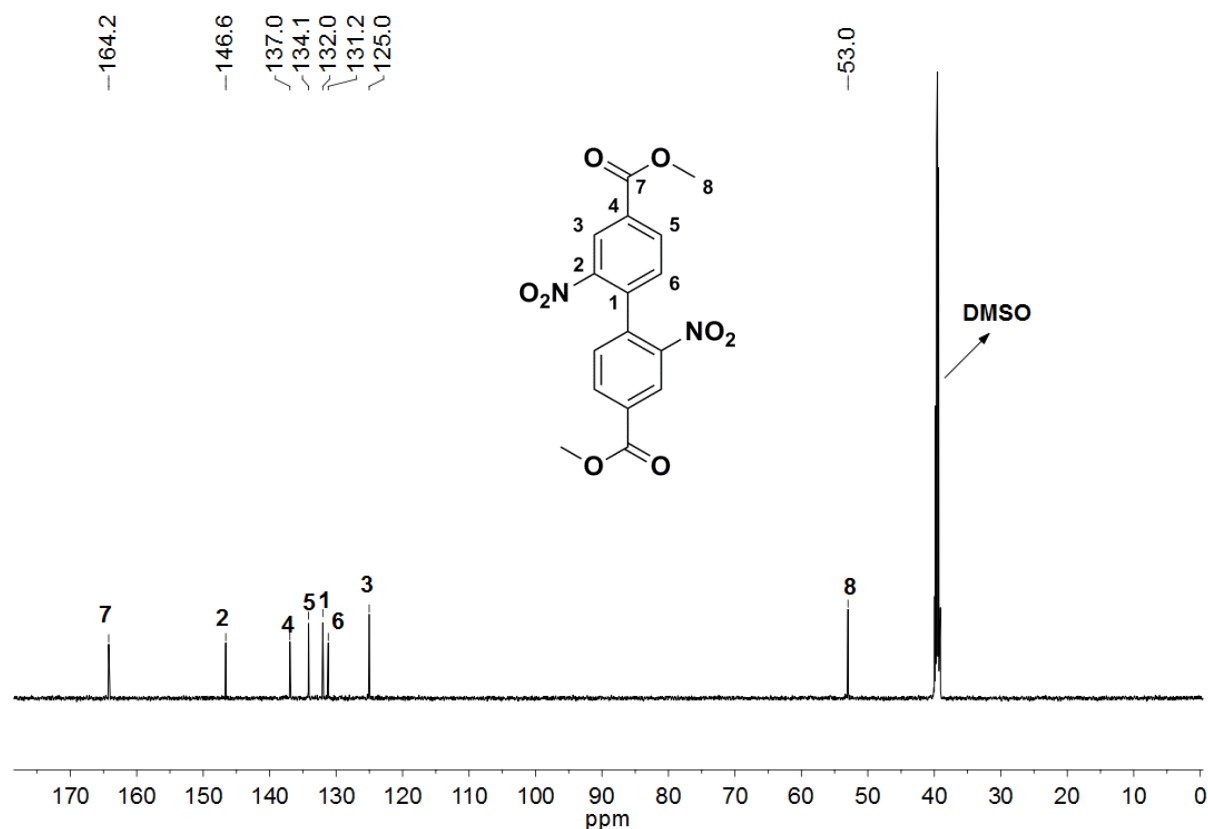


Figure 2.13 ^{13}C NMR spectrum of **4** recorded in DMSO-d_6 .

4 was hydrolyzed by using KOH in a MeOH/water mixture as described for the bromo derivative. The formation of the carboxylic acid **5** was proved by ^1H and ^{13}C NMR as well as by elemental analysis. The disappearance of the methoxy resonance in both spectra clearly proves the formation of the target compound **5**.

2.2.3 Synthesis of the NH_2 -BPDC Linker

A reduction of nitro groups to amino groups can be performed by using different reducing agents like SnCl_2/HCl ,¹¹⁵ $\text{NaBH}_4/\text{Raney Nickel}$,¹¹⁶ $\text{Zn}/\text{hydrazinium monoformate}$,¹¹⁷ Fe/HCl ,¹¹⁸ $\text{Al}/\text{NH}_4\text{Cl}/\text{MeOH}$ ¹¹⁹ etc. In general, the reduction of nitro compounds follows the path below (Scheme 2.5). First, the nitro group is reduced to a nitroso group, then the reductive addition of hydrogen forms hydroxylamine, which is further reduced to the amine.¹¹⁴

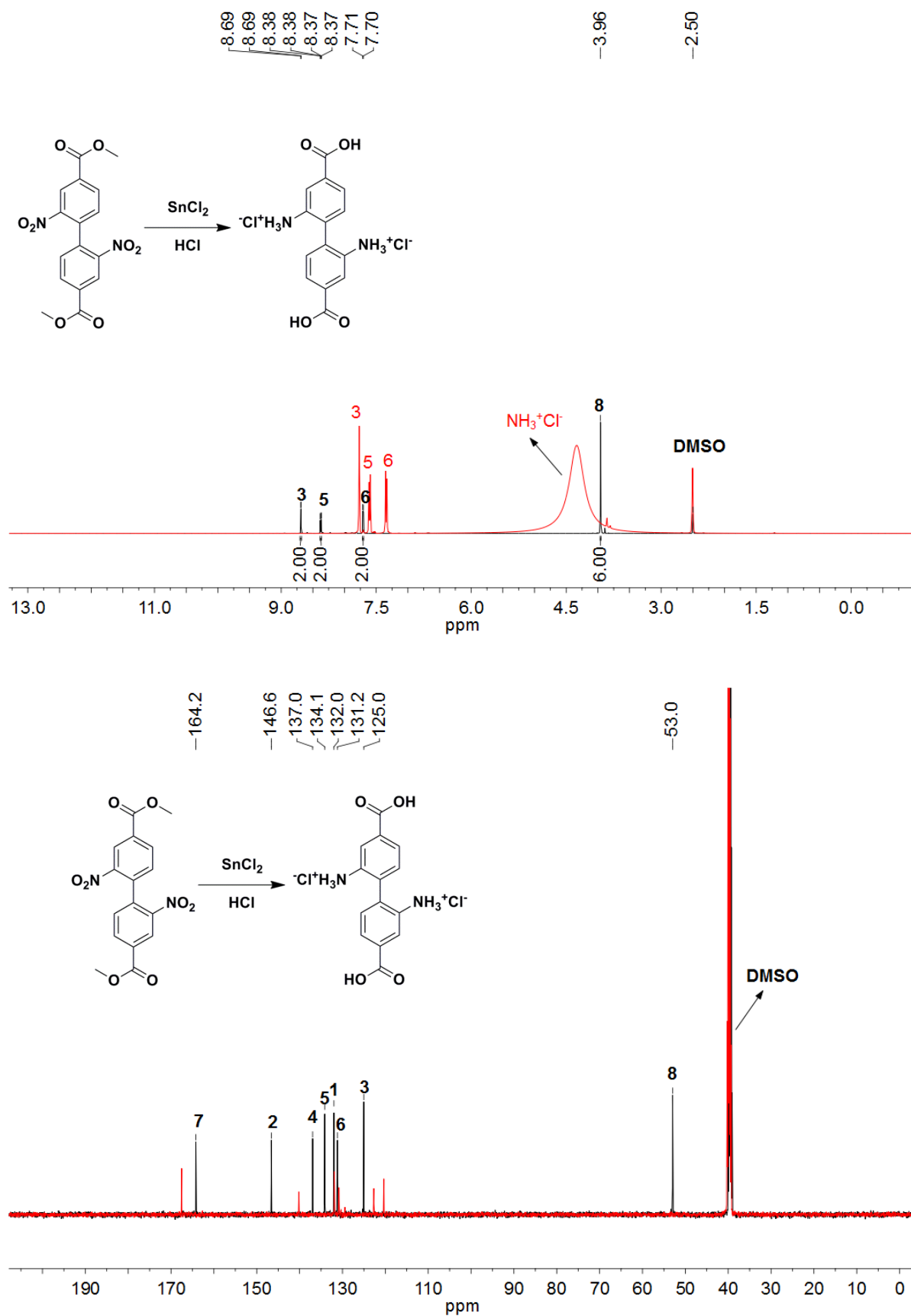


Scheme 2.5 Reduction of the nitro group.

In this study, the first attempt to obtain the amino derivative was applying SnCl_2/HCl as the reducing agent.¹²⁰ Both ^1H NMR and ^{13}C NMR spectra reveal the reduction of the nitro group as well as the hydrolysis of ester by the disappearance of the $-\text{OCH}_3$ group at 3.96 ppm in the ^1H NMR spectrum and at 53.0 ppm in the ^{13}C NMR spectrum (Figure 2.14). Elemental analysis strongly supported the desired structure containing one mole of HCl per formula unit (Table 2.1). This is due to the excess amounts of acid used, since the hydrolysis of the esters can also occur in an acidic medium.¹²¹ The ammonium salt could not be purified by the treatment with a base because of the low solubility of the carboxylic acid. Moreover, when lower amounts of acid are used in order to prevent the salt formation, the complete reduction could not be achieved.

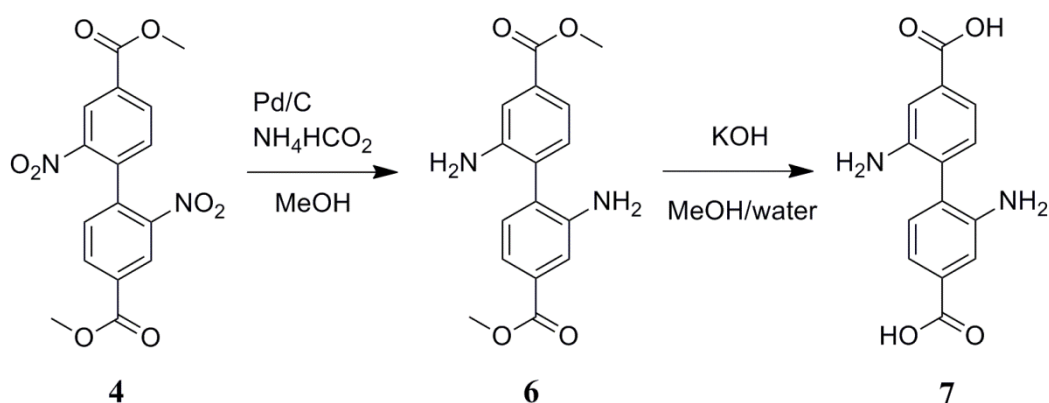
Table 2.1 Calculated and found elemental composition of $\text{C}_{14}\text{H}_{12}\text{N}_2\text{O}_4\cdot\text{HCl}$.

$\text{C}_{14}\text{H}_{12}\text{N}_2\text{O}_4\cdot\text{HCl}$ (308.72 g/mol)			
	C	H	N
Calculated	54.47 %	4.24 %	9.07 %
Found	54.27 %	4.60 %	8.97 %



Although the target carboxylic acid was obtained in a one step reaction, the presence of HCl in the molecule failed the MOF synthesis resulting in a precipitation of a microcrystalline material instead of crystal formation.

To prevent the formation of ammonium salts, another synthesis routes without the use of acid was applied. It was carried out with Pd/C as the reducing agent and NH_4HCO_2 as the hydrogen transfer agent (Scheme 2.6).¹²² Due to the low solubility of **4** large amounts of methanol had to be used, since it was observed that if the starting material was not completely dissolved, the reaction ended with very low yields. Moreover, in contrast to the stated reaction times (3-120 min) in the literature, the reaction medium had to be refluxed for at least 4 h for full conversion. After optimization of the reaction conditions, **6** was synthesized successfully. Recrystallization of the resulting yellow solid from methanol yielded yellow crystals suitable for an X-ray analysis (Figure 2.15).



Scheme 2.6 Overall reaction for the synthesis of linker **7**.

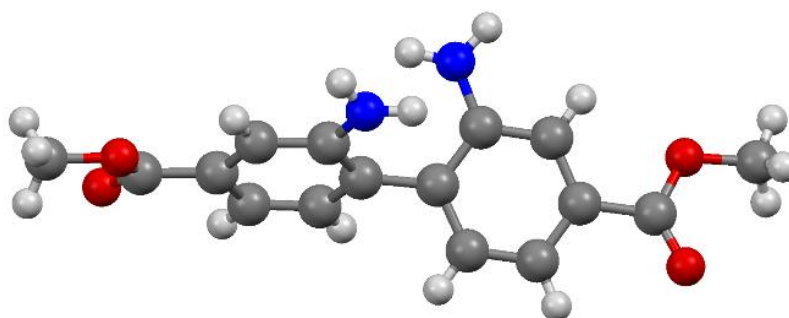


Figure 2.15 Crystal structure of **6**. Atom colors: C grey, O red, H white, N blue.

The ^1H NMR spectrum of **6** reveals three peaks in the aromatic region and one resonance in the aliphatic region as expected (Figure 2.16). A doublet in the aromatic region at 7.44 ppm with coupling constant 1.2 Hz belongs to the proton neighboring the $-\text{NH}_2$ group. The ortho protons appear at 7.23 and 7.08 ppm as a doublet of doublet ($J = 8.0$ Hz, 1.2 Hz) and a doublet ($J = 8.0$ Hz) respectively. A singlet peak at 3.83 belongs to the $-\text{OCH}_3$ group. It can be seen that all aromatic protons shift to higher field when compared with the ^1H NMR spectrum of **4**, due to the increase in electron density of the product. The lone pair of amine donates the electrons to the phenyl ring providing delocalization of the electrons on the ring, as a result of this phenyl protons resonate in higher field. The ^{13}C NMR spectrum shows eight peaks as expected (Figure 2.17). The determination of the carbon atoms was done by HMBC technique.

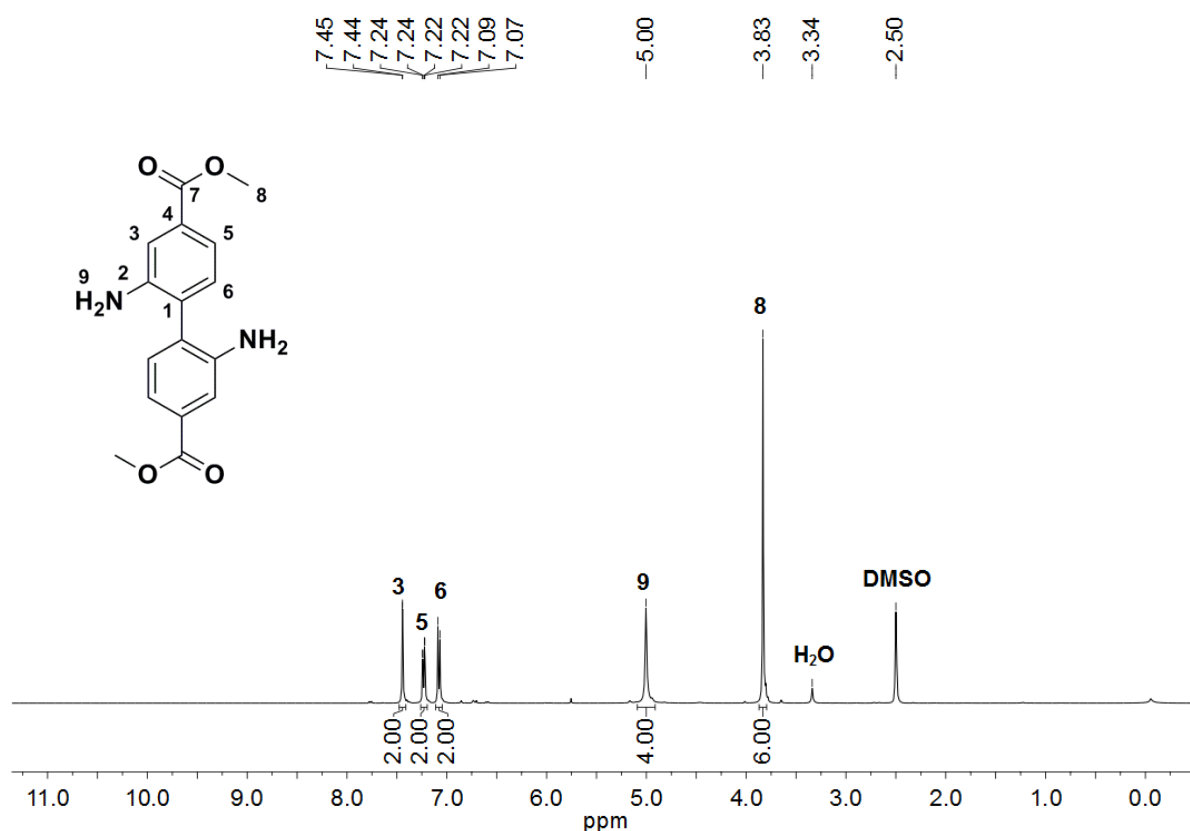


Figure 2.16 ^1H NMR spectrum of **6** recorded in $\text{DMSO}-d_6$.

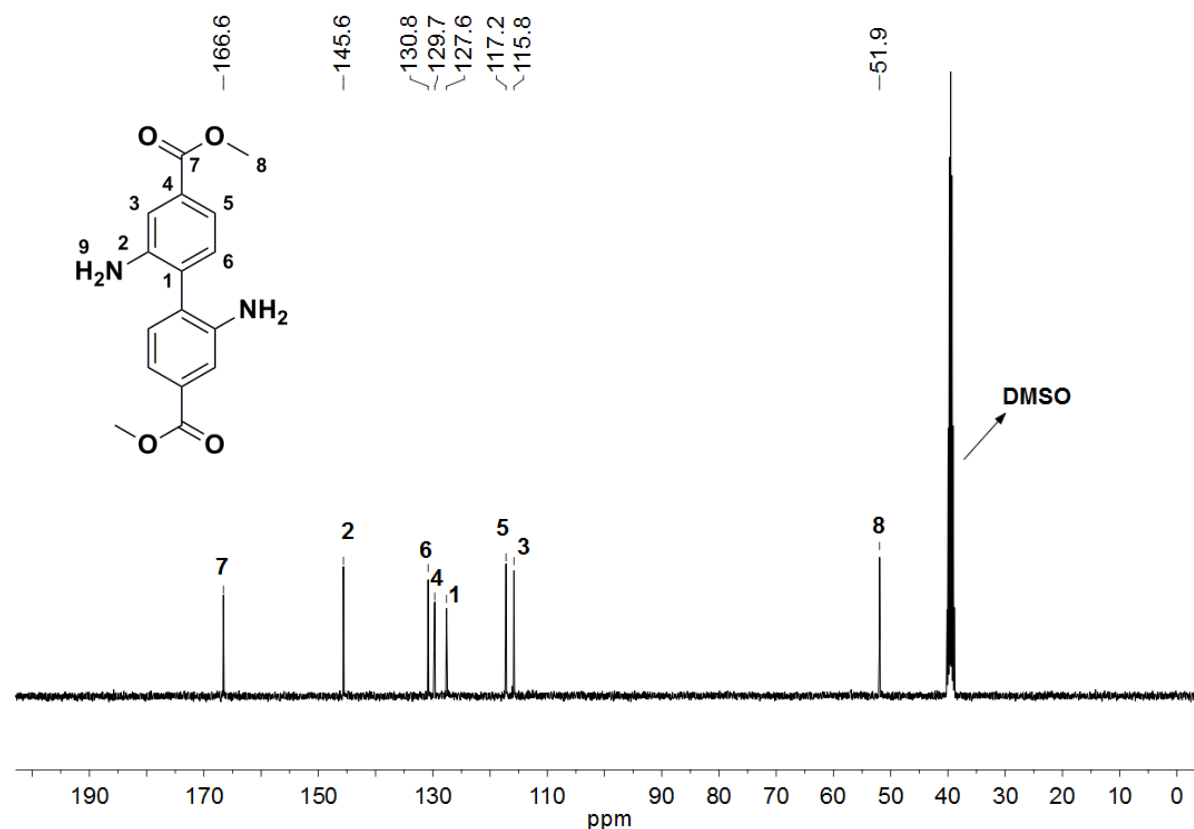


Figure 2.17 ^{13}C NMR spectrum of **6** recorded in DMSO-d_6 .

For the desired carboxylic acid (**7**), the ester **6** was again hydrolyzed by using KOH in a MeOH/water mixture. Performing the hydrolysis with HCl led to the corresponding ammonium salt. Since this group affects the MOF synthesis causing an acidic reaction medium, acetic acid was applied to obtain the desired amino carboxylic acid derivative **7** (Scheme 2.6).

2.3 Synthesis of the $-\text{Br}$, $-\text{NO}_2$ and $-\text{NH}_2$ Functionalized BPDC MOFs; ZnBrBPDC , ZnNO_2BPDC and ZnNH_2BPDC

Three different MOFs were synthesized solvothermally according to methods which were previously published by Yaghi *et al.*¹²³ $\text{Zn}(\text{NO}_3)_2 \cdot 4\text{H}_2\text{O}$ was used as the metal source and DMF as the solvent. Ligands **3**, **5** and **7** were applied as linkers to build up the framework. The reaction was performed in 60 ml (linker **5** and **7**) and 125 ml (linker **3**) PP-bottles which were tightly closed before placing them into the oven.

Formation of colorless cubic crystals was observed for the bromo functionalized linker **3** after 36 h. For the linkers **5** and **7**, solely precipitation was observed under similar conditions. Therefore the bottles were shaken periodically during the reaction in order to

prevent the precipitation. After 48 h, linker **5** yielded light yellow crystals and linker **7** yielded dark yellow crystals. SEM pictures of the crystals are presented below (Figure 2.18).

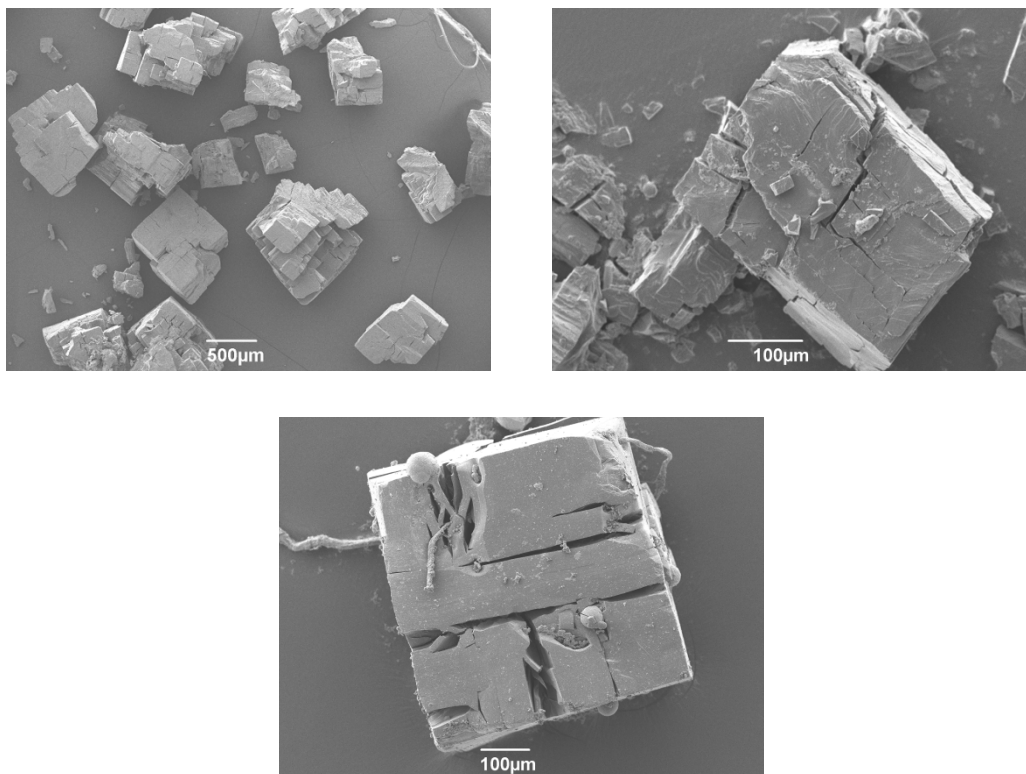


Figure 2.18 SEM pictures of the MOF crystals synthesized with linker **3** (top, left), linker **5** (top, right) and linker **7** (bottom).

We named these MOFs as **ZnBrBPDC**, **ZnNO₂BPDC** and **ZnNH₂BPDC** according to the functional group on the phenyl groups of the linkers (Figure 2.19).

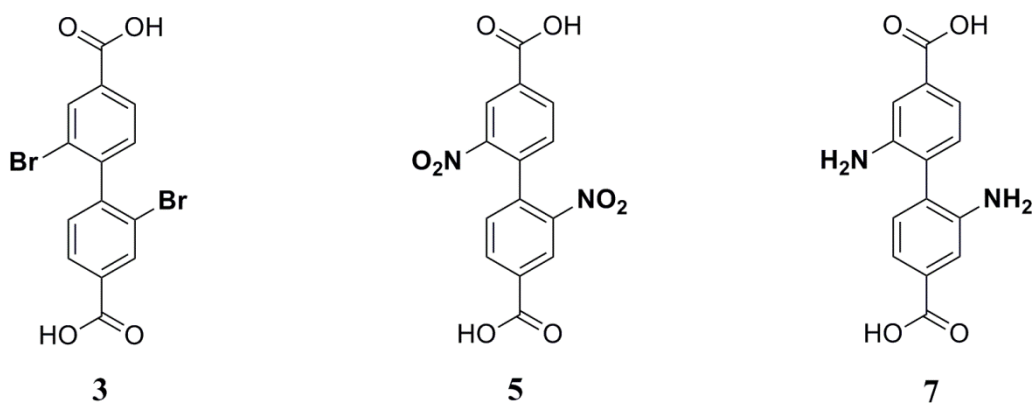


Figure 2.19 Linkers **3**, **5** and **7** used for the synthesis of **ZnBrBPDC**, **ZnNO₂BPDC** and **ZnNH₂BPDC**.

2.3.1 Characterization of ZnBrBPDC, ZnNO₂BPDC and ZnNH₂BPDC

Characterization of the materials was done using different techniques. Single crystal X-ray diffraction, as well as powder XRD (PXRD) measurements were used to determine the structure of the MOFs. FT-IR and solid state NMR measurements were used to prove the chemical constitution of the materials. The microporosities of the materials were confirmed by N₂ adsorption measurements. Thermogravimetric analyses (TGA) were used to find out the stabilities and as well as the chemical composition of the MOFs along with the elemental analysis.

2.3.1.1 Single Crystal X-Ray Diffraction Measurements of ZnBrBPDC, ZnNO₂BPDC and ZnNH₂BPDC

Colorless cubic shaped crystals of **ZnBrBPDC** were characterized by using single crystal X-ray diffraction. The results revealed that a catenated structure was obtained. Catenation can be explained as an intergrowing of two or more similar frameworks.⁴² In general, 2- and 3-fold catenation is observed,⁹¹ but higher degrees are also reported in the literature.¹²⁴ Catenation may occur in either interpenetration or interweaving. Networks which are displaced from each other in a maximum distance are named as interpenetrated, if they are in close contact and displaced from each other minimally, the network is described as interwoven. In an interwoven structure pores of two networks superimpose and remain empty.¹²⁵ It is shown in the literature that longer linkers favor the formation of interpenetrated structures.¹²³

Figure 2.20 and 2.21 show the crystal structure for **ZnBrBPDC** with different modes of presentation. To clarify the interpenetrated framework, linkers are shown as single lines in Figure 2.21.

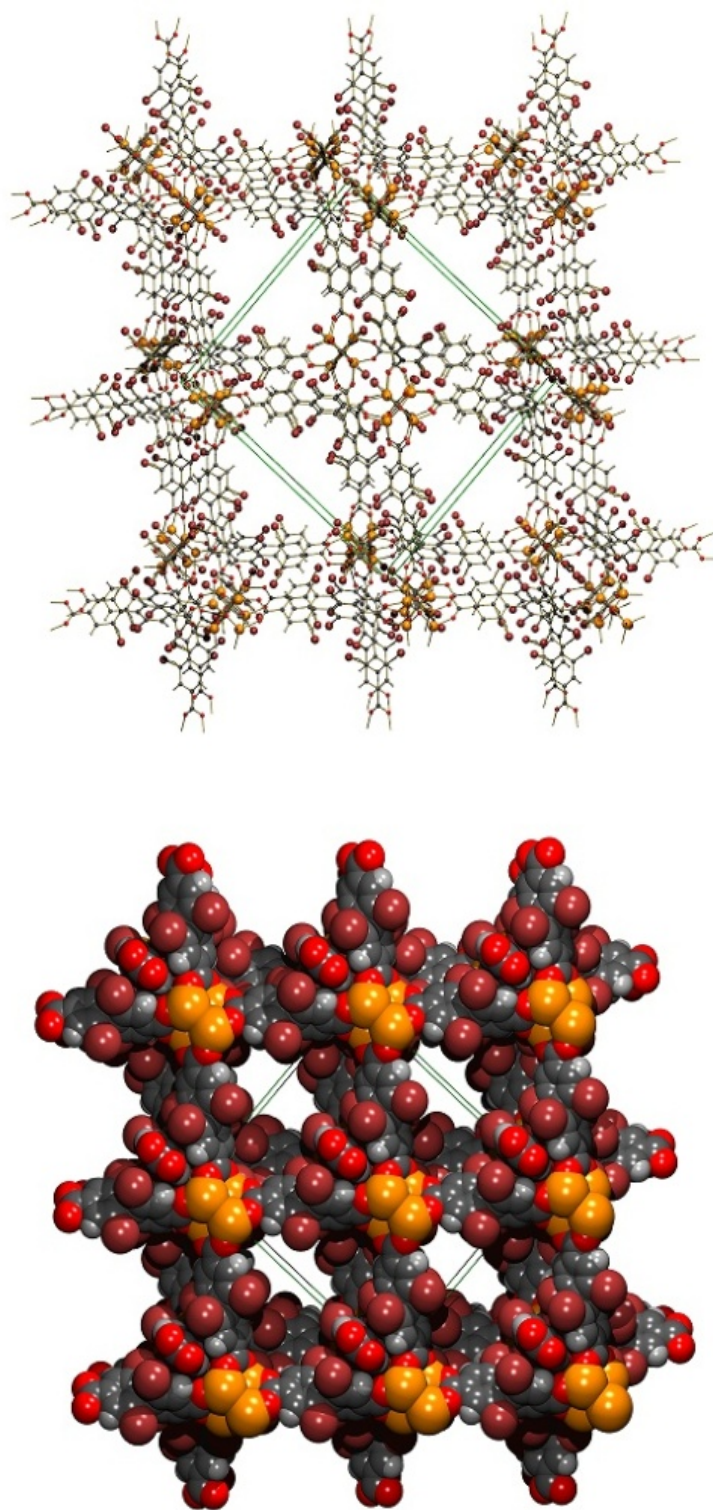


Figure 2.20 Crystal structure of **ZnBrBPDC**. Atom colors: C grey, O red, Zn orange.

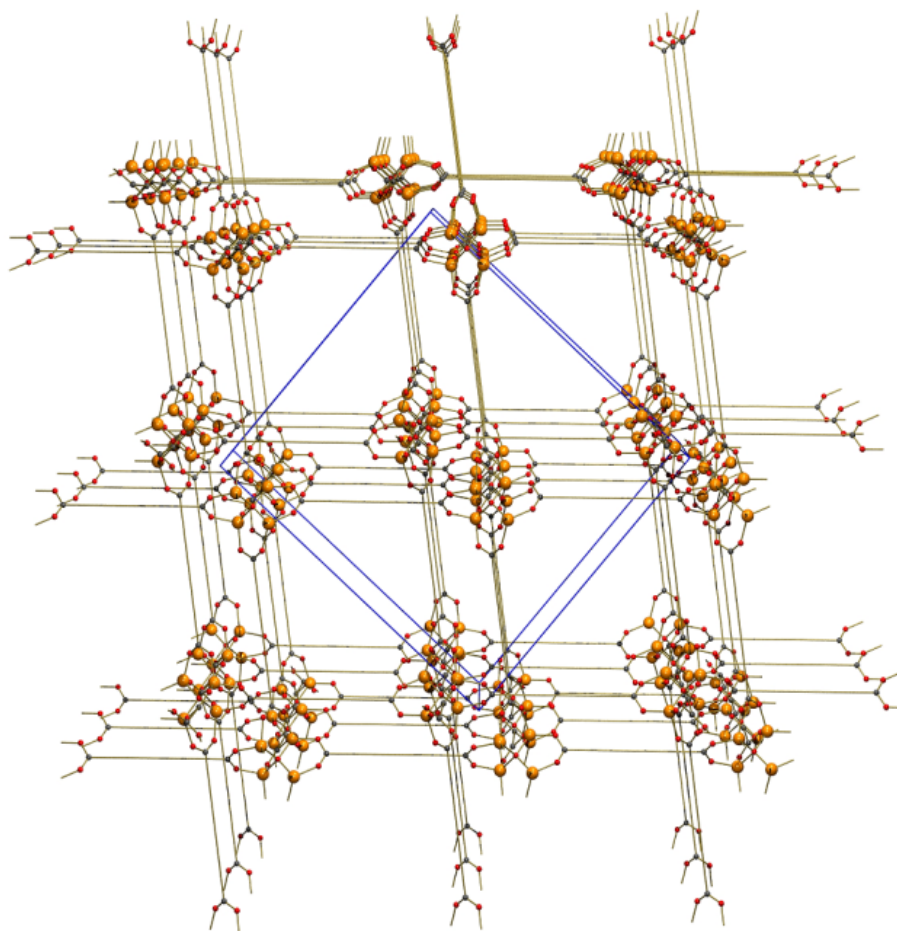


Figure 2.21 Crystal structure of **ZnBrBPDC**. Atom colors: C grey, O red, Zn orange. For clarification linkers are shown as single lines.

When we have a closer look to the structure, we find that each edge contains a Zn_4O tetrahedron being formed by four Zn^{2+} atoms bound to a central oxygen anion. Each Zn^{2+} ion in this tetrahedron is linked by a carboxylate group of the linker yielding a $\text{Zn}(\text{O})(\text{R}-\text{CO}_2)_6$ cluster with an octahedral geometry.

The single crystal X-ray measurements of **ZnNO₂BPDC** showed that also an interpenetrated structure was obtained for this MOF (Figure 2.22). In contrast to **ZnBrBPDC**, which crystallizes in a cubic system, **ZnNO₂BPDC** crystallizes in a hexagonal system. The octahedral Zn-O-C clusters are linked by the NO_2 functionalized biphenyldicarboxylate struts.

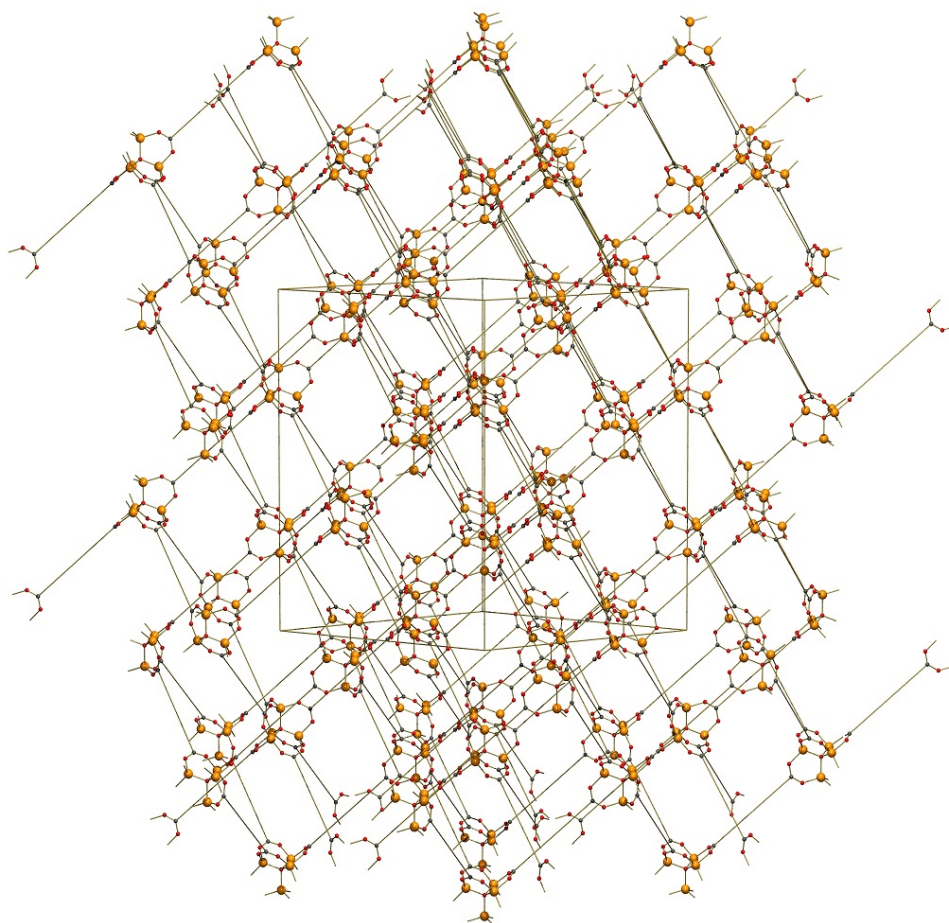


Figure 2.22 Crystal structure of **ZnNO₂BPDC**. Atom colors: C grey, O red, Zn orange. To clarify the interpenetrated framework, linkers are shown as single lines.

Due to the low crystal quality, the **ZnNH₂BPDC** structure could not be measured by single crystal X-ray measurements. PXRD measurements were used for the structural elucidation of **ZnNH₂BPDC**.

2.3.1.2 Powder X-Ray Diffraction (PXRD) Measurements of ZnBrBPDC, ZnNO₂BPDC and ZnNH₂BPDC

The PXRD pattern of the as-synthesized **ZnBrBPDC** shows a pattern similar to the calculated PXRD pattern of the crystals. The splitting of the reflection at $2\theta = 7.4^\circ$ can be attributed to the interpenetrated structure of **ZnBrBPDC** which resembles the PXRD pattern of the interpenetrated IRMOF-9 (linker: 4,4'-biphenyldicarboxylic acid).¹²³

The PXRD pattern of the **ZnBrBPDC** crystals activated with acetone is also shown in Figure 2.23. Before the measurements, crystals were kept in dry acetone for one day in order to remove DMF and the residues of the starting materials. When the PXRD pattern of the acetone exchanged **ZnBrBPDC** crystals is compared with the as-synthesized system and the calculated pattern, a slight shift to lower degrees was observed for all reflections. This can be due to using different instruments having different calibrations. The disappearance of some peaks becomes obvious. This can be due to the removal of solvents from the pores which causes a flexible movement of organic struts.¹²⁶ The broadening of the reflections at $2\theta = 7.0^\circ$ and 11.2° can be attributed to a loss of crystallinity.¹²⁷

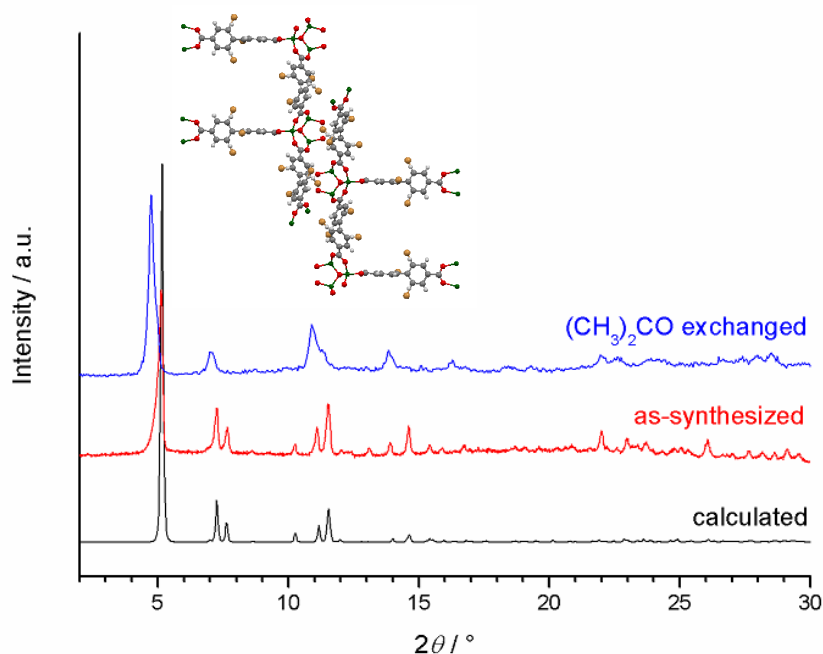


Figure 2.23 PXRD patterns of **ZnBrBPDC**. Calculated pattern from the crystal structure (black), as-synthesized sample (red) and the acetone exchanged sample (blue).

The PXRD pattern of **ZnNO₂BPDC** reveals reflections very similar to the calculated pattern (Figure 2.24). A splitting of the reflection at $2\theta = 7.2^\circ$ can again be attributed to an interpenetrated structure. For the acetone exchanged samples, the PXRD pattern shows almost the same positions of the reflections of the as-synthesized one, but a strong change is observed in the intensities of the reflections. While the intensities of the reflections at $2\theta = 5.2^\circ$, 7.2° and 7.4° decrease, the intensity of the reflection at $2\theta = 10.3^\circ$ increases. Differences in the intensities of the reflections can be attributed to guest molecules in the pores. In general materials having large pores which are accessible to guest molecules show reflection intensities highly dependent on the amount and scattering power of the species located inside the cavities especially the reflections at low angles.⁴⁵ Such a behavior is not observed for the **ZnBrBPDC** pattern. This can be attributed to an insufficient removal of the guest molecules from **ZnBrBPDC** samples. Contrary to **ZnBrBPDC**, the acetone exchanged sample of **ZnNO₂BPDC** shows almost no peak broadening. The slight shift to higher degrees was also observed for all reflections which can be again explained as the different instruments with different calibrations.

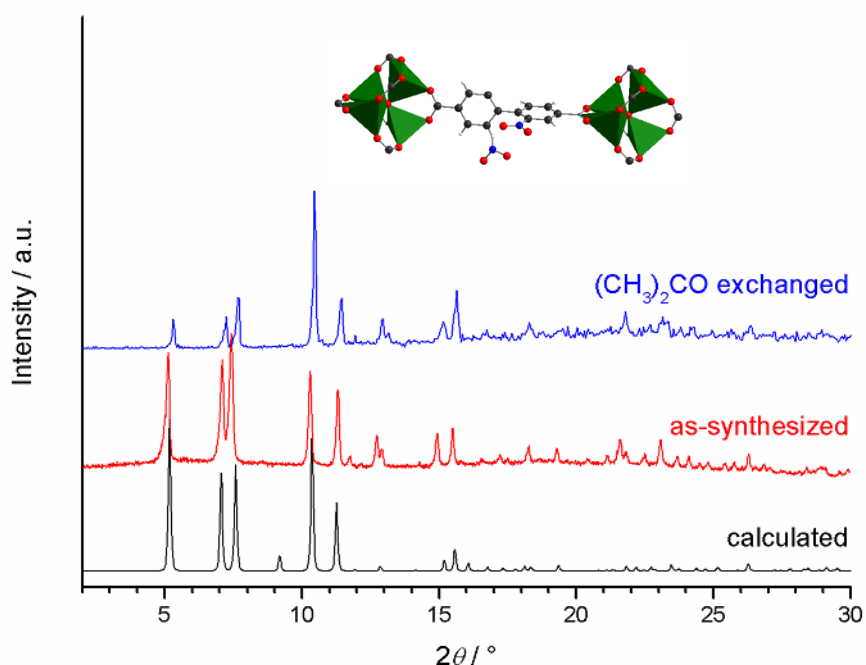


Figure 2.24 PXRD patterns **ZnNO₂BPDC**. The calculated pattern from the crystal structure (black), the as-synthesized sample (red) and the acetone exchanged sample (blue).

Figure 2.25 shows the PXRD patterns of **ZnNH₂BPDC** and the calculated pattern from the crystal structure of IRMOF-9. Before the measurements, the crystals were kept in dry acetone for one day in order to remove DMF and the residues of the starting materials. Although, comparison of the **ZnNH₂BPDC** patterns with the calculated IRMOF-9 patterns shows peaks at almost similar 2θ angles, it clearly demonstrates that after solvent exchange, the structure loses its crystallinity. When the **ZnNH₂BPDC** pattern is compared with the acetone exchanged samples of **ZnBrBPDC** and **ZnNO₂BPDC**, almost same reflections are observed. Low intensities of the reflections at low angles can be again attributed to the presence of the guest molecules inside the cavities. A slight shift to lower degrees in all reflections can be due to using different instruments having different calibrations.

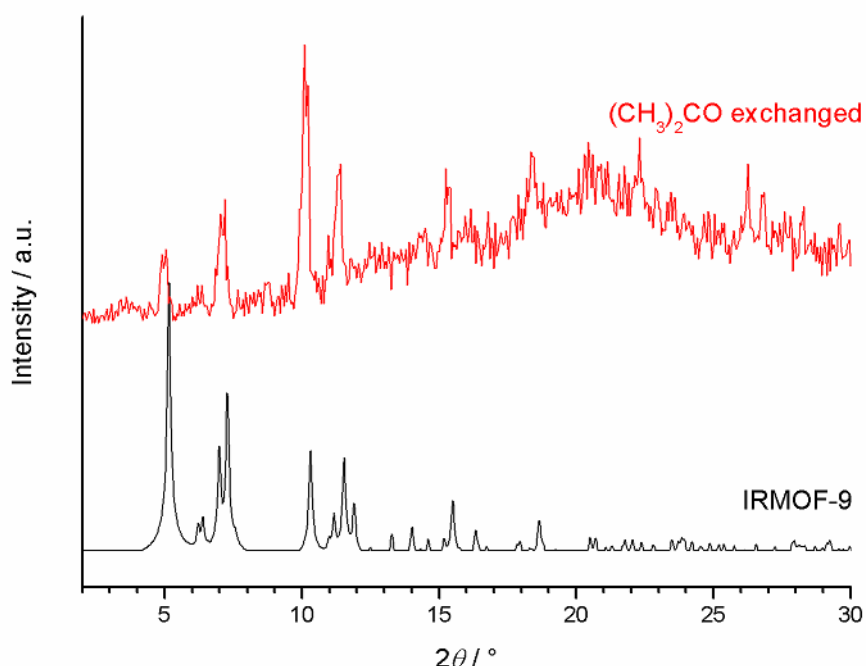


Figure 2.25 PXRD pattern of the acetone exchanged **ZnNH₂BPDC** sample (red) and the calculated pattern of IRMOF-9 (black).

2.3.1.3 Thermogravimetric Analysis (TGA) of ZnBrBPDC, ZnNO₂BPDC and ZnNH₂BPDC

The stability of the MOF samples was determined using thermogravimetric analysis (TGA). Before the measurements, the samples were soaked into acetone to remove the solvents

and the unreacted starting materials from the pores. The measurements were performed under ambient atmosphere at a constant heating rate of $5\text{ }^{\circ}\text{C min}^{-1}$ from room temperature up to $600\text{ }^{\circ}\text{C}$.

For **ZnBrBPDC**, two weight loss steps were observed: the first one starting at $100\text{ }^{\circ}\text{C}$ can be attributed to a loss of solvents (DMF, water) which is compatible with the elemental analysis data. The second mass loss above $400\text{ }^{\circ}\text{C}$ can be attributed to the complete collapse of the structure as a result of linker decomposition. According to the TGA results, it can be concluded that **ZnBrBPDC** is stable up to $400\text{ }^{\circ}\text{C}$ (Figure 2.26).

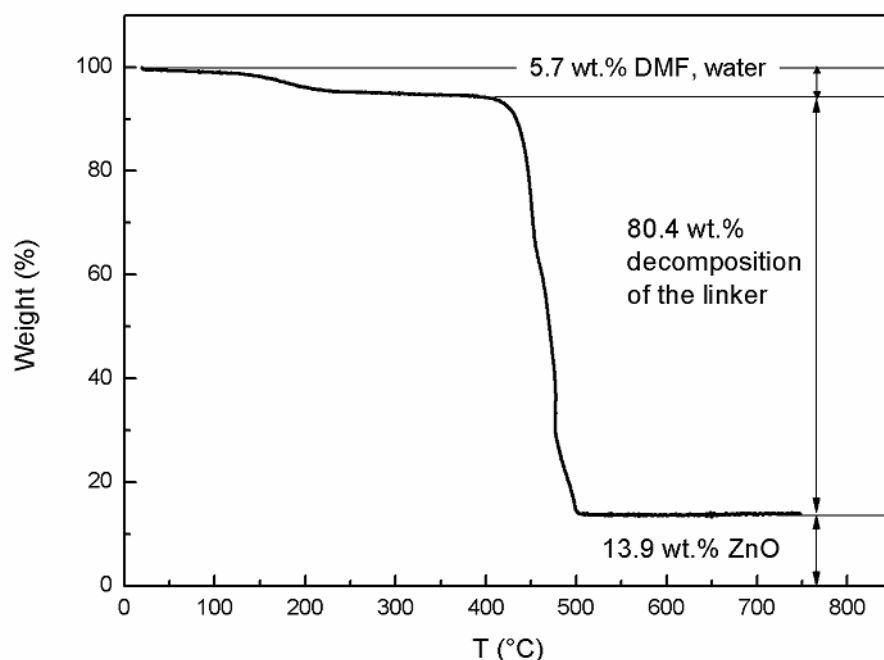


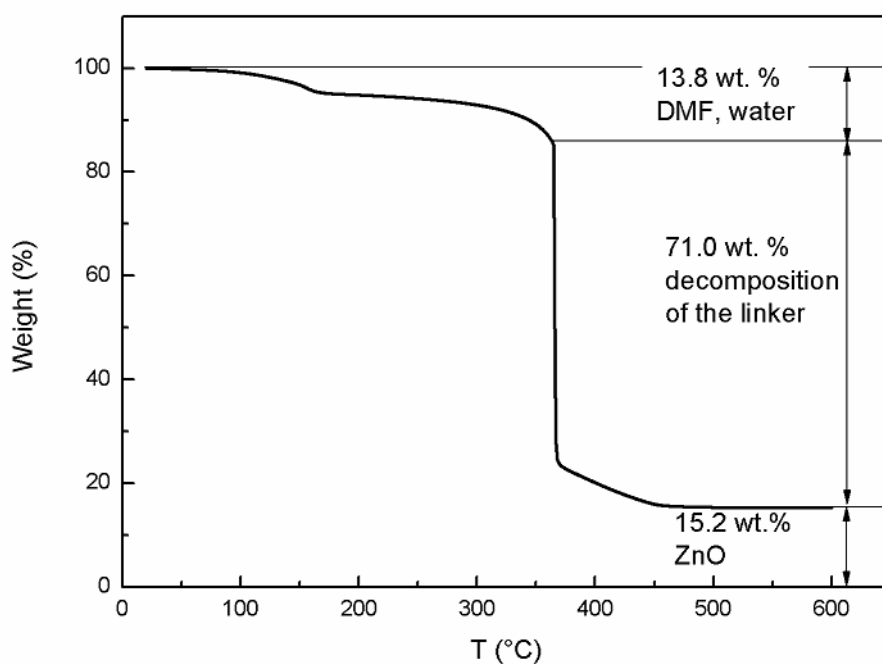
Figure 2.26 TGA of evacuated **ZnBrBPDC**.

Elemental analysis results can be also used to determine the composition of the evacuated **ZnBrBPDC** sample (Table 2.2). The results reveal that the weight loss of 5.73 % up to $250\text{ }^{\circ}\text{C}$ in TGA belongs to DMF molecules (5.91 wt. %). According to the elemental analysis, it also becomes clear that 2.49 wt. % of linker **3** remained inside the pores of **ZnBrBPDC**.

Table 2.2 Calculated and found elemental composition of evacuated **ZnBrBPDC**.

	$\text{C}_{42}\text{H}_{18}\text{Br}_6\text{O}_{13}\text{Zn}_4 \cdot (\text{DMF})_{1.30} \cdot (\text{C}_{14}\text{H}_6\text{Br}_2\text{O}_4)_{0.10}$		
	C	H	N
Calculated	35.26 %	1.75 %	1.13 %
Found	35.37 %	1.66 %	1.20 %

For **ZnNO₂BPDC**, two weight loss steps were observed too: the first one between 100 °C and 300 °C is due to the solvents (DMF, water) in the pores. The second mass loss above 300 °C can be attributed to the collapse of structure as a result of the linker decomposition. **ZnNO₂BPDC** is stable up to 350 °C (Figure 2.27).

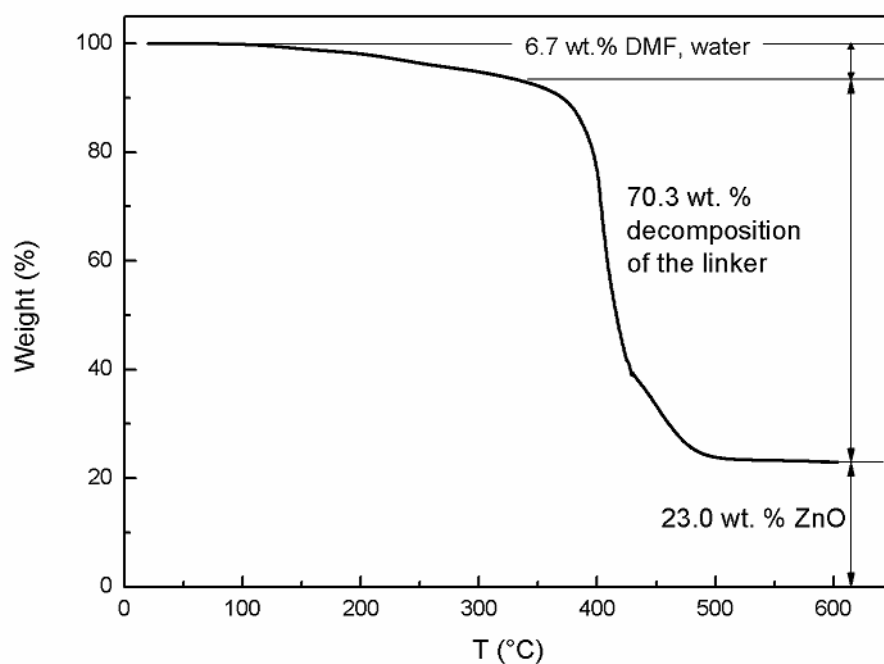
**Figure 2.27** TGA of evacuated **ZnNO₂BPDC**.

The elemental analysis of an evacuated **ZnNO₂BPDC** sample is in agreement with the TGA. It shows 14.16 wt. % of solvent in the pores. According to TGA, the solvent amount is calculated as 13.80 wt. %. It is also noticed that, besides solvent molecules, pores also contain molecules of linker **5** used in the synthesis (Table 2.3).

Table 2.3 Calculated and found elemental composition of evacuated **ZnNO₂BPDC**.

	C₄₂H₁₈N₆O₂₅Zn₄·(DMF)_{3.35}·(H₂O)_{0.15}·(C₁₄H₈N₂O₈)_{0.70}		
	C	H	N
Calculated	42.49 %	2.73 %	8.61 %
Found	43.83 %	4.08 %	7.26 %

ZnNH₂BPDC shows the same behavior in the TGA with two weight loss steps. When it is compared to the two other MOFs, the most remarkable difference is the higher ZnO amount (22.96 wt. %). This is due to the lower mass of the functional group –NH₂ in the linker compared to –Br and –NO₂. **ZnNH₂BPDC** is stable up to 380 °C (Figure 2.28).

**Figure 2.28** TGA of evacuated **ZnNH₂BPDC**.

The elemental analysis of an evacuated **ZnNH₂BPDC** sample reveals results compatible with the TGA data. According to the elemental analysis, the solvent amount in the pores is calculated to 6.57 wt. %, compared to 6.72 wt. % from the TGA results. It is also observed

that besides solvent molecules, the pores of the sample contain some of the linker **7** (3.38 wt. %) used in the synthesis (Table 2.4).

Table 2.4 Calculated and found elemental composition of evacuated **ZnNH₂BPDC**.

C₄₂H₃₀N₆O₁₃Zn₄·(DMF)_{1.00}·(H₂O)_{0.35}·(C₁₄H₁₂N₂O₄)_{0.15}			
	C	H	N
Calculated	46.35 %	2.78 %	7.72 %
Found	47.04 %	3.49 %	8.26 %

2.3.1.4 ¹³C CP-MAS NMR Measurements of ZnBrBPDC, ZnNO₂BPDC and ZnNH₂BPDC

The chemical structure of the MOF materials was further confirmed by solid state NMR measurements. Due to the cubic structure of the MOFs, one would expect one set of resonances in the solid state ¹³C NMR spectra for each chemically inequivalent carbon atom of the biphenyl linkers. This may be modified due to the fact that the rotation around the central C-C bond might be hindered leading to different rotamers. However, the differences in chemical shift for these rotamers should be small with respect to the resolution of the solid state NMR spectroscopy.

All solid state ¹³C CP-MAS NMR spectra of the MOF materials give two very small signals at about 30-35 ppm, corroborating the presence of small amounts of DMF in the cavities. The solid state ¹³C CP-MAS NMR spectrum of **ZnBrBPDC** shows five signals in the aromatic region which are in complete agreement with the seven resonances of the precursor compound (Figure 2.29). While some of the resonances are quite sharp, the others tend to become broad.

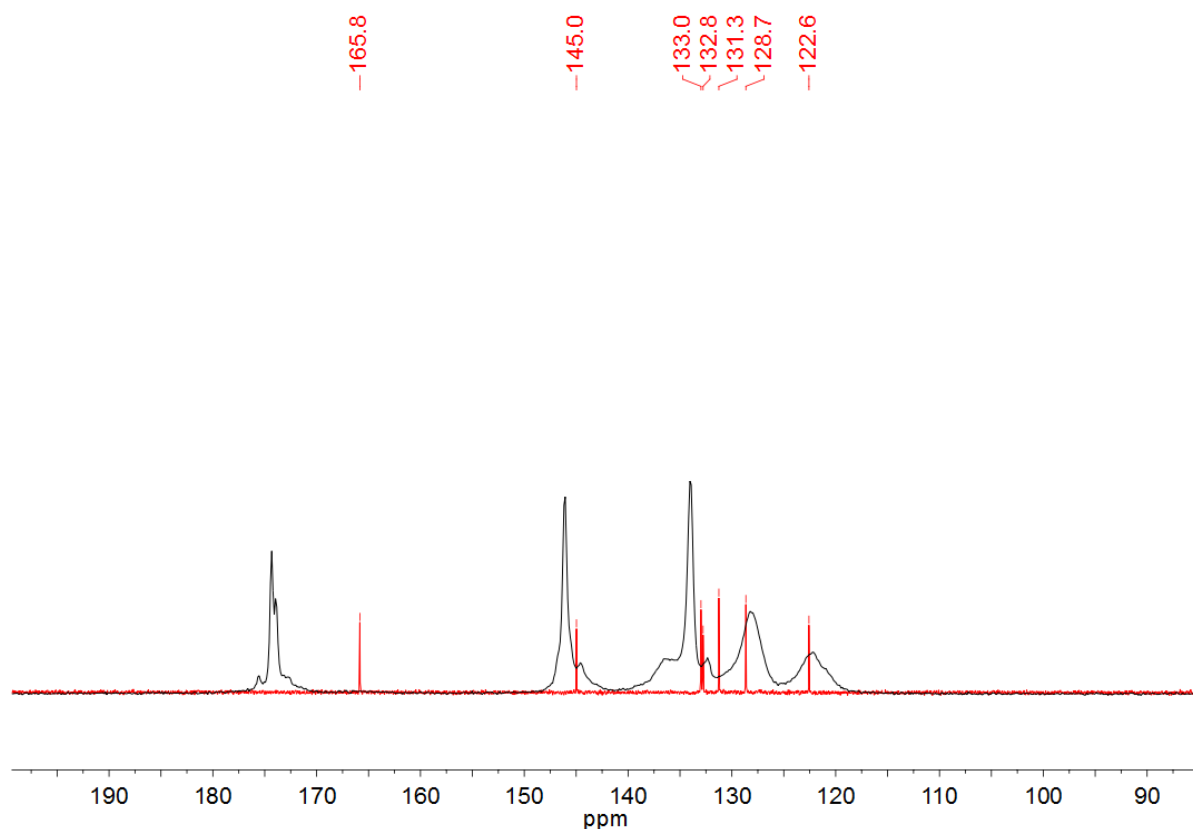


Figure 2.29 ^{13}C CP-MAS NMR spectrum of **ZnBrBPDC** (black) and high resolution ^{13}C NMR spectrum of the linker **3** (red).

The situation is different with **ZnNO₂BPDC** (Figure 2.30) that looks like if some of the resonances have become doubled. The bulky nitro groups in two of the *meta*-positions of the phenylene linker probably hinder the free rotation around the central C-C bond and therefore give rise to the presence of rotamers on the NMR time scale.

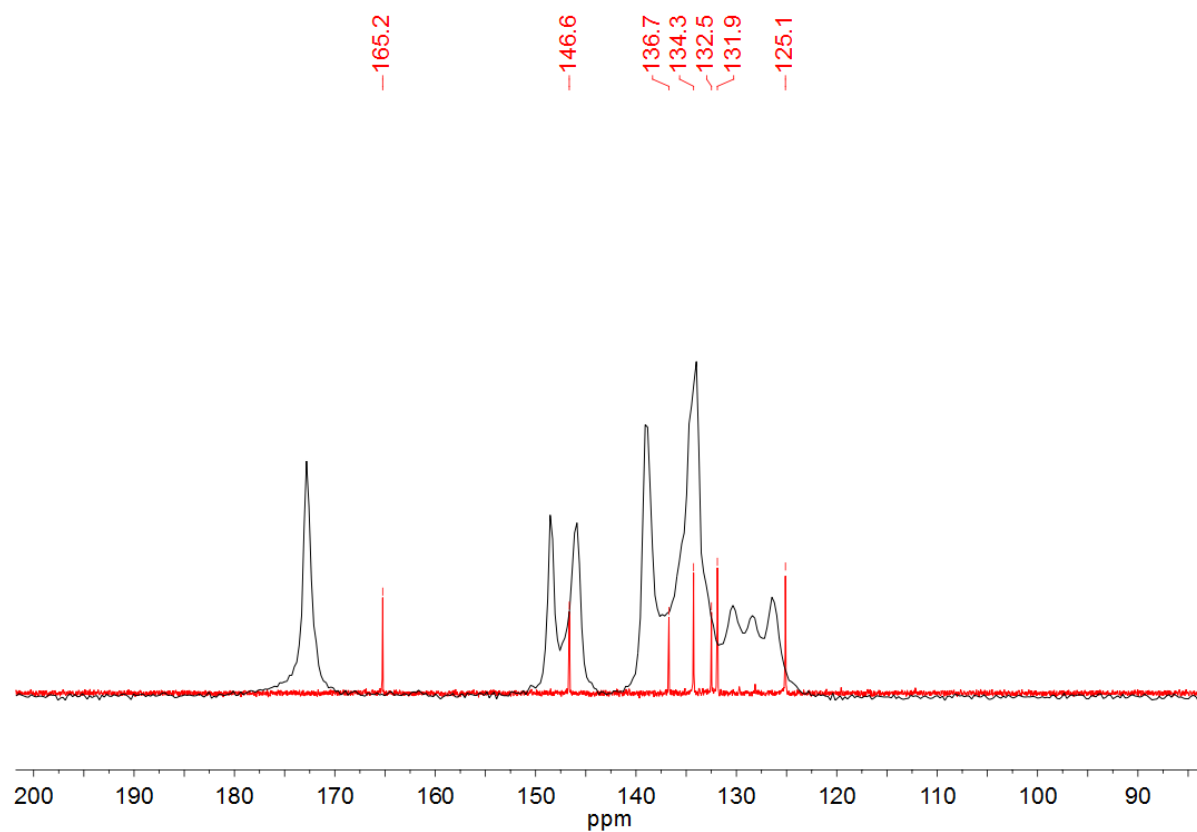


Figure 2.30 ^{13}C CP-MAS NMR spectrum of ZnNO_2BPDC (black) and high resolution ^{13}C NMR spectrum of the linker **5** (red).

The NMR spectrum of ZnNH_2BPDC (Figure 2.31) shows broader resonances than of ZnBrBPDC but in general the number of resonances is correct. This might indicate that the internal rotations of the biphenyl unit are near to the NMR timescale.

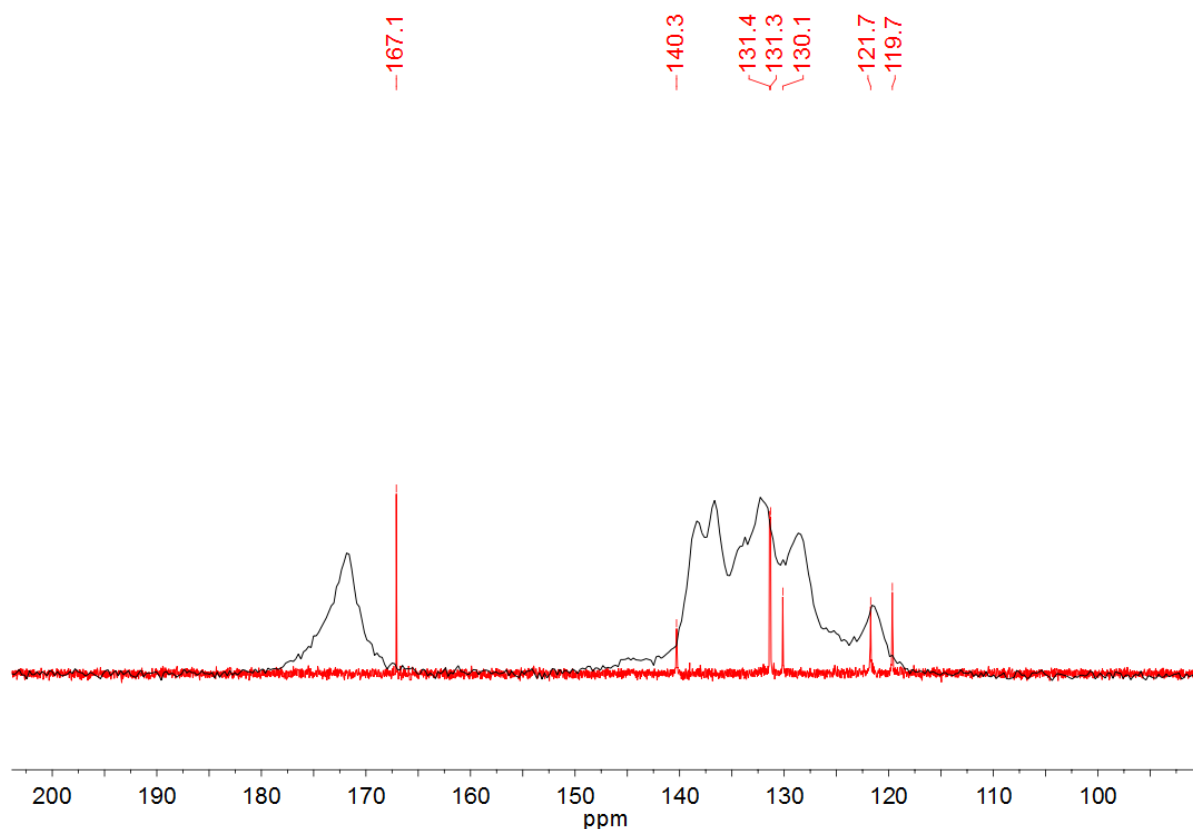


Figure 2.31 ^{13}C CP-MAS NMR spectrum of ZnNH_2BPDC (black) and high resolution ^{13}C NMR spectrum of the linker **7** (red).

2.3.1.5 IR Measurements of ZnBrBPDC , ZnNO_2BPDC and ZnNH_2BPDC

Figure 2.32 shows the infrared spectra of the synthesized MOFs and their corresponding linkers. While the dicarboxylic acid precursors **3**, **5** and **7** exhibit intense $\text{C}=\text{O}$ absorptions around 1690 cm^{-1} , typical for aromatic carboxylic acids associated by hydrogen bonds, the $-\text{CO}_2$ fragments of the MOF materials give rise for absorptions at around 1600 and 1450 cm^{-1} , which again is typical for symmetrically coordinating carboxylate anions.

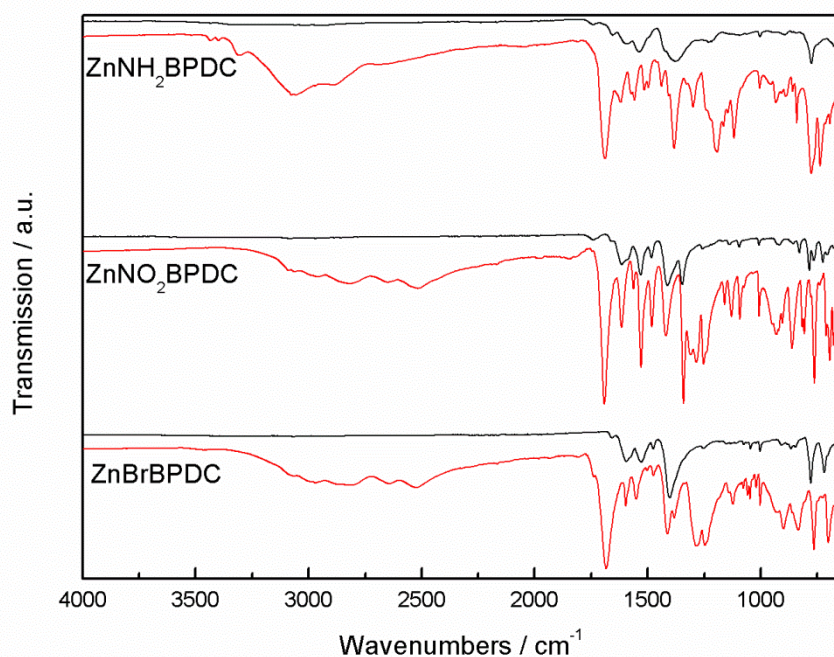


Figure 2.32 IR spectra of **ZnBrBPDC**, **ZnNO₂BPDC** and **ZnNH₂BPDC** (black) and their linkers **3**, **5** and **7** (red).

2.3.1.6 N₂ Adsorption Measurements of ZnBrBPDC, ZnNO₂BPDC and ZnNH₂BPDC

The samples were activated at a pressure of $p < 1 \cdot 10^{-5}$ mbar and at a temperature of 353 K overnight. The BET equation was used to determine the specific surface areas of the samples in the pressure range of 0.01 to 0.05 p/p_0 . All three samples showed a reversible Type I isotherm which is typical for a microporous material (Figure 2.33).³⁷

In order to compare with analogue MOFs, Langmuir and BET models were used to calculate the specific surface areas. The micropore volume was evaluated with the t-plot method. In general the synthesized MOFs show comparable pore sizes in comparison to the analogue MOFs.

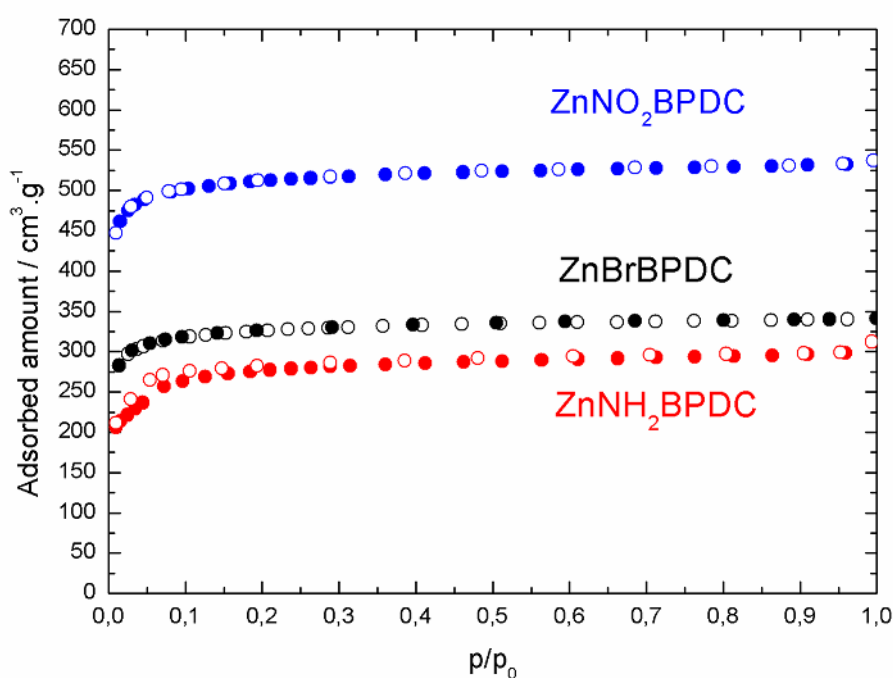


Figure 2.33 N₂ adsorption (close circles) and desorption (open circles) isotherms of **ZnBrBPDC** (black), **ZnNO₂BPDC** (blue) and **ZnNH₂BPDC** (red).

For **ZnBrBPDC**, the specific surface area was calculated as 1300 m²/g. When it is compared with IRMOF-2 (linker: 2-bromobenzene-1,4-dicarboxylic acid) it shows a lower surface area although **ZnBrBPDC** contains a longer linker (Table 2.5). This is due to the non-interpenetrated structure of IRMOF-2. On the other hand, when it is compared to interpenetrated IRMOF-9 structure (linker: 4,4'-biphenyldicarboxylic acid), **ZnBrBPDC** shows lower surface area due to the presence of bulky bromine atoms in the structure.

In the case of **ZnNO₂BPDC**, the obtained surface area is higher than both IRMOF-2 and IRMOF-9. Although an interpenetrated structure was obtained like for **ZnBrBPDC**, the higher surface area can be the result of a well activated sample before N₂ adsorption.

A considerably low surface area of **ZnNH₂BPDC** was observed compared to IRMOF-3 which contains the 2-aminobenzene-1,4-dicarboxylic acid linker. This difference can be attributed to the interpenetrated structure of **ZnNH₂BPDC**. Moreover, another important point in

adsorptive evaluation, which is the activation method used before the adsorption measurements, might have also affected the BET surface area.

Table 2.5 Comparison of the porosity measurements of **ZnBrBPDC**, **ZnNO₂BPDC** and **ZnNH₂BPDC** with the analogue MOFs.¹²³

	A_{LANG} (m ² /g)	A_{BET} (m ² /g)	V_p (cm ³ /g)
IRMOF-2	2544	1722	0.88
IRMOF-3	3062	2446	1.07
IRMOF-9	2613	1904	0.90
ZnBrBPDC	1403	1300	0.53
ZnNO₂BPDC	2206	2000	0.83
ZnNH₂BPDC	1087	1100	0.43

Acronyms: A_{LANG} ; Langmuir surface area, A_{BET} ; BET surface area, V_p ; measured pore volume.

Although all three MOFs were highly affected by interpenetration, their specific surface areas are still larger than those of zeolites or mesoporous materials.

2.3.2 Adsorption of Light Alkanes (C₁ – C₄) at Different Temperatures

Recently, metal organic frameworks are found to be good alternatives to zeolites and other nonporous materials in terms of their adsorption properties.¹²⁸⁻¹³⁰ Most of the adsorption studies are concentrated on H₂ and CO₂ adsorptions¹³¹⁻¹³⁶ and there are few studies based on the alkane adsorption^{137,138} of MOFs.

In this study, **ZnBrBPDC**, **ZnNO₂BPDC** and **ZnNH₂BPDC** were tested for their adsorption behaviors on light (short chain) alkanes in order to determine their separation and storage capabilities. Adsorption measurements for **ZnBrBPDC**, **ZnNO₂BPDC** and **ZnNH₂BPDC** were performed at three different temperatures (273 K, 293 K and 313 K) for the pure alkanes CH₄, C₂H₆, C₃H₈, and *n*-C₄H₁₀ using a static volumetric method at the given temperatures. The adsorbent was activated over night at a pressure of $p < 10^{-5}$ mbar and 298 K. The isotherms were measured in a thermostated system. A separation valve H12 was placed between the dosing valve H11 and the adsorption vessel. The desired pressure was adjusted and valve H12 was rapidly opened. The adsorbed amounts were determined by the pressure changes

in the system compared with the calibration measurement. The volumes of the different parts of the apparatus and the weight of the sorbent have been taken into account. The pressure change in the sorption vessel was measured with a high-accuracy piezo-membrane transmitter of type Ceravac CTR100.

All synthesized materials show the similar adsorption isotherms for the same gas (Figure 2.34). At 273 K, while *n*-butane and propane were adsorbed very efficiently, ethane and methane showed weak affinities to the materials. This low affinity of methane and ethane can be due to the large pores which are between micropores to mesopores levels.¹³⁸ Almost same amount of methane adsorption was observed for all three MOFs (Table 2.6).

Although, **ZnNO₂BPDC** showed the highest ethane uptake when compared to other two MOFs, in the adsorption of propane and *n*-butane maximum loadings were obtained by **ZnBrBPDC** and **ZnNH₂BPDC**. For propane and *n*-butane, saturation was observed for all three MOFs. Maximum loadings of 3.50 – 4.30 mmol/g of *n*-butane and 4.00 – 4.50 mmol/g of propane indicate high capacities for the storage of these two gases in synthesized the MOFs at 273 K.

Table 2.6 Maximum loadings of the adsorbents at 273 K.

	CH ₄	C ₂ H ₆	C ₃ H ₈	<i>n</i> -C ₄ H ₁₀
ZnBrBPDC	0.44 mmol/g	1.66 mmol/g	4.52 mmol/g	4.31 mmol/g
ZnNO₂BPDC	0.48 mmol/g	2.26 mmol/g	3.86 mmol/g	3.57 mmol/g
ZnNH₂BPDC	0.44 mmol/g	2.07 mmol/g	4.49 mmol/g	4.19 mmol/g

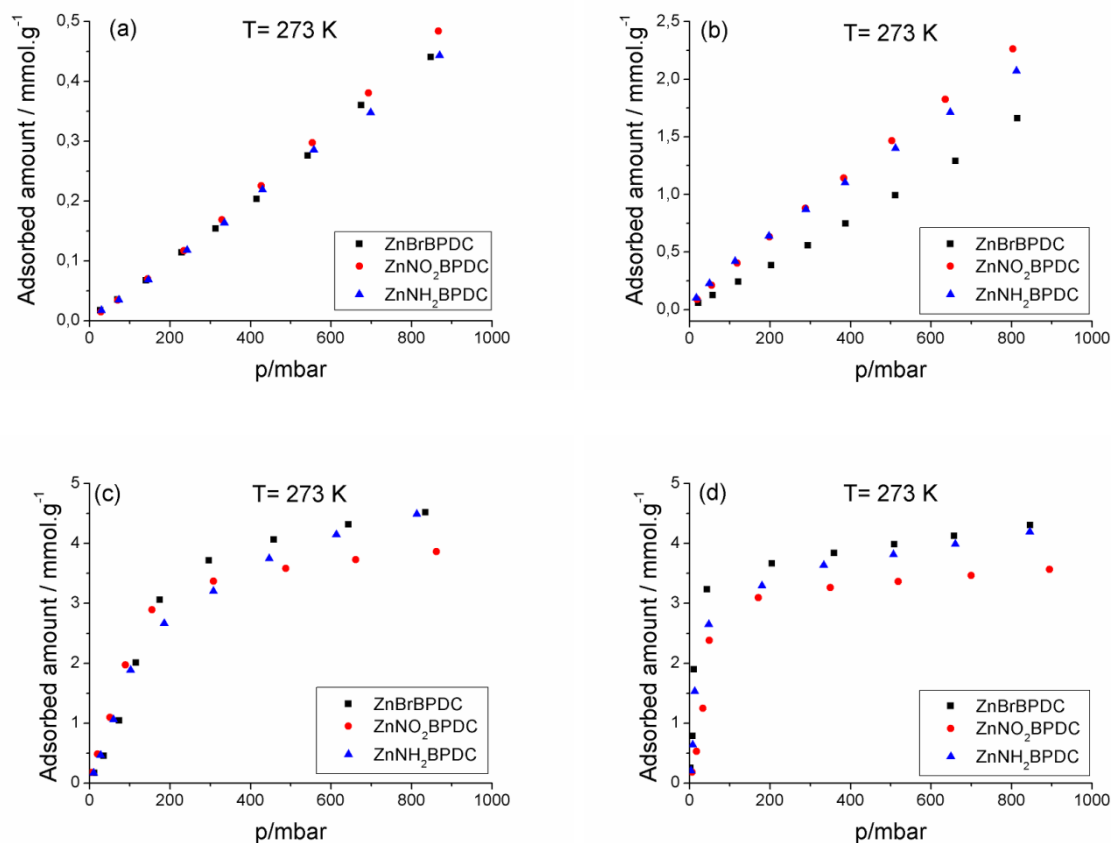
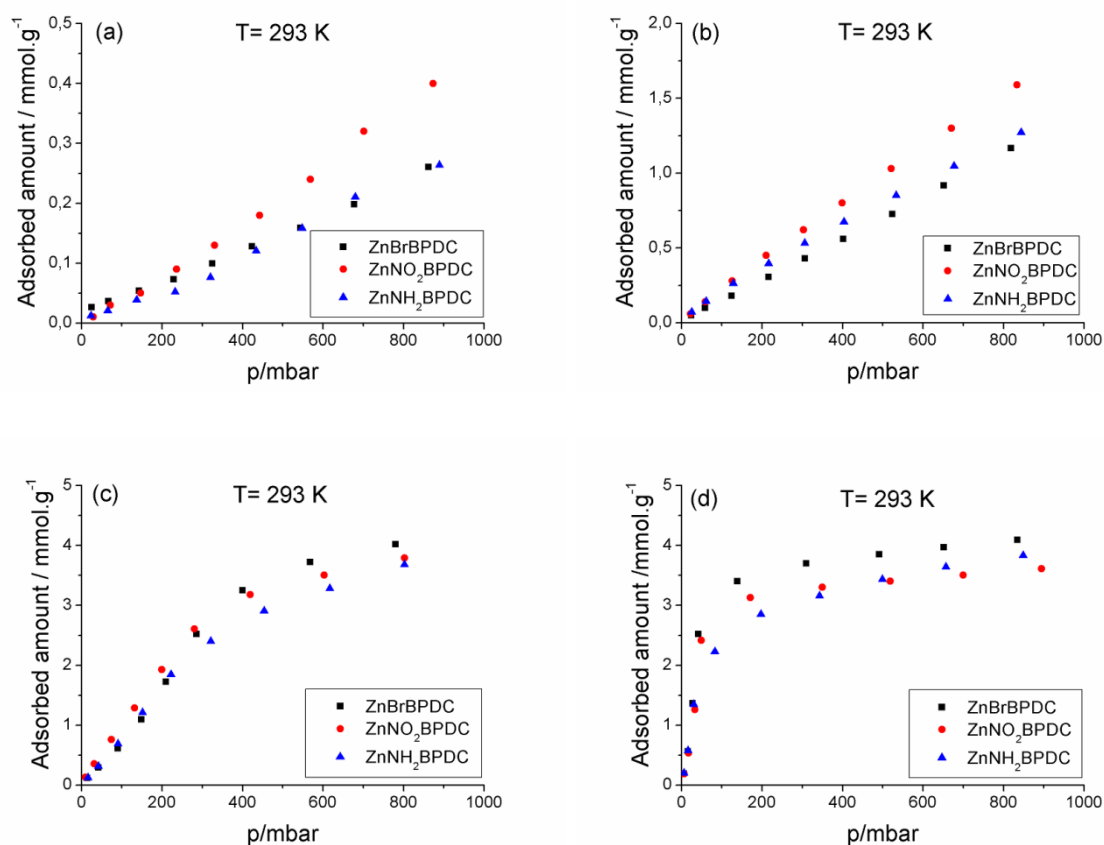


Figure 2.34 Adsorption isotherms of **ZnBrBPDC**, **ZnNO₂BPDC** and **ZnNH₂BPDC** for the gases CH_4 (a), C_2H_6 (b), C_3H_8 (c), $n\text{-C}_4\text{H}_{10}$ (d) at $T = 273\text{ K}$.

When the temperature was raised to 293 K, a decrease at the adsorption capacities was observed, however, *n*-butane and propane were still adsorbed with high efficiencies, saturation was again observed in the adsorption of these two gases for all three MOFs (Figure 2.35). While **ZnNO₂BPDC** shows the highest uptake for methane and ethane, **ZnBrBPDC** has a better affinity for propane and *n*-butane (Table 2.7).

Table 2.7 Maximum loadings of the adsorbents at 293 K.

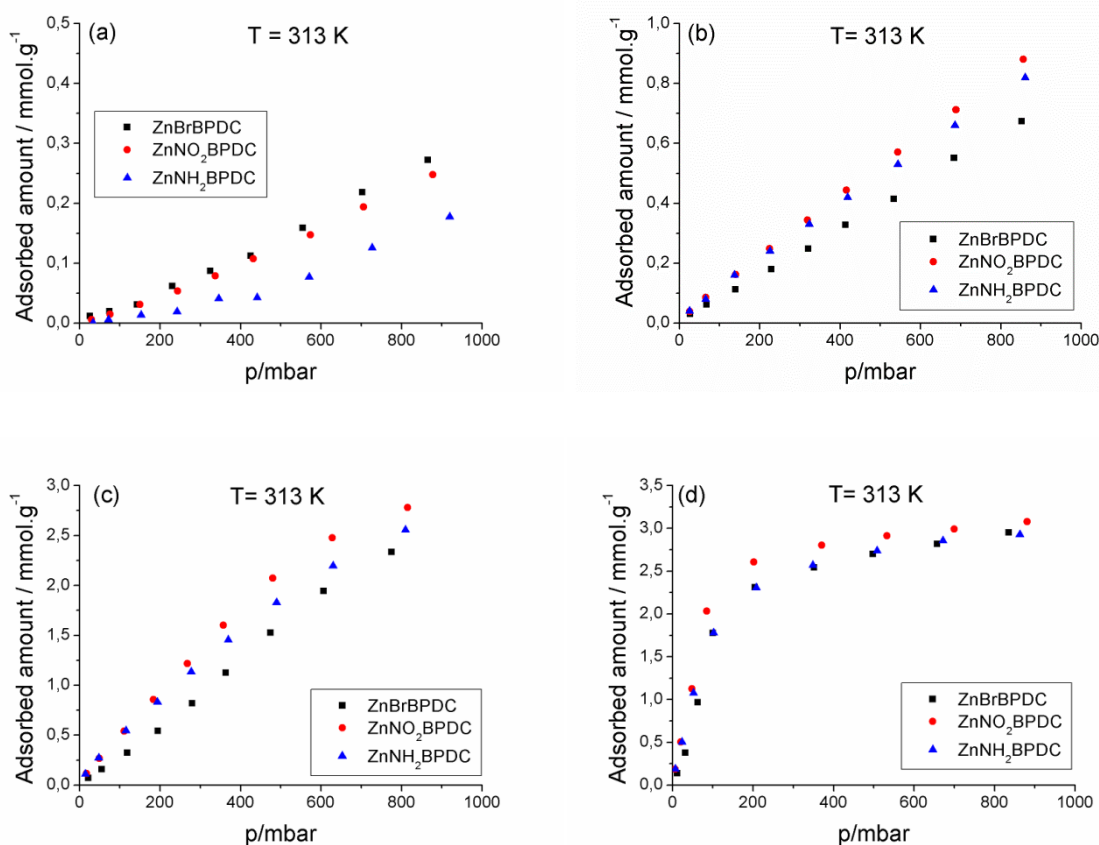
	CH ₄	C ₂ H ₆	C ₃ H ₈	<i>n</i> -C ₄ H ₁₀
ZnBrBPDC	0.26 mmol/g	1.17 mmol/g	4.01 mmol/g	4.09 mmol/g
ZnNO₂BPDC	0.40 mmol/g	1.59 mmol/g	3.79 mmol/g	3.61 mmol/g
ZnNH₂BPDC	0.26 mmol/g	1.27 mmol/g	3.68 mmol/g	3.83 mmol/g

**Figure 2.35** Adsorption isotherms of **ZnBrBPDC**, **ZnNO₂BPDC** and **ZnNH₂BPDC** for the gases CH₄ (a), C₂H₆ (b), C₃H₈ (c), *n*-C₄H₁₀ (d) at T= 293 K.

Alkane adsorption at 313 K shows a decrease for the all three MOFs (Table 2.8). As a similar trend, the maximum uptakes were observed for *n*-C₄H₁₀ and the lowest uptakes were observed for CH₄. It is also viewed that, the temperature influence is much more significant for *n*-C₄H₁₀ adsorption of **ZnBrBPDC** compared to the other gases (Figure 2.36).

Table 2.8 Maximum loadings of the adsorbents at 313 K.

	CH ₄	C ₂ H ₆	C ₃ H ₈	<i>n</i> -C ₄ H ₁₀
ZnBrBPDC	0.27 mmol/g	0.67 mmol/g	2.33 mmol/g	2.95 mmol/g
ZnNO₂BPDC	0.25 mmol/g	0.88 mmol/g	2.78 mmol/g	3.08 mmol/g
ZnNH₂BPDC	0.18 mmol/g	0.82 mmol/g	2.56 mmol/g	2.92 mmol/g

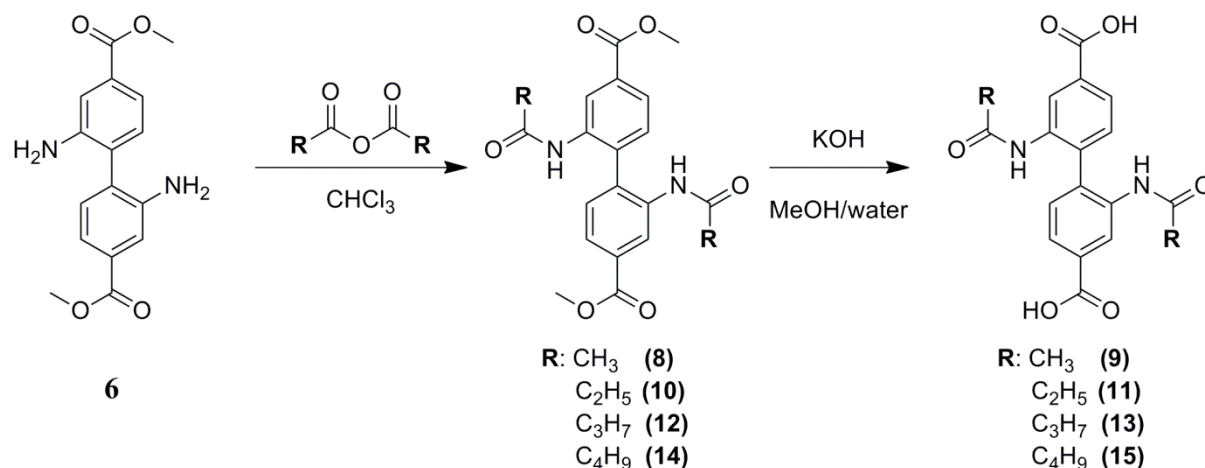
**Figure 2.36** Adsorption isotherms of ZnBrBPDC, ZnNO₂BPDC and ZnNH₂BPDC for the gases CH₄ (a), C₂H₆ (b), C₃H₈ (c), *n*-C₄H₁₀ (d) at T= 313 K.

For all gases examined, the maximum uptakes were observed at 273 K. When the temperature was increased, the amount of the adsorbed gas decreased. This might be due to the increased thermal energy of the gas molecules at higher temperatures.¹³⁹

As it is mentioned before, all three MOFs showed the higher uptakes to the longer chain alkanes. A study by Dören *et al.* on different IRMOF materials explains the higher adsorption affinities to the longer chain alkanes via sorbate-sorbate and sorbate-framework interactions. The sorbate-sorbate interaction decreases with increasing cavity size.¹³⁸ Since **ZnBrBPDC**, **ZnNO₂BPDC** and **ZnNH₂BPDC** have similar backbones and pore volumes to each, the sorbate-framework interaction might have a stronger effect on the adsorption behaviors resulting in a better adsorption of the longer chain alkanes C₃H₈ and *n*-C₄H₁₀. When the alkane-framework interaction energy increases, the loading also increases and the molecules are forced to the center of the cavities resulting in higher loadings than shorter chain alkanes.¹³⁸ Since all three MOFs show strong affinities for *n*-butane, they might be good candidates for the separation of *n*-butane from natural gas.

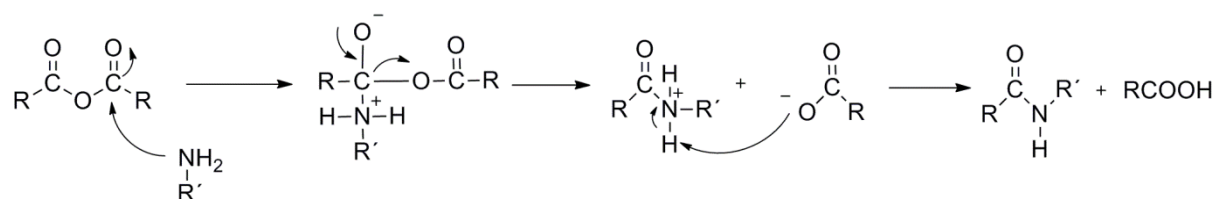
2.4 Amide Functionalized BPDC Linkers

The effect of functional groups on the IRMOF series was also examined by synthesizing amide functionalized biphenyl linkers. For this purpose, four linkers containing amides with different alkyl chains (C1-C4) were designed (Scheme 2.7).



Scheme 2.7 Overall reaction for the synthesis of linkers **9**, **11**, **13** and **15**.

Amides can generally be synthesized using acyl chlorides or acid anhydrides in the presence of a tertiary or secondary amine.¹⁴⁰ The mechanism with acid anhydrides involves an attack of the amine to form a zwitterionic intermediate. This intermediate decomposes and forms the corresponding amide and the carboxylic acid (Scheme 2.8).¹⁴¹



Scheme 2.8 Mechanism for the amide formation.

Amide functionalized linkers were synthesized by using the ester **6** as the starting material and the corresponding anhydride as the acetylation agent.¹⁴² After the reaction, the formed carboxylic acids were removed from the reaction medium by treatment with ammonium chloride solution. The structure elucidation of compounds **8**, **10**, **12** and **14** was done with ¹H and ¹³C NMR spectroscopy (Figure 2.37 and 2.38).

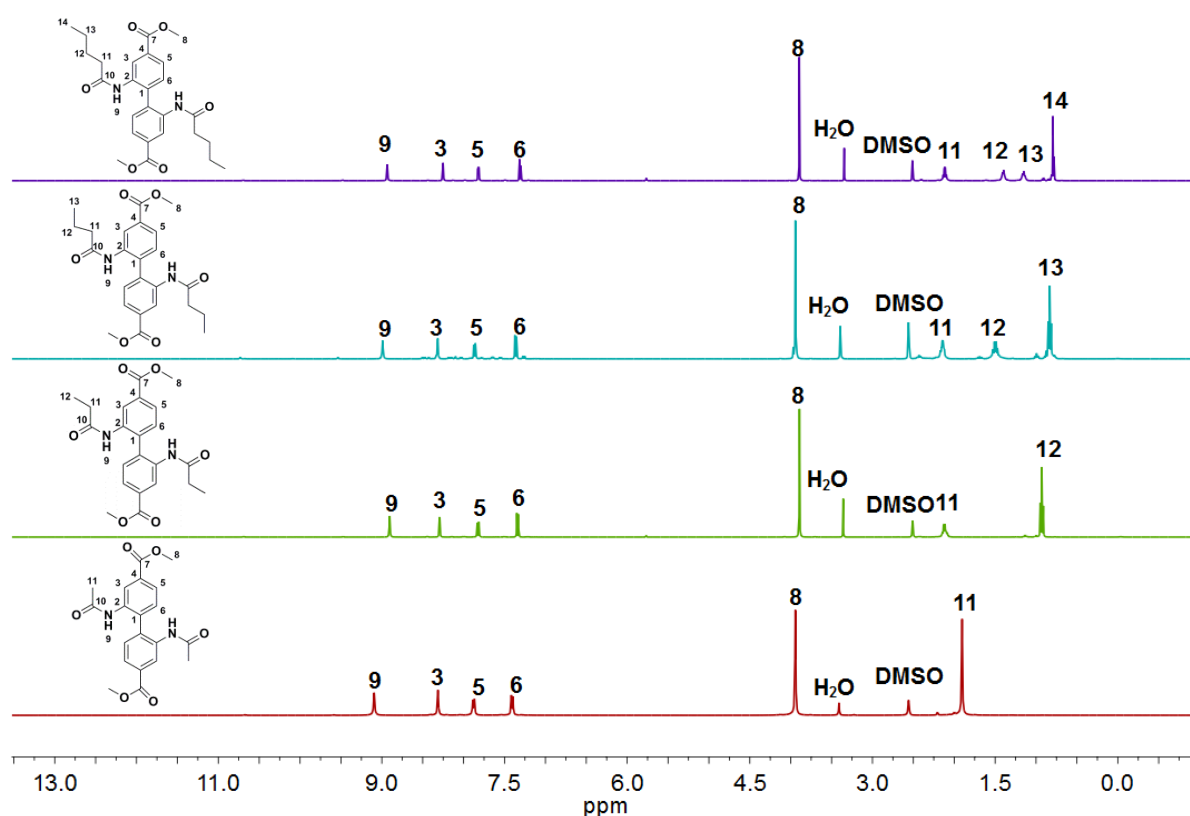


Figure 2.37 ¹H NMR spectra of **8**, **10**, **12** and **14** recorded in DMSO-d₆.

The ¹H NMR spectra of the amide functionalized biphenyls show four peaks in the aromatic region. For all of them, the NH protons resonate at 8.90 ppm as a singlet. Protons neighboring the amide groups (H3) appear as a doublet at 8.30 ppm with a coupling constant 1.8 Hz for all amide derivatives. The aromatic protons H5 and H6 give a doublet of doublet

and a doublet respectively as expected. The coupling constants for the H5 protons were measured as 8.0 Hz and 1.8 Hz indicating the couplings with the H6 and H3 protons respectively. The $-\text{OCH}_3$ groups resonate as a singlet at 3.88 ppm in all four esters. The methyl groups in compound **8** bound to the carbonyl group appear as a singlet at 1.85 ppm. In compound **10**, although a quartet was expected for the $-\text{CH}_2$ groups (H11), a doublet of a quartet is observed. Most probably the H11 protons are coupling with the $-\text{NH}$ protons and therefore appear as a doublet of a quartet (Figure 2.38). In compounds **12** and **14**, the H11 protons also resonate as a multiplet. The methyl groups; H13 in **12** and H14 in **14** give triplets.

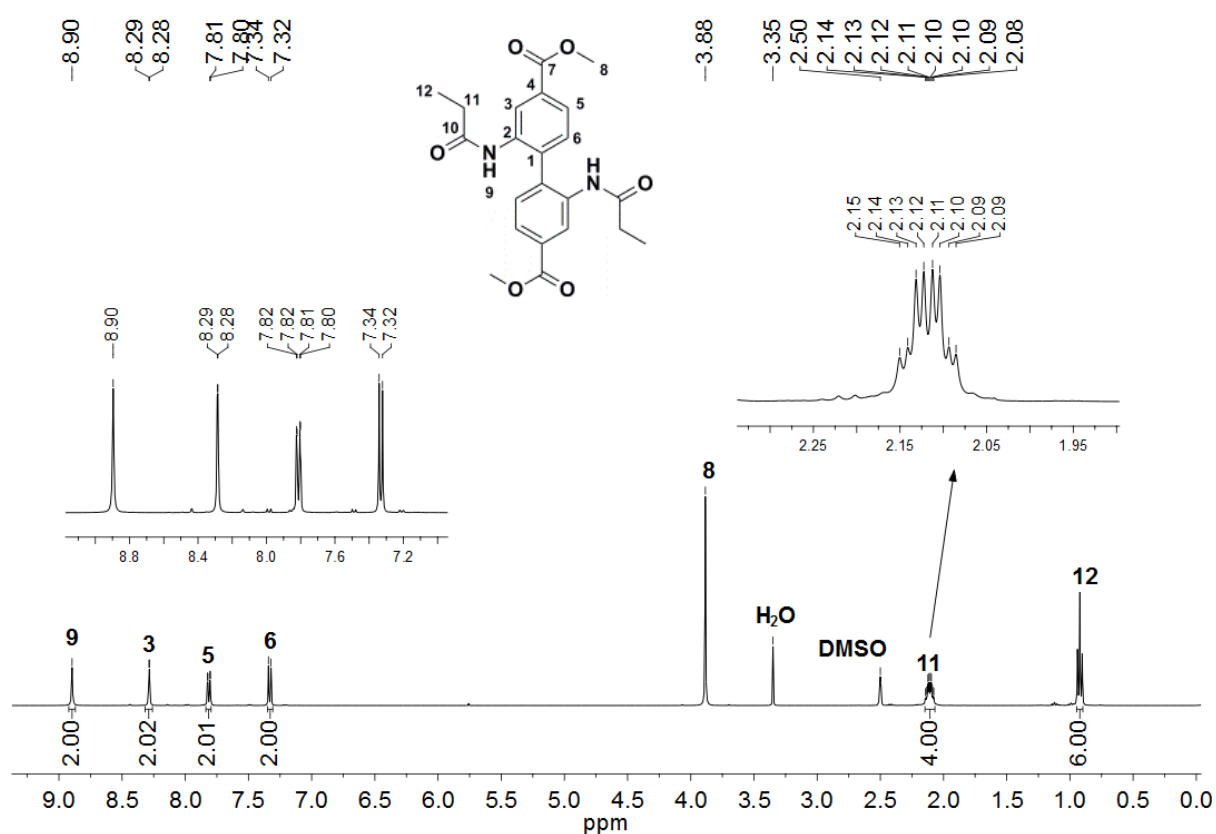


Figure 2.38 ^1H NMR spectrum of **10** recorded in $\text{DMSO}-d_6$.

As expected, the ^{13}C NMR spectra of **8**, **10**, **12** and **14** reveal ten, eleven, twelve and thirteen carbons respectively (Figure 2.39). The assignments of the carbon atoms were done by HMBC and HMQC techniques.

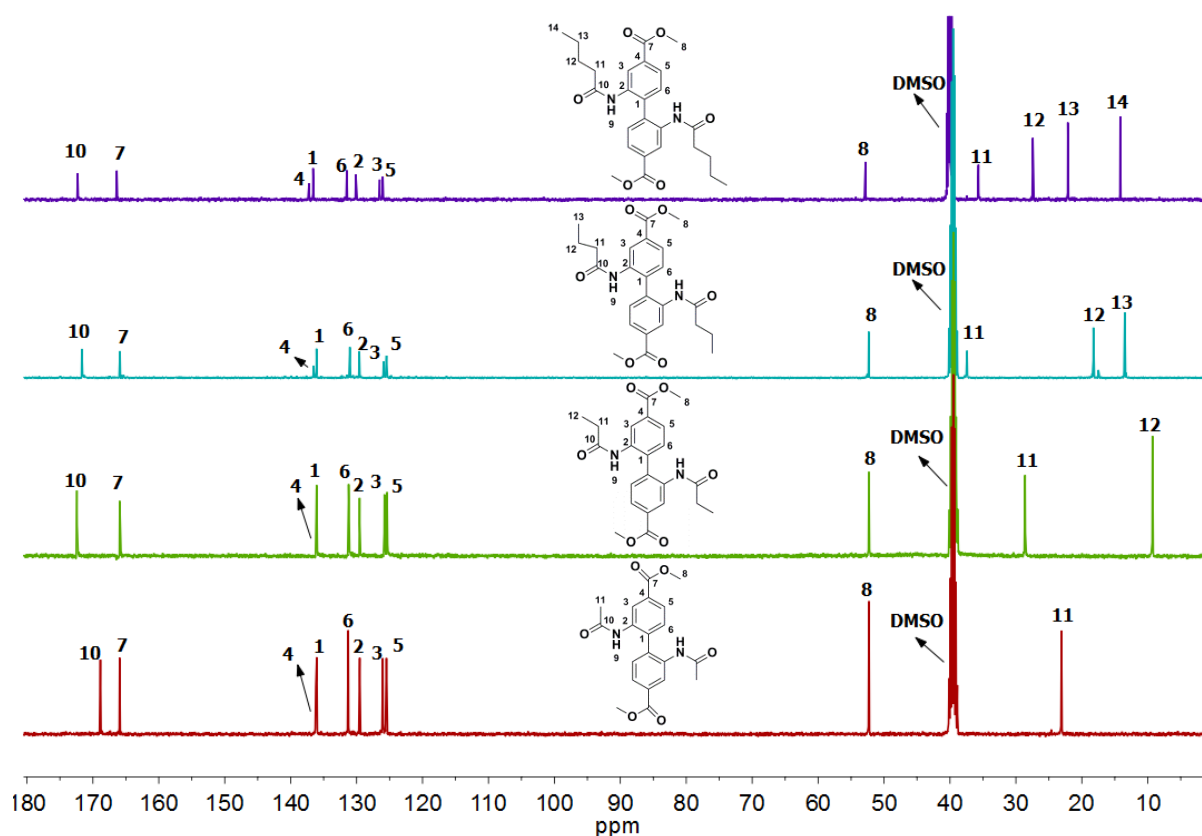


Figure 2.39 ^{13}C NMR spectra of **8**, **10**, **12** and **14** recorded in DMSO-d_6 .

All amide derivatives were recrystallized from methanol. Among these four compounds, single crystal X-ray measurements could be applied to **8** and **10**. The crystal structures of these compounds are shown in Figure 2.40.

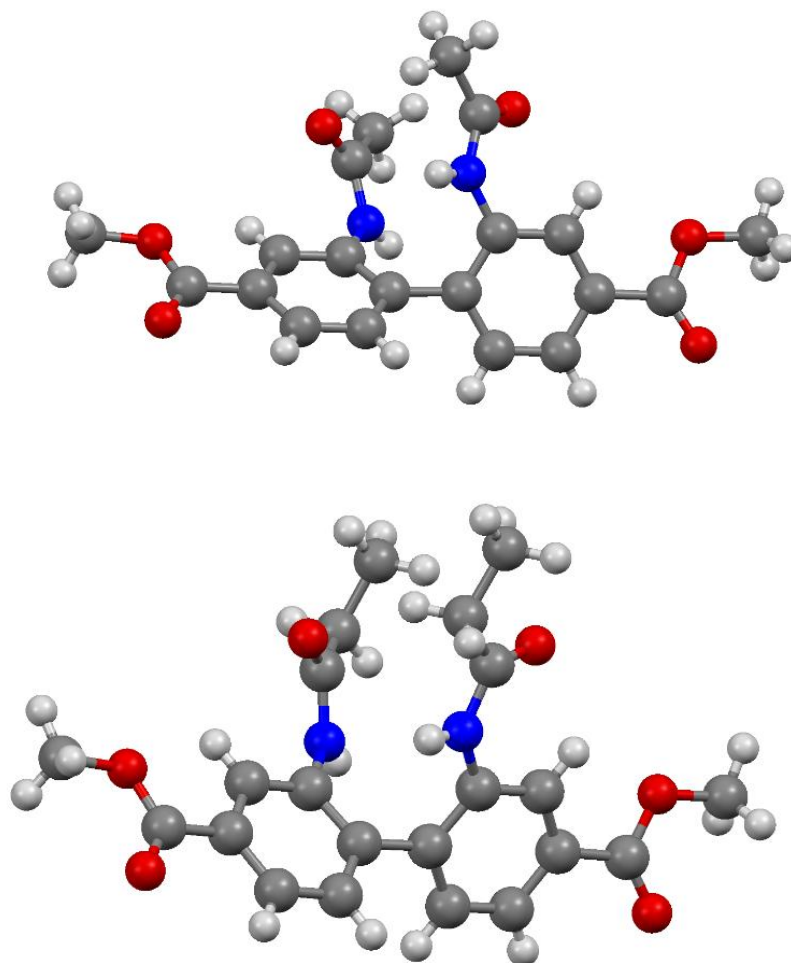


Figure 2.40 Crystal structures of **8** (top) and **10** (bottom).
Atom colors: C grey, O red, H white, N blue.

After the successful synthesis of the amide esters, hydrolysis using KOH in a MeOH/water mixture yielded desired carboxylic acids (Scheme 2.7). Contrary to the previous linkers, the reactions were performed at room temperature instead of refluxing. It was observed that applying reflux conditions causes cleavage of the nitrogen-carbonyl bond. Besides, shorter reaction times resulted in incomplete hydrolysis.

Structure elucidations of the compounds **9**, **11**, **13** and **15** were done by ^1H and ^{13}C NMR spectroscopy, showing the disappearance of the $-\text{OCH}_3$ group which is an obvious evidence of the formation of the target carboxylic acids. The presence of resonances of the alkyl chains of the amides gave a good evidence for the successful hydrolysis which did not cause any cleavage of the nitrogen-carbonyl bond. No other differences were observed for these

compounds when compared to the ^1H and ^{13}C NMR spectra of corresponding esters (Figure 2.41 and 2.42).

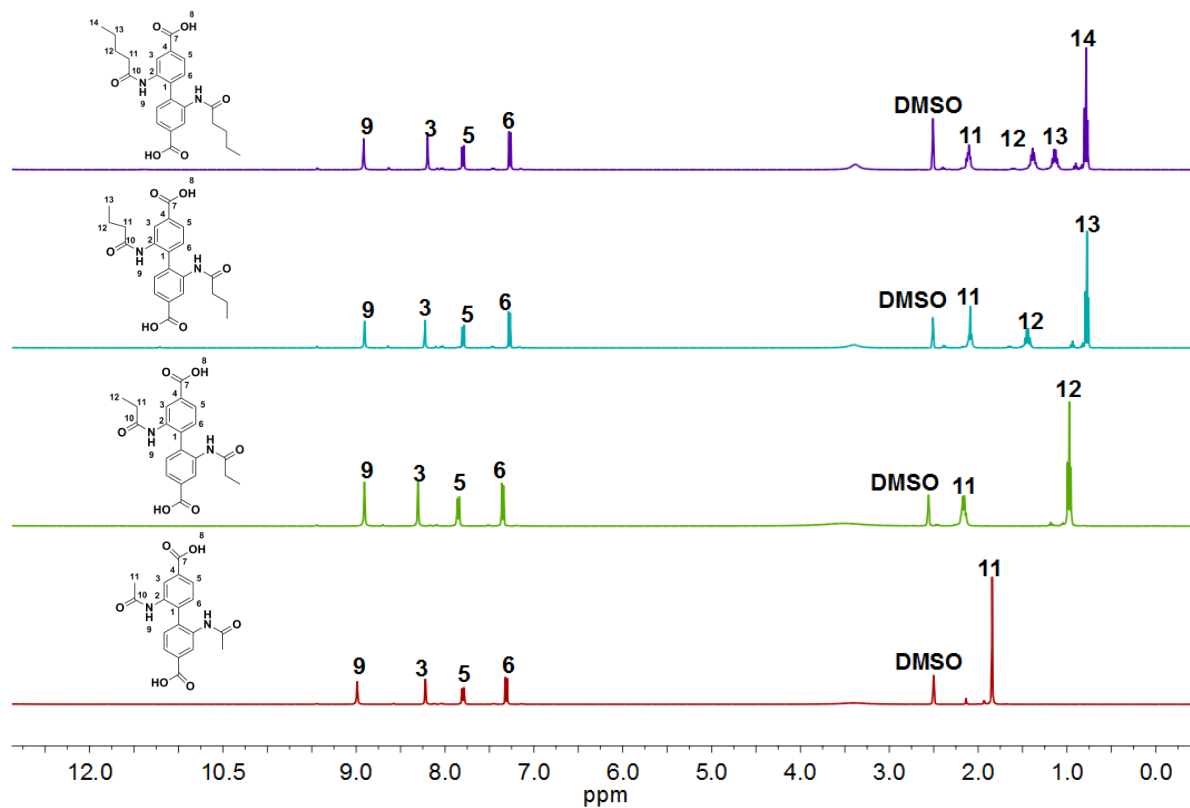


Figure 2.41 ^1H NMR spectra of 9, 11, 13 and 15 recorded in DMSO-d_6 .

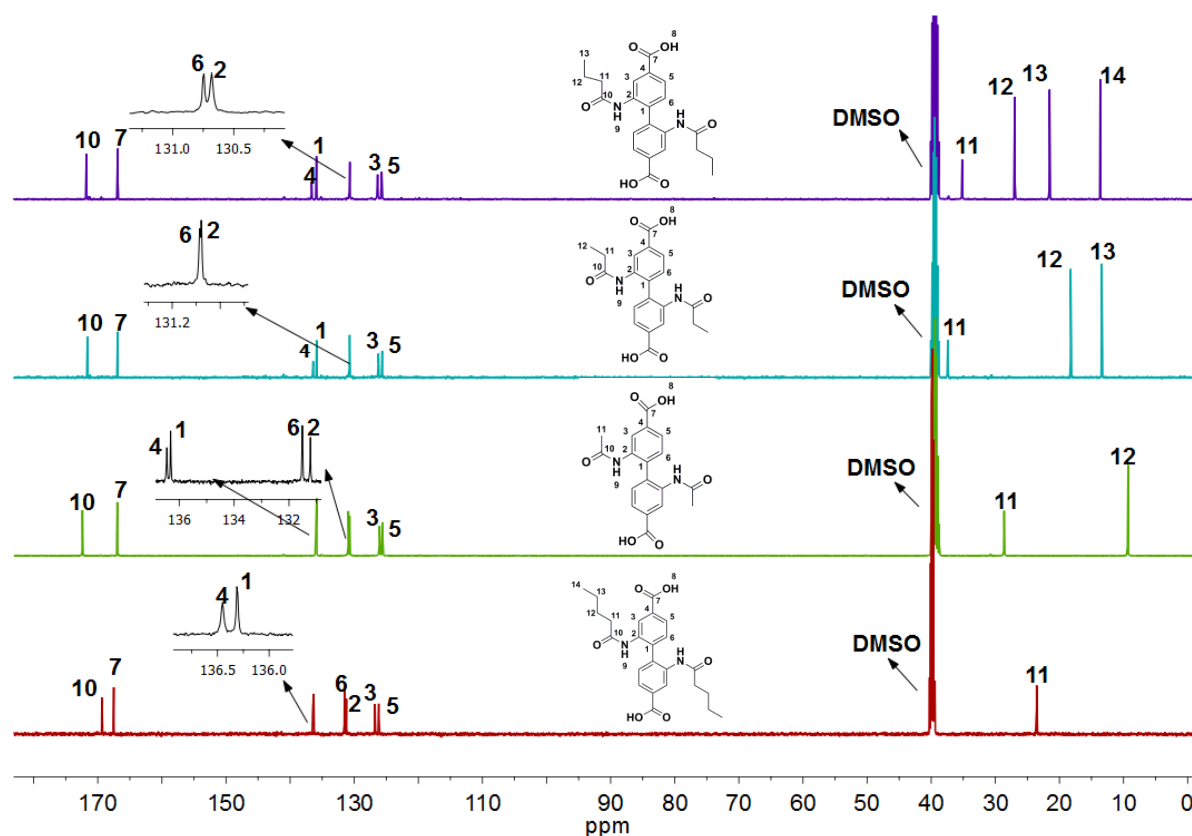
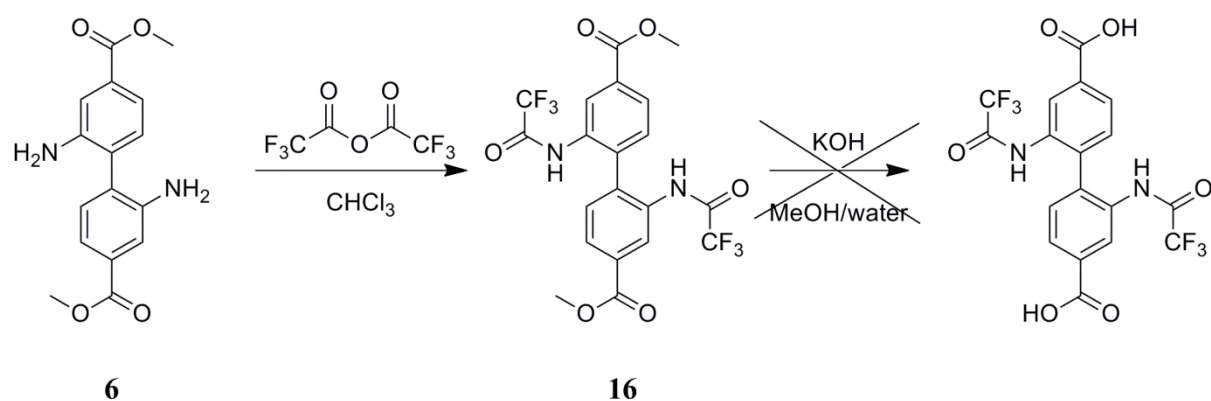


Figure 2.42 ^{13}C NMR spectra of **9**, **11**, **13** and **15** recorded in DMSO-d_6 .

Another amide linker which has a CF_3 group bonded to the carboxylate group of the amide groups was also designed (Scheme 2.9). Such a linker could have a good affinity for CO_2 due to an increase of polarity of the $-\text{NH}$ bond. To synthesize the trifluoroacetamide functionalized linker **16**, the previous method described for the other amide linkers was applied using **6** as the starting material and trifluoroacetic anhydride as the acetylation agent. The ^1H and ^{13}C NMR spectra confirmed synthesis of the desired ester **16**.



Scheme 2.9 Synthesis route for the trifluoromethyl amide functionalized linker.

After the successful synthesis of the compound **16**, the hydrolysis was performed applying the previously described procedure for the other amides. The ^1H and ^{13}C NMR spectra of the compound showed that the reaction resulted not only in the cleavage of the ester group but also in the cleavage of the amide bond. With this information, the weaker bases NaOH and LiOH were used instead of KOH. However the same result was obtained.

2.5 Synthesis of the Amide Functionalized BPDC MOFs; ZnAcBPDC, ZnPrBPDC, ZnBuBPDC and ZnPeBPDC

First attempts for the synthesis of the amide functionalized MOFs were carried out using linkers **9** and **13**. The procedure used for the synthesis of the **ZnNH₂BPDC** was applied using 125 ml PP-bottles. After keeping the reaction bottles for 24 h in an oven at 100 °C, the formation of fine precipitates was observed besides crystal development.

It is known that reaction conditions such as time, temperature, reagent concentrations and solvent type strongly influence the growth of large, high quality single crystals. Other important factors on the crystal quality are the type of the vessel and fractional volume filling of the vessel. This can be explained as the difference in the density of heterogeneous nucleus sites present on the walls and bottom of the vessel.¹²³

In order to increase the amount of crystal formed, the reaction conditions were optimized by utilization of different linker to $\text{Zn}(\text{NO}_3)_2 \cdot 4\text{H}_2\text{O}$ molar ratios. Instead of large scale reactions in PP-bottles, these experiments were done in 15 ml glass vials with small scales to obtain

high quality crystals. Temperature was kept constant at 100 °C and the vials were checked periodically to determine the time of crystal growth.

For this purpose, the amounts of linkers (**9** and **13**) were kept constant (0.02 g), 4 ml DMF was used as a solvent and the amount of $\text{Zn}(\text{NO}_3)_2 \cdot 4\text{H}_2\text{O}$ was changed. The reactants were introduced into the 15 ml glass vials and DMF was added. After stirring for 15 min, the glass vials were placed in an oven at 100 °C.

The vials were checked periodically and after 24 h, the formation of colorless cubic crystal was observed in vials 4 to 9 (Table 2.9). It was also observed that, when the linker to $\text{Zn}(\text{NO}_3)_2$ ratio increases, the size of the crystals also increases. For this reason two other sets were prepared for two linkers, using ratios between 1:10 and 1:15, but no further visible size change was observed compared to the 1:10 molar ratio. The following characterizations and applications of the MOFs were done with the crystals formed using the synthesis conditions of vial 9 for linkers **9** and **13**.

Table 2.9 Optimization of the reaction conditions.

	Linker 9	Linker 13	Linker to $\text{Zn}(\text{NO}_3)_2 \cdot 4\text{H}_2\text{O}$ molar ratio
Vial 1	---	---	1:2
Vial 2	---	---	1:3
Vial 3	---	---	1:4
Vial 4	✓	✓	1:5
Vial 5	✓	✓	1:6
Vial 6	✓	✓	1:7
Vial 7	✓	✓	1:8
Vial 8	✓	✓	1:9
Vial 9	✓	✓	1:10

The influence of the solvent type on the crystal growth was checked by changing the solvent from DMF to DEF. By using the same conditions as described above, the same type of

crystals were obtained. The effect of fractional filling of the vessel was also checked by changing the solvent amount from 4 ml to 3 and 5 ml. When 3 ml of solvent was used, the amount of the crystals was decreased, when 5 ml of solvent was used, a slight decrease of the crystal size was observed. SEM pictures of the crystals after optimization of the synthesis conditions are given below (Figure 2.43).

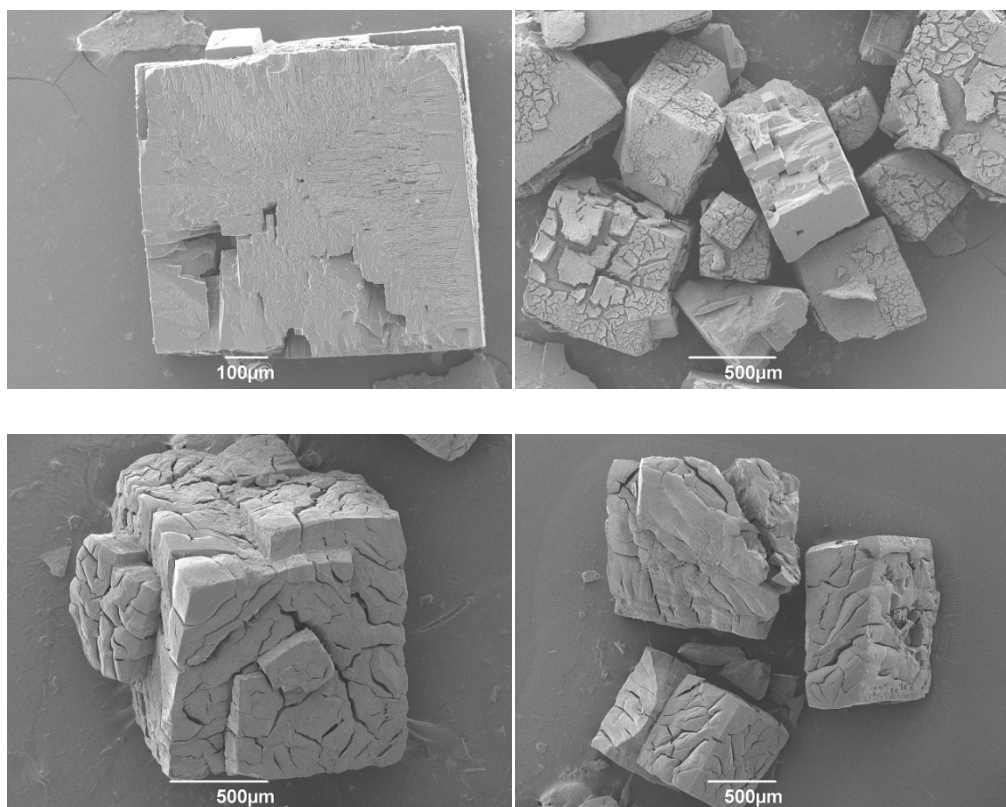


Figure 2.43 SEM pictures of the MOF crystals synthesized with linker **9** (top) and **13** (bottom).

The same approach was applied for linkers **11** and **15** using the sets below (Table 2.10). 0.052 mmol (0.02 g) of linker **11** and 0.045 mmol (0.02 g) of linker **15** were used. Since no crystal formation was observed with low amounts of $\text{Zn}(\text{NO}_3)_2 \cdot 4\text{H}_2\text{O}$, molar ratios from 1:2 to 1:4 were omitted and molar ratios starting from 1:5 to 1:13 were used.

Table 2.10 Optimization of the reaction conditions.

	Linker 11	Linker 15	Linker to $\text{Zn}(\text{NO}_3)_2 \cdot 4\text{H}_2\text{O}$ molar ratio
Vial 1	✓	✓	1:5
Vial 2	✓	✓	1:6
Vial 3	✓	✓	1:7
Vial 4	✓	✓	1:8
Vial 5	✓	✓	1:9
Vial 6	✓	✓	1:10
Vial 7	✓	✓	1:11
Vial 8	✓	✓	1:12
Vial 9	✓	✓	1:13

The formation of colorless cubic crystals was observed in all vials. It was further observed that, when the linker to $\text{Zn}(\text{NO}_3)_2$ ratio increases, the size of the crystals also increases. In both sets, the same crystal size and morphology were obtained in the ratios between 1:10 and 1:13 (vial 6 to 13). The conditions of vial 6 were decided to be used for further characterization and applications. SEM pictures of the crystals after optimization of the synthesis conditions are given below (Figure 2.44).

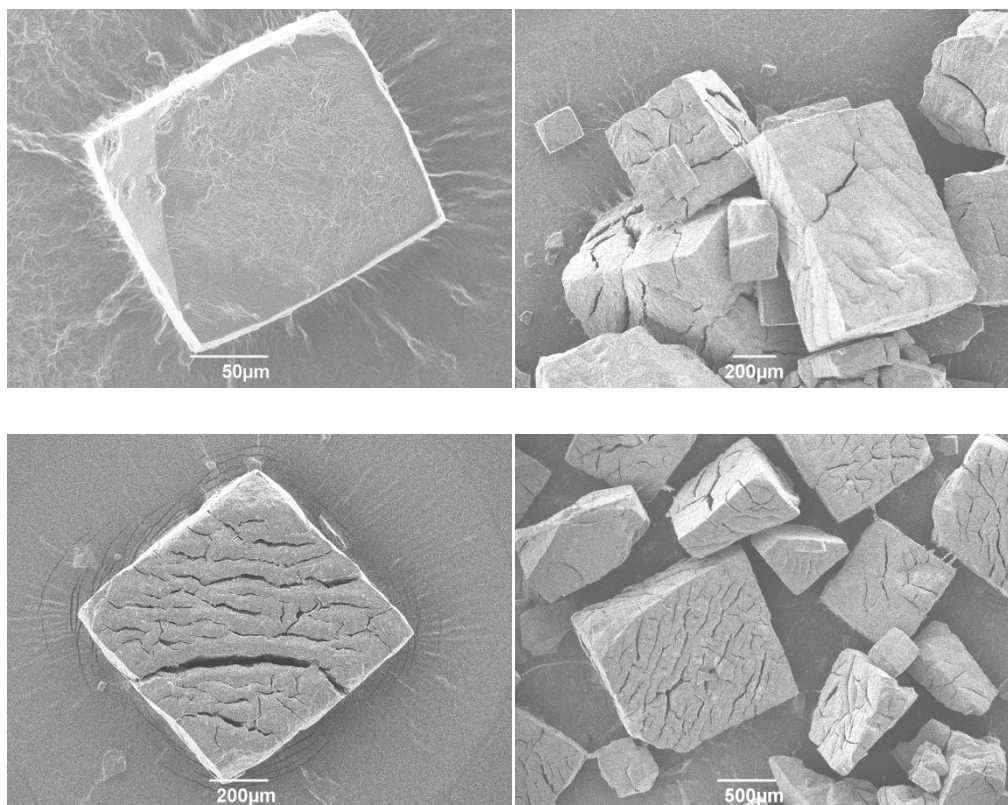


Figure 2.44 SEM pictures of the MOF crystals synthesized with linker **11** (top) and **15** (bottom).

These MOFs were named as **ZnAcBPDC**, **ZnPrBPDC**, **ZnBuBPDC** and **ZnPeBPDC** according to the amide chain of the linkers (Figure 2.45).

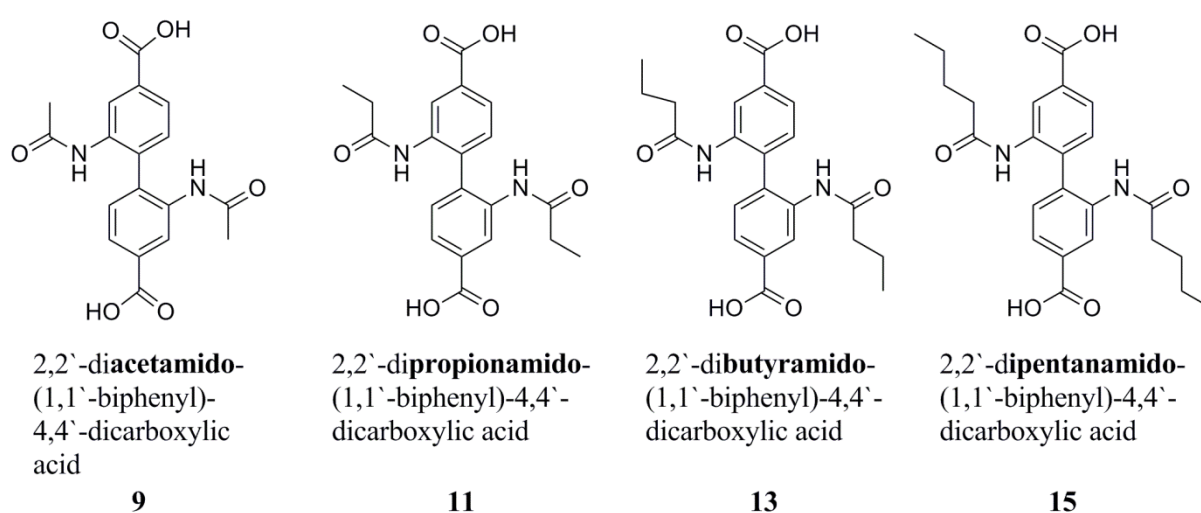


Figure 2.45 Linkers used for the synthesis of **ZnAcBPDC**, **ZnPrBPDC**, **ZnBuBPDC** and **ZnPeBPDC**.

2.5.1 Characterization of ZnAcBPDC, ZnPrBPDC, ZnBuBPDC and ZnPeBPDC

Structural characterization of the synthesized MOFs were carried out by single-crystal X-ray diffraction, powder X-ray diffraction (PXRD), X-ray absorption spectroscopy, solid state NMR spectroscopy, IR spectroscopy, thermogravimetric analysis (TGA) and elemental analysis.

Solvent removal from the MOFs was performed by using different solvents and different methods. The first method applied was using acetone as the exchanging solvent. The as-synthesized samples were immersed in acetone and left for soaking for a period of one day. Dichloromethane was also tried as the exchanging solvent, but the PXRD patterns of these samples showed decomposition of the structures. When diethyl ether was used, MOFs were decomposed except of **ZnAcBPDC**.

The second activation method was supercritical CO₂ drying (SCD). The as-synthesized crystals in DMF were soaked in acetone for 3 days. The soaking solution was replaced 10 times per day. Samples in acetone were placed inside the supercritical CO₂ dryer and the acetone was exchanged against liquid CO₂ eight times. After that, the temperature was raised above the critical temperature of CO₂ (40°C). Samples were kept in the autoclave for one day. Then the chamber was slowly vented. SCD activated MOF samples were stored inside a glovebox.

2.5.1.1 Single Crystal X-Ray Diffraction Measurements of ZnAcBPDC, ZnPrBPDC, ZnBuBPDC and ZnPeBPDC

The colorless cubic shaped crystals were characterized by single-crystal X-ray diffraction. **ZnPrBPDC**, **ZnBuBPDC** and **ZnPeBPDC** showed the same structural motif (Figure 2.46 and 2.47). Due to the low quality of the **ZnAcBPDC** crystals, this crystal structure could not be solved; however it was observed that the cell parameters obtained during the measurements were as same as the cell parameters of **ZnPrBPDC**.

The structure of these MOFs was found to be isorecticular with other IRMOFs,⁶⁰ having linear linkers connecting the octahedral (Zn₄O)(O₂C-)₆ units. Although it was not possible to determine the functional groups crystallographically due to the disordering of the substituent over four positions with a probability of 25 %, it was observed that the substituents are directed to the inside of the pores.

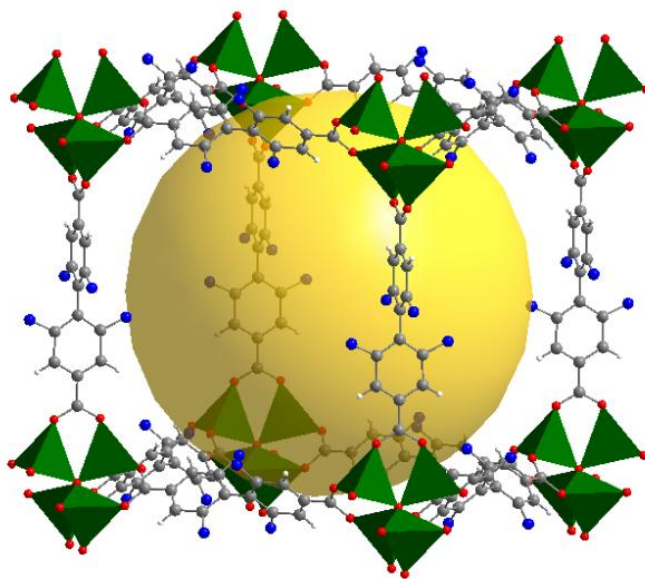


Figure 2.46 The framework connectivity of **ZnPrBPDC** with the zinc coordination sphere (green tetrahedron). One spherical pore (yellow sphere). Atom colors: C dark grey, H white, O red, amide groups blue.

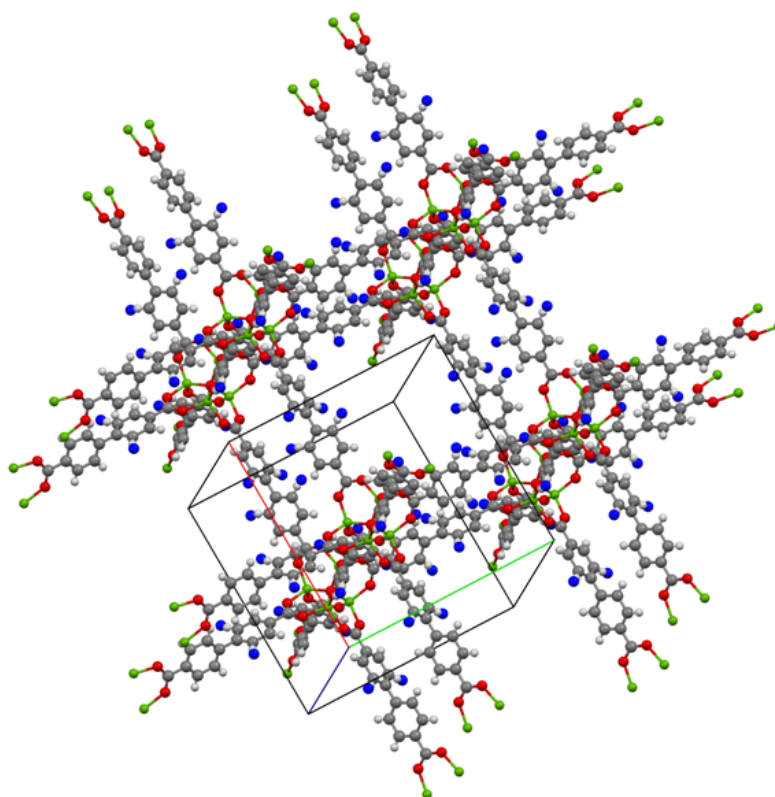


Figure 2.47 Crystal structure of **ZnBuBPDC**. Atom colors: C dark grey, H white, O red, Zn green, amide groups blue.

Contrarily to the first three MOFs described above, no interpenetration was observed for **ZnPrBPDC**, **ZnBuBPDC** and **ZnPeBPDC**. This can be attributed to the long chain amide groups, which prevent the structure undergoing interpenetration. Since single crystal X-ray diffraction of **ZnAcBPDC** could not be measured, PXRD and X-ray spectroscopy techniques were used to clarify this structure.

2.5.2.2 Powder X-Ray Diffraction (PXRD) Measurements of ZnAcBPDC, ZnPrBPDC, ZnBuBPDC and ZnPeBPDC

The powder XRD patterns for **ZnPrBPDC** are shown in Figure 2.48. The patterns of the as-synthesized crystals show a good agreement with the calculated patterns from the single crystal analysis data. The good crystallinity of the crystals can be clearly proved by the high intensities of the diffraction peaks of the as-synthesized material.⁹⁷ All 2θ peaks of **ZnPrBPDC** exposed to supercritical CO₂ activation are consistent with the 2θ peaks of the as-synthesized material. The broadened peaks indicate the fragmentation into microcrystalline material after activation. This phenomenon is frequently observed for highly porous MOFs, wherein the removal of guest solvents results in structural distortion.^{127,143,144} The PXRD was also recorded for the sample washed with acetone. A significantly different pattern and partial loss of crystallinity were observed.

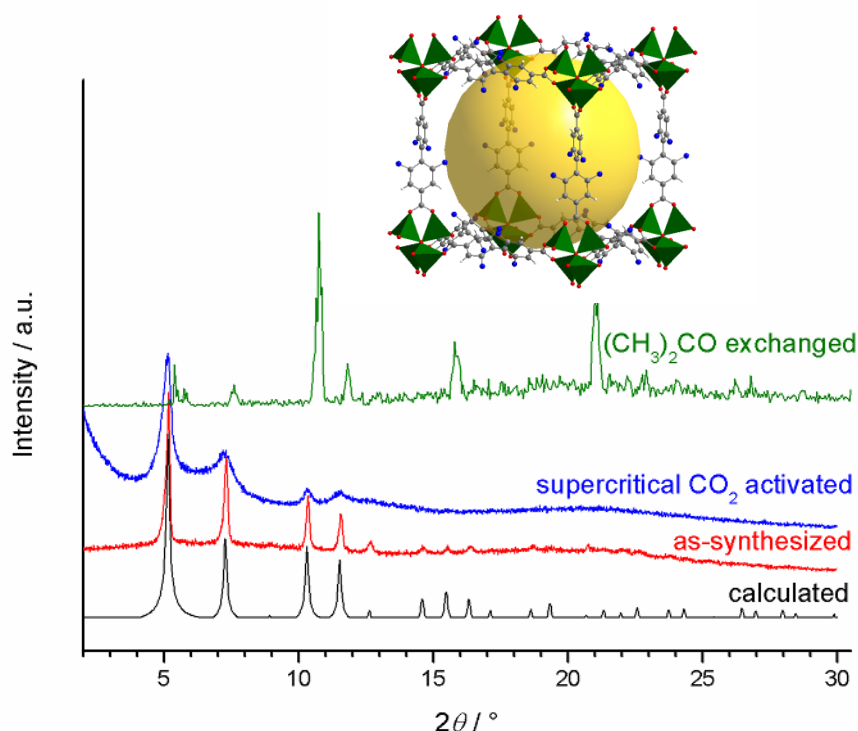


Figure 2.48 PXRD patterns of **ZnPrBPDC**. The calculated pattern from the crystal structure (black), the as-synthesized sample (red), the supercritical CO_2 activated sample (blue) and the acetone exchanged sample (green).

Similar PXRD patterns were obtained for **ZnBuBPDC** (Figure 2.49). After activation with supercritical CO_2 , intensity of the peaks decreases, moreover the peaks become broadened, which means that the structure loses the crystallinity. Since the pattern reveals no change in the 2θ values, it can be concluded that, sample activated with supercritical CO_2 preserves its integrity. PXRD measurements were also performed for the samples washed with acetone. Although, almost no change was observed for the number of reflections up to $2\theta = 11.6^\circ$, a slight shift to higher degrees was observed which can be due to using different instruments having different calibrations.

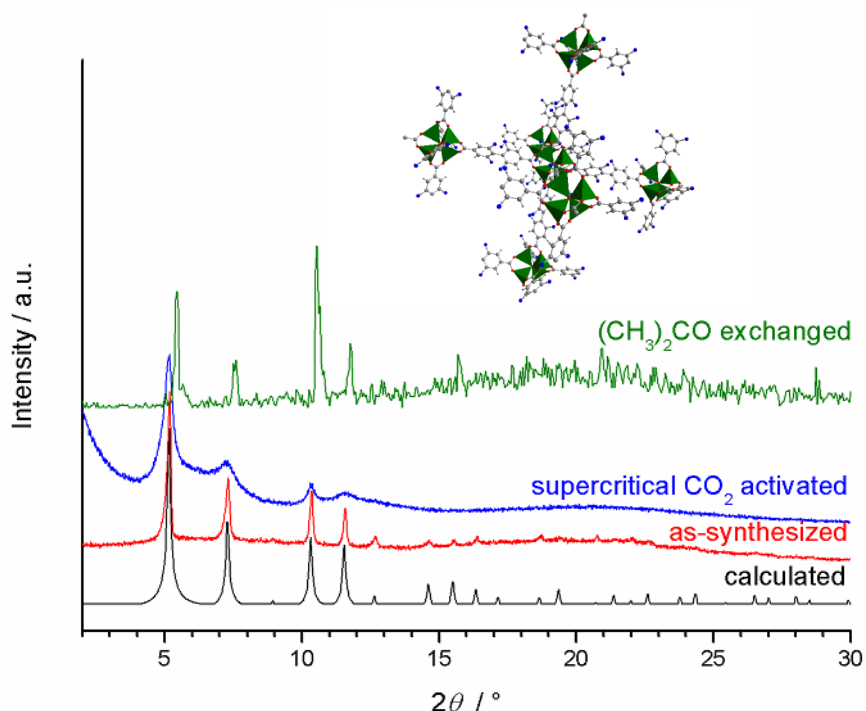


Figure 2.49 PXRD patterns of **ZnBuBPDC**. The calculated pattern from the crystal structure (black), the as-synthesized sample (red), the supercritical CO_2 activated sample (blue) and the acetone exchanged sample (green).

Figure 2.50 shows the PXRD patterns of **ZnPeBPDC**. When the as-synthesized sample is compared with the calculated pattern of the crystals, same reflections with similar intensities are found. As for the **ZnPrBPDC** and **ZnBuBPDC** patterns, sharp reflections indicate a good crystallinity of the material. The supercritical CO_2 activated sample's reflections appear at same 2θ degrees. The reflections at $2\theta = 7.3^\circ$, 10.3° and 11.6° show a strong broadening due to the removal of guest molecules. The pattern of the acetone exchanged sample clearly shows the change of structure by the disappearance of the sharp $2\theta = 7.3^\circ$ reflection.

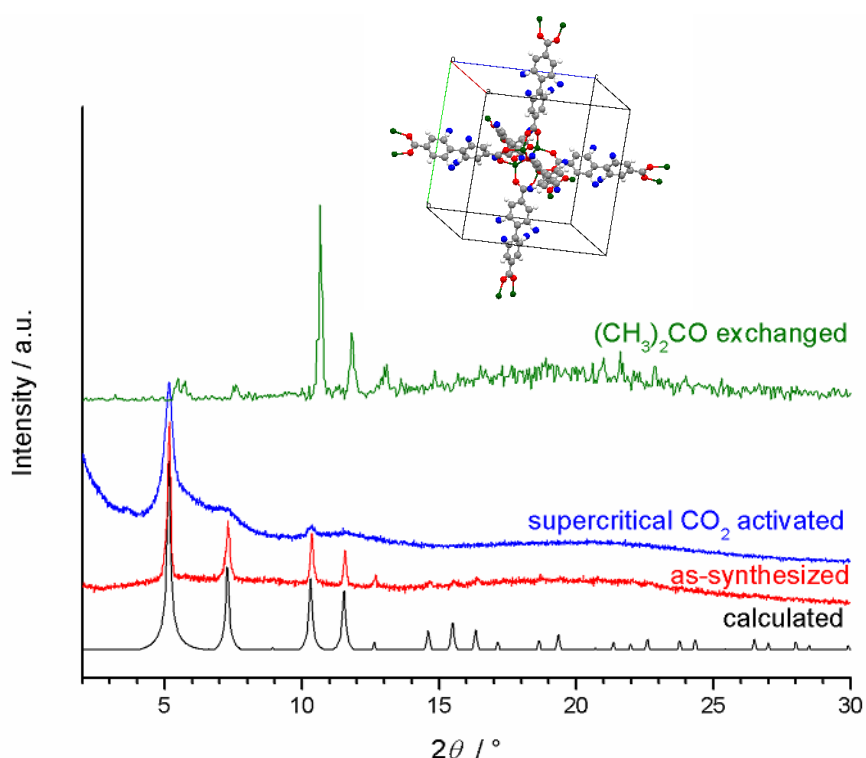


Figure 2.50 PXRD patterns of **ZnPeBPDC**. The calculated pattern from the crystal structure (black), the as-synthesized sample (red), the supercritical CO₂ activated sample (blue) and the acetone exchanged sample (green).

Since single crystal X-ray measurement could not be applied for **ZnAcBPDC** because of the low quality of the crystals, firstly PXRD pattern of the as-synthesized material was compared with the calculated pattern of **ZnPrBPDC** to solve the structure (Figure 2.51). In contrast to the strong reflections of **ZnPrBPDC**, and also **ZnBuBPDC** and **ZnPeBPDC** at $2\theta = 5.2^\circ$, it shows a very weak reflection at $2\theta = 5.2^\circ$. Moreover, the appearance of a very strong reflection at $2\theta = 5.8^\circ$ is observed which means that the structure of **ZnAcBPDC** is different to the others, perhaps it contains two phases. The splitting of the reflection at $2\theta = 10.3^\circ$ can be a further hint for these two phases.

The supercritical CO₂ activated sample shows the same reflections as the as-synthesized sample. The broadening of the $2\theta = 7.3^\circ$ reflection can be attributed to the removal of the guest molecules from the pores. Besides this, it also resembles the interpenetrated IRMOF-9 structure. Since the amide groups on the phenyl rings are not as bulky as the other three MOFs, an interpenetrated structure might be possible for **ZnAcBPDC**.

The PXRD pattern of the acetone exchanged sample shows a very strong increase of the $2\theta = 5.2^\circ$ reflection and a strong decrease in $2\theta = 5.8^\circ$ reflection. Also a broadening of the reflection at $2\theta = 10.3^\circ$ is observed. When this pattern is compared with the **ZnPrBPDC** pattern, it can be concluded that the second phase might be non-interpenetrated as **ZnPrBPDC**, **ZnBuBPDC** and **ZnPeBPDC**. Moreover, it can be also said that the phase which is thought to be interpenetrated is strongly affected by the exchange of the solvent acetone. However a slight shift to higher degrees was also observed and can be attributed to different instruments having different calibrations. Diethyl ether was also used for the activation and the sample was evacuated after solvent exchange. The PXRD pattern of this sample shows reflections very similar to those of the as-synthesized sample. A broadening of the $2\theta = 5.2^\circ$ reflection can be clearly observed, which means the phase which is thought to be non-interpenetrated is strongly affected by the solvent exchange with diethyl ether.

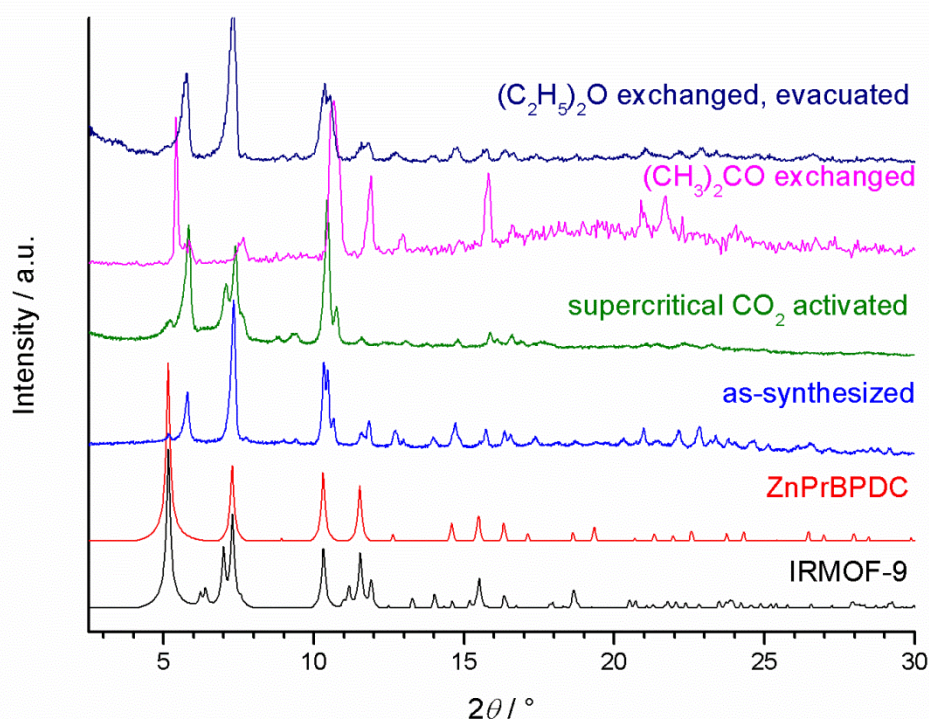


Figure 2.51 The simulated pattern of IRMOF-9 (black), the calculated pattern from the crystal structure of **ZnPrBPDC** (red), the as-synthesized **ZnAcBPDC** sample (red), the supercritical CO_2 activated **ZnAcBPDC** sample (blue), the acetone exchanged **ZnAcBPDC** sample (green) and the diethyl ether exchanged **ZnAcBPDC** sample (pink).

2.5.2.3 X-ray Absorption Spectroscopy of ZnAcBPDC, ZnPrBPDC, ZnBuBPDC and ZnPeBPDC

X-ray absorption spectroscopy measurements were performed at the XAS beamline at the Ångströmquelle Karlsruhe (ANKA) under ambient conditions at 20 °C. The synchrotron beam current was between 80 – 140 mA at 2.5 GeV storage ring energy. A Si(111) double crystal monochromator was used for measurements at the Zn K-edge (9.696 keV). The second monochromator crystal was tilted for optimal harmonic rejection. The spectra were recorded in fluorescence mode with a hyperpure 7-element Ge-detector. Energy calibration was performed with a zinc metal foil. To avoid mistakes in the XANES region due to small changes in the energy calibration between two measurements, all spectra were corrected to the theoretical edge energy of iron foil, which was measured before every scan. For the determination of the smooth parts of the spectra, corrected for pre-edge absorption, a piece-wise polynomial was used. It was adjusted in such a way that the low-R components of the resulting Fourier transform were minimal.^{145,146} After division of the background-subtracted spectrum by its smooth part, the photon energy was converted to photo-electron wave numbers k . The resulting $\chi(k)$ -function was weighted with k^3 . Data analysis was performed in k -space according to the curved wave formalism of the EXCURV98 program with XALPHA phase and amplitude functions.¹⁴⁷ The mean free path of the scattered electrons was calculated from the imaginary part of the potential (VPI set to -4.00).

Figure 2.52 shows the X-ray absorption near edge structure (XANES) spectra of the samples **ZnAcBPDC**, **ZnPrBPDC**, **ZnBuBPDC** and **ZnPeBPDC**. No obvious differences can be found in the XANES spectra for the different samples. The XANES region is dominated by multiple scattering effects, which take mainly place among the nearest neighbor atoms. Therefore the nearest neighbor coordination can be assumed to be the same in all samples. This is also reflected in the Fourier transformed EXAFS spectra shown in Figure 2.53 and the structural parameters obtained by fitting the experimental data with theoretical models as given in Table 2.11. All samples exhibit a first Zn-O contribution with a coordination number of four, according to a tetrahedral environment of the central zinc. Although the coordination number of the next Zn-C contribution, resulting from the carboxy-group is systematically underestimated, it is also four within the error bar for all compounds.

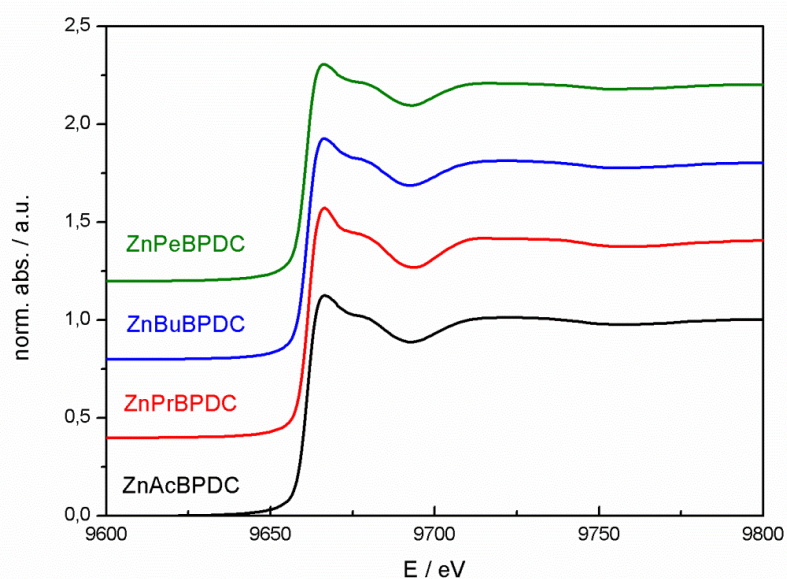


Figure 2.52 XANES spectra of the samples **ZnAcBPDC**, **ZnPrBPDC**, **ZnBuBPDC** and **ZnPeBPDC**. Spectra were shifted for clarity.

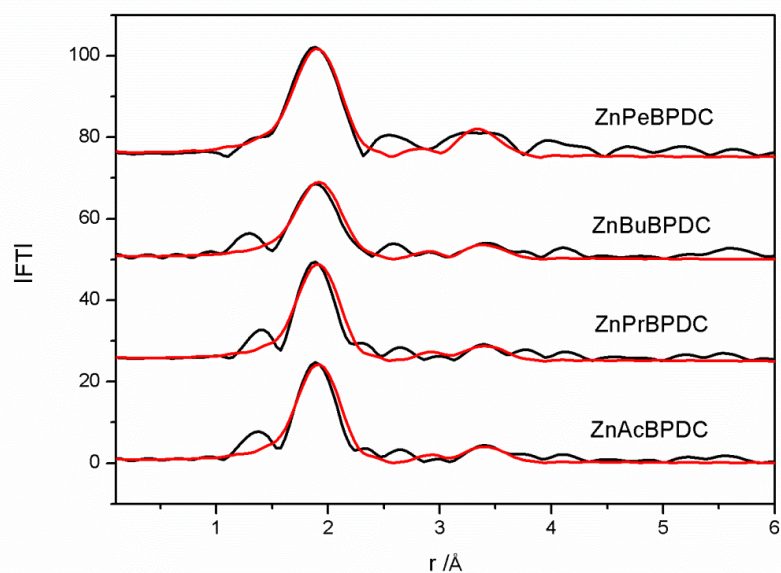


Figure 2.53 Experimental (black) and fitted (red) Fourier transformed EXAFS spectra of the samples **ZnAcBPDC**, **ZnPrBPDC**, **ZnBuBPDC** and **ZnPeBPDC**. Spectra were shifted for clarity.

The similarity between the four samples is continued in the Zn-Zn shell of all samples, where identical coordination numbers and distances are obtained. This coordination number is smaller than the value of four, which is expected according to the single crystal diffraction data. Since these data were obtained on samples taken out of the natant solution, they are containing solvent molecules, while the EXAFS data so far are obtained for dried MOFs. Therefore a distortion of the structure caused in the solvent evaporation process cannot be excluded, which can cause a reduction of the Zn-Zn coordination number. Form the present data it is however not clear, if a real reduction in the coordinating Zn neighbors takes place, or if the structure is strained, leading to an increased disorder in the Zn-Zn coordination, smearing out the Zn-Zn signal.

Table 2.11 Structural parameters obtained by fitting the experimental spectra with theoretical models.

Sample	Abs-Bs ^a	N(Bs) ^b	R(Abs-Bs) ^c / Å	σ^d / Å
ZnAcBPDC	Zn-O	4.2 ± 0.4	1.97 ± 0.02	0.011 ± 0.001
	Zn-C	3.4 ± 0.4	3.03 ± 0.03	0.025 ± 0.003
	Zn-Zn	1.9 ± 0.4	3.23 ± 0.04	0.025 ± 0.005
ZnPrBPDC	Zn-O	4.0 ± 0.4	1.96 ± 0.02	0.010 ± 0.001
	Zn-C	3.2 ± 0.4	3.01 ± 0.03	0.025 ± 0.003
	Zn-Zn	1.8 ± 0.4	3.23 ± 0.03	0.025 ± 0.005
ZnBuBPDC	Zn-O	4.1 ± 0.4	1.98 ± 0.02	0.014 ± 0.001
	Zn-C	3.8 ± 0.6	3.03 ± 0.03	0.025 ± 0.002
	Zn-Zn	1.7 ± 0.4	3.23 ± 0.03	0.025 ± 0.005
ZnPeBPDC	Zn-O	4.0 ± 0.4	1.96 ± 0.02	0.014 ± 0.001
	Zn-C	3.4 ± 0.6	2.99 ± 0.03	0.025 ± 0.002
	Zn-Zn	2.1 ± 0.2	3.19 ± 0.03	0.025 ± 0.005
ZnAcBPDC in DMF	Zn-O	4.4 ± 0.4	1.96 ± 0.02	0.012 ± 0.001
	Zn-C	3.8 ± 0.4	2.97 ± 0.03	0.025 ± 0.003
	Zn-Zn	3.6 ± 0.4	3.16 ± 0.04	0.025 ± 0.005
ZnAcBPDC in DMF after CO₂ ads.	Zn-O	4.3 ± 0.4	1.95 ± 0.02	0.011 ± 0.001
	Zn-C	4.3 ± 0.4	2.98 ± 0.03	0.025 ± 0.003
	Zn-Zn	3.6 ± 0.4	3.17 ± 0.04	0.025 ± 0.005

^a Abs= X-ray absorbing atom, Bs= neighbor backscattering atom. ^b Number of backscattering neighbors. ^c Distance between Abs and Bs. ^d Debye-Waller like disorder factor.

This changes if the solvent-containing MOF structure is considered. In Table 2.11, the EXAFS results for **ZnAcBPDC** in DMF before and after CO₂ adsorption are also given. The spectra are compared in Figure 2.54 with the dry sample. The increased Zn-Zn contribution is visible in the Fourier transformed EXAFS data, and also reflected in the structural parameters obtained by fitting these data. The expected value of four is found within the error bar for both samples. Similar behavior was found in a study by Henke *et. al.*,¹⁴⁸ where in dried MOFs also a reduction of the Zn-Zn contribution was found, which was fully reversible after reabsorption of the solvent. This suggests rather a strained structure than a real destruction after drying of the MOFs. The adsorption of CO₂ in contrast does not lead to visible changes in the spectra, indicating identical structures.

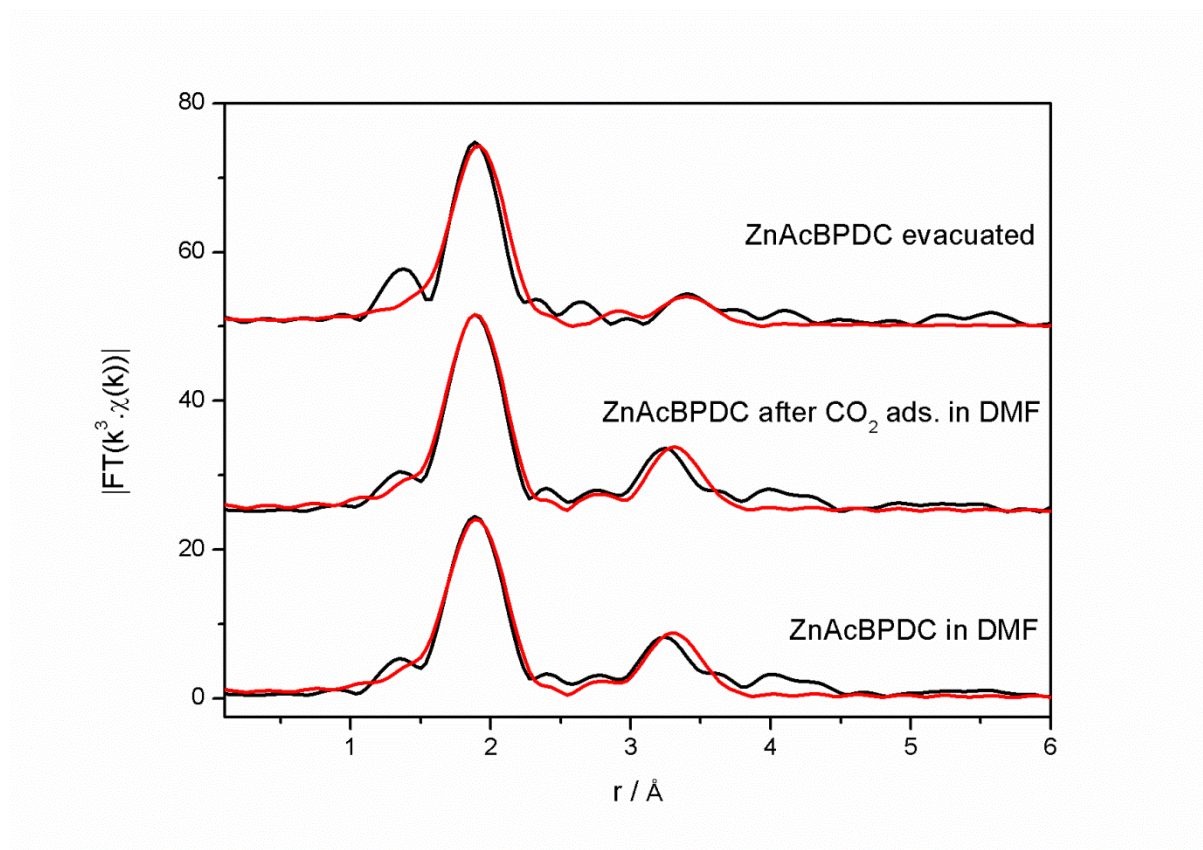


Figure 2.54 Experimental (black) and fitted (green) Fourier transformed EXAFS spectra of the sample **ZnAcBPDC** in the dry state and before and after CO₂ adsorption in DMF.

2.5.2.4 Thermogravimetric Analysis (TGA) of ZnAcBPDC, ZnPrBPDC, ZnBuBPDC and ZnPeBPDC

Thermogravimetric analysis (TGA) measurements were performed with the as-synthesized samples which were kept in DMF. The measurements were performed in ambient atmosphere at a constant heating rate of $5\text{ }^{\circ}\text{C min}^{-1}$ from room temperature up to $800\text{ }^{\circ}\text{C}$.

For **ZnAcBPDC**, two weight loss steps were observed: the first one up to $220\text{ }^{\circ}\text{C}$ can be attributed to the solvents (DMF, water) which is compatible with the elemental analysis data. The second mass loss above $350\text{ }^{\circ}\text{C}$ can be attributed to the collapse of structure as a result of linker decomposition and oxidation. According to the TGA results, it can be concluded that **ZnAcBPDC** is stable up to $350\text{ }^{\circ}\text{C}$ (Figure 2.55).

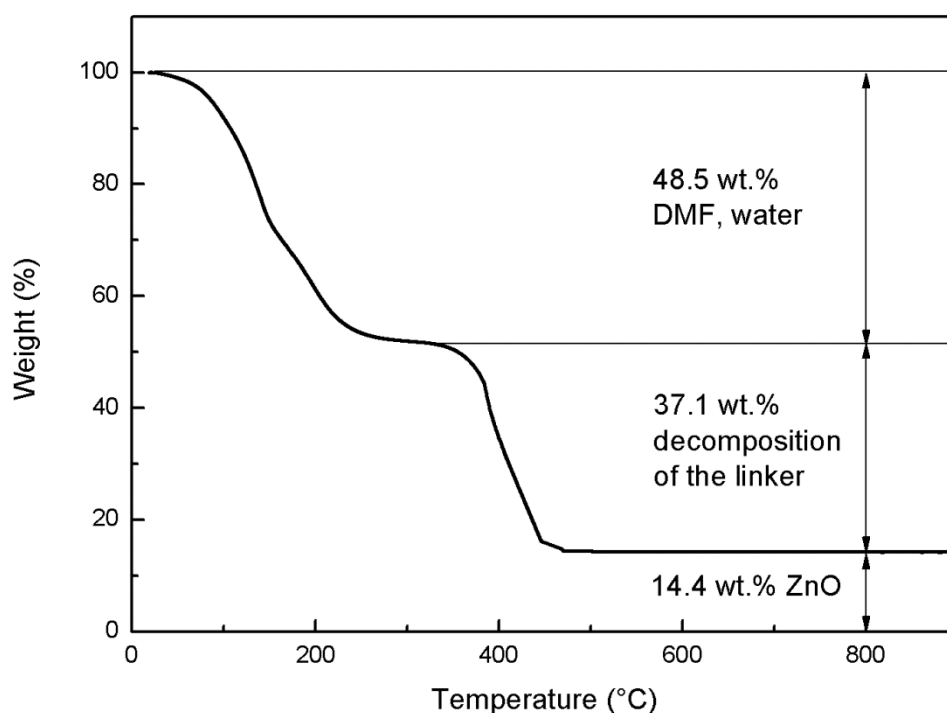


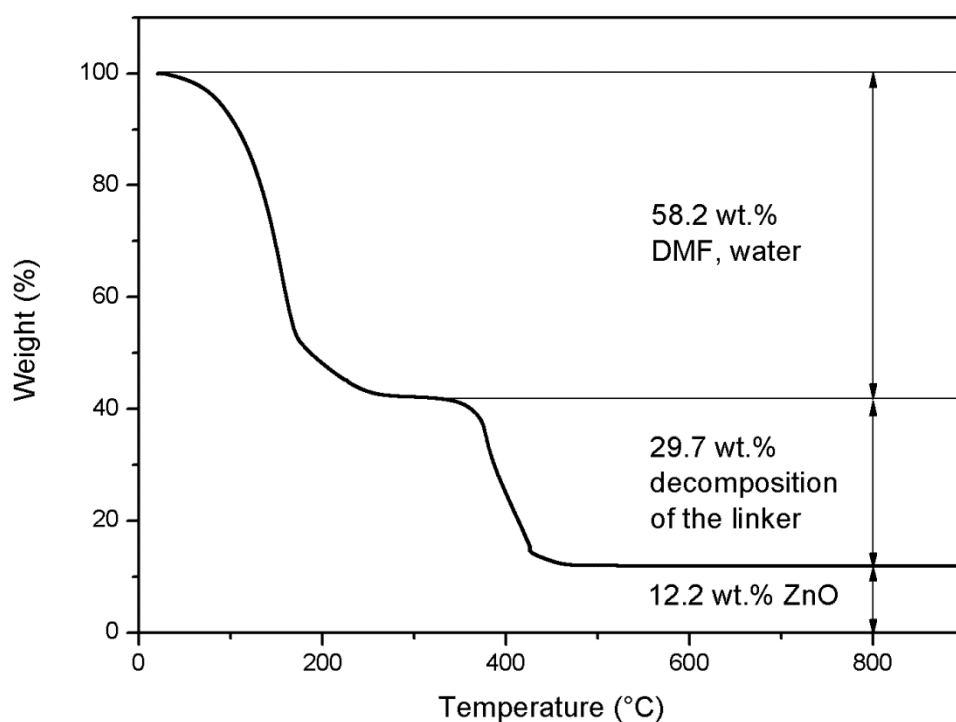
Figure 2.55 TGA of the as-synthesized **ZnAcBPDC** sample.

According to the elemental analysis results, the content of solvents is found as 47.78 wt. % (Table 2.12), which is corroborated with the TGA (48.46 wt. %).

Table 2.12 Calculated and found elemental composition of the as-synthesized **ZnAcBPDC**.

	$\text{C}_{54}\text{H}_{42}\text{N}_6\text{O}_{19}\text{Zn}_4 \cdot (\text{DMF})_{15.7} \cdot (\text{H}_2\text{O})_{4.40}$		
	C	H	N
Calculated	47.30 %	6.31 %	11.84 %
Found	47.21 %	6.22 %	11.93 %

ZnPrBPDC, shows also two weight loss steps: the first one up to 250 °C can be assigned to the solvents (DMF, water). The second mass loss above 350 °C can be attributed to the collapse of the structure as a result of linker decomposition and oxidation. TGA shows that **ZnPrBPDC** is stable up to 350 °C (Figure 2.56).

**Figure 2.56** TGA of the as-synthesized **ZnPrBPDC** sample.

For **ZnPrBPDC**, elemental analysis data reveal 59.16 wt. % of solvent which is absolutely compatible with the TGA results (Table 2.13). According to the elemental analysis, pores do not contain any traces of linker after solvent exchange.

Table 2.13 Calculated and found elemental composition of the as-synthesized **ZnPrBPDC**.

	$\text{C}_{60}\text{H}_{54}\text{N}_6\text{O}_{19}\text{Zn}_4 \cdot (\text{DMF})_{26.00} \cdot (\text{H}_2\text{O})_{9.20}$		
	C	H	N
Calculated	47.48 %	7.35 %	12.84 %
Found	47.59 %	7.46 %	12.73 %

ZnBuBPDC shows two weight loss as the above discussed MOFs: the first one between 100 °C and 300 °C is due to the solvents (DMF, water, 55.93 wt. %) which occupy the pores. The second mass loss above 300 °C can be attributed to the collapse of structure as a result of linker decomposition and oxidation. **ZnBuBPDC** is stable up to 350 °C (Figure 2.57) as **ZnPrBPDC**.

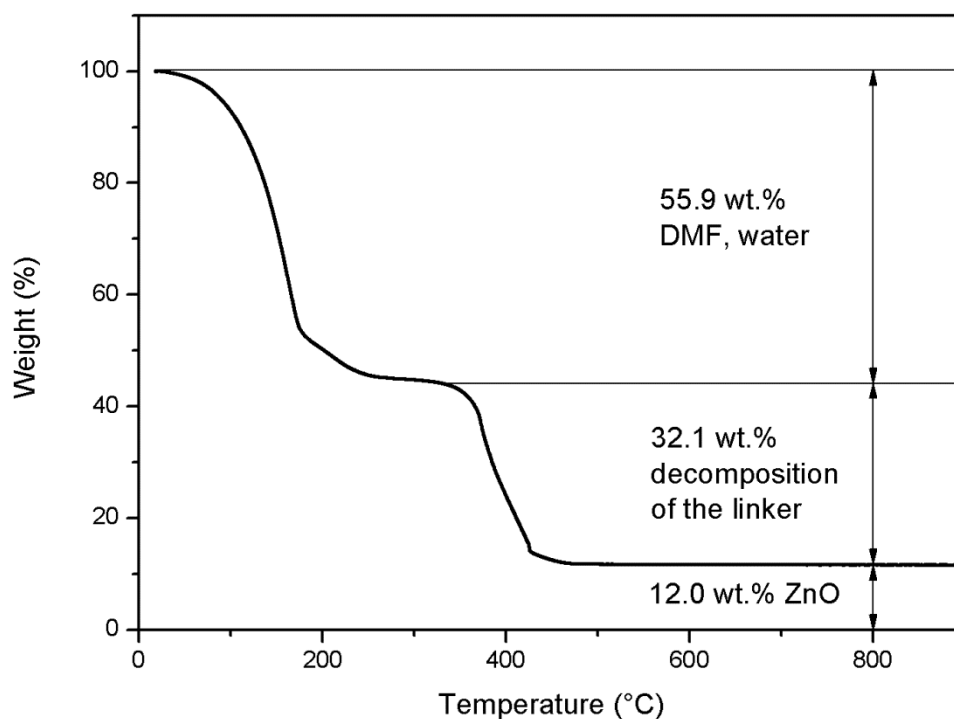


Figure 2.57 TGA of the as-synthesized **ZnBuBPDC** sample.

The elemental analysis of **ZnBuBPDC** is again in good agreement with TGA results (Table 2.14). The solvent amount in the pores is found as 55.01 wt. %. The results also reveal that the pores do not contain any free linkers.

Table 2.14 Calculated and found elemental composition of the as-synthesized **ZnBuBPDC**.

	$\text{C}_{66}\text{H}_{66}\text{N}_6\text{O}_{19}\text{Zn}_4 \cdot (\text{DMF})_{24.25} \cdot (\text{H}_2\text{O})_{4.15}$		
	C	H	N
Calculated	49.66 %	7.33 %	12.62 %
Found	49.77 %	7.45 %	12.51 %

The TGA data of **ZnPeBPDC** reveals a similar behavior as found for the other three MOFs. Two weight loss steps were observed, which belong to the solvents in the pores (up to 200 °C) and the decomposition and oxidation of the linker (between 300 to 430 °C) (Figure 2.58).

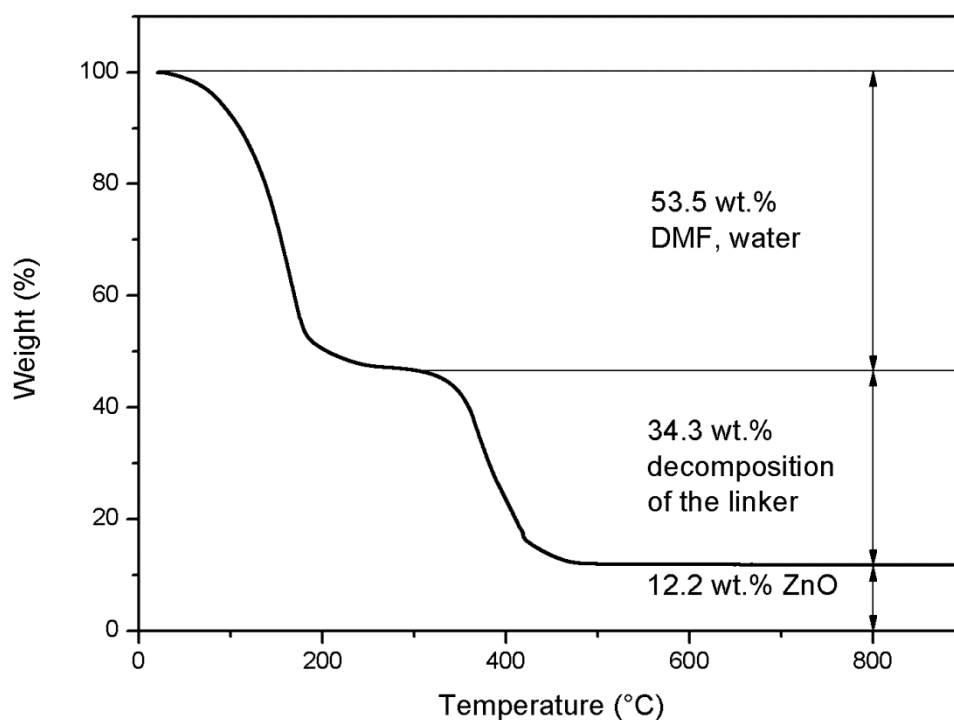


Figure 2.58 TGA analysis of as-synthesized **ZnPeBPDC** sample.

The elemental analysis data and TGA results of **ZnPeBPDC** are absolutely compatible with each other. The solvent amount is found as 53.91 wt. % (53.54 wt. % in TGA analysis). **ZnPeBPDC** also does not contain any free linker in its pores (Table 2.15).

Table 2.15 Calculated and found elemental composition of the as-synthesized **ZnPeBPDC**.

C₇₂H₇₈N₆O₁₉Zn₄· (DMF)_{23.10}· (H₂O)_{9.70}			
	C	H	N
Calculated	49.10 %	7.56 %	11.79 %
Found	49.03 %	7.48 %	11.87 %

2.5.2.5 IR Measurements of ZnAcBPDC, ZnPrBPDC, ZnBuBPDC and ZnPeBPDC

Infrared spectra of the synthesized MOFs and their corresponding linkers are presented in Figure 2.59. The IR measurements, show a pronounced C=O shift. It can be clearly seen that the dicarboxylic acid precursors exhibit intense C=O absorptions around 1690 cm⁻¹, typical for aromatic carboxylic acids associated by hydrogen bonds, the C=O fragments of the MOF materials give rise for absorptions at around 1600 and 1450 cm⁻¹, which again is typical for symmetrically coordinating carboxylate anions.

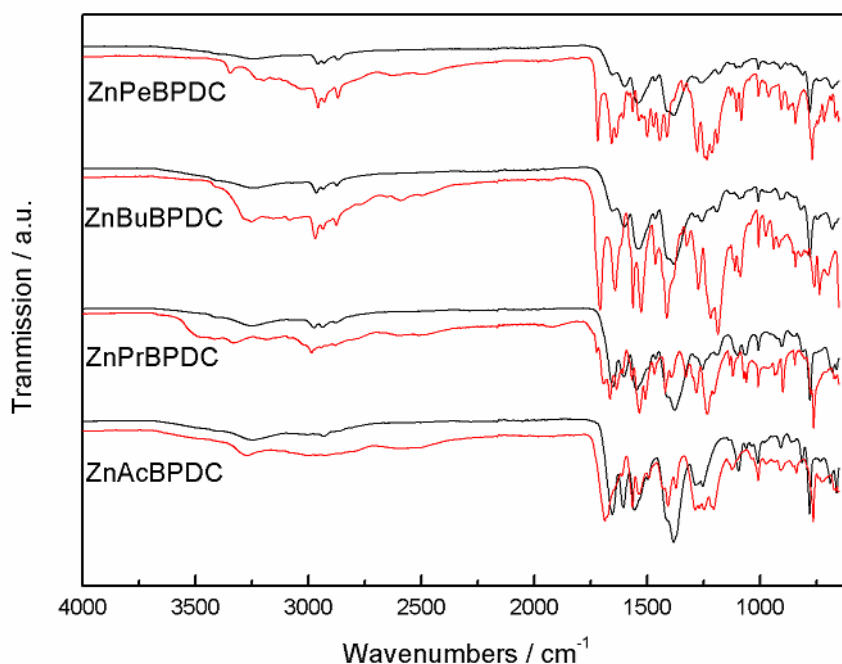


Figure 2.59 IR spectra of **ZnAcBPDC**, **ZnPrBPDC**, **ZnBuBPDC** and **ZnPeBPDC** (black) and their linkers **9**, **11**, **13** and **15** (red).

2.5.2.6 ^{13}C CP-MAS NMR Measurements of **ZnAcBPDC**, **ZnPrBPDC**, **ZnBuBPDC** and **ZnPeBPDC**

Characterization of amide functionalized MOFs was also carried out with solid state ^{13}C CP-MAS NMR measurements (Figure 2.60). The solid state NMR spectra of these MOFs show a great agreement with the high resolution ^{13}C NMR spectra of the corresponding linkers in solution. The carboxylate carbon atoms resonate between 160 to 180 ppm as two broad peaks. The solid state ^{13}C CP-MAS NMR spectra of **ZnAcBPDC** and **ZnPrBPDC** show one broad signal for the other carbon atoms in the aromatic region, while **ZnBuBPDC** and **ZnPeBPDC** show two broad signals which are in complete agreement with the positions of the seven resonances of the corresponding linkers. The aliphatic region of the NMR spectra reveals the expected number of the carbon atoms. In all spectra, a peak around 35 ppm belongs to DMF remaining in the pores of the MOFs.

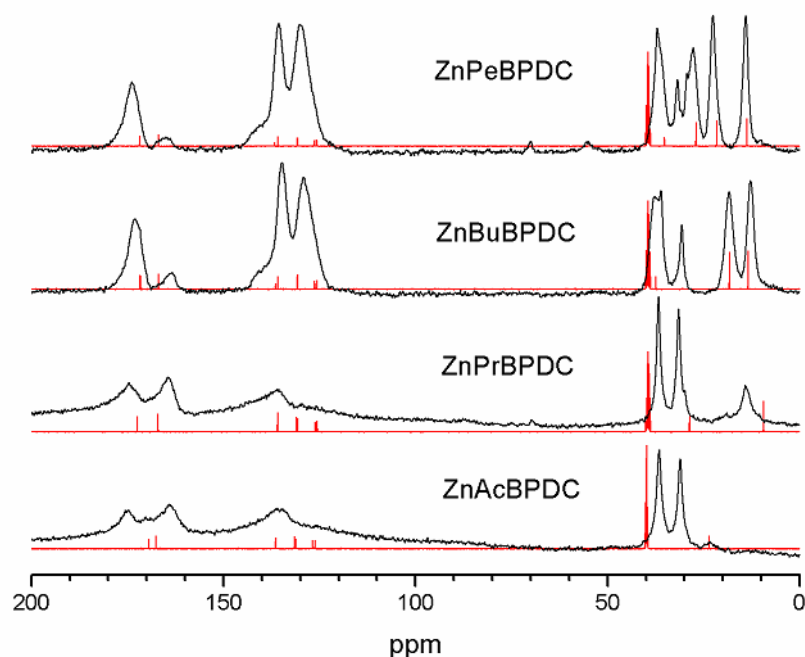


Figure 2.60 ^{13}C CP-MAS NMR spectra **ZnAcBPDC**, **ZnPrBPDC**, **ZnBuBPDC** and **ZnPeBPDC** (black) and high resolution ^{13}C NMR spectra of their linkers **9**, **11**, **13** and **15** (red).

Temperature dependent ^{13}C CP-MAS NMR measurements were applied to **ZnPeBPDC**. The measurements were performed at five different temperatures (20, 30, 40, 50 and 80 °C). When the temperature was increased, sharpening of the peaks was observed especially in the aromatic region (Figure 2.61).

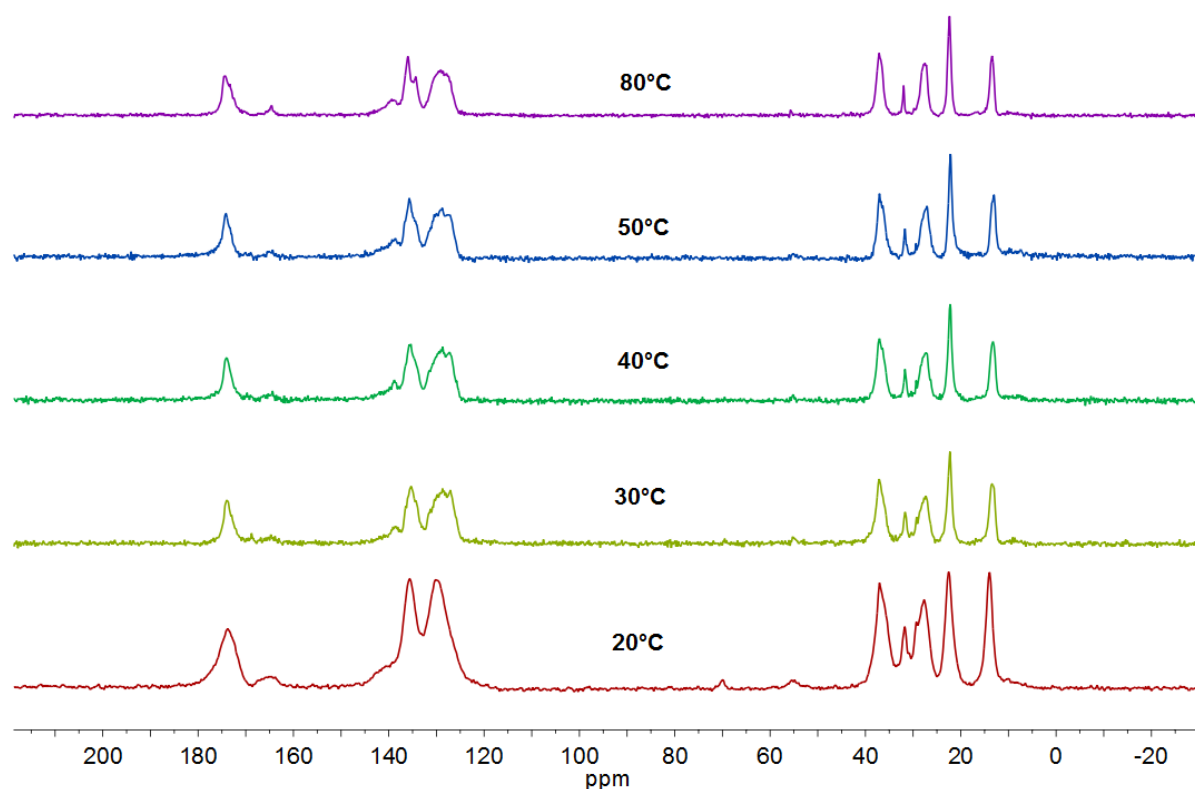


Figure 2.61 Temperature dependent ^{13}C CP-MAS NMR spectra of **ZnPeBPDC**.

2.5.2.7 N_2 Adsorption Measurements of ZnAcBPDC, ZnPrBPDC, ZnBuBPDC and ZnPeBPDC

To confirm the porosity of the MOFs and determine their surface area, N_2 adsorption measurements at 77 K were performed with samples activated by two different evacuation methods (first method: acetone exchanged, second method: supercritical CO_2 dried). The acetone exchanged samples were activated under high vacuum at 80 °C for 24 hours. The supercritical CO_2 dried samples were used without further activation.

ZnAcBPDC showed porosity after both activation methods (Figure 2.62). In both cases a Type I isotherm³⁷ was observed with a hysteresis at $0.4 < p < 0.9$. The hysteresis can be due to the intercrystalline voids in the sample.¹⁴⁹ The hysteresis is smaller in the supercritical CO_2 activated sample. The size difference between the two hysteresis might be the result of the difference in the volume of the adsorbents.¹⁵⁰

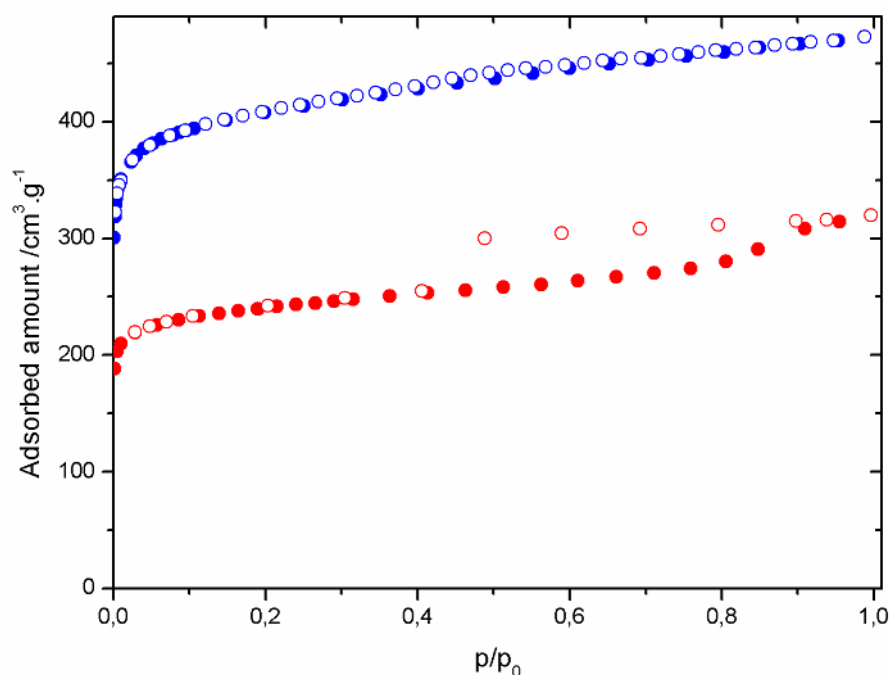


Figure 2.62 N₂ adsorption (close circles) and desorption (open circles) isotherms of **ZnAcBPDC**. The supercritical CO₂ activated sample (blue), the acetone activated sample (red).

The specific surface area of **ZnAcBPDC** showed differences according to the activation method used: For the supercritical CO₂ activated sample 1588 m²/g were found and for the acetone exchanged and evacuated sample 920 m²/g were found.

Such two different surface areas for the same material reveal how important the activation step is. It is also expressed in the literature that the solvent removal methods results in a diversity of the surface areas^{45,126} because of the insufficient removal of the guest molecules in the pores which reduces the surface area remarkably. For instance, for MOF-5 which is one of the most studied MOFs, applying different procedures, different surface areas varying in the range of 570-3800 m²/g were found.^{125,151-154}

As expected the pore volumes calculated for the samples activated with two different methods show also diversity. For the supercritical CO₂ activated sample, the pore volume was found to be 0.73 cm³/g, while for the acetone exchanged and evacuated sample the pore volume was found to be 0.50 cm³/g.

ZnPrBPDC showed porosity only after supercritical CO₂ activation (Figure 2.63). A large hysteresis was observed between $0.05 < p < 1.0$. Such a behavior is not observed for the other three MOFs. The reason for this can be the difference in the size of the chains. Most probably this is because of the position of the amide chain in the network. It should be also stated that the N₂ adsorption measurements for **ZnPrBPDC** took a longer time compared to the other samples' measurements. In other words, the equilibrium state was hard to achieve for **ZnPrBPDC** which means it was difficult for the N₂ molecules to enter the pores. When they were inside the pores it also seems to be difficult for them to leave the structure, probably N₂ molecules were trapped inside resulting in a large hysteresis. This is a very interesting behavior since the material opens the way to selectively catch the molecules, but not let them to leave.

The BET surface area was calculated to be 325 m²/g, which is lower than the surface area of **ZnAcBPDC**. This low surface area can be the result of the selectivity of the material which also resulted in a low pore volume to be 0.15 cm³/g. According to our knowledge, such a material does not exist in the literature and it can be a good candidate for selective gas adsorption.

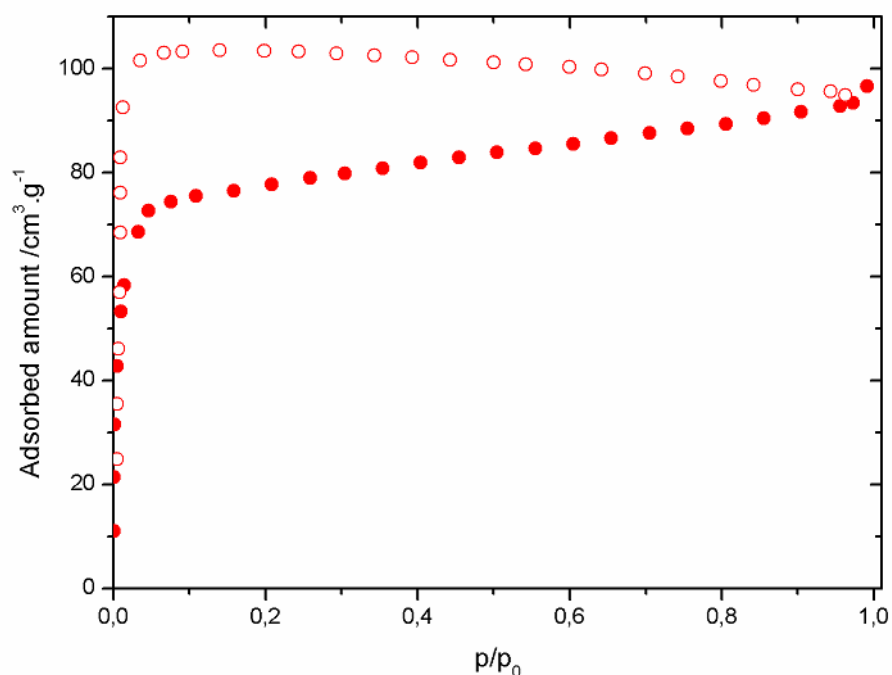


Figure 2.63 N₂ adsorption (close circles) and desorption (open circles) isotherms of the acetone exchanged and evacuated **ZnPrBPDC** sample.

N₂ adsorption measurements were also applied to differently activated **ZnBuBPDC** samples. In this case, the supercritical CO₂ activated samples did not show any porosity. The acetone exchanged and evacuated sample showed a reversible Type I isotherm (Figure 2.64). A small hysteresis was observed between $0.4 < p < 0.7$. This can be again attributed to the intercrystalline voids.

The BET surface area of non-interpenetrated **ZnBuBPDC** was calculated as 850 m²/g, which is lower than the **ZnAcBPDC** sample activated with the same method (920 m²/g) that contains two phases. The lower surface area of **ZnBuBPDC** can be attributed to the longer amide chains in the pores. Moreover poor activation of the material can be another reason for the lower surface area. The pore volume was calculated as 0.43 cm³/g.

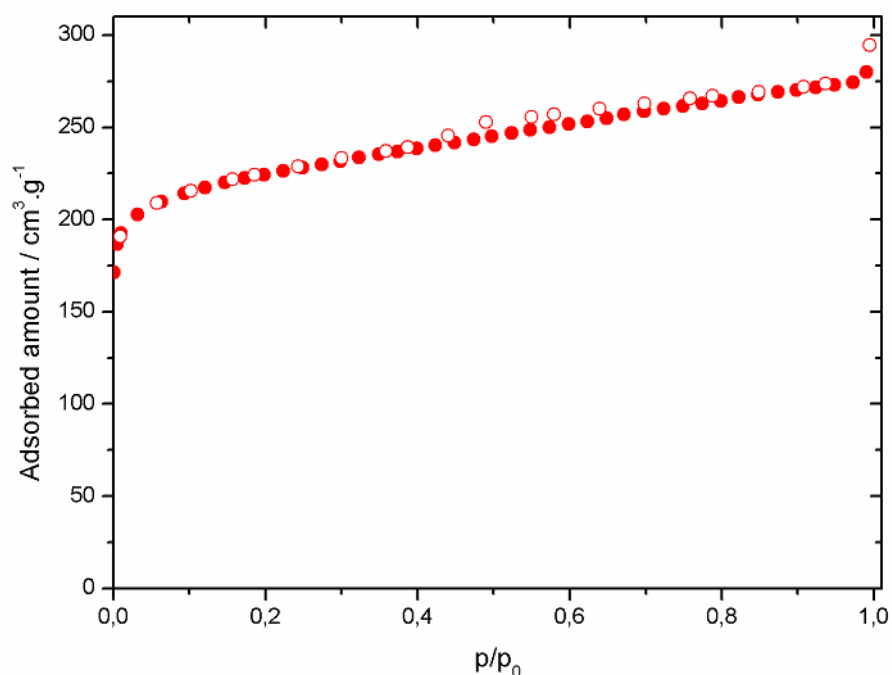


Figure 2.64 N₂ adsorption (close circles) and desorption (open circles) isotherms of the acetone exchanged and evacuated **ZnBuBPDC** sample.

A similar behavior was also observed for the N₂ adsorption of **ZnPeBPDC**. The supercritical CO₂ activated sample did not show any porosity. The acetone exchanged and evacuated sample showed a Type I isotherm with a small hysteresis (Figure 2.65). The BET surface area for **ZnPeBPDC** was found as 1100 m²/g, which is higher than the surface areas found for **ZnAcBPDC** and **ZnBuBPDC** samples activated with the same method. Although **ZnPeBPDC** has a longer amide chain, this higher surface area can be the result of an efficient activation of the material. The pore volume of 0.60 cm³/g which is higher than the other two MOFs' pore volumes also supports this attribution showing the effective activation of the material.

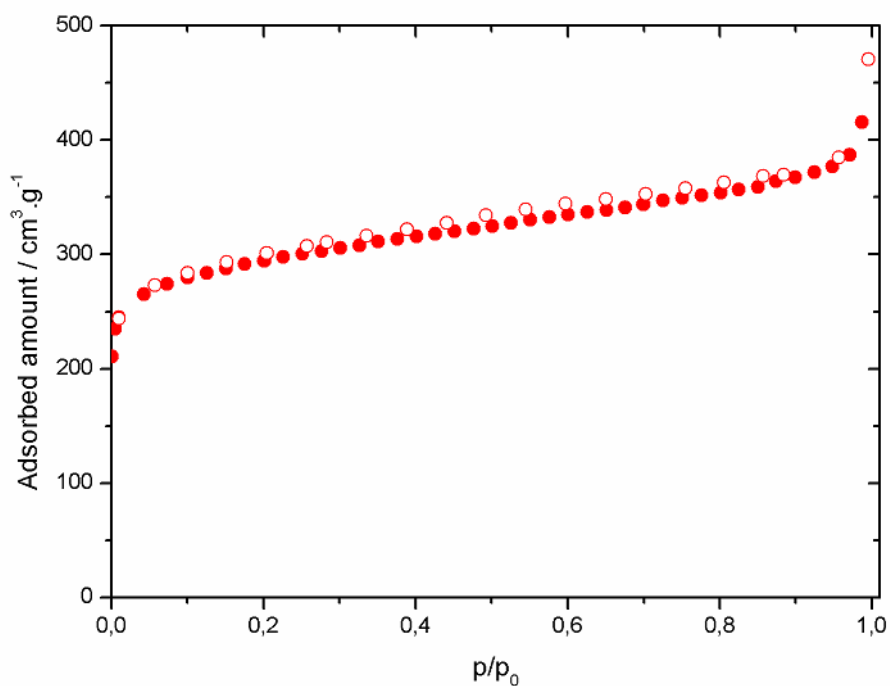


Figure 2.65 N₂ adsorption (close circles) and desorption (open circles) isotherms of acetone exchanged and evacuated ZnPeBPDC sample.

Table 2.16 Summary of the N₂ adsorption measurements of ZnAcBPDC, ZnPrBPDC, ZnBuBPDC and ZnPeBPDC.

	A_{BET} (m ² /g) ^a	A_{BET} (m ² /g) ^b	V_p (cm ³ /g) ^a	V_p (cm ³ /g) ^b
ZnAcBPDC	920	1588	0.50	0.73
ZnPrBPDC	--	325	--	0.15
ZnBuBPDC	850	--	0.43	--
ZnPeBPDC	1100	--	0.60	--

Acronyms: A_{BET} ; BET surface area, V_p ; measured pore volume. ^a the sample exchanged with acetone and evacuated at 80°C for 24h. ^b the super critical CO₂ activated samples.

2.5.3 Alkane and Alkene Adsorptions of ZnAcBPDC and ZnBuBPDC

ZnAcBPDC and **ZnBuBPDC** were tested for alkane and alkene adsorptions. For this study pure alkanes (CH_4 , C_2H_6 , C_3H_8 , and $n\text{-C}_4\text{H}_{10}$) and alkenes (C_2H_4 , C_3H_6 and $n\text{-C}_4\text{H}_8$) were used. The static volumetric method was applied for the temperatures 273 K, 293 K and 313 K. The acetone exchanged samples were activated over night at 298 K and a pressure of $p < 10^{-5}$ mbar. The thermostated system which was described in the adsorption measurements of **ZnBrBPDC**, **ZnNO₂BPDC** and **ZnNH₂BPDC** was used to measure the isotherms.

ZnAcBPDC showed good affinities for C_3H_8 and $n\text{-C}_4\text{H}_{10}$ at all temperatures (Table 2.17, Figure 2.66). For both gases the maximum uptake was observed at 273 K as 6.75 and 6.85 mmol/g respectively. When the temperature was increased to 293 K and 313 K, a decrease of the uptakes is observed for all gases as it was also observed for **ZnBrBPDC**, **ZnNO₂BPDC** and **ZnNH₂BPDC**, which is the result of the increasing thermal energy of the gas molecules at higher temperatures.

Table 2.17 Maximum alkane loadings of **ZnAcBPDC** at 273, 293 and 313 K.

	T = 273 K	T = 293 K	T = 313 K
CH_4	1.06 mmol/g	0.79 mmol/g	0.70 mmol/g
C_2H_6	1.13 mmol/g	0.87 mmol/g	0.63 mmol/g
C_3H_8	6.75 mmol/g	6.04 mmol/g	5.33 mmol/g
$n\text{-C}_4\text{H}_{10}$	6.85 mmol/g	6.07 mmol/g	5.96 mmol/g

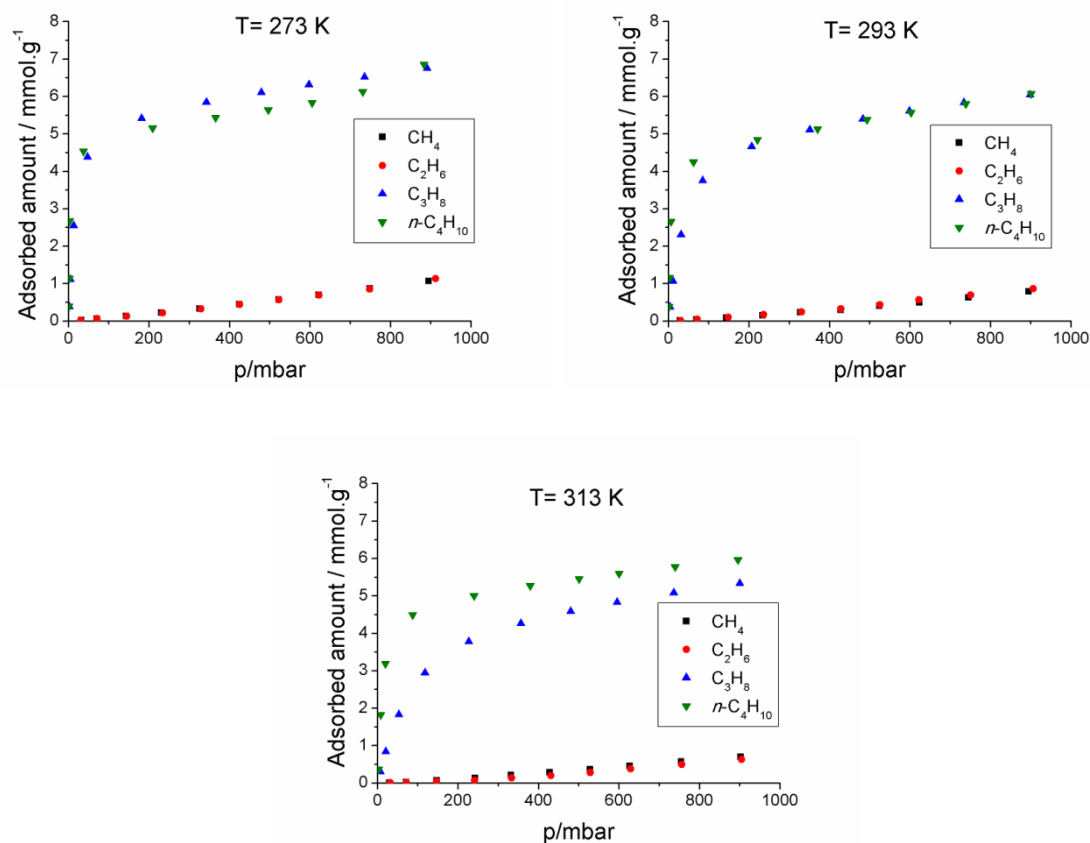


Figure 2.66 Alkane adsorptions of **ZnAcBPDC** at 273, 293 and 313 K.

Among the alkenes, **ZnAcBPDC** showed the maximum uptake for C_3H_6 at all temperatures (Table 2.18). It is also observed for alkenes that when the temperature increases, the adsorbed amount decreases (Figure 2.67). The lowest affinity was observed for the smallest alkene; C_2H_4 at all temperatures. Such a tendency was also noted for the alkane adsorption. Contrary to the alkanes, the maximum loading was obtained for C_3H_6 , not for the longest chain alkene $n-C_4H_8$.

Table 2.18 Maximum alkene loadings of **ZnAcBPDC** at 273, 293 and 313 K.

	T = 273 K	T = 293 K	T = 313 K
C_2H_4	5.98 mmol/g	4.44 mmol/g	2.94 mmol/g
C_3H_6	7.12 mmol/g	6.46 mmol/g	5.72 mmol/g
$n-C_4H_8$	6.92 mmol/g	5.98 mmol/g	5.53 mmol/g

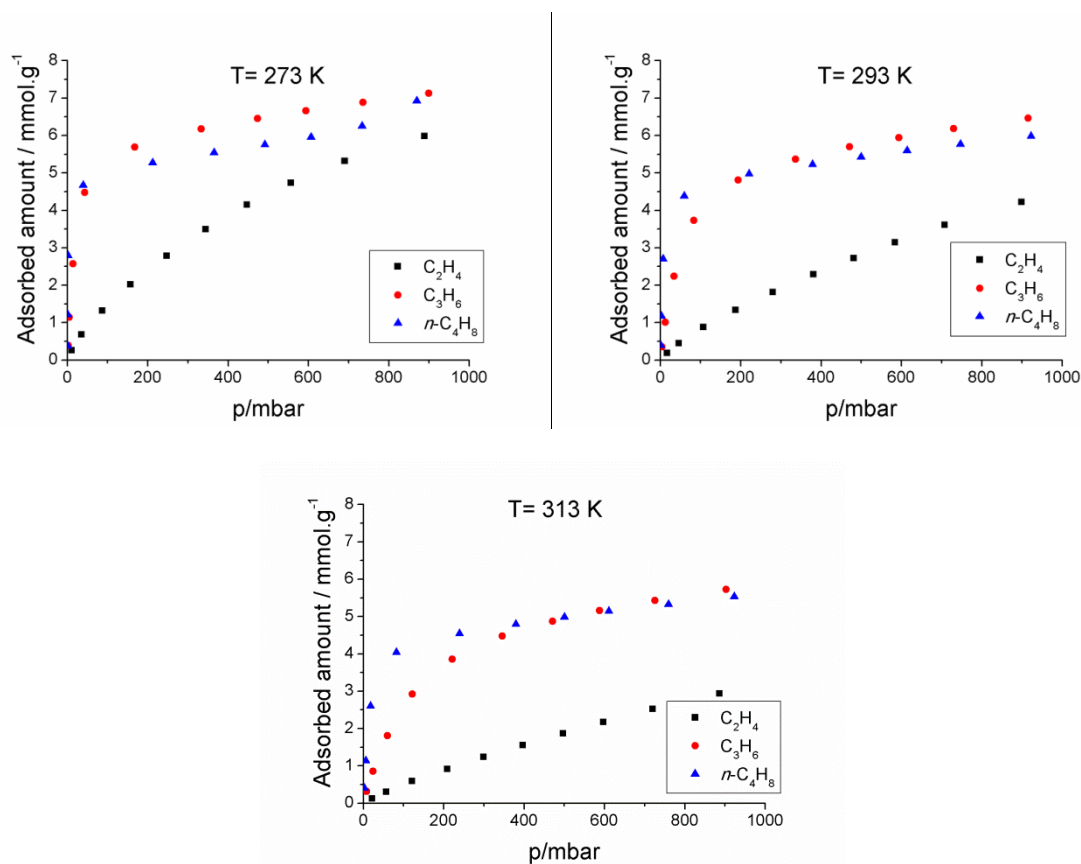


Figure 2.67 Alkene adsorptions of **ZnAcBPDC** at 273, 293 and 313 K.

ZnBuBPDC showed also similar behaviors as **ZnAcBPDC** for the examined gases (Figure 2.68). The maximum uptakes were observed for C_3H_8 and $n-C_4H_{10}$ at all temperatures. When the adsorption behaviors of **ZnBuBPDC** are compared with **ZnAcBPDC**, it is clearly seen that **ZnBuBPDC** reveals weaker affinities to the all alkanes examined. This can be attributed to the longer chain functional group in **ZnBuBPDC**, which also decreases the surface area.

The adsorbent showed the similar affinities to all gases at different temperatures. The maximum loadings of **ZnBuBPDC** are shown in Table 2.19.

Table 2.19 Maximum alkane loadings of **ZnBuBPDC** at 273, 293 and 313 K.

	273 K	293 K	313 K
CH ₄	1.04 mmol/g	0.75 mmol/g	0.61 mmol/g
C ₂ H ₆	2.52 mmol/g	1.79 mmol/g	1.29 mmol/g
C ₃ H ₈	3.26 mmol/g	2.87 mmol/g	2.55 mmol/g
<i>n</i> -C ₄ H ₁₀	3.96 mmol/g	3.79 mmol/g	3.41 mmol/g

When the temperature was increased to 293 K and 313 K, a decrease is again viewed in the gas uptakes. For *n*-C₄H₁₀, the temperature effect is lower than for the other gases and very close uptakes were obtained. Such a behavior can be an advantage for the industrial applications. Since the adsorption or separation of *n*-butane can be effectively performed at room temperature with **ZnBuBPDC**, extra energy consumption for the heating or cooling processes may not be necessary.

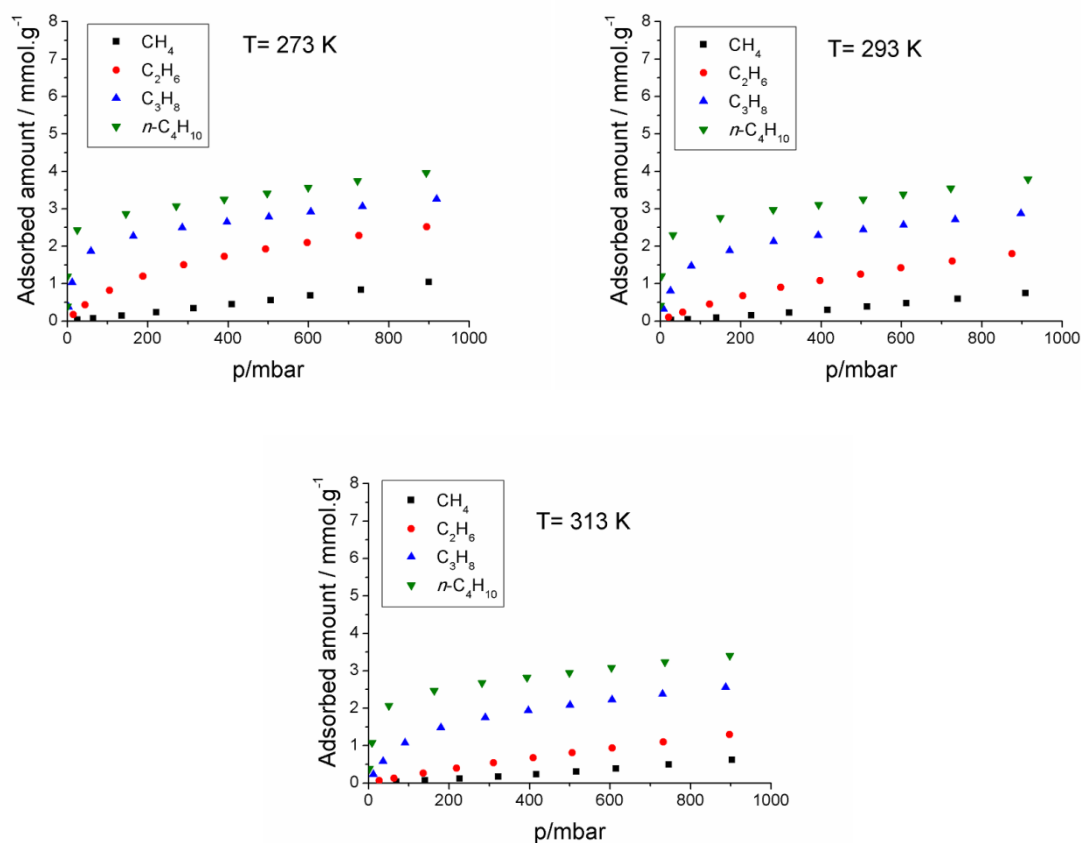


Figure 2.68 Alkane adsorptions of **ZnBuBPDC** at 273, 293 and 313 K.

ZnBuBPDC was also tested for alkene adsorption. Lower uptakes were observed compared to **ZnAcBPDC** (Table 2.20, Figure 2.69). The effect of temperature on adsorption amounts is also quite smooth for alkenes. Especially for C_3H_6 and $n-C_4H_8$ maximum gas uptakes are very close to each other at all temperatures. Among these three alkenes, maximum affinity was viewed for C_3H_6 as in the adsorption by **ZnAcBPDC**.

Table 2.20 Maximum alkene loadings of **ZnBuBPDC** at 273, 293 and 313 K.

	T = 273 K	T = 293 K	T = 313 K
C_2H_4	3.57 mmol/g	2.67 mmol/g	1.88 mmol/g
C_3H_6	3.65 mmol/g	3.57 mmol/g	3.40 mmol/g
$n-C_4H_8$	3.61 mmol/g	3.48 mmol/g	3.10 mmol/g

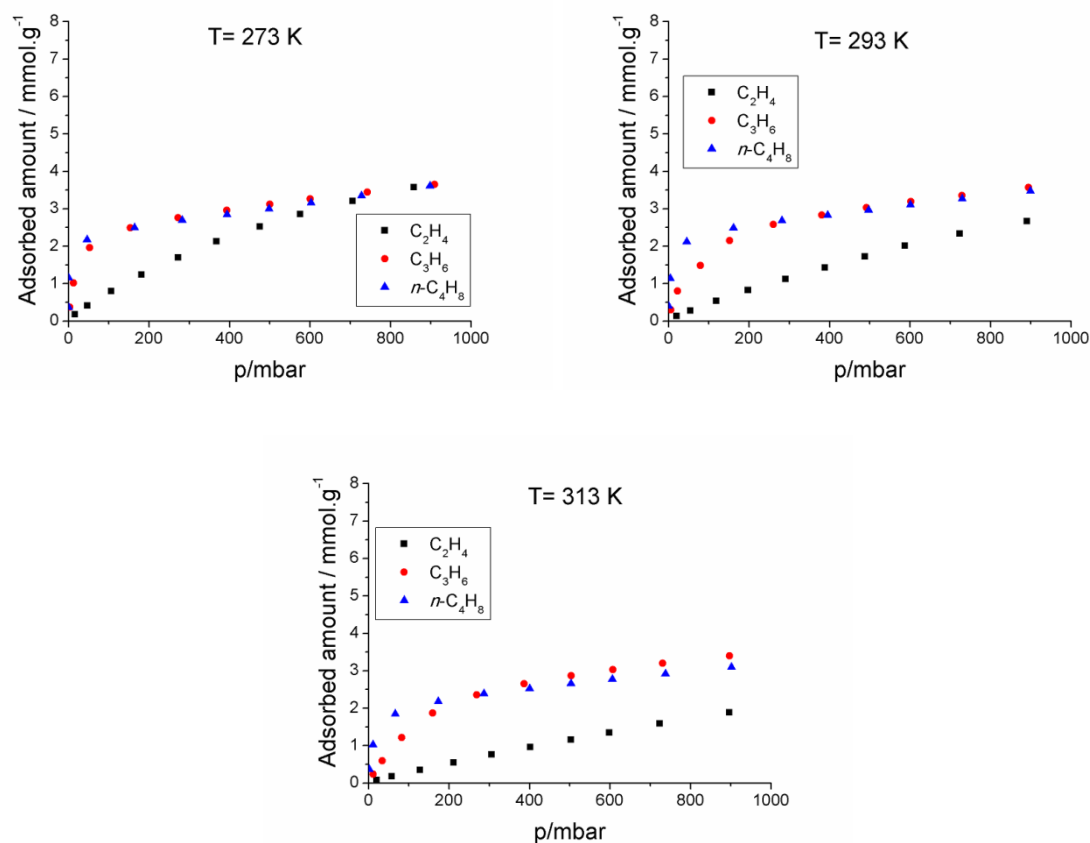


Figure 2.69 Alkene adsorptions of ZnBuBPDC at 273, 293 and 313 K.

2.5.4 CO₂ Adsorptions of ZnAcBPDC and ZnBuBPDC

World's energy demand is mostly met by the combustion of the fossil fuels which causes CO₂ emission.¹⁵⁵ Besides the fuel combustion, it is also known that at least 40 % of annual CO₂ emissions are produced by coal-fired power plants.¹⁵⁶ No doubt, this value will increase because of the rising living standards and the growing population worldwide. Therefore the development of CO₂ capturing methods is one of the most important issues.

The usage of porous materials showing affinity for the CO₂ capture is thought to be an alternative and a more promising solution¹³⁹ than storing CO₂ in the underground geological formations¹⁵⁷ or using the amine scrubbers.¹⁵⁸ Due their properties, such as porous nature, high surface areas and tunable structures, MOFs are among the most promising porous materials for CO₂ capturing and adsorption.^{131, 132,135,159}

In this study, we tested **ZnBrBPDC**, **ZnNO₂BPDC**, **ZnNH₂BPDC**, **ZnAcBPDC** and **ZnBuBPDC** for CO₂ adsorption. Among these, **ZnAcBPDC** and **ZnBuBPDC** showed good affinities for CO₂ adsorption (Table 2.21, Figure 2.70).

As a similar trend to alkane and alkene adsorption, the maximum uptakes were observed at 273 K. Moreover, when the temperature was increased, the uptakes decreased as expected.

Table 2.21 Maximum CO₂ uptakes of the adsorbents **ZnAcBPDC** and **ZnBuBPDC** at 273, 293 and 313 K.

	273 K	293 K	313 K
ZnAcBPDC	4.65 mmol/g	2.91 mmol/g	2.06 mmol/g
ZnBuBPDC	2.97 mmol/g	1.75 mmol/g	1.28 mmol/g

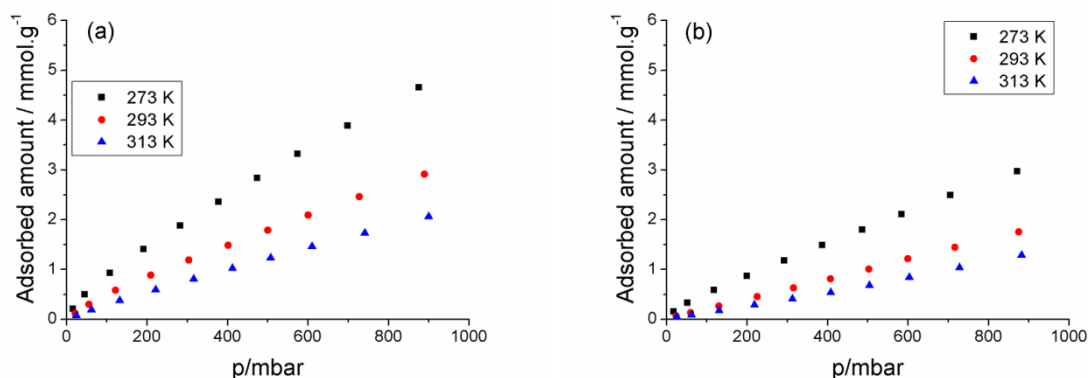


Figure 2.70 CO₂ adsorption of (a) **ZnAcBPDC** and (b) **ZnBuBPDC**.

The maximum uptake was observed by **ZnAcBPDC** (4.65 mmol/g) at 273 K. When this result is compared with the CH₄ adsorption at the same temperature, **ZnAcBPDC**'s selectivity for CO₂ is clearly seen even at high temperatures. In the separation processes, the relative selectivity of the adsorbent for different sorbates is the most important and determining factor.¹³⁷ Therefore, according to these results **ZnAcBPDC** can be used for the CO₂/CH₄ separations (Table 2.22).

Table 2.22 Maximum uptakes of **ZnAcBPDC** for CO₂ and CH₄ adsorptions at different temperatures.

	273 K	293 K	313 K
CH₄	1.06 mmol/g	0.79 mmol/g	0.70 mmol/g
CO₂	4.65 mmol/g	2.91 mmol/g	2.06 mmol/g

2.5.5 Dye Adsorption of **ZnAcBPDC**, **ZnPrBPDC**, **ZnBuBPDC** and **ZnPeBPDC**

Besides N₂ adsorption, another method to determine the porosity of the MOFs is dye adsorption.⁸⁵ Having this knowledge, **ZnAcBPDC**, **ZnPrBPDC**, **ZnBuBPDC** and **ZnPeBPDC** were tested for their dye adsorption capabilities. In this very simple experiment, saturated solutions of para red were prepared using DMF as a solvent. The colorless crystals of MOFs were added into the dye solutions. 2 min after the addition, a color change from colorless to red was observed for **ZnPrBPDC**, **ZnBuBPDC** and **ZnPeBPDC** (Figure 2.71).

For **ZnAcBPDC**, 2 h after the addition, a color change from colorless to dark yellow was observed. This color difference can be attributed to the two different phases present in **ZnAcBPDC**. This means, one of the phases, most probably the non-interpenetrated phase adsorbs para red, but the other phase has no affinity to para red. Therefore, not only the adsorption took longer time but also a very small amount of para red was adsorbed resulting in a dark yellow color instead of red.

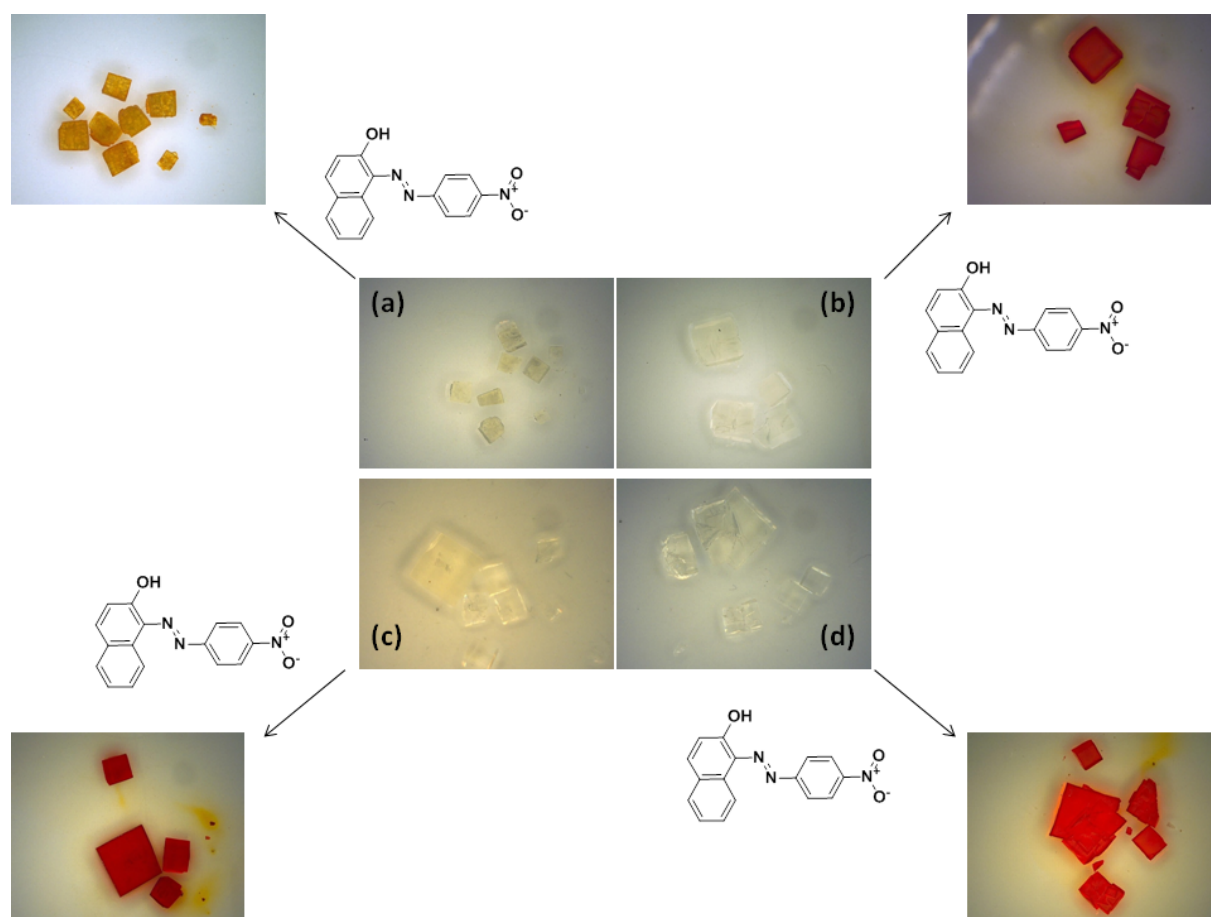


Figure 2.71 Adsorption of para red. **ZnAcBPDC** (a), **ZnPrBPDC** (b), **ZnBuBPDC** (c) and **ZnPeBPDC** (d).

2.6 The Thiophene Linkers

The structure of the MOFs can be easily altered by the linker choice. Since large surface areas and pore volumes are always desirable for catalysis or gas adsorption applications, the linker design is one of the key points of the MOF synthesis. The usage of long linkers is the most common strategy to reach high surface areas and large pores. We, therefore, thought about modifying the three aryl dihalides which were previously synthesized by our group¹⁶⁰ to yield long carboxylate linkers suitable for the large pore volume MOF synthesis (Figure 2.72). Besides the length of the compounds, another interesting feature of these linkers is their highly fluorescent backbone which could be used as a portable sensor kit like MOF-A-GO which was reported by Lee *et al.*¹⁶¹

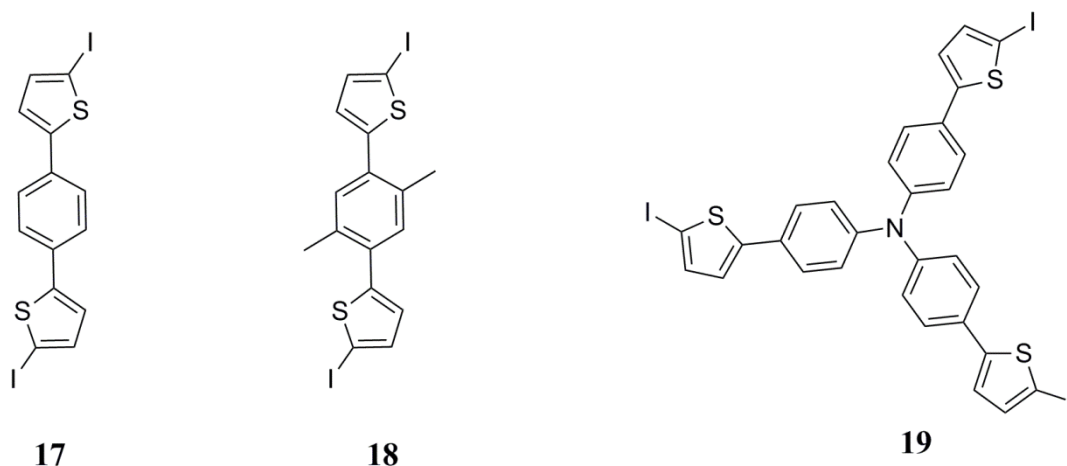
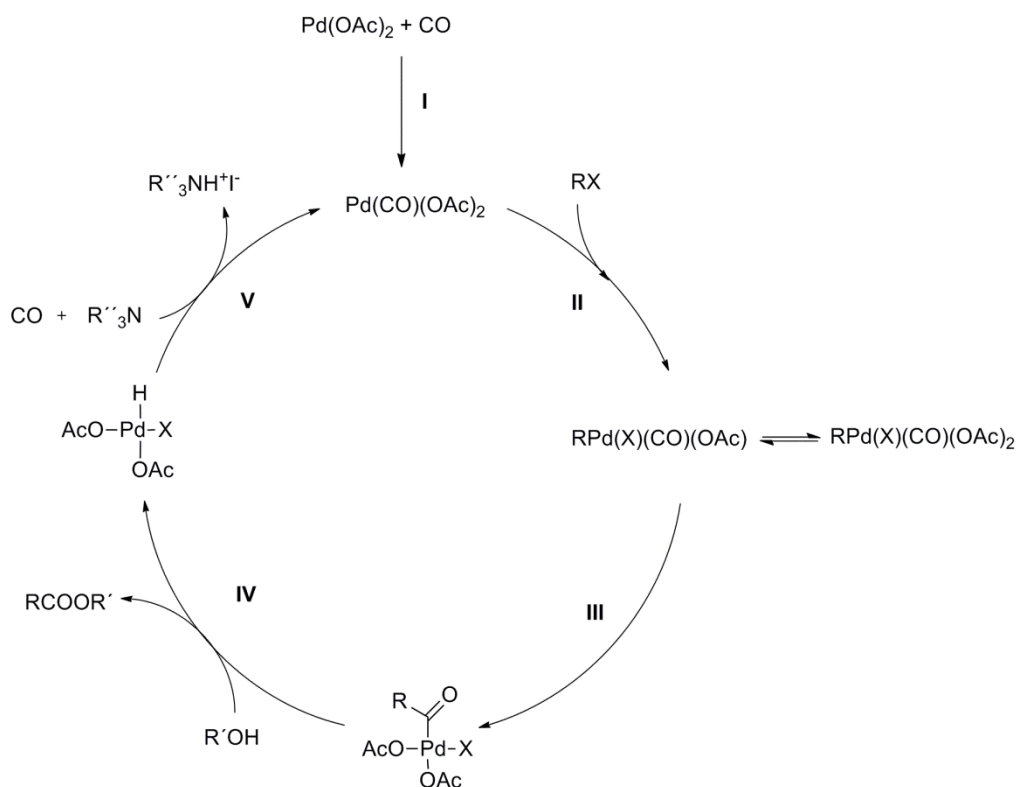


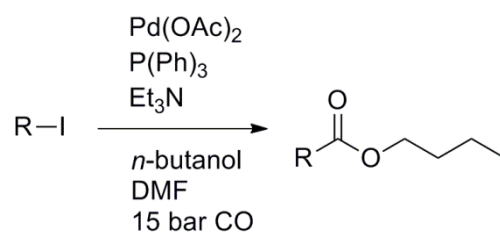
Figure 2.72 Precursors for the thiophene linkers.

A study by Heck *et al.* shows that the esters can be catalytically synthesized with good yields using palladium acetate as a catalyst in the presence of an alcohol and a tertiary amine.¹⁶² The possible mechanism includes firstly the catalyst activation by CO insertion (I). Oxidative addition of aryl halide to the palladium complex (II) is followed by an insertion of the alkyl group into the carbonyl group (III).¹⁶³ Reductive elimination of the palladium complex by attack of the alcohol results in the formation of a hydrido-palladium complex (III) and the ester. Then, the hydride loses HX in the presence of a tertiary amine and regenerates the catalyst (IV) (Scheme 2.10).



Scheme 2.10 Mechanism for the palladium catalyzed carboalkylation.

For the synthesis of aryl substituted thienyl esters, the corresponding iodo derivatives **17**, **18** and **19** were used. It was shown in the literature that different palladium complexes such as dihalo or haloarylbis(triphenylphosphine)palladium(II) can be used for such carboalkoxylation reactions.¹⁶² It was also shown that using palladium acetate as the catalyst with the addition of triphenylphosphine can lead to identical activities. Moreover, a usage of an excess triphenylphosphine results in an acceleration of the CO insertion. For this reason palladium acetate was preferred and three equivalents of triphenylphosphine were applied to the reaction medium. The reduction of palladium(II) acetate was performed by carbon monoxide. Due to the low solubility of the thienyl compounds, *n*-butanol was used to obtain a longer chain ester to overcome the solubility problem for the following steps (Scheme 2.11).



Scheme 2.11 Carboalkylation reaction of **17**, **18** and **19**.

For the first attempts, carbon monoxide was passed through the reaction medium with a continuous flow for 30 hours at 100 °C. The NMR analysis showed that a mixture of the ester and the starting material was obtained at the end of the reaction. Increasing the reaction time and the amount of the reactants did not increase the conversion. The reason for incomplete reaction was attributed to the insufficient carbonmonoxide interaction with the catalyst. For this reason, instead of passing a CO stream, a constant pressure of carbonmonoxide was applied by performing the reaction in a stainless steel autoclave. After the optimization of the reaction conditions, NMR, IR and elemental analysis confirmed that the target esters **20**, **21** and **22** were successfully synthesized in good yields (Figure 2.73).

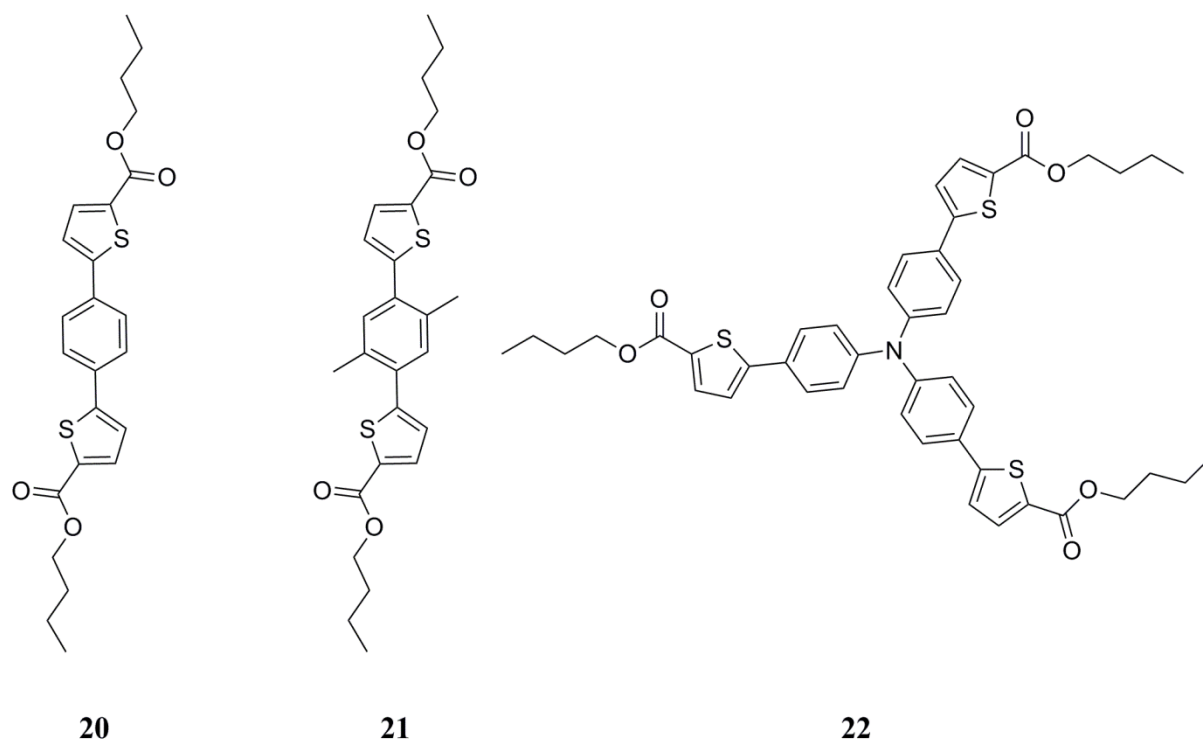


Figure 2.73 Esters **20**, **21** and **22**.

The ^1H NMR spectrum of **20** reveals three peaks in the aromatic region (Figure 2.74). The four protons of the phenyl ring (H1) give a singlet at 7.65 ppm. The thiophene protons neighboring the carboxyl group (H5) appear as a doublet at 7.76 ppm with a coupling constant of 4.0 Hz. Similar to the second thiophene protons (H6) appearing at 7.31 ppm. The methylene protons neighboring to oxygen (H8) show a triplet at 4.31 ppm with a coupling constant of 6.8 Hz, while the other methylene units (H9 and H10) of the butoxy groups appear as multiplets at 1.78–1.71 and 1.52–1.43 ppm respectively. The methyl groups (H11) show a triplet at 0.98 ppm with a coupling constant of 7.2 Hz. Eleven signals in the ^{13}C NMR spectrum also confirm the structure (Figure 2.75). The carbon atoms of the carboxylic group resonate at 162.3 ppm. HMBC and HMQC techniques were used to assign the other carbon atoms.

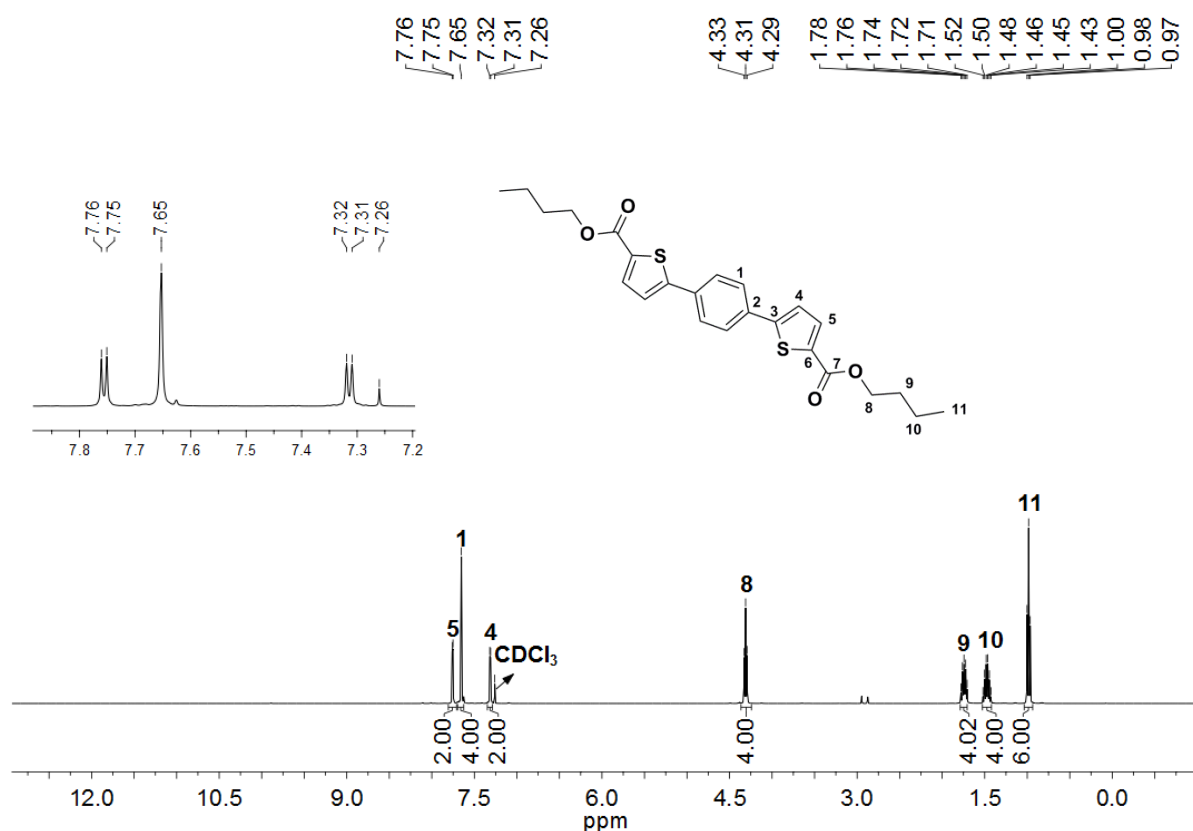


Figure 2.74 ^1H spectrum of **20** recorded in CDCl₃.

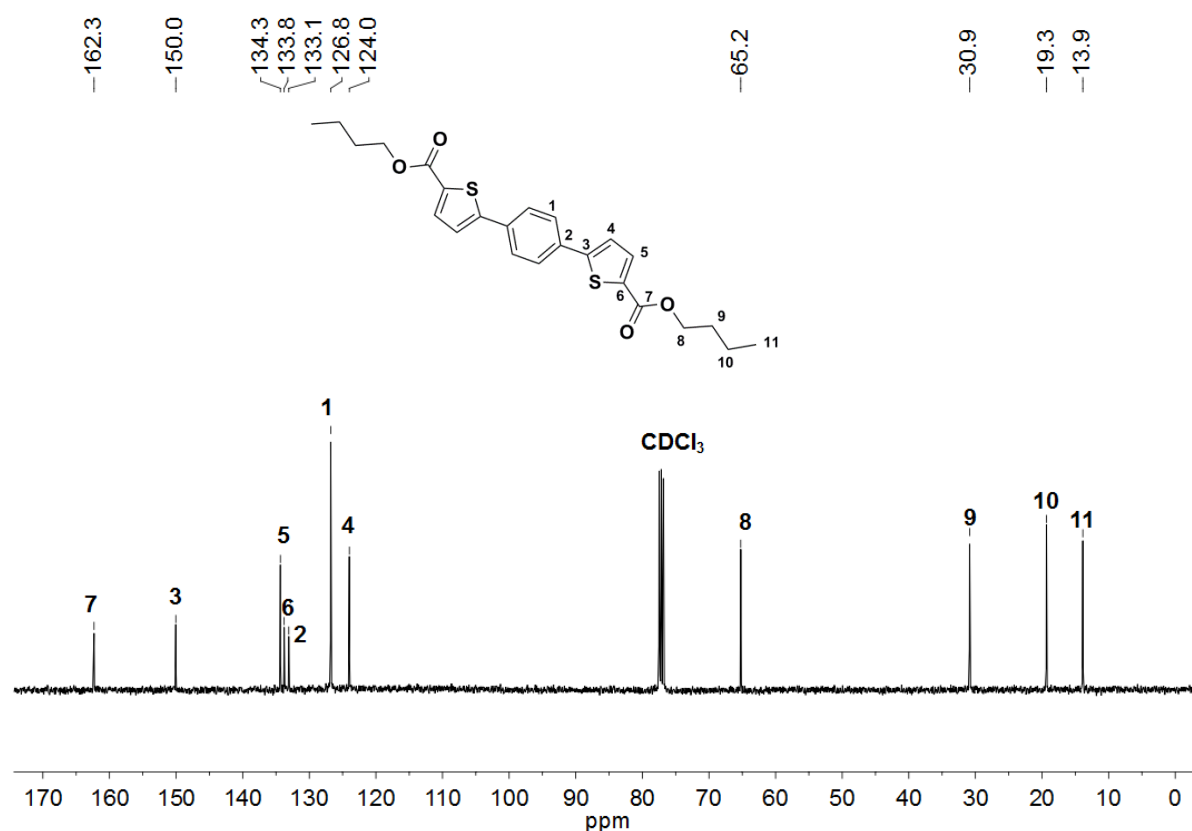


Figure 2.75 ^{13}C NMR spectrum of **20** recorded in CDCl_3 .

In the ^1H NMR spectrum of **21**, the two protons of the phenyl ring (H1) give a singlet at 7.34 ppm (Figure 2.76), while the methyl groups attached to the phenyl ring (H13) give a singlet at 2.43 ppm. The thiophene protons neighboring the carboxyl group (H6) appear as a doublet at 7.78 ppm with a coupling constant of 3.7 Hz, and the other thiophene protons (H5) show also a doublet at 7.09 ppm. The methylene protons neighboring the oxygen atom (H10) are assigned to a triplet at 4.32 ppm ($J = 6.6$ Hz). While the other methylene units of the butoxy groups (H11 and H12) appear as multiplets at 1.78–1.71 and 1.52–1.43 ppm respectively. The methyl groups (H12) show a triplet at 0.98 ppm with a coupling constant of 7.4 Hz.

As expected, the ^{13}C NMR spectrum shows the resonances of eleven carbon atoms (Figure 2.76). The carbonyl carbons appear at 162.5 ppm. The assignments of the carbon resonances were done by HMBC and HMQC techniques.

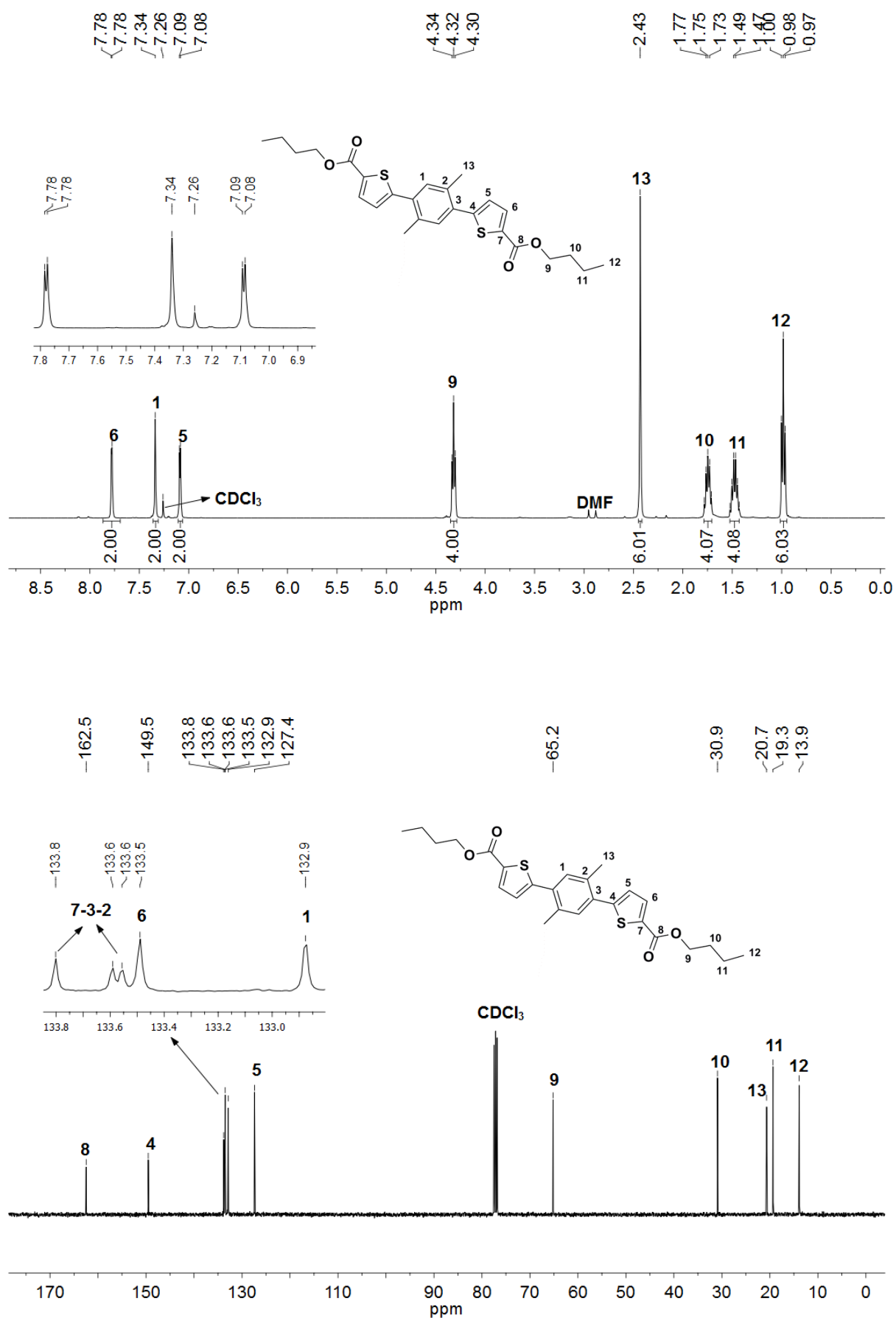


Figure 2.76 ^1H and ^{13}C NMR spectra of **21** recorded in CDCl_3 .

The ^1H NMR spectrum of **22** reveals four peaks in the aromatic region (Figure 2.77). Six protons neighboring the nitrogen atom of the phenyl ring (H2) give a doublet at 7.56 ppm with coupling constant of 8.6 Hz, the other protons of the phenyl ring (H3) also show a doublet at 7.16 ppm. The thiophene protons (H7) neighboring the carboxyl group resonate as a doublet at 7.75 ppm ($J = 3.9$ Hz), the other thiophene protons (H6) appear again as a doublet at 7.23 ppm. The methylene protons neighboring the oxygen (H10) show a triplet at 4.31 ppm ($J = 6.6$ Hz). While the other methylene units of the butoxy groups (H11 and H12) appear as multiplets at 1.78–1.71 ppm and 1.52–1.43 ppm respectively. The methyl groups (H13) show a triplet at 0.98 with coupling constant of 7.4 Hz. The ^{13}C NMR spectrum shows thirteen signals confirming the structure (Figure 2.78). The carbonyl carbon atoms appear at 162.5 ppm. HMBC and HMQC techniques were used for labeling the protons and carbon atoms.

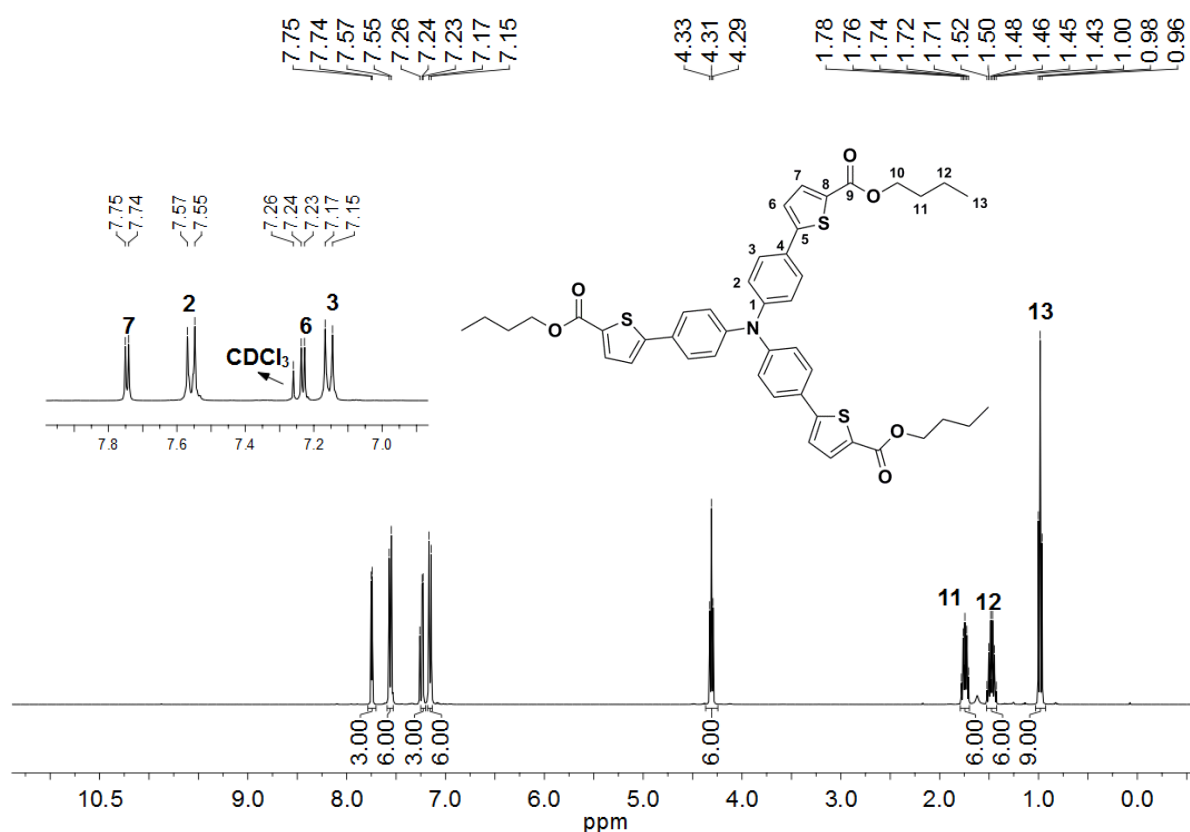


Figure 2.77 ^1H spectrum of **22** recorded in CDCl_3 .

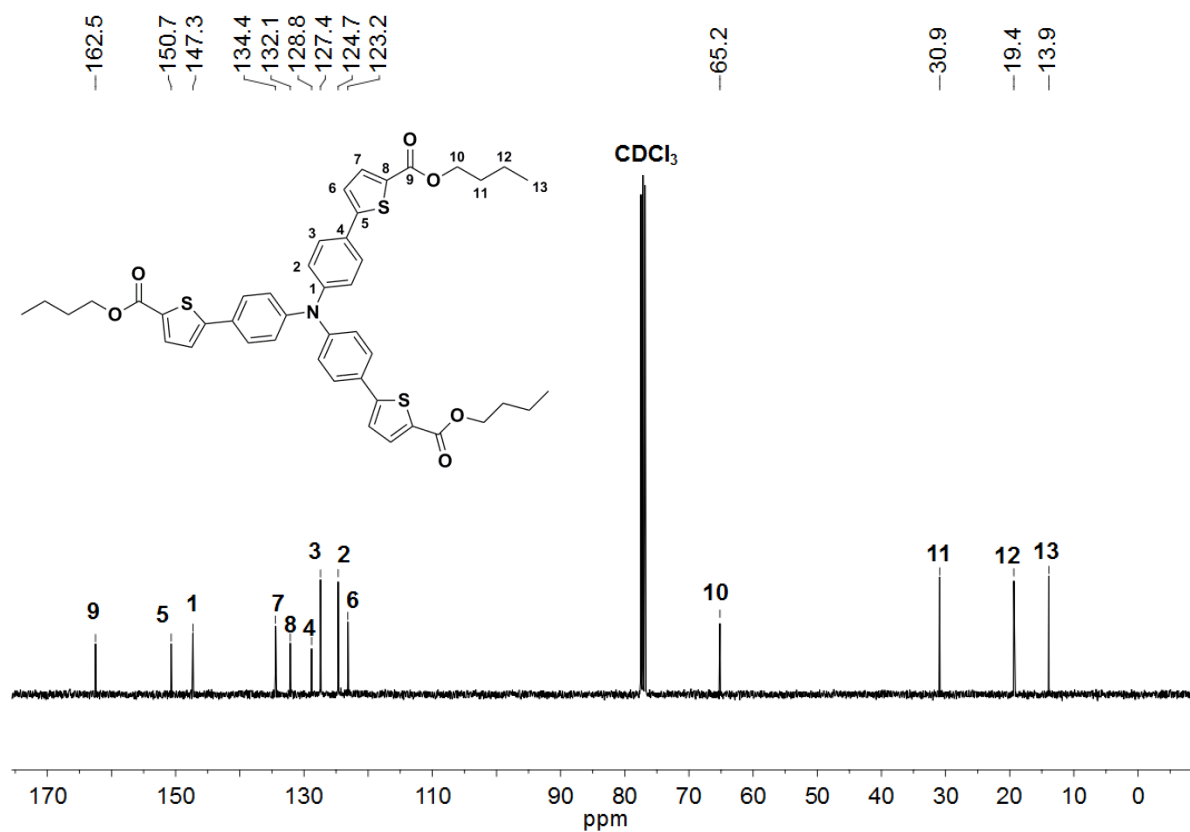


Figure 2.78 ¹³C NMR spectrum of **22** recorded in CDCl₃.

All three esters were recrystallized from DMF. Single crystal X-ray measurements could not be applied for the needle-like orange crystals of **22**. The crystal structures of **20** and **21** are given in Figure 2.79 and 2.80.

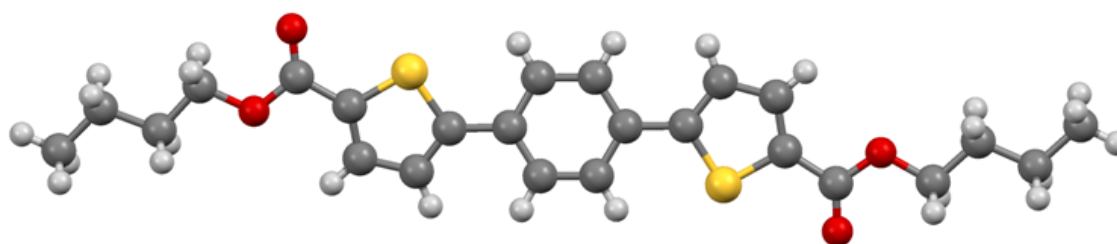


Figure 2.79 Crystal structure of **20**. Atom colors: C grey, O red, H white, S yellow.

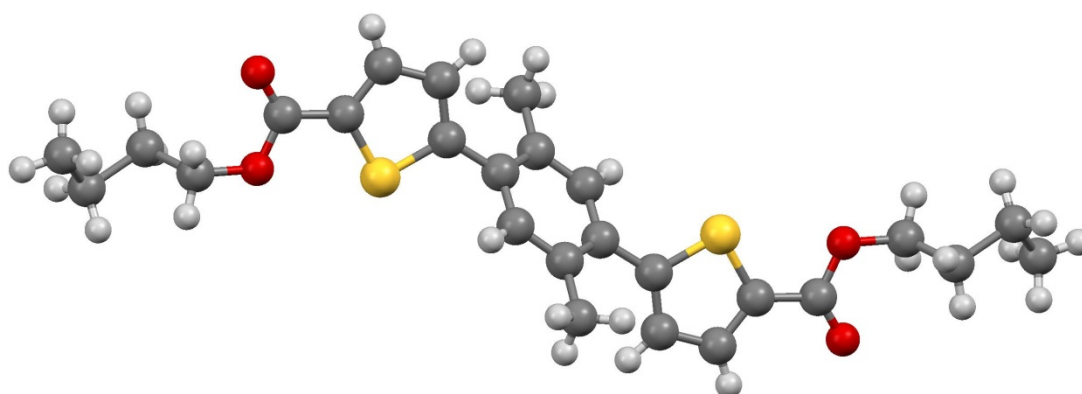


Figure 2.80 Crystal structure of **21**. Atom colors: C grey, O red, H white, S yellow.

The hydrolysis of the esters was performed applying the previously described procedure for the hydrolysis of the biphenyl linkers. In this case, excess amounts of potassium hydroxide had to be used for complete hydrolysis. Instead of methanol, ethanol was preferred as a solvent due to the low solubility of the esters. For the first attempts, it was observed that short reaction times resulted in a transesterification reaction and a mixture of ethoxy esters and carboxylic acids were obtained. When the reflux time was increased, a complete hydrolysis of the esters was achieved and the carboxylic acids **23**, **24** and **25** could be synthesized successfully (Figure 2.81).

The structural elucidations of the carboxylic acids were again done with ^1H and ^{13}C NMR spectroscopy. The disappearance of the butoxy group was observed for all three compounds which gives the evidence for a successful synthesis of the carboxylic acids. The elemental analyses as well as IR measurements also proved the formation of the compounds.

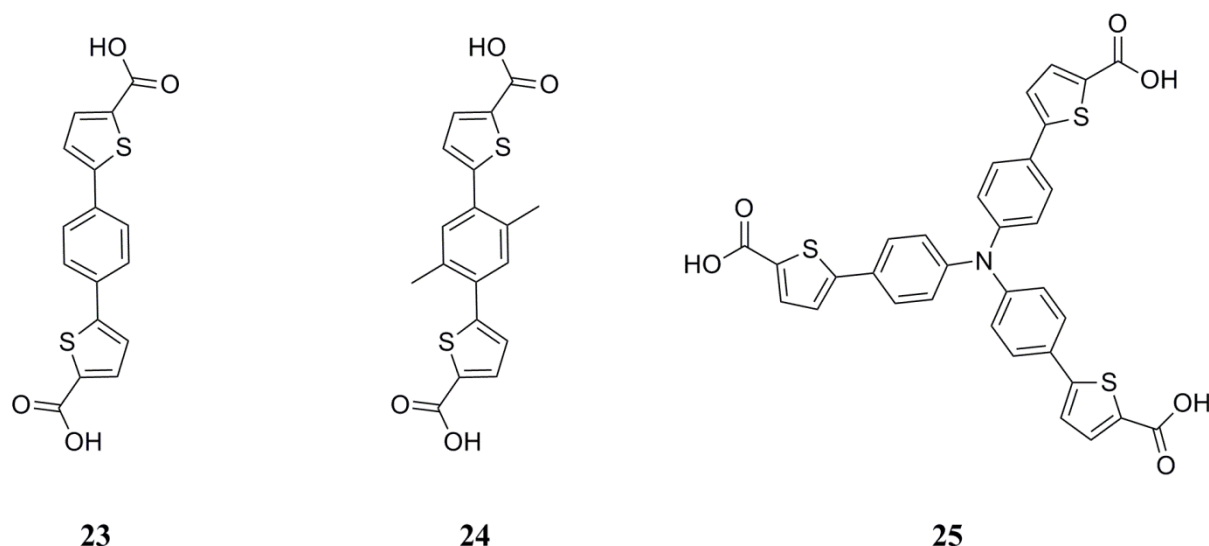


Figure 2.81 Carboxylic acid derivatives **23**, **24** and **25**.

2.7 MOF Synthesis using the Thiophene Linkers

The first experiments for the MOFs synthesis were carried out by using linkers **23** and **24**. The synthesis protocol applied for the amide functionalized MOFs was used. For this purpose, different sets of reaction vials were prepared by keeping the linker amount constant (0.02 g) and changing the amount of $\text{Zn}(\text{NO}_3)_2 \cdot 4\text{H}_2\text{O}$ (Table 2.23). DMF (4 ml) was used as a solvent.

Table 2.23 Optimization of the reaction conditions.

Linker to $\text{Zn}(\text{NO}_3)_2$ $\cdot 4\text{H}_2\text{O}$ molar ratio	
Vial 1	1:4
Vial 2	1:5
Vial 3	1:6
Vial 4	1:7
Vial 5	1:8
Vial 6	1:9
Vial 7	1:10
Vial 8	1:11
Vial 9	1:12

After stirring the reaction mediums for 15 min in order to dissolve all the reactants, the tightly closed vials were placed in an oven at 100 °C. After 48 h, formation of yellow crystals was observed in vials 5 to 9. Single crystal X-ray measurements of these crystals showed that zinc formate crystals were formed instead of the target MOF. A possible explanation for the zinc formate formation could be the slow decomposition of DMF to formate and dimethylamine at high temperatures and/or under acidic conditions.¹⁶⁴ Having this knowledge, another two sets were prepared. A few drops of HBF₄ and Et₃N were added into each set. The vials containing HBF₄, revealed the same type of crystal formation, in the vials containing Et₃N precipitation was occurred.

An alternative method was applied using different solvent mixtures. For this purpose, different ratios of *N*-methyl-2-pyrrolidone (NMP) and DMF mixtures were prepared. The vials containing DMF showed again the same type of crystal formation. The vials containing only NMP, showed neither crystallization nor precipitation.

The addition of ligands having one coordination site such as acetic acid, benzoic acid, HBF₄, oxalic acid etc. to induce a competition for coordination to the metal cations is known as the modulator approach.^{165,166} A regulation of the reaction rate and the crystal morphology is achieved by using such ligands. Since the nucleation is a fast process in the synthesis of MOFs, the monotopic modulators compete with the multitopic linkers in the reaction mixture due to the presence of the same functional groups. Since the modulators cannot build up a framework, they reduce the nucleation rate generating an exchange equilibrium between the modulator and the linker at the inorganic building units. It is therefore easier to get crystalline products. In other words, the reactants have enough time to slowly build up a crystalline framework. Moreover it is possible to tune the crystal size or degree of aggregation using modulators.¹⁶⁷

Having this knowledge, oxalic acid, DABCO and benzoic acid were used as modulators. Keeping the amounts of the linker, Zn(NO₃)₂·4H₂O and solvents (DMF or NMP) constant, the amount of the modulator was changed. Unfortunately the target MOFs could not be synthesized under these conditions. Moreover, instead of zinc, cobalt and copper were used as metals by using Co(NO₃)₂·6H₂O and Cu(NO₃)₂·3H₂O. The precipitate formed in the vials was found to be amorphous material by the PXRD measurements. Similar experiments applied for **25** were also failed.

The most probable reason for the unsuccessful synthesis is the non-linear orientation of the carboxylic acid groups in the molecules in **23** and **24**. In order to prove this idea, another linker (**30**) was designed which has its carboxylic acid groups linearly oriented towards each other (Figure 2.82).

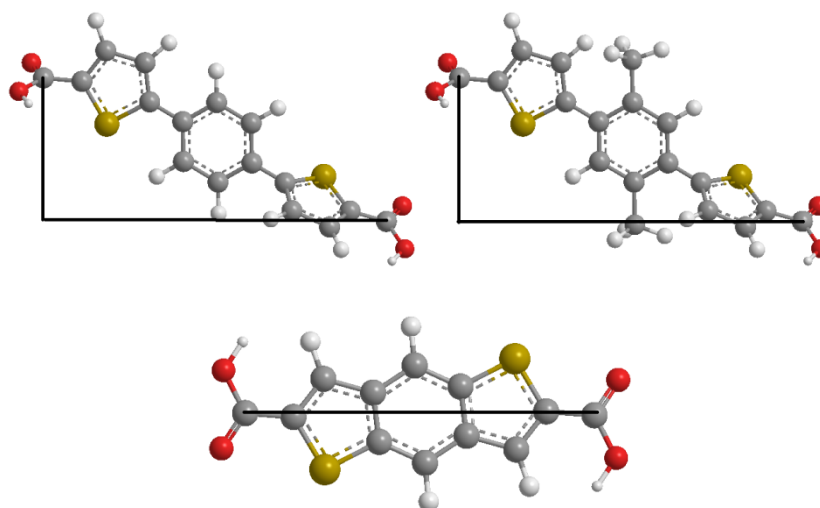
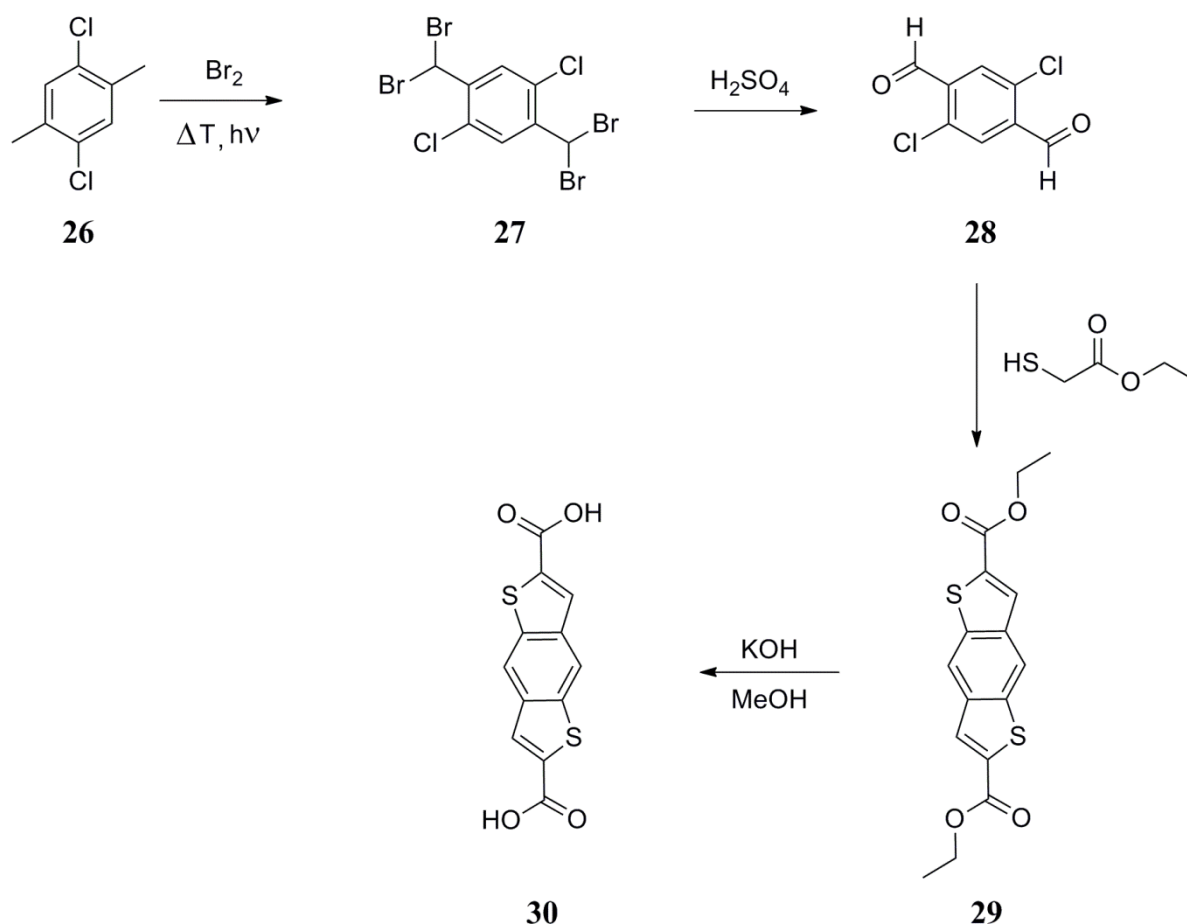


Figure 2.82 Representation of the non-linear carboxylic acid groups in **23** (top left), **24** (top right) and the linear carboxylic acid groups in **30** (bottom).

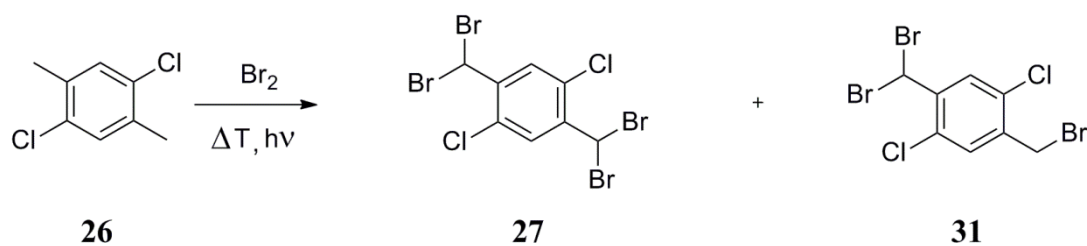
In this very recent project, starting from 1,4-dichloro-2,5-dimethylbenzene (**26**), the desired linker will be obtained in four steps (Scheme 2.12).



Scheme 2.12 Overall reaction for the synthesis of linker **30**.

For the synthesis of **27**, the procedure published by Ruggli *et al.* was used.¹⁶⁸ In order to obtain a large amount of bromine radicals, radiation with visible light using 350 Watt daylight lamp and elevated temperature were applied.

After the reaction, the structural elucidation of the obtained white solid was done by 1H and ^{13}C NMR spectroscopy. It was observed from the NMR spectra that, both the desired compound **27**, as well as small amounts of the side product 1-(Bromomethyl)-2,5-dichloro-4-(dibromomethyl)benzene (**31**) were formed (Scheme 2.13).



Scheme 2.13 Bromination of **26**.

The recrystallization of this mixture from chloroform did not change the ratio of **27** and the side product (**31**). Since it was observed that, in the aldehyde step, it is possible to purify **27**, further cleaning was not applied. For the spectroscopic data, the column chromatography was applied to a small amount of the raw product.

The ^1H NMR spectrum of purified **27** shows two singlet peaks as expected (Figure 2.83). The peak at 7.95 ppm belongs to the phenyl protons. The $-\text{CHBr}_2$ protons resonate at 6.97 ppm as a singlet. The ^{13}C NMR spectrum also reveals the successful bromination of **26** by showing the expected four peaks (Figure 2.84).

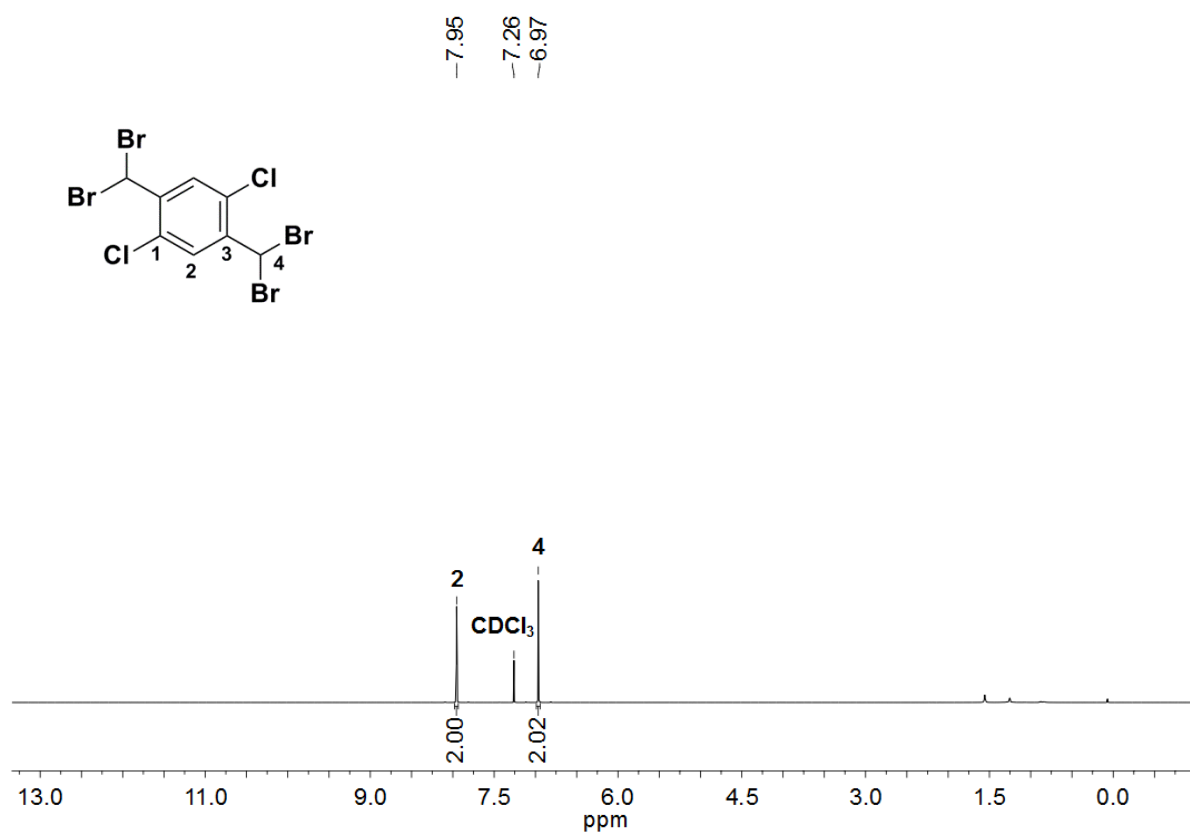


Figure 2.83 ^1H and spectrum of **27** recorded in CDCl_3 .

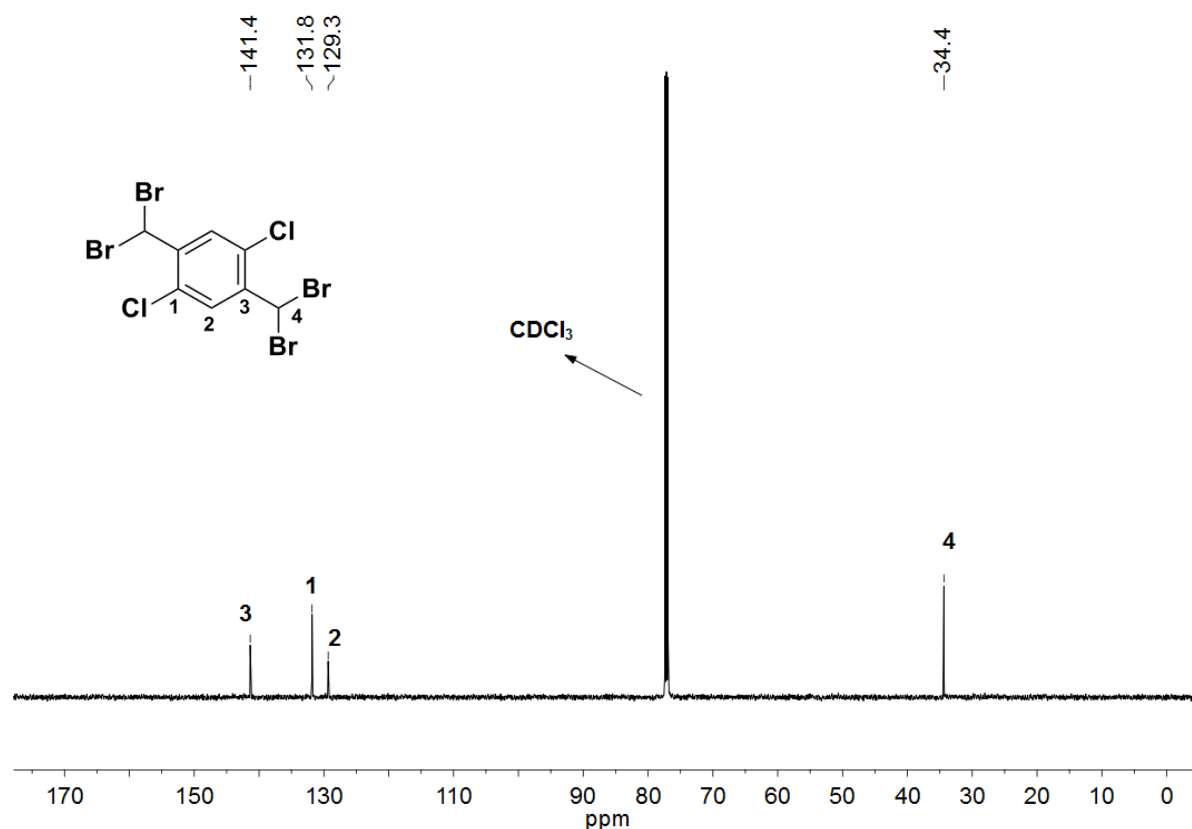


Figure 2.84 ^{13}C NMR spectrum of **27** recorded in CDCl_3 .

For the synthesis of **28**, the hydrolysis was performed using H_2SO_4 and heating at $125\text{ }^\circ\text{C}$ under pressure.¹⁶⁸ Purification of the obtained yellow solid with pentane yielded **28**. The ^1H NMR spectrum of the compound proves the successful aldehyde formation with the formyl-H peak resonating at 10.47 ppm (Figure 2.85).

The ^{13}C NMR spectrum of **28** also strongly reveals the formation of the desired aldehyde. The aldehyde carbon atoms resonate at 188.1 ppm (Figure 2.85). The elemental analysis and IR measurements also confirmed the formation of **28**.

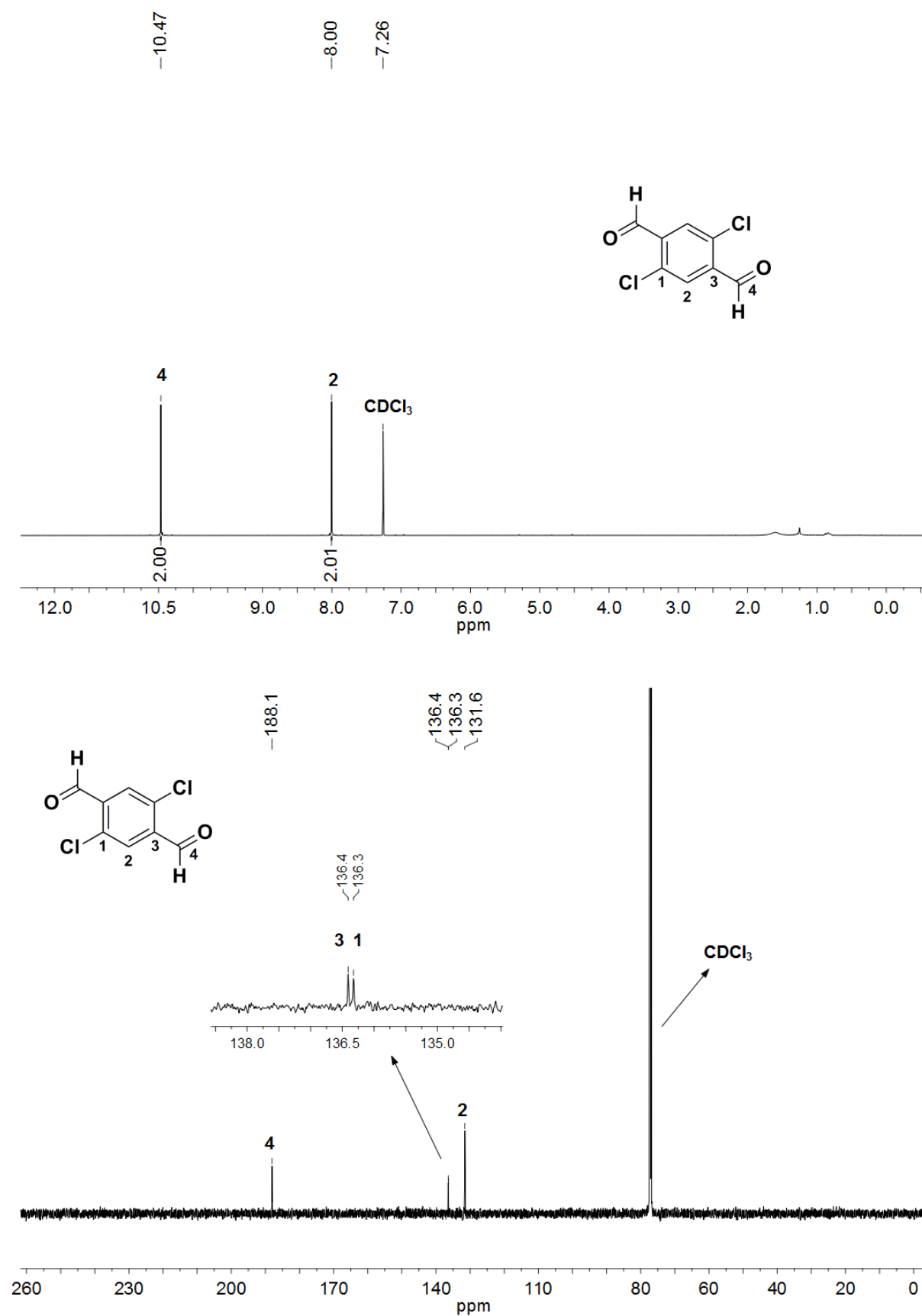


Figure 2.85 ^1H NMR and ^{13}C NMR spectra of **27** recorded in CDCl_3 .

Up to date, **27** and **28** were synthesized successfully. A ring closing reaction with ethyl mercaptoacetate followed by hydrolysis with KOH in MeOH will be performed to obtain the desired linker **30** as a future project.

2.8 Zirconium MOFs with linkers **7** and **9**; ZrNH₂BPDC and ZrAcBPDC

The principal limitation of the MOFs is their limited stability.¹⁶⁹ Recent studies by Huang and Hirscher groups^{151,152} clearly showed the decomposition of MOF-5 when it is exposed to air. Moreover, thermal stability of MOFs is also limited. In general MOFs are stable up to 350-400 °C¹⁷⁰ and there are few MOFs which start to decompose above 500 °C such as MIL-53 (aluminum 1,4-benzenedicarboxylate, Al(OH)[O₂C-C₆H₄-CO₂].[HO₂C-C₆H₄-CO₂H]_{0.70}).¹⁷¹

Recently, Zirconium-MOFs having higher thermal and chemical stabilities were reported. The choice of zirconium metal can be explained by the strong interaction of the group four elements with oxygen which resulting in stable building blocks for oxygen containing. One of the first examples of Zr-MOFs is UiO-67 that contains 4,4'-biphenyldicarboxylic acid (BPDC) as the linker and Zr as the metal (Figure 2.86).¹⁷⁰

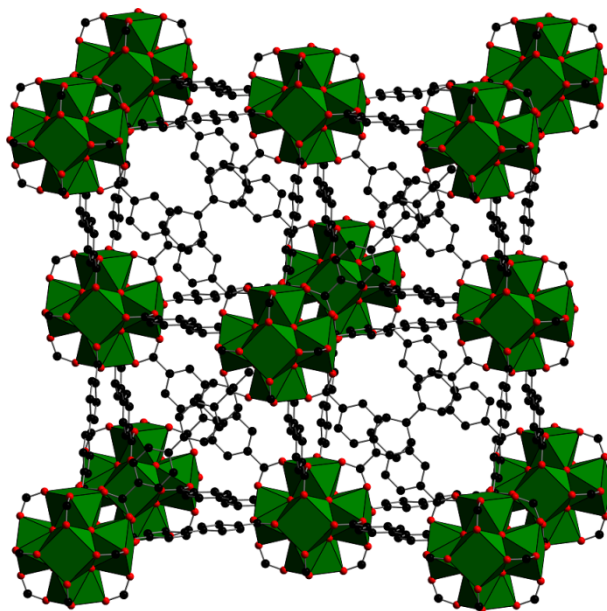


Figure 2.86 The framework connectivity of UiO-67 with the zirconium coordination sphere (green tetrahedron). Atom colors: C black, O red. Hydrogen atoms were omitted for the simplification of the structure.¹⁷⁰

However Behrens *et. al* reported that usage of the published synthesis method resulted in poorly crystalline materials and in order to obtain a reproducible synthesis, they suggested a modulation approach for UiO-67 which has been explained before in Section 2.7.¹⁶⁷

According to our knowledge, functionalized BPDC linkers have so far not been reported for Zr-MOFs, which can be good candidates for a comparison with IRMOF series by means of their properties. Moreover, the usage of these linkers can be a good basis to obtain porous MOFs with UiO-67 topology, which has potential for postsynthetic modification using the modulation approach. Therefore, linkers **7** and **9** were decided to be used to synthesize Zr-MOFs having UiO-67 topology. In this very recent project, a cooperation was set up with the group of Prof. Dr. Behrens from the University of Hannover.

The Zr-MOFs containing linker **7** (**ZrNH₂BPDC**) and linker **9** (**ZrAcBPDC**) were synthesized solvothermally in the presence of benzoic acid (30 equiv.), using ZrCl₄ as the metal source and DMF as the solvent at 120 °C. After 24 h, crystal formation was observed (Figure 2.87). For the characterization of the MOFs, the reaction medium was centrifuged, washed with DMF and ethanol.

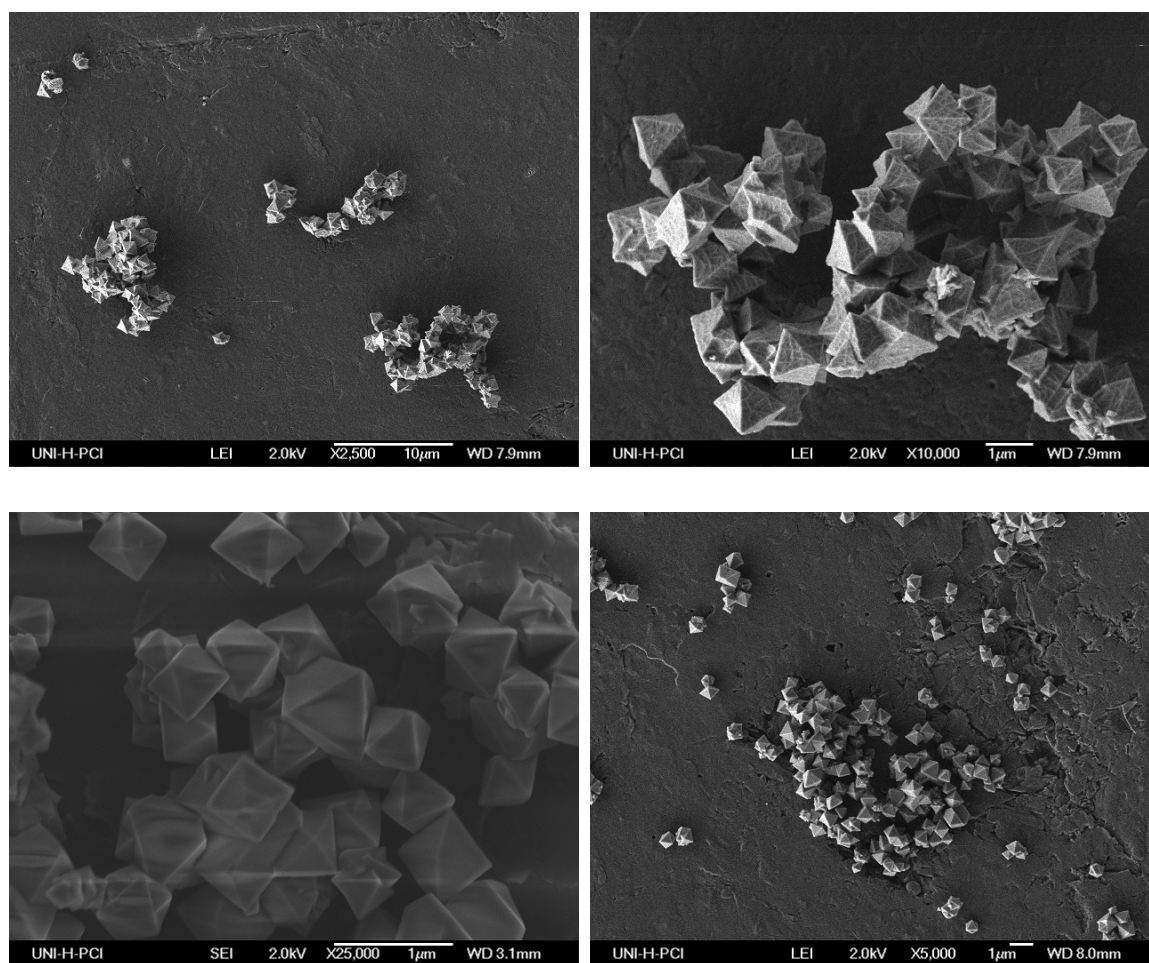


Figure 2.87 SEM pictures of **ZrNH₂BPDC** (top) and **ZrAcBPDC** (bottom).

2.8.1 Characterization of **ZrNH₂BPDC** and **ZrAcBPDC**

Single crystal X-ray measurements of **ZrNH₂BPDC** and **ZrAcBPDC** have not been carried out yet, but the crystallinity of the materials was proved by PXRD measurements.

2.8.1.1 Powder X-Ray Diffraction (PXRD) Measurements of **ZrNH₂BPDC** and **ZrAcBPDC**

The comparison of the PXRD pattern of the new synthesized MOFs with UiO-67 is shown in Figure 2.88. While the pattern of **ZrNH₂BPDC** is in good agreement with the PXRD pattern of UiO-67, the PXRD pattern of **ZrAcBPDC** shows additional reflections.

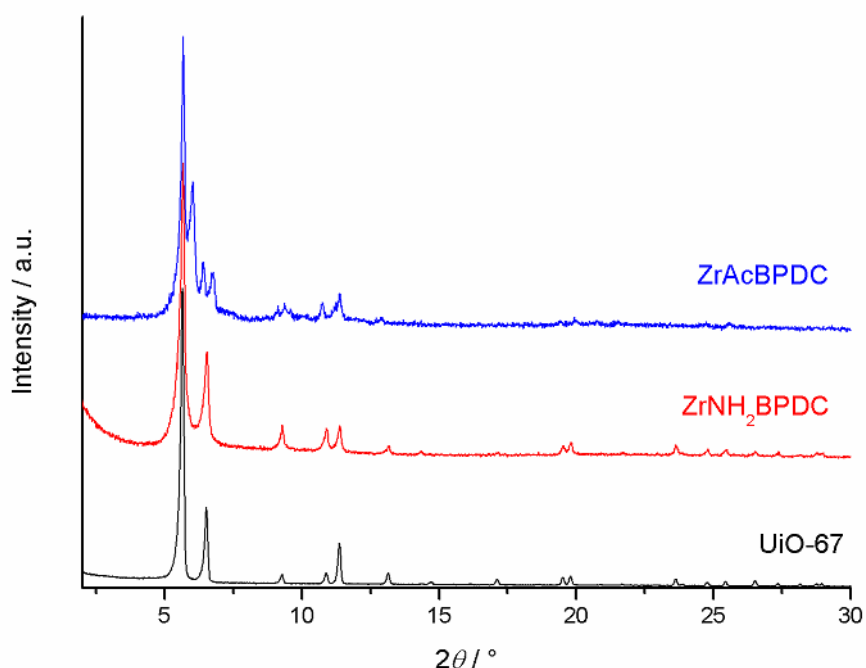


Figure 2.88 PXRD patterns of the synthesized MOFs and UiO-67.

The first attempts for the synthesis of these MOFs were done by using 30 equiv. of benzoic acid. In order to determine the modulator effect and obtain well-defined crystals, additional benzoic acid to zirconium(IV) chloride ratios were also tried out for both MOFs. The PXRD measurements were used to determine the effect.

In all ratios, the **ZrNH₂BPDC** reflections are in excellent agreement with the UiO-67 reflections (Figure 2.89). It can be clearly seen that, when 10 equiv. benzoic acid were used, broadened peaks were obtained, revealing the poor crystallinity of the material. Upon further increasing the amount of modulator benzoic acid to 20 equiv., smaller width reflections were recorded, which is an indication of the formation of larger crystals. The addition of 40 equiv. of benzoic acid resulted in again broadened reflections, which were similar to the above mentioned sample obtained using 10 equiv. benzoic acid

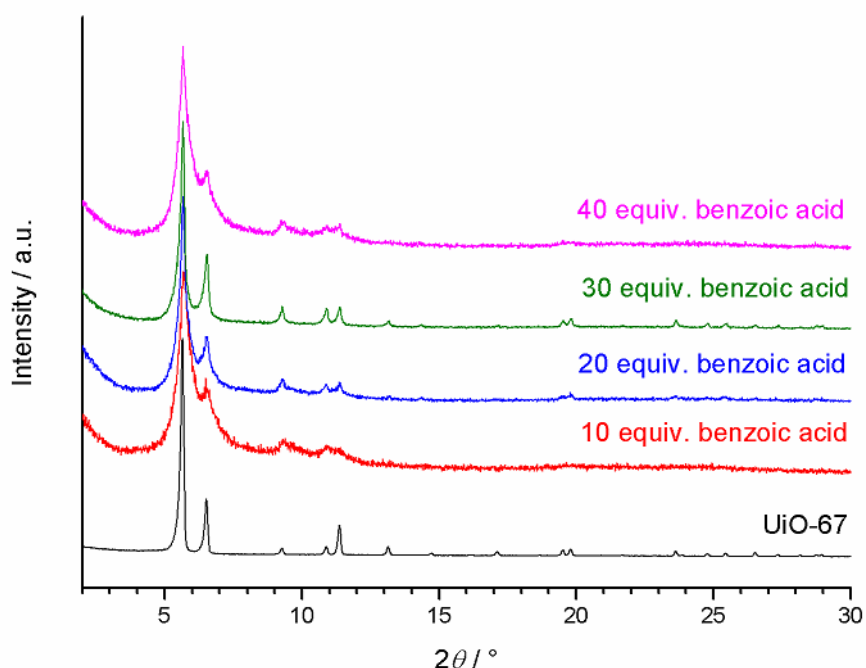


Figure 2.89 PXRD patterns of UiO-67 and **ZrNH₂BPDC** MOFs prepared with different amounts of benzoic acid (given as equivalents with respect to **ZrCl₄**).

For **ZrAcBPDC**, the modulator effect is much more significant (Figure 2.90). When 15 equiv. of the modulator were used, different reflections were observed compared to the reflections of UiO-67. The $2\theta = 5.6^\circ$ reflection in the UiO-67 pattern shifts to $2\theta = 6.1^\circ$, which can be attributed to a different phase. Upon further increasing the modulator amount to 30 equiv., another phase forms which resembles the pattern of UiO-67 with the reflections at $2\theta = 5.6^\circ$ and 6.5° . The reflections at $2\theta = 6.1^\circ$ and 6.8° belong to the other phase which was also formed in the sample with 10 equiv. of benzoic acid. When the modulator amount was increased to 40 and 50 equiv., the reflection at $2\theta = 6.1^\circ$ completely disappears and the reflection at $2\theta = 6.8^\circ$ loses its intensity. It can be expected that the further increasing of the amount of modulator above 50 equiv. could be resulted in pure phase **ZrAcBPDC**. Different amounts of modulator will be tried out in a future project.

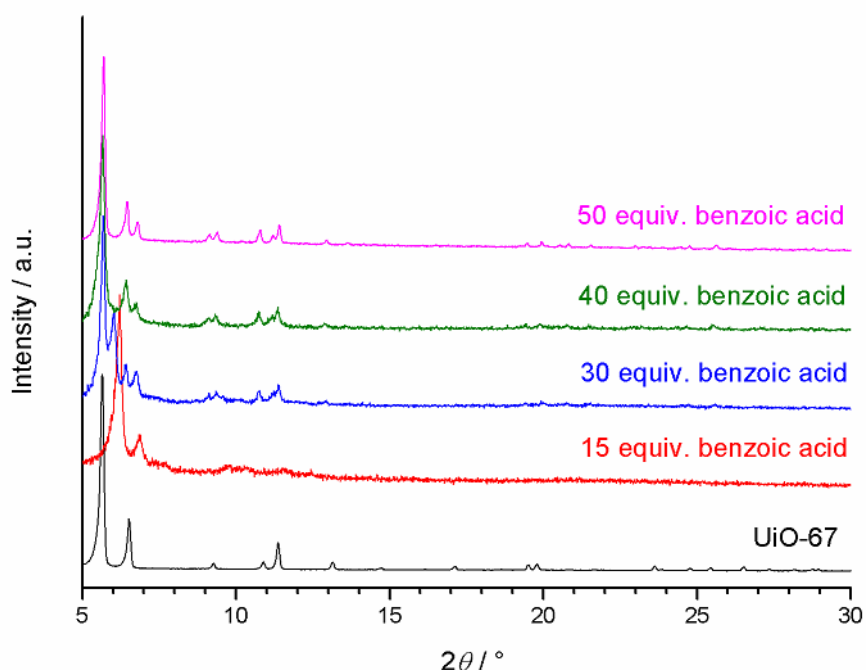


Figure 2.90 PXRD patterns of UiO-67 and **ZrAcBPDC** MOFs prepared with different amounts of benzoic acid (given as equivalents with respect to ZrCl_4).

2.8.2 Thermogravimetric Analysis (TGA) of ZrNH_2BPDC and **ZrAcBPDC**

The thermal stability of the synthesized Zr-MOFs was checked by TGA measurements. Similar decomposition steps were observed as previously described MOFs.

The thermal stability of the synthesized Zr-MOFs was checked by TGA measurements. Similar decomposition steps were observed as previously described MOFs. For **ZrNH₂BPDC**, the first step up to 400 °C can be attributed to the guest molecules such as solvents and benzoic acid in the pores (Figure 2.90). After 400 °C, decomposition of the linker starts and results in a complete collapse of the structure at around 500 °C. After the decomposition of the linkers, the remaining residue was found to be ZrO_2 according to the PXRD measurements. **ZrAcBPDC** also revealed similar decomposition steps as expected. The decomposition of the linkers started around 250 °C. TGA measurements show that **ZrAcBPDC** is stable up to 400 °C (Figure 2.91).

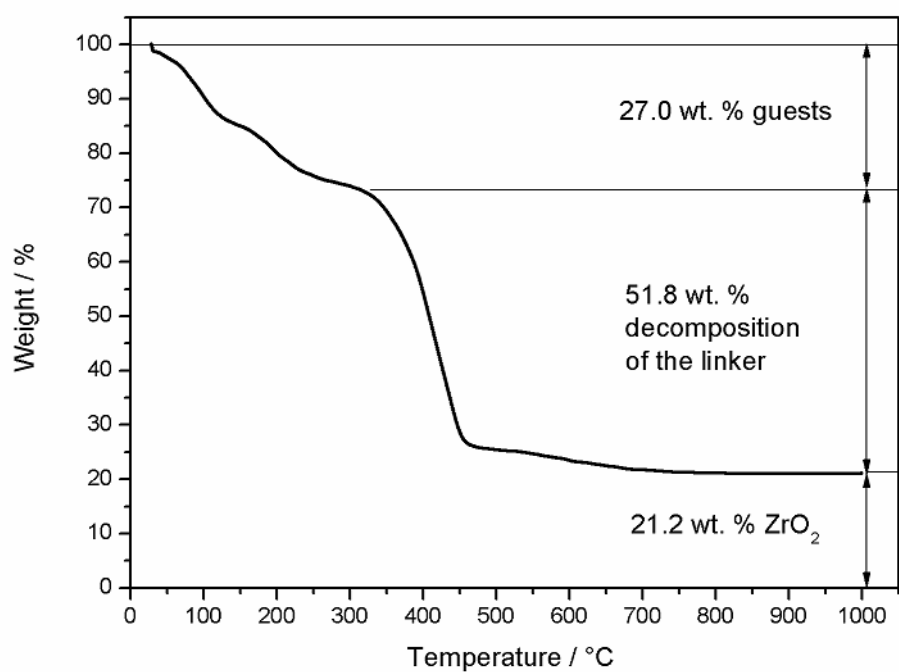
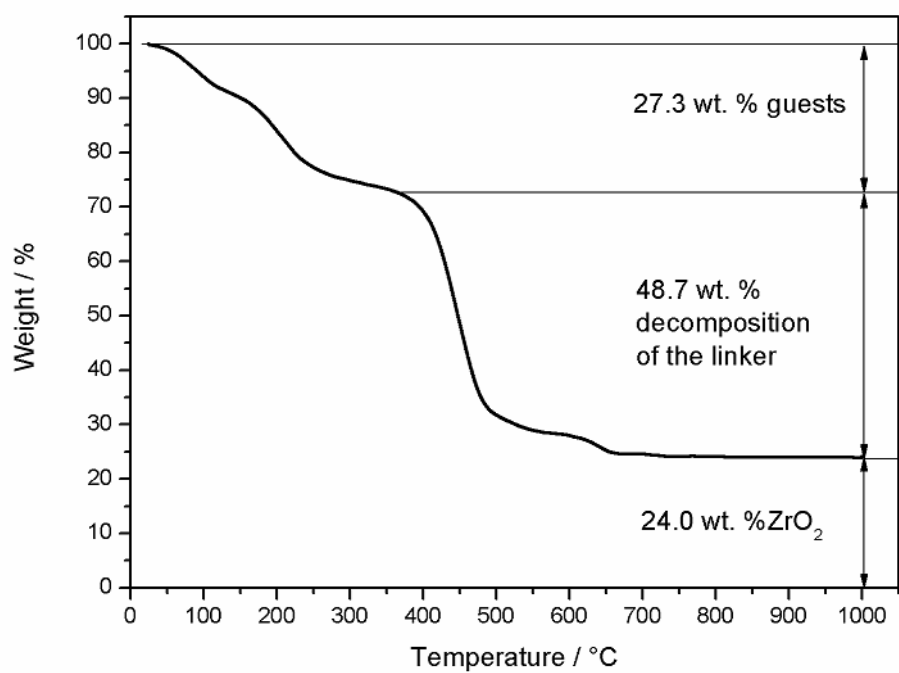


Figure 2.91 TGA of **ZrNH₂BPDC** (top) and **ZrAcBPDC** (bottom).

3. Surface Modification of the Metal Oxides Using Phosphonates as Coupling Molecules

As previously mentioned, organic-inorganic hybrid materials attracted a lot interest due to their special properties combining the physical and the chemical features of both inorganic and organic compounds. Besides the MOFs which were described in the previous sections, another highlighted subgroup of the organic-inorganic hybrid materials are high surface metal oxides like Al_2O_3 , TiO_2 , ZrO_2 which are modified with organic molecules. Without doubt, the interest in those modified ceramics arises from a variety of possible applications such as self assembled monolayers,¹⁷² ceramic membranes,^{173,174} photo-electrochemical cells,^{175,176} and adsorbents.¹⁷⁷⁻¹⁷⁹

The preparation of the modified surfaces can be performed by either grafting the organic groups to the preformed inorganic surfaces (surface modification) or by preparing the inorganic substrate *in situ* (sol-gel processing).¹⁸⁰ In general, a sol-gel method can be explained as the development of the M-O-M bridges by hydrolysis and polycondensation resulting in sols or gels where the organic groups are anchored to an inorganic network.¹⁸¹ In the case of surface modification, organic groups are anchored to the inorganic surface by the coupling molecules as illustrated in Figure 3.1.¹⁸²

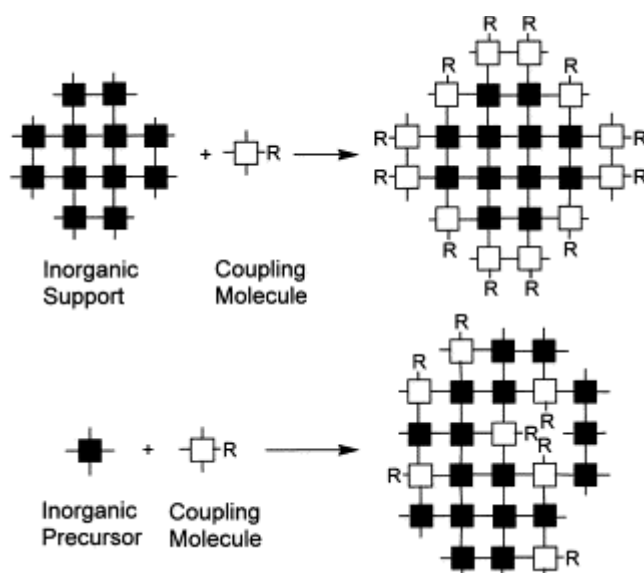


Figure 3.1 Preparation of the surfaces by the surface modification (top) and the sol-gel method (bottom).¹⁸³

Organosilanes,^{1,184} organotitanates¹⁸⁵ and the strong complexing ligands^{24,27} have been established as the most common coupling molecules. Among these, most of the studies were based on the silicon based precursors used to bind the organic units onto inorganic supports because of the hydrolytic stability of the Si-C bond.¹⁸⁶

Recent studies show that organophosphorous compounds can be used as coupling molecules instead of organosilanes. As the Si-C bond; the P-C bond shows a high stability against hydrolysis. Besides the advantage of high stability, organophosphorous coupling molecules give access to a variety of functional organic groups.¹⁸⁰

Mainly, organophosphorous coupling molecules are monoalkyl or dialkyl phosphoric acids,^{172,187,188} phosphonic acids and phosphinic acids.^{182,186} Vioux *et al.* explained the anchoring of these acids by a formation of M-O-P bridges which occur by the condensation of the surface hydroxyl groups with the P-OH groups and by complex formation of the phosphoryl oxygen with surface metal ions (Figure 3.2).¹⁸⁰

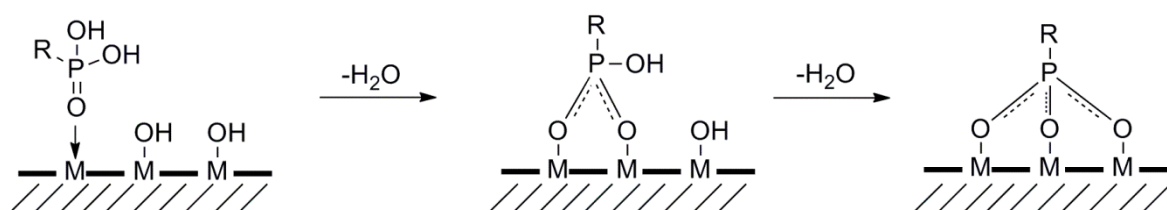


Figure 3.2 Schematic representation of the anchoring of phosphonic acid on the metal oxide surface.¹⁸⁰

It is also known that, aside from the acids described above, phosphonic esters as well as trimethylsilyl and alkyl esters^{186,189,190} can also be used as coupling molecules. In these cases, anchoring occurs by the cleavage of P-O-R groups with surface -OH groups being facilitated by the increasing electronegativity of the phosphorous atoms due to the phosphoryl oxygen coordination to the surface (Figure 3.3).¹⁸⁰

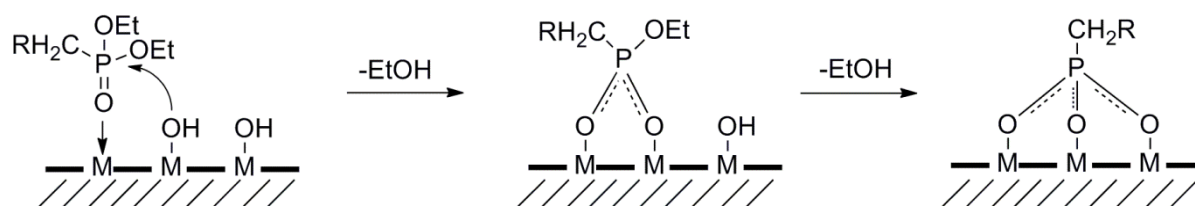


Figure 3.3 Schematic representation of the anchoring of diethylphosphonate on the metal oxide surface.¹⁸⁰

In this study, we decided to use phosphonate derivatives of the compounds **20**, **21** and **22** as coupling molecules for a surface modification of ZrO_2 , TiO_2 and Al_2O_3 . These organophosphorous coupling agents containing thiophene units are good candidates for surface modification of the metal oxides due to their strong luminescence when exposed to UV light.¹⁶⁰ Therefore coated surfaces with these agents can be used for applications such as sensors. In order to synthesize the desired phosphonates, a four step synthesis route shown in Scheme 3.1, was followed. Reaction details and characterization of the compounds are given in the following sections.



Scheme 3.1 Reaction scheme for the synthesis of phosphonates starting from the corresponding esters.

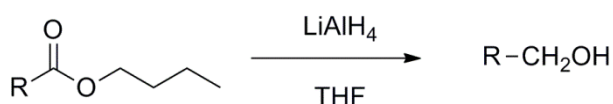
3.1 Synthesis of the Coupling Molecules

3.1.1 Reduction of the Esters to Alcohols

The reduction of the esters to alcohols can be performed by several methods.¹⁹¹ Among others NaBH_4 and LiAlH_4 are the most commonly used reducing agents, THF or ether can be used as a solvent.¹⁹² The workup of the reaction can be done in either acidic or basic conditions.¹⁹³

Firstly, the reduction of the ester **20** was tried out using NaBH_4 as the reducing agent.¹⁹² THF was preferred as solvent because of the low solubility of the ester in ether. Moreover, the

reaction medium was heated because of the low reactivity of the esters compared to aldehydes and ketones,¹⁹¹ but under these conditions almost no conversion was observed. Secondly LiAlH_4 was used, after refluxing over night, the resulting precipitate was treated with an aqueous K_2CO_3 solution. However, according to the elemental analysis data, it was clear that the formed salts could not be completely removed from the product after the reaction. Using 10 % HCl solution for the workup led to good yields of the target alcohols **32**, **33** and **34** (Figure 3.4).



Scheme 3.2 Reaction scheme for the alcohol synthesis.

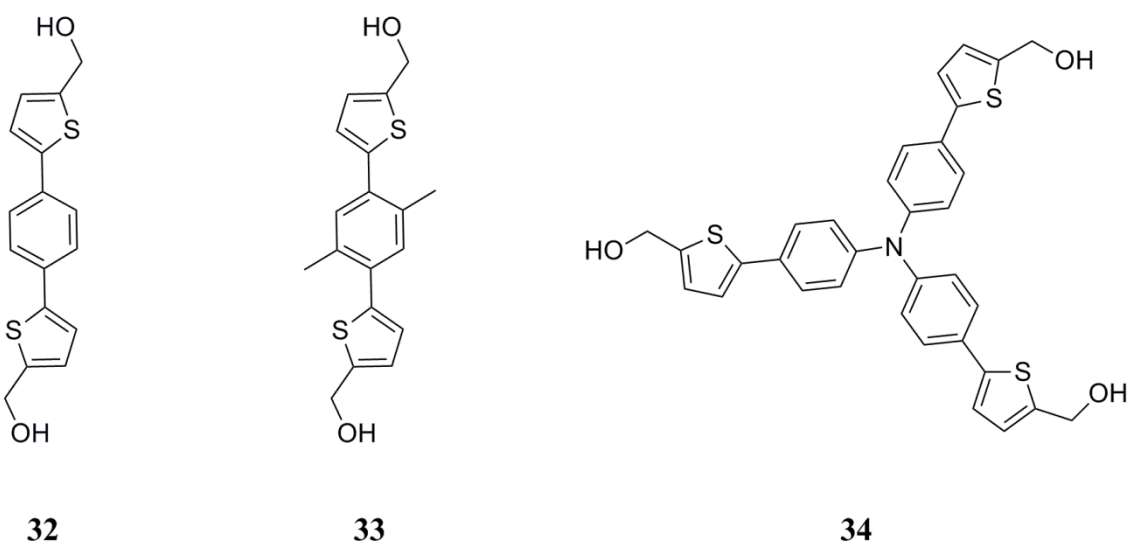


Figure 3.4 Alcohol derivatives **32**, **33** and **34**.

20 and **22** were reduced to the corresponding alcohols (**32** and **34**) by applying the same procedure. In the synthesis of **33**, extraction with dichloromethane was required; since during the treatment with the HCl solution, no precipitation was observed. After the extraction, the removal of dichloromethane resulted in an oily product. The addition of pentane to the oily material precipitated the target alcohol as a yellow solid. An interesting behavior was observed in the ^1H NMR spectrum of **33** (Figure 3.5). It was observed that when $\text{DMSO}-d_6$ is used as the NMR solvent, the methanol groups show a triplet at 5.52 ppm

and a doublet at 4.67 ppm, which can be explained as the coupling of the -OH protons with the -CH_2 protons. When CDCl_3 is used as the NMR solvent, the expected singlet was observed at 4.84 ppm (Figure 3.6). This difference can be explained by traces of the acids (HCl or DCl) in CDCl_3 which form hydrogen bonds with the -OH groups and thus prevent the splitting of the $\text{-CH}_2\text{OH}$ peak (Figure 3.6). For **32** and **34**, such a behavior was not observed.

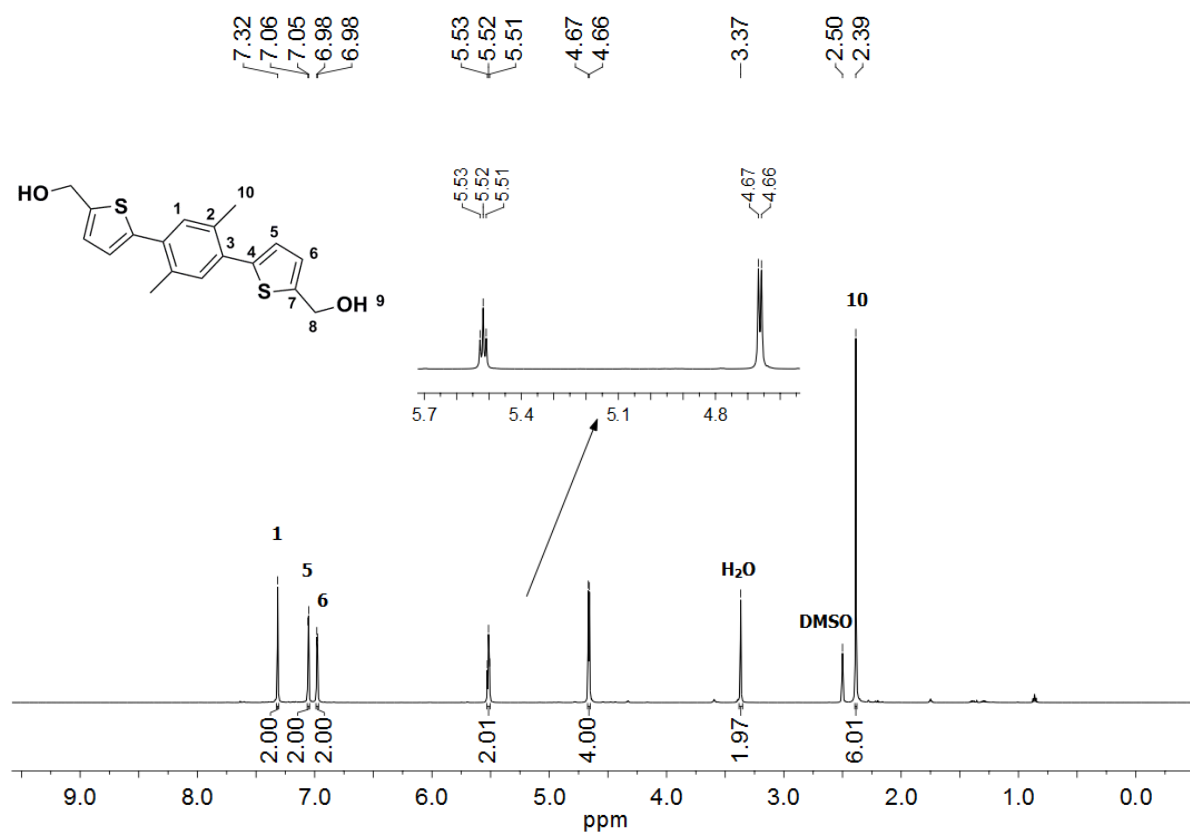


Figure 3.5 ^1H NMR spectrum of **33** recorded in DMSO-d_6 .

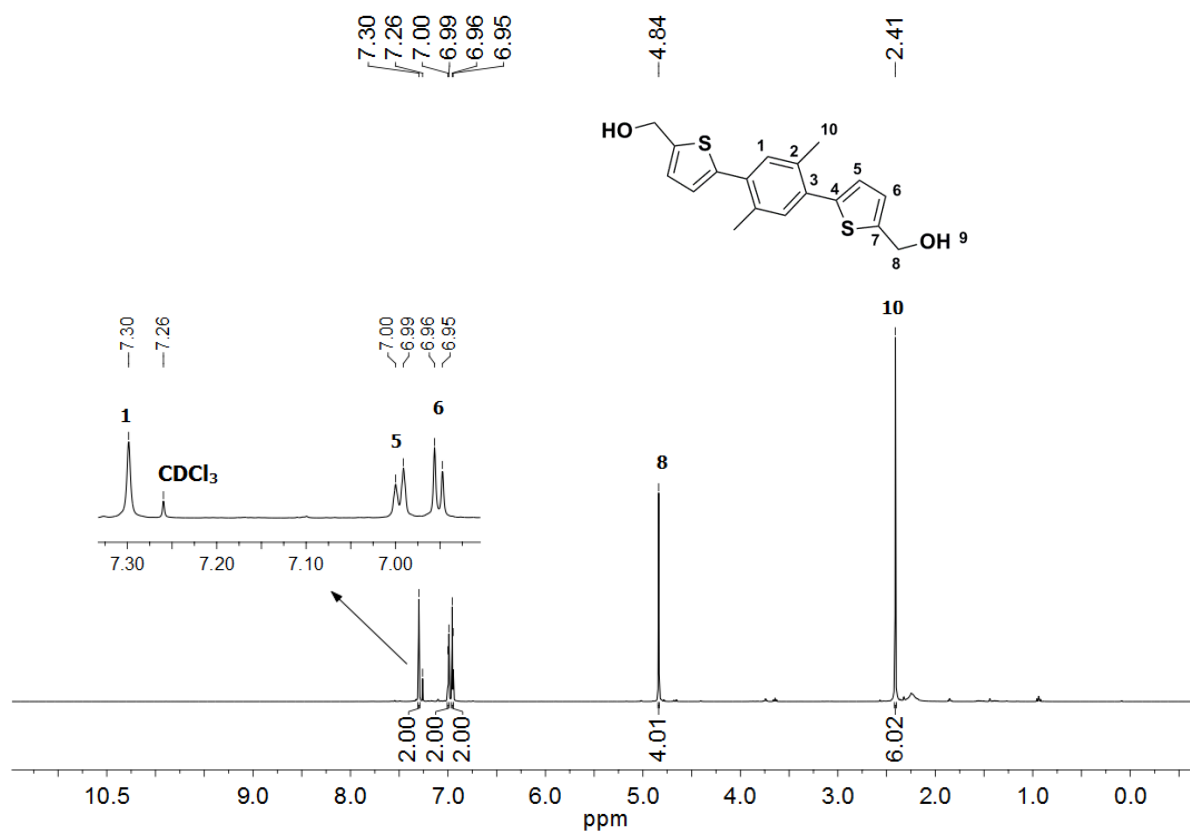


Figure 3.6 ^1H NMR spectrum of **33** recorded in CDCl_3 .

The ^{13}C NMR spectrum of **33** reveals nine carbon atoms as expected (Figure 3.7). The disappearance of the carbonyl peak clearly confirms the structure. HMBC and HMQC techniques were used to assign all carbon atom resonances. The presence of the $-\text{CH}_2\text{OH}$ groups shifts the thiophene carbon atoms (H5 and H6) to higher field compared to the ester derivatives' ^{13}C NMR spectrum.

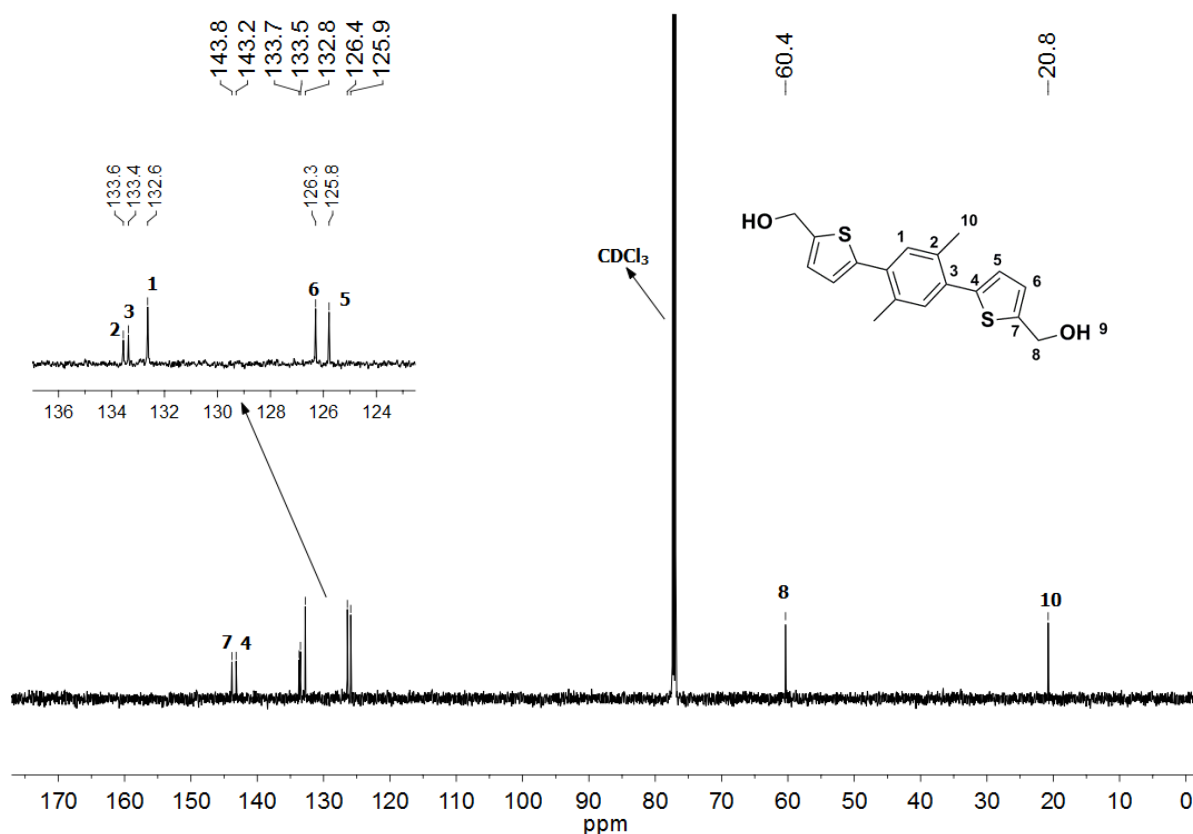


Figure 3.7 ^{13}C NMR spectrum of **33** recorded in CDCl_3 .

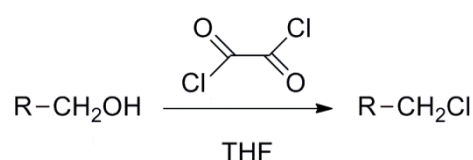
The structural elucidation of **32** and **34** was also done by ^1H and ^{13}C NMR spectroscopy. The elemental analysis and the IR measurements also strongly support the formation of the target alcohols. HMBC and HMQC techniques were used for the structural elucidation of the compounds.

3.1.2 Chlorination of the Alcohols

For the conversion of the alcohols to the chlorides, the most common method is the usage of thionyl chloride.¹⁹⁴ The alcohol derivatives **32**, **33** and **34** were reacted with thionyl chloride according to the procedure published in the literature.¹⁹⁵ In this reaction, thionyl chloride was distilled and freshly used. However, low yields were obtained (30-40 %). Increasing the reaction time and using different amounts of thionyl chloride did not increase the yields. According to the elemental analysis data, it was observed that, the chlorosulfite derivative formed at the first step of the reaction could not be brought to the target chloro derivative. According to the literature, to promote the reaction an organic base like

triethylamine or pyridine ¹⁹⁶ can be used by reacting with the HCl formed during the reaction. However, using either one of the tertiary amines could not increase the yields.

To overcome the low reaction yields, another method had to be applied for the chlorination. For this purpose, alternative to thionyl chloride, oxalyl chloride which is mainly preferred for the chlorination of the carboxylic acids was thought to be used. The procedure published by Fraser *et al.* ¹⁹⁷ was applied and the target compounds **35**, **36** and **37** (Figure 3.8) were successfully synthesized in good yields. The reaction was performed using THF as a solvent and DMF as the catalyst. DMF plays a crucial role in the reaction since it activates the oxalyl chloride (Scheme 3.3).^{198,199}



Scheme 3.3 Reaction scheme for the chlorination of the alcohols.

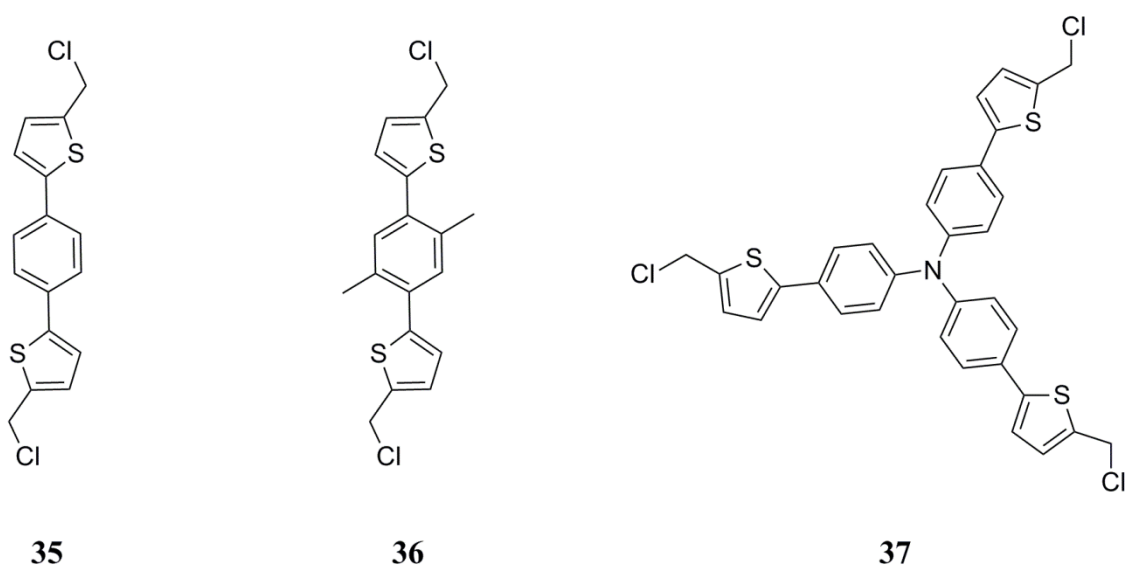


Figure 3.8 Chloro derivatives **35**, **36** and **37**.

The structural elucidation of **35**, **36** and **37** was done by ¹H and ¹³C NMR spectroscopy. Elemental analysis and IR measurements also strongly supported the formation of the target chlorides. HMBC and HMQC techniques were used for the elucidation of the compounds, too. The ¹H and ¹³C NMR spectra of **36** are given below as an example.

The ^1H NMR spectrum of **36** reveals three protons in the aromatic region (Figure 3.9). The phenyl protons (H1) resonate at 7.31 ppm as a singlet. The thiophene protons neighboring the $-\text{CH}_2\text{Cl}$ groups (H6) appear as a doublet at 7.08 ppm with a coupling constant of 3.6 Hz. This AB system's other thiophene protons (H5) show a doublet at 6.94 ppm. The four methylene protons and the six methyl protons resonate as singlets at 4.44 ppm and 2.42 ppm respectively.

In the ^{13}C NMR spectrum, eight peaks were observed as expected. The shift of the methylene carbon resonances to the higher field strongly supports the formation of the target compound (Figure 3.10).

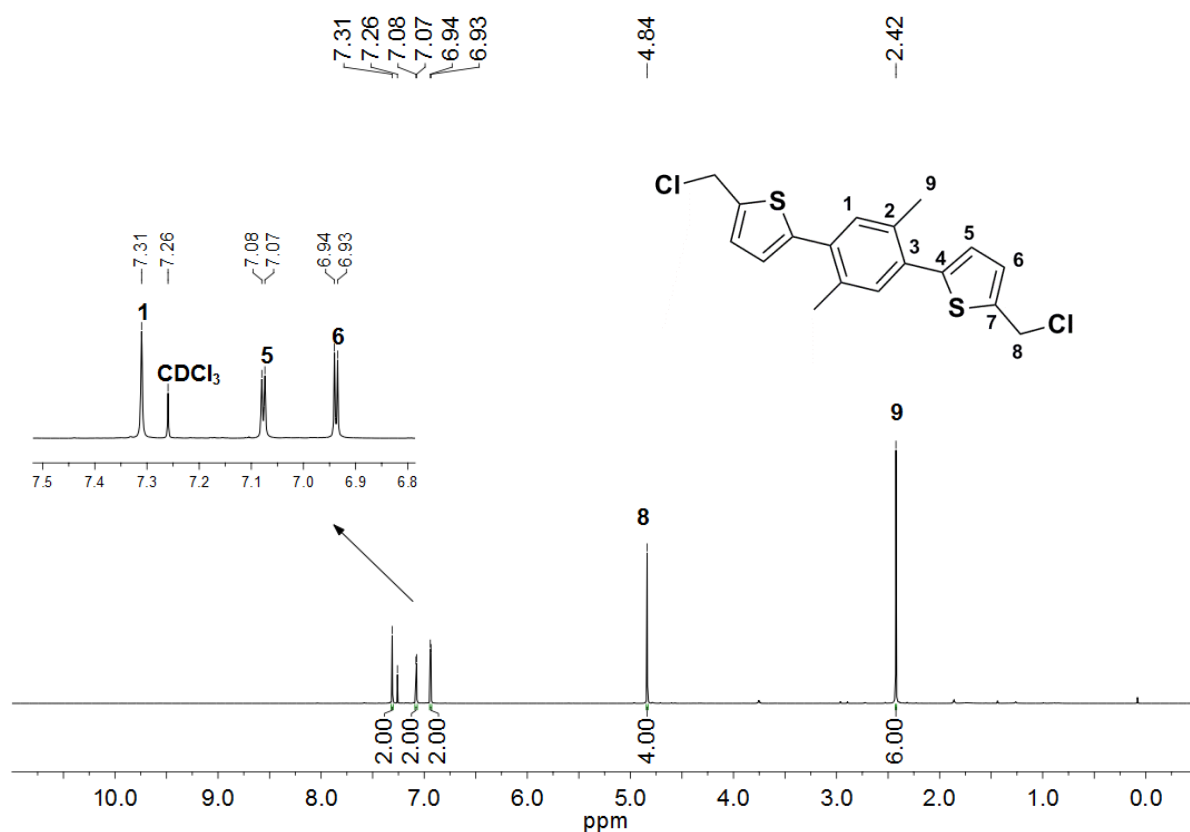


Figure 3.9 ^1H NMR spectrum of **36** recorded in CDCl_3 .

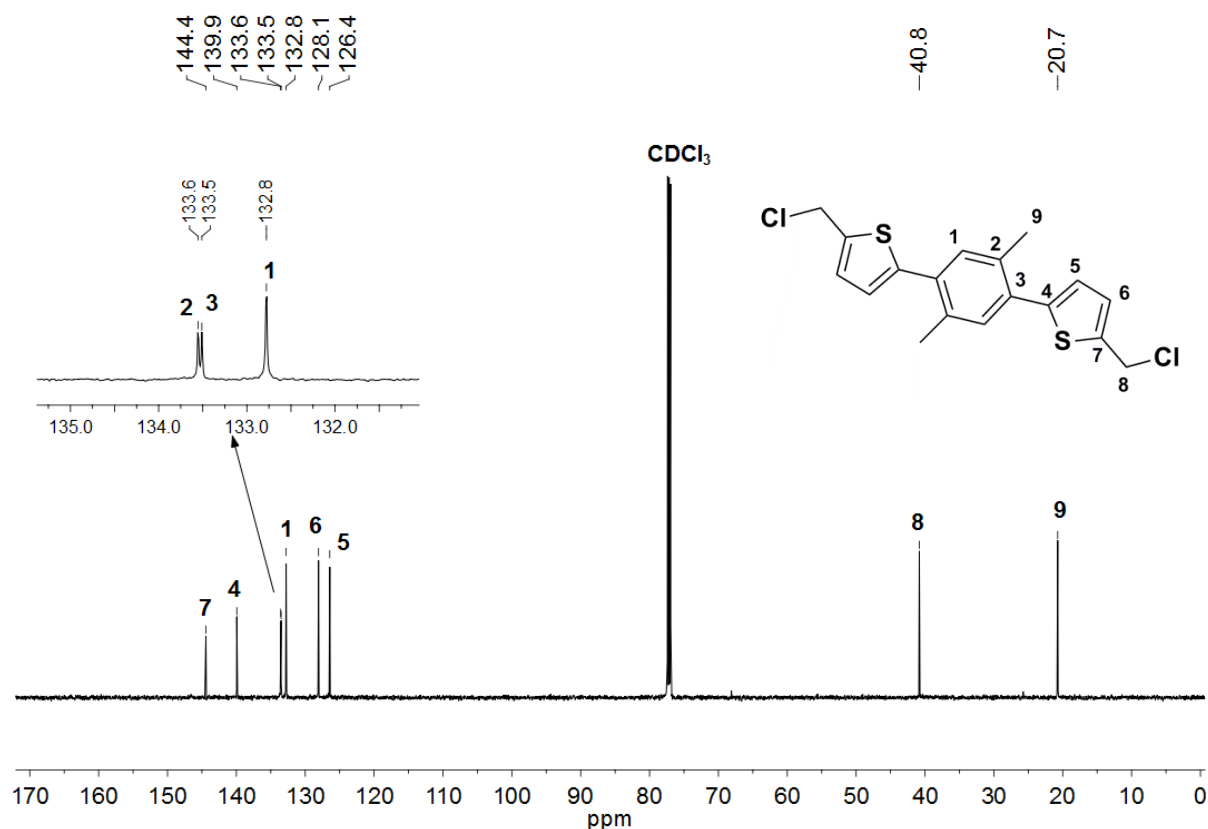
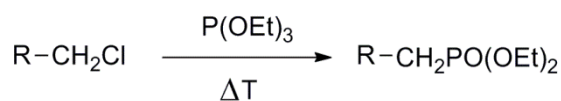


Figure 3.10 ^{13}C NMR spectrum of **36** recorded in CDCl_3 .

3.1.3 Synthesis of the Phosphonates

The phosphonate derivatives were synthesized according to a procedure published in the literature.²⁰⁰ Different conditions were tried out. Firstly, benzene was used as a solvent. The reaction was heated to reflux for 2 days under continuous stirring. The desired phosphonates **38**, **39** and **40** were synthesized successfully (Figure 3.11). However, although excess amounts of triethylphosphite (15 mol eq. for each methylchloride moiety) were used, low yields were obtained (30-40 %). Secondly, without using benzene, the reaction mediums were heated to 120 °C and kept at this temperature for 3 days, the yields were increased to 50 - 55 % (Scheme 3.4). After the reaction, the obtained solids were washed several times with pentane in order to remove the unreacted triethylphosphite and the side product triethylphosphate.



Scheme 3.4 Reaction scheme for the synthesis of the phosphates.

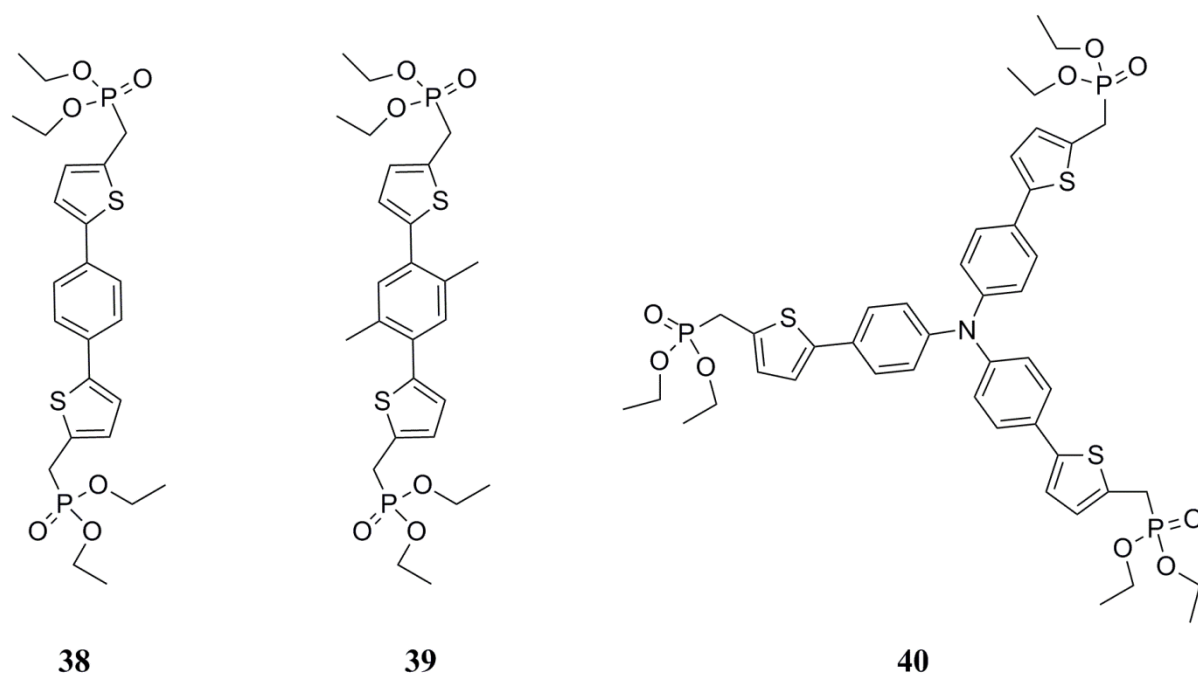


Figure 3.11 The phosphonates **38**, **39** and **40**.

The ^1H NMR spectrum of **39** reveals three peaks in the aromatic region (Figure 3.12). The phenyl protons (H1) show a singlet at 7.31 ppm. The thiophene protons (H5) appear as a doublet at 7.09 ppm with coupling constant of 3.6 Hz, while the other thiophene protons neighboring the phosphonate group (H6) resonate at 6.99 ppm. Although a doublet was expected, these protons show a triplet ($J = 3.6$ Hz) because of the coupling of these protons with the phosphorous atoms. The methylene protons bound to the oxygen atoms (H9) appear as a doublet of quartet at 4.02 ppm ($^3J_{\text{PH}} = 14.1$ and $J_{\text{HH}} = 7.1$ Hz). The other methylene protons neighboring the thiophene rings (H8) show a doublet ($^2J_{\text{PH}} = 20.8$ Hz) at 3.52 ppm as a result of the coupling with the phosphorous atoms. The methyl protons of the phenyl ring (H11) appear as a singlet at 2.38 ppm.

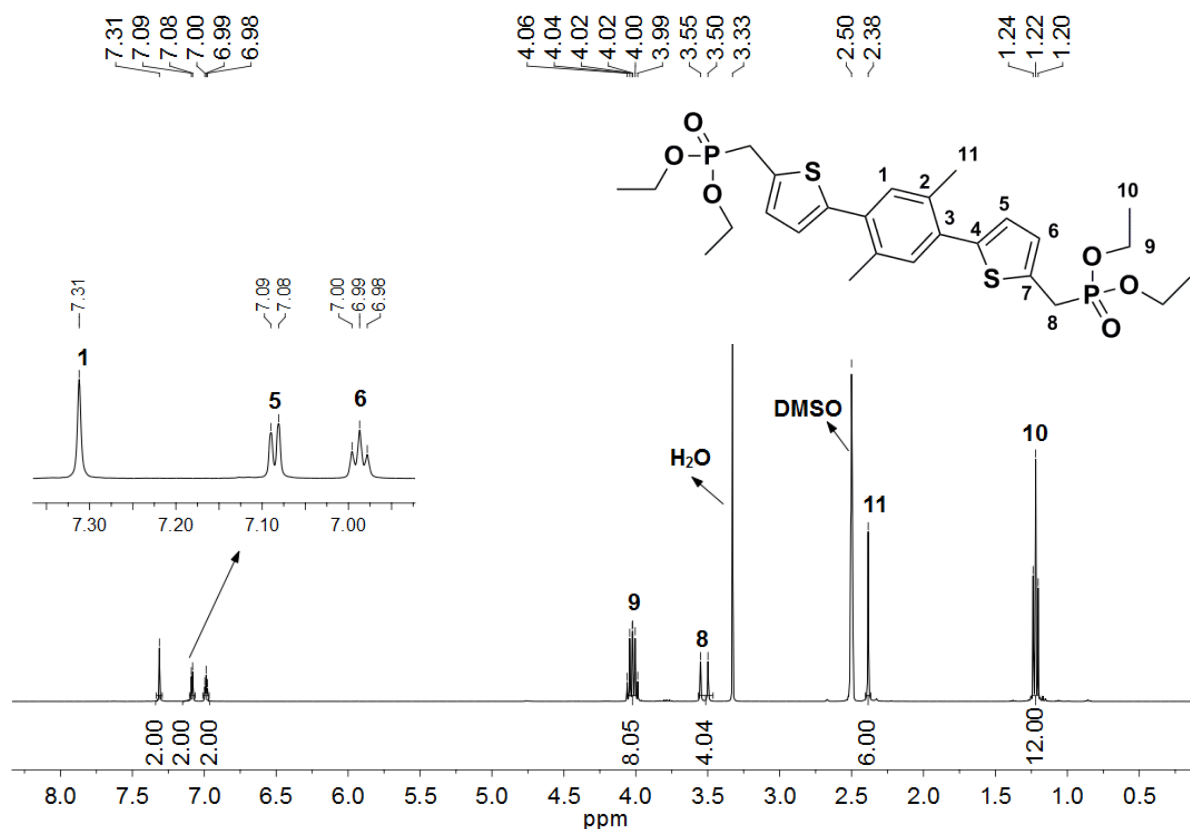


Figure 3.12 ^1H NMR spectrum of **39** recorded in DMSO- d_6 .

The ^{13}C NMR spectrum reveals eleven carbon atoms as expected (Figure 3.13). Long range couplings were observed in the spectrum. The C4 carbon atoms show a coupling with the phosphorous atoms and appear as a doublet at 140.7 ppm ($^5J_{\text{PC}} = 3.5$ Hz). For the C5, C6 and C7 carbon atoms, a coupling was also observed with phosphorous atoms ($^4J_{\text{PC}} = 2.3$ Hz, $^3J_{\text{PC}} = 9.0$ Hz and $^2J_{\text{PC}} = 10.2$ Hz respectively). C2, C3 (132.7 ppm) and C1 (132.2 ppm) carbon atoms resonate as singlets. The C8 carbon atoms neighboring the $\text{PO}(\text{OEt})_2$ groups show strong coupling to phosphorous atoms as expected and resonate at 26.8 ppm with a doublet ($^2J_{\text{PC}} = 135.9$ Hz).

The ^{31}P NMR spectrum of **39** also proves the formation of the pure phosphonate by showing one singlet at 24.48 ppm (Figure 3.13).

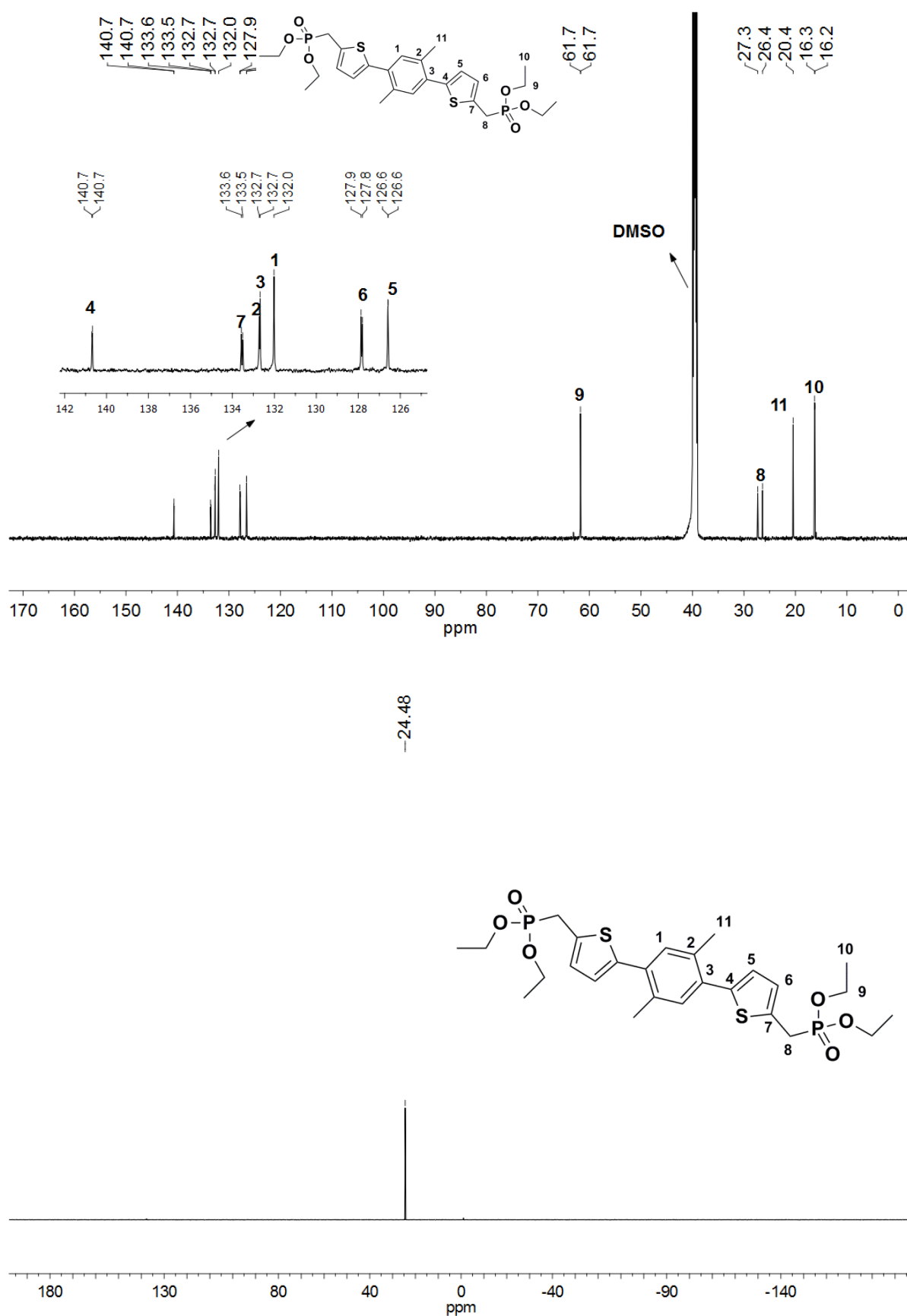


Figure 3.13 ^{13}C and ^{31}P NMR spectra of **39** recorded in DMSO-d_6 .

3.2 Surface Modification of the Metal Oxides; TiO_2 , Al_2O_3 , ZrO_2

Surface modification of the metal oxides (TiO_2 , Al_2O_3 , ZrO_2) was performed by grafting **38**, **39** and **40** on the supports. It is known that the reaction conditions, such as concentration, temperature and solvent affect the surface modification which may result in dissolution-precipitation instead of surface modification.¹⁸⁰ Therefore, two different reaction conditions were tried in order to reach the maximum grafting.

First experiments were performed for ZrO_2 using **38** as the coupling molecule. Two sets were prepared. For the first one, dichloromethane was selected as the solvent and the reaction was performed at room temperature. In the second method reflux conditions were applied using chloroform. **38** was dissolved and the metal oxide was added afterwards. After 24 h, the reaction was stopped and the obtained solids were washed with dichloromethane, methanol and diethyl ether in order to remove unreacted coupling molecules and dried under ambient pressure for 10 h at 50 °C.

The elemental analysis data revealed a successful grafting under both conditions, but room temperature reaction resulted in a better loading (Table 3.1). Therefore, all reactions were performed at room temperature using dichloromethane.

Table 3.1 Elemental composition of ZrO_2 after surface modification.

	Elemental Analysis			
	C	H	N	S
38@ZrO₂ (RT)	1.01 %	0.60 %	--	0.76 %
38@ZrO₂ (reflux)	0.48 %	0.40 %	--	0.26 %

In all reactions, the amounts of metal oxide and coupling molecule were kept constant in order to compare the loadings. For 1.00 g of each metal oxide, 160.00 mg of **38** and **39** were used. In the case of the modification with **40**, for 1.00 g of each metal oxide 80.00 mg of **40** was used due to the presence of three $-\text{PO}(\text{OEt})_2$ groups in the molecule. Before the reactions, the surfaces were dried at 120° C for 12 h.

3.3 Characterization of the Immobilized Surfaces

The characterization of the materials was done by elemental analysis, ^{31}P CP MAS NMR and IR spectroscopy. The BET surface areas of the materials were determined by N_2 adsorption measurements. TGA was used to determine the stability of the materials.

Besides the characterization of the materials, another important point is the determination of the loading (B) which can be defined as the amount of the immobilization of phosphonic esters per gram of the metal oxide. The loading was calculated by using the formula below:

$$B = \frac{P_x}{A_x \cdot n_x}$$

B = moles of immobilized molecule per gram of modified material

P_x = percentage of the element X in immobilized molecule of modified material found in elemental analysis

A_x = relative atomic weight of element X in mol/g

N_x = number of atoms in immobilized material

3.3.1 Characterization of the Modified ZrO_2 Surface

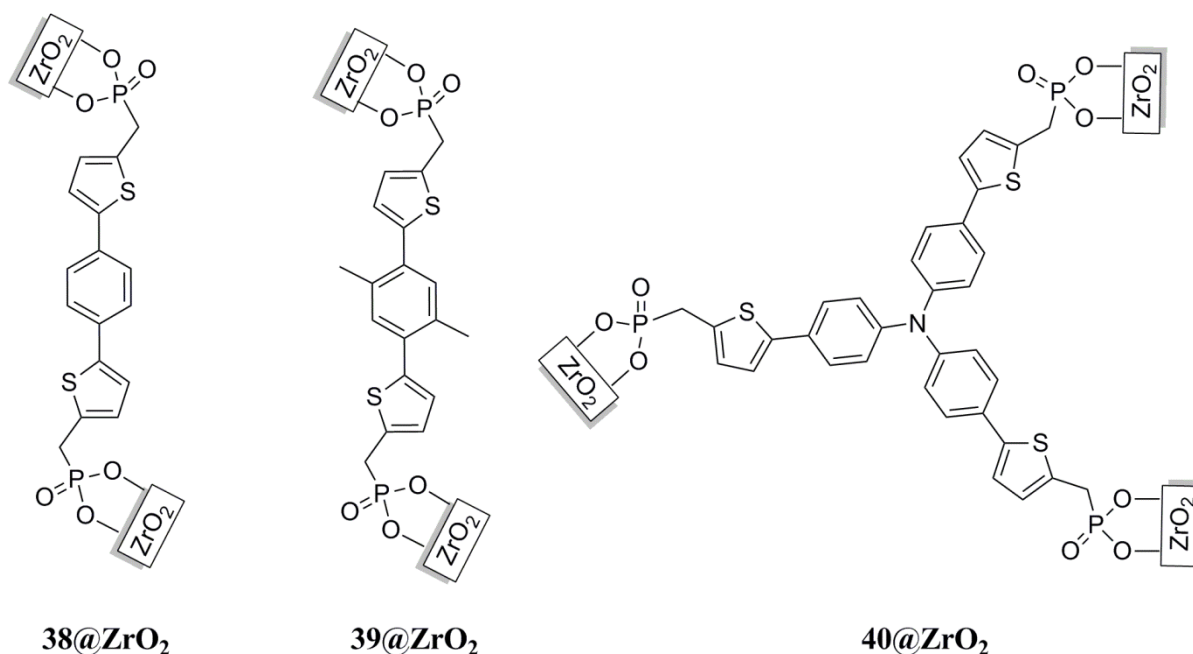


Figure 3.14 Modified ZrO_2 surfaces.

The characterization of the modified ZrO_2 surfaces (Figure 3.14) was done using elemental analysis. The results revealed the successful modification of the surfaces. For all three surfaces **38@ZrO₂**, **39@ZrO₂** and **40@ZrO₂**, the expected elemental composition was observed (Table 3.2). In order to calculate the loading amount, the sulfur percentage was used in the calculations. The loading was found to be 0.12 mmol/g for **38@ZrO₂**. Although the same conditions were used for the grafting of **39**, a lower loading was observed for **39@ZrO₂**, which is 0.07 mmol/g. For **40**, which features three $-\text{P}(\text{OEt})_2$ groups, the loading was found to be 0.08 mmol/g.

Table 3.2 Characterization of **38@ ZrO₂**, **39@ ZrO₂** and **40@ZrO₂**.

	Elemental Analysis				S_{BET}	B
	C	H	N	S	(m^2/g)	(mmol/g)
ZrO₂	--	--	--	--	92.5	--
38@ZrO₂	1.01 %	0.60 %	--	0.76 %	95.7	0.12
39@ZrO₂	1.09 %	0.48 %	--	0.45 %	105.0	0.07
40@ZrO₂	1.60 %	0.56 %	0.11 %	0.75 %	91.2	0.08

Acronyms: S_{BET} ; BET surface area, B; Loading.

Nitrogen adsorption measurements were used to determine the BET surface areas. Before the measurements, the samples were activated at 100 °C for 72 h under pressure. All three modified ZrO_2 surfaces showed Type IV isotherms (Figure 3.15). A hysteresis was observed at $0.3 < p < 0.9$ in all isotherms which is typical for the mesoporous materials.²⁰¹ The BET surface areas for **38@ZrO₂**, **39@ZrO₂** and **40@ZrO₂** were found to be 95.7, 105.0 and 91.2 m^2/g respectively (Table 3.2). When these results are compared with the unmodified ZrO_2 surface, it is clear that almost the same BET surface areas were found which was expected. The slight differences can be the result of the measurement conditions.

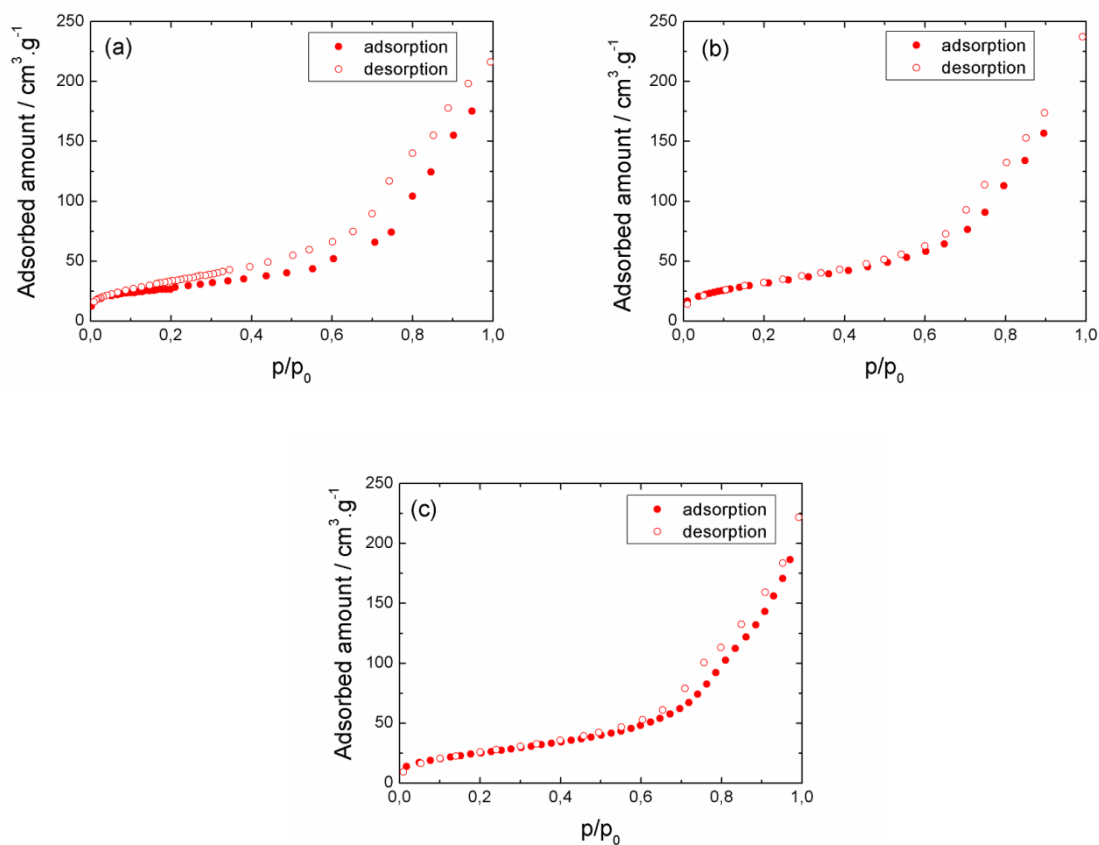


Figure 3.15 N_2 adsorption isotherms of $38@ZrO_2$ (a), $39@ZrO_2$ (b) and $40@ZrO_2$ (c).

3.3.2 Characterization of the Modified TiO_2 Surface

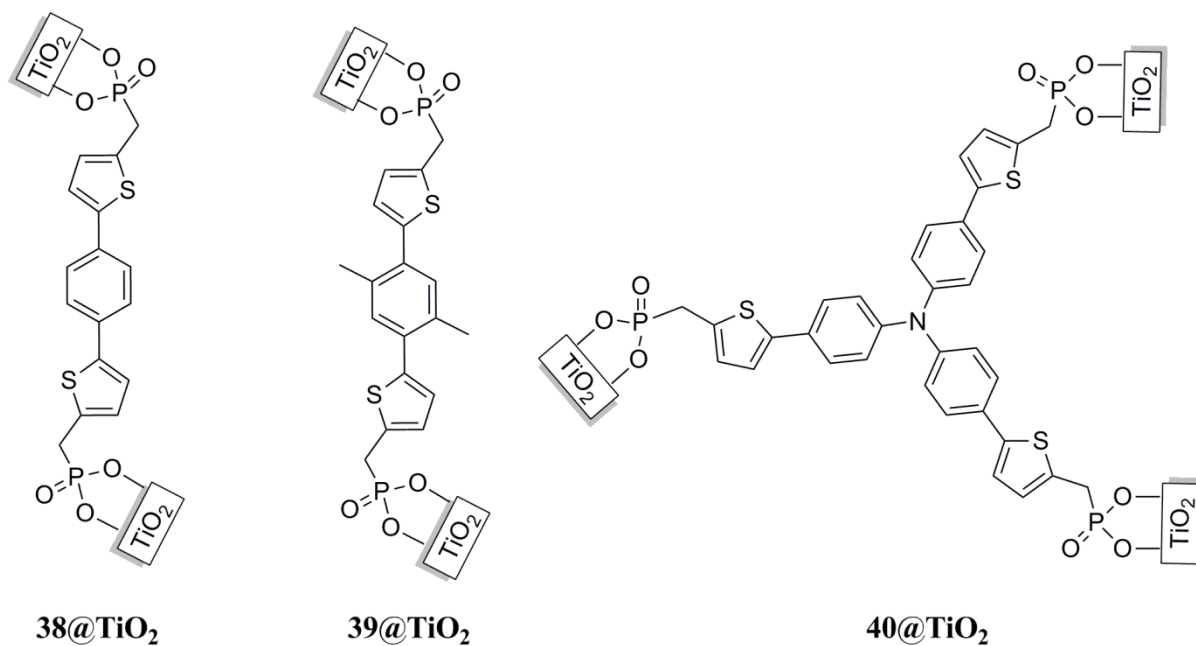


Figure 3.16 Modified TiO_2 surfaces.

For the modified TiO₂ surfaces with **38**, **39** and **40** (Figure 3.16), elemental analysis results again show the grafting of the phosphonic esters (Table 3.3). When the results are compared with the modified ZrO₂ surfaces, lower loadings were found. The loadings were again calculated using the percentages of sulfur found by elemental analysis. According to the results, for **38@TiO₂**, 0.07 mmol of **38** was grafted on 1.00 g of TiO₂ surface, compared to 0.12 mmol on ZrO₂. A slight decrease of the loading was also observed for **39**. The loading was found to be 0.06 mmol/g for **39@TiO₂**. For the immobilization of **40**, the loading was found to be 0.03 mmol/g, compared to 0.08 mmol/g for ZrO₂.

Table 3.3 Characterization of **38@TiO₂**, **39@TiO₂** and **40@TiO₂**.

	Elemental Analysis				S _{BET} (m ² /g)	B (mmol/g)
	C	H	N	S		
TiO ₂	--	--	--	--	111	--
38@TiO₂	0.79 %	0.39 %	--	0.42 %	105	0.07
39@TiO₂	1.03 %	0.39 %	--	0.38 %	105	0.06
40@TiO₂	1.31 %	0.56 %	0.12 %	0.33 %	105	0.03

Acronyms: S_{BET}; BET surface area, B; Loading.

The BET surface areas of the modified TiO₂ samples were determined using the N₂ adsorption measurements. For the all three samples, the measurements revealed Type IV isotherms which indicate well defined mesoporous materials (Figure 3.17). A small hysteresis was also observed in all isotherms between 0.6 < p < 0.9. Moreover N₂ condensation was observed in the isotherms which can be due to the large crystal size of the TiO₂ material. The same BET surface area was found for each material (105 m²/g) which is slightly lower than the surface area of the unmodified TiO₂ (111 m²/g) (Table 3.3).

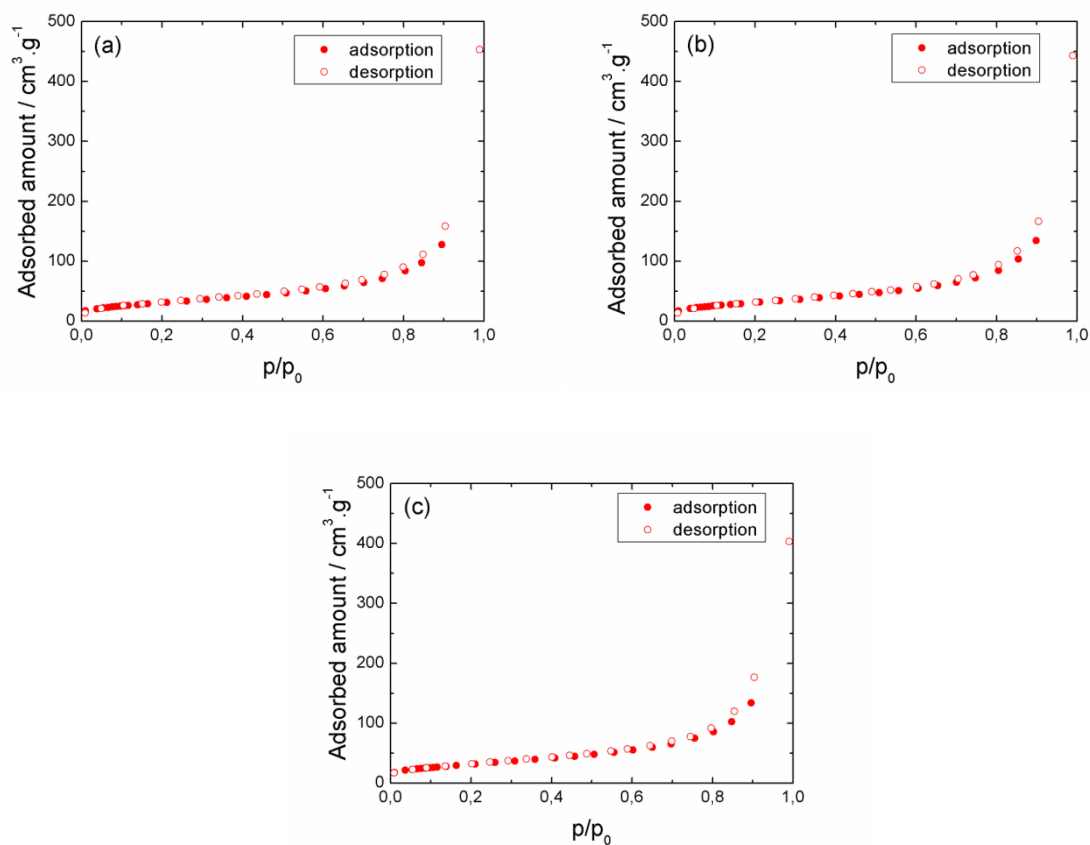


Figure 3.17 N_2 adsorption isotherms of **38@TiO₂** (a), **39@TiO₂** (b) and **40@TiO₂** (c).

3.3.3 Characterization of the Modified Al_2O_3 Surface

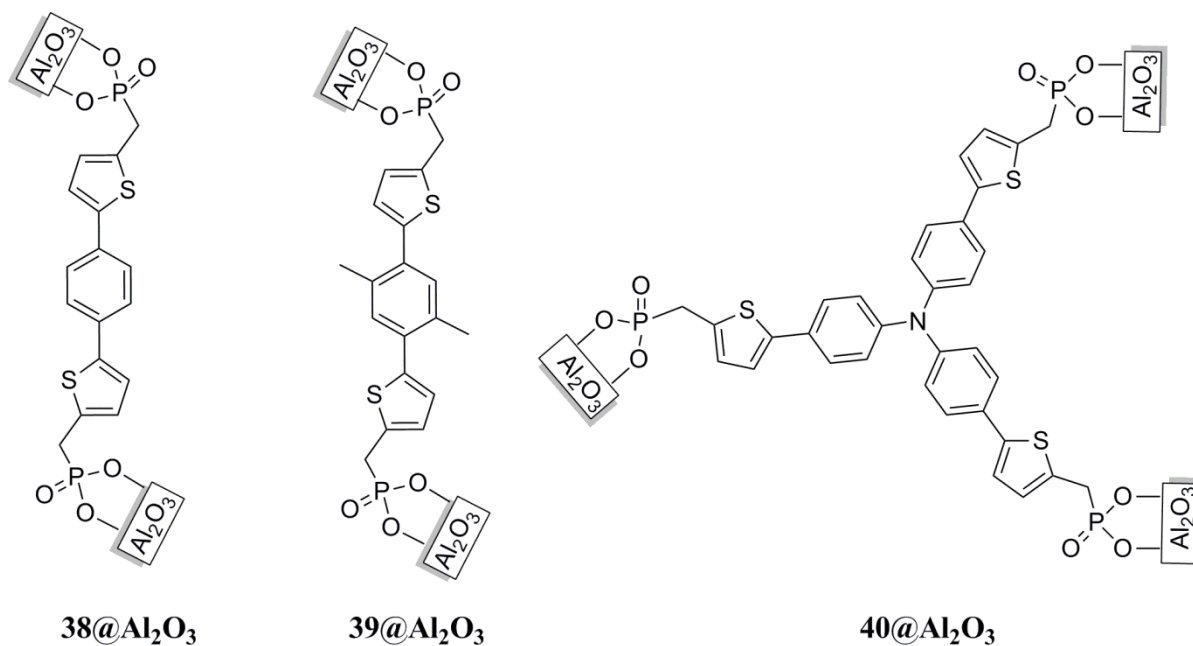


Figure 3.18 Modified Al_2O_3 surfaces.

The elemental analysis data of the modified Al_2O_3 surfaces (Figure 3.18) clearly reveal the modification. The compositions of the materials found in the analysis are in agreement with the other metal oxide surfaces. The loadings for **38@Al₂O₃**, **39@Al₂O₃** and **40@Al₂O₃** are calculated as 0.06, 0.05 and 0.04 mmol/g' respectively by using the sulfur percentage (Table 3.4).

Table 3.4 Characterization of **38@Al₂O₃**, **39@Al₂O₃** and **40@Al₂O₃**.

	Elemental Analysis				S_{BET}	B

Acronyms: S_{BET} ; BET surface area, B; Loading.

The N_2 adsorption isotherms showed the similar type of isotherm, as expected (Figure 3.19). A Type IV isotherm with small hysteresis was observed for all three modified surfaces. N_2 condensation also exists in the Al_2O_3 surfaces as in the TiO_2 surface. The BET surface areas for **38@Al₂O₃** and **40@Al₂O₃** are found as 125 m²/g and 150 m²/g for **40@Al₂O₃** (Table 3.4).

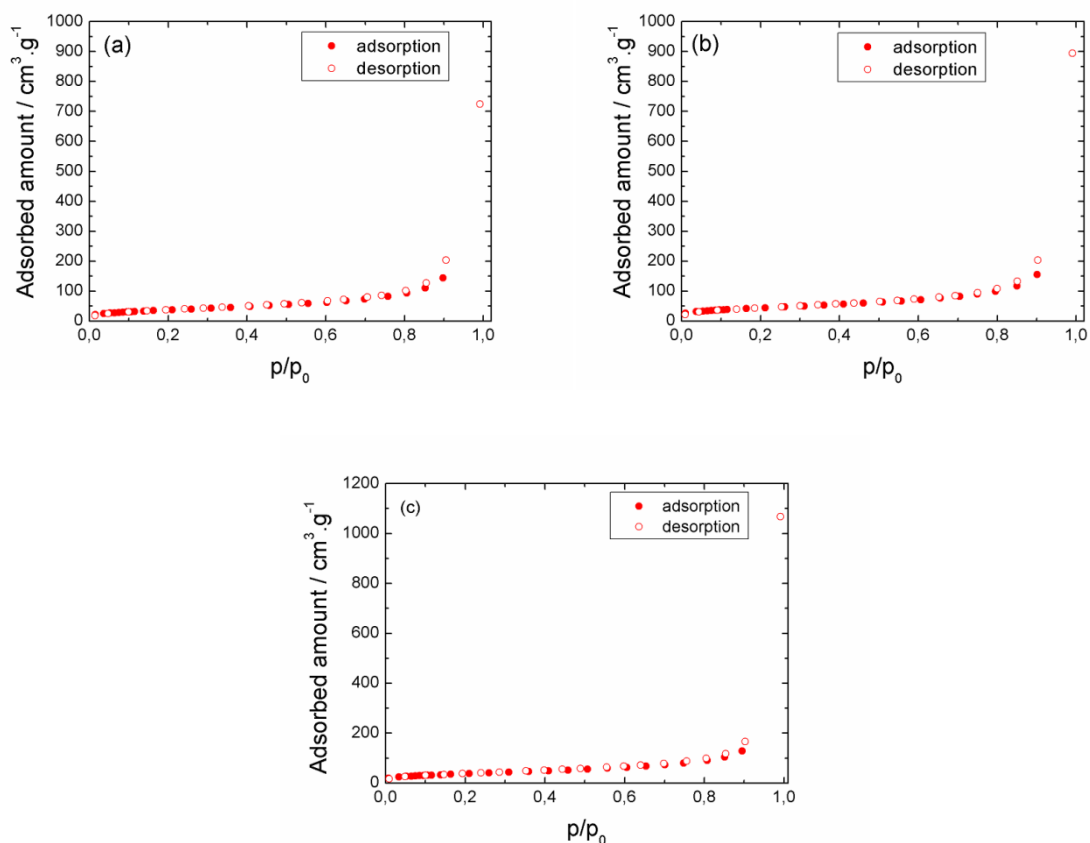


Figure 3.19 N₂ adsorption isotherms of **38@Al₂O₃** (a), **39@Al₂O₃** (b) and **40@Al₂O₃** (c).

3.3.4 IR Measurements of the Modified Surfaces

Figure 3.20 shows the infrared spectra of the metal oxides before and after surface modification. The frequencies of all the surfaces before and after modification are similar to each other. The absorptions between 1300-800 cm⁻¹ are assigned to the P-O stretching region.¹⁷² In the IR spectra of the samples this stretching could only be observed for two ZrO₂ surfaces. The peak at 1023 cm⁻¹ in **38@ZrO₂** and **39@ZrO₂** surfaces clearly indicates the P-O stretching.

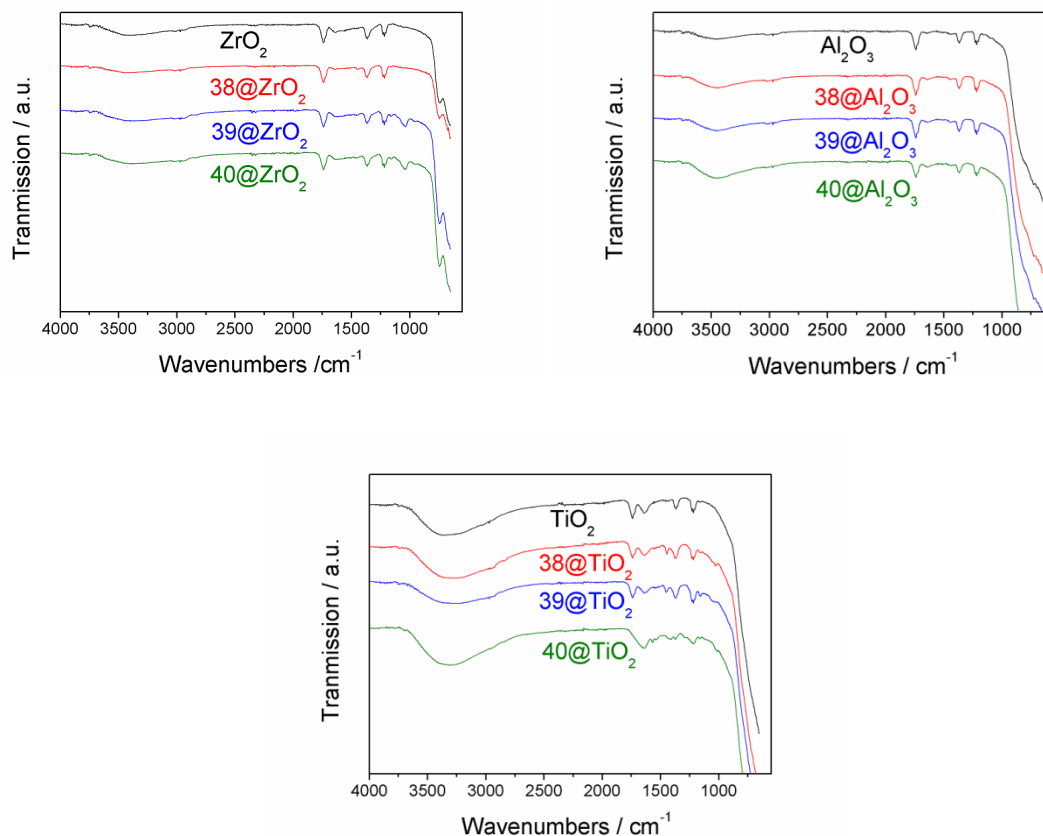


Figure 3.20 IR spectra of the metal oxides before and after surface modification.

3.3.5 ^{31}P CP MAS NMR of the Modified Surfaces

^{31}P CP MAS NMR measurements were performed for all modified surfaces. However all the surfaces except **40@ZrO₂** did not show any ^{31}P resonances at all.

In the ^{31}P CP MAS NMR spectrum of **40@ZrO₂**, two sets of resonances are observed (Figure 3.21). The broad peak at 25.51 ppm is assigned to phosphonate groups.²⁰² All other resonances are rotational side bands.

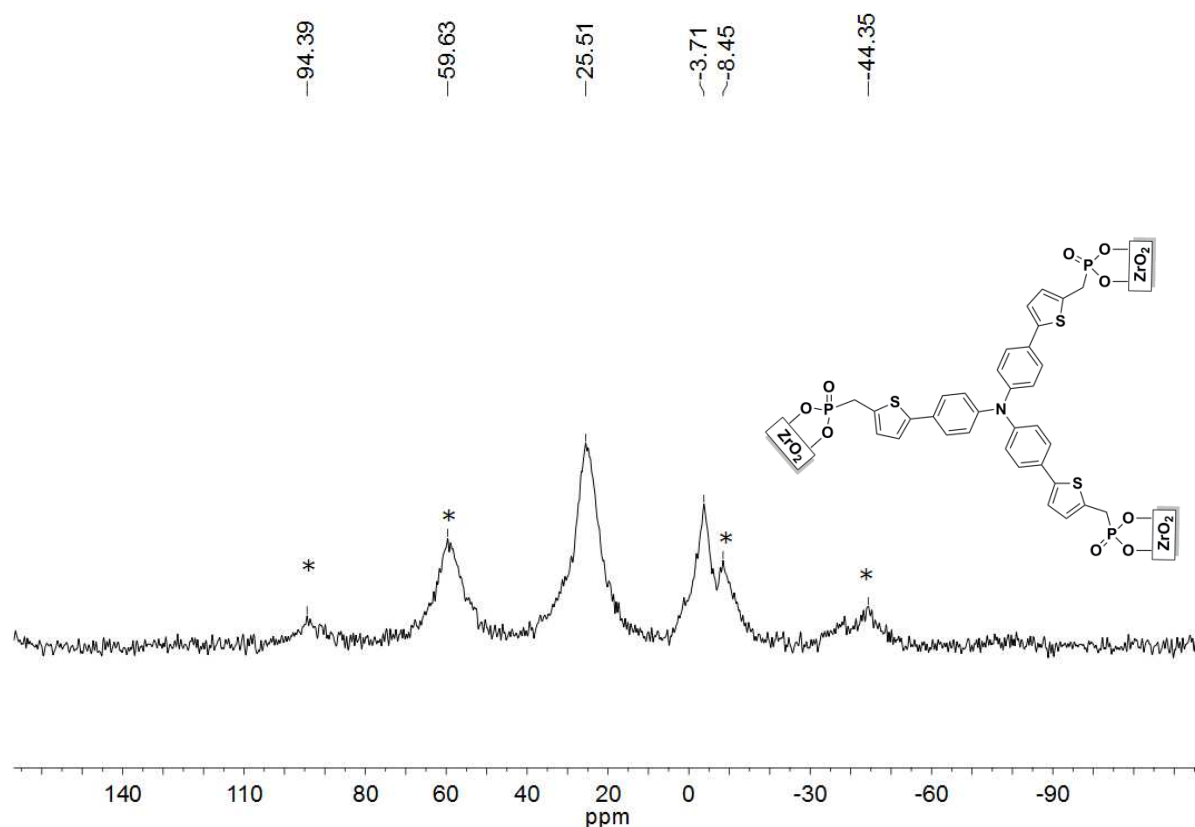


Figure 3.21 ^{31}P CP MAS NMR spectrum of **40@ZrO₂**.

3.3.6 TGA Measurements of **38@Al₂O₃**, **38@TiO₂** and **38@ZrO₂**

TGA measurements were performed to determine the thermal stability of the immobilized materials. For this purpose, the samples of the same coupling molecule (**38**) on different surfaces were used. The measurements show that all three samples (**38@Al₂O₃**, **38@TiO₂** and **38@ZrO₂**) are stable up to 500 °C (Figure 3.22).

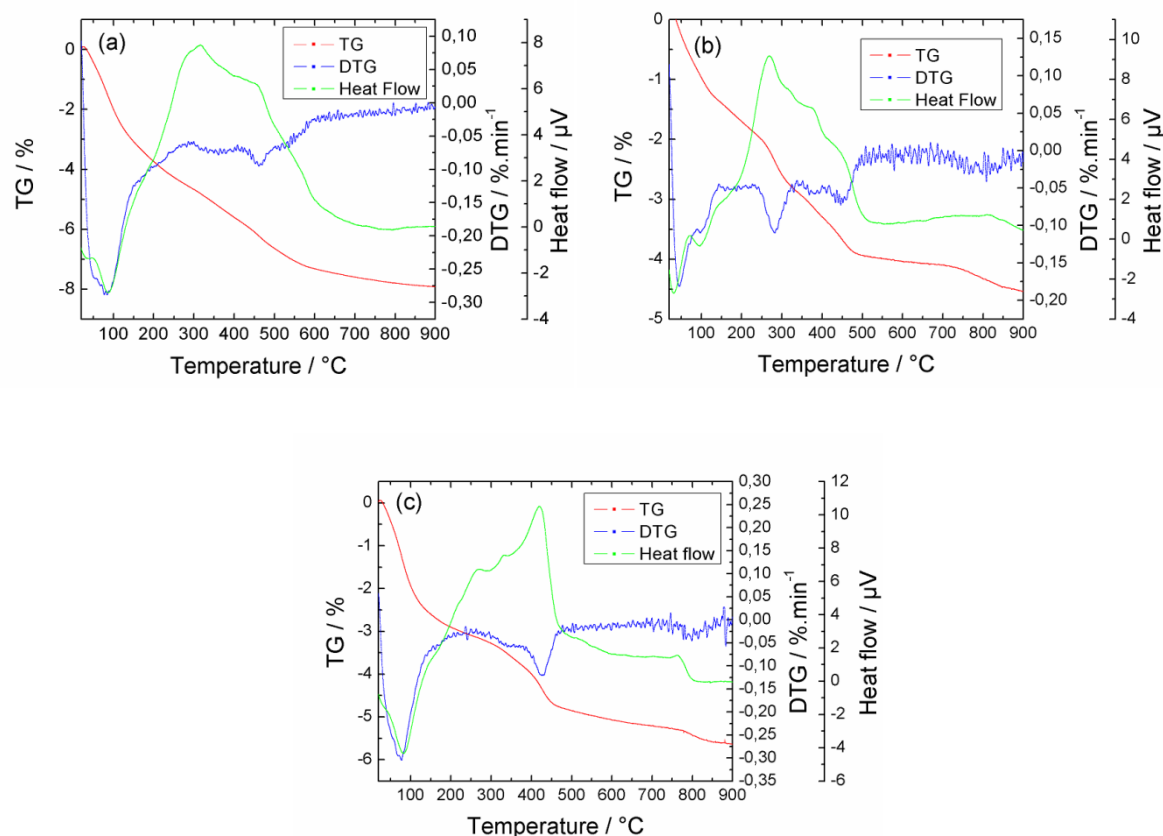


Figure 3.22 TGA of **38** on Al_2O_3 (a), TiO_2 (b), ZrO_2 (c).

3.4 Fluorescence Data of the modified TiO_2 , Al_2O_3 , ZrO_2 Surfaces

Regarding the strong luminescence of the coupling molecules **38**, **39** and **40**, the modified surfaces were checked for their light emission. The modified TiO_2 and ZrO_2 surfaces were excited at 325 nm and Al_2O_3 surface was excited at 365 nm. All ZrO_2 and Al_2O_3 surfaces showed fluorescence except of **40@Al₂O₃** (Figure 3.23). On the other hand, for the modified TiO_2 surfaces, no fluorescence could be observed at all. Most probably the low loading on the TiO_2 surface and luminescence quenching close to the surface caused such a result.

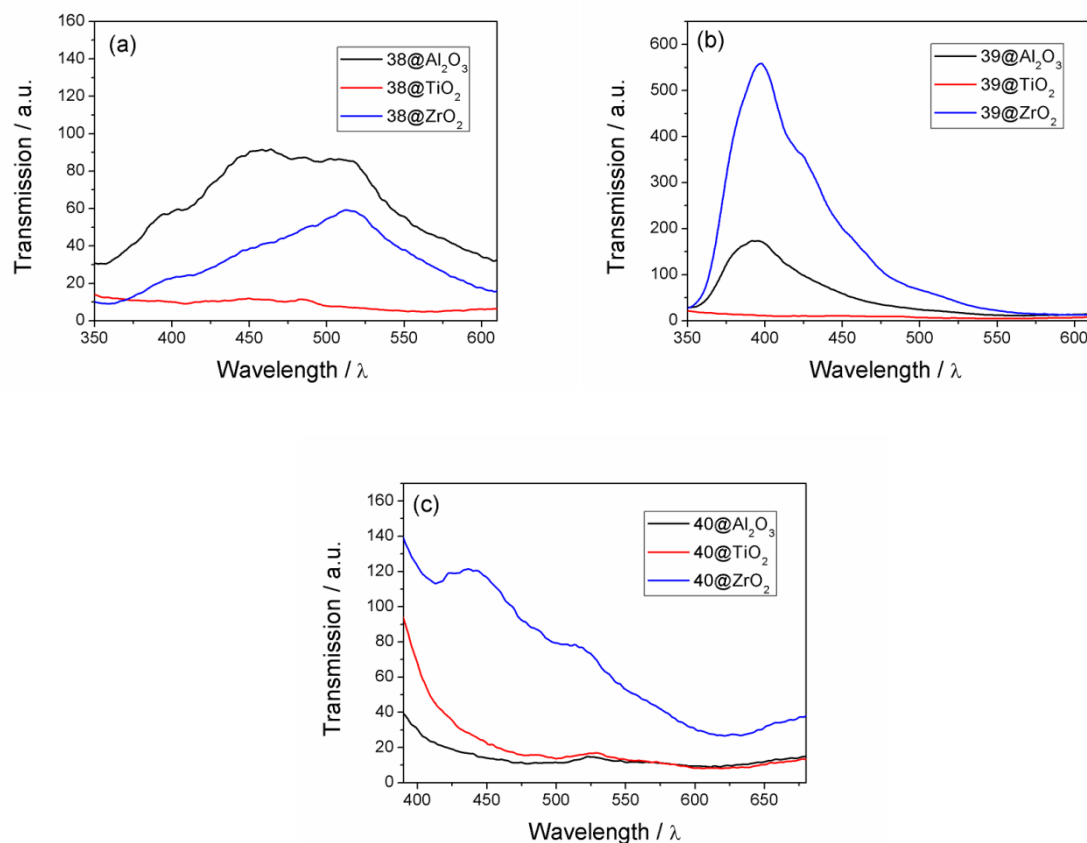


Figure 3.23 Emission spectra of 38@ Al_2O_3 , 38@ ZrO_2 , 38@ TiO_2 (a), 39@ Al_2O_3 , 39@ ZrO_2 , 39@ TiO_2 (b) and 40@ Al_2O_3 , 40@ ZrO_2 , 40@ TiO_2 (c). Excitation wavelengths: modified TiO_2 and ZrO_2 surfaces: 325 nm, modified Al_2O_3 surfaces: 365 nm.

4. Conclusion

In summary, our study on two subgroups of organic-inorganic hybrid materials have led to following conclusions and insights:

In the first part of the work which covers metal organic frameworks, seven functionalized biphenyl dicarboxylate linkers were synthesized successfully. These linkers yielded seven metal organic frameworks with different properties and features.

Firstly three functionalized MOF structures; **ZnBrBPDC**, **ZnNO₂BPDC** and **ZnNH₂BPDC** were synthesised using 4,4'-biphenyldicarboxylic acid derivatives with different functional groups (-Br, -NO₂, -NH₂). Powder XRD measurements indicated that the synthesised MOFs posses the interpenetrated IRMOF-9 structure with a cubic topology which was also confirmed with single crystal X-ray measurements. The chemical structure of the MOF materials was further proved by solid state NMR and IR measurements.

All three structures showed Type I isotherms with large surface areas which are comparable with their analogues:

Table 4.1 Comparison of the porosity measurements of **ZnBrBPDC**, **ZnNO₂BPDC** and **ZnNH₂BPDC** with the analogue MOFs.

	A_{LANG} (m ² /g)	A_{BET} (m ² /g)	V_p (cm ³ /g)
IRMOF-2	2544	1722	0.88
IRMOF-3	3062	2446	1.07
IRMOF-9	2613	1904	0.90
ZnBrBPDC	1403	1300	0.53
ZnNO₂BPDC	2206	2000	0.83
ZnNH₂BPDC	1087	1100	0.43

Acronyms: A_{LANG} ; Langmuir surface area, A_{BET} ; BET surface area, V_p ; measured pore volume.

TGA measurements of the evacuated samples showed great agreement with the elemental analysis data. The results proved that their thermal stability is between 325 °C - 450 °C.

Adsorption properties of these MOF structures were tested using light alkanes (CH₄, C₂H₆, C₃H₈, and *n*-C₄H₁₀) at three different temperatures. For all adsorbents, the maximum uptakes

were observed at 273 K. When the temperature was increased, the amount of the adsorbed gas decreased. All three MOFs show strong affinities for *n*-butane. The lowest uptakes were observed for CH₄.

The effect of functional groups on the IRMOF series was also examined by synthesizing amide functionalized biphenyl linkers. For this purpose, four different linkers containing amides with different alkyl chains (C1-C4) were synthesized and used for the synthesis of four new MOF structures **ZnAcBPDC**, **ZnPrBPDC**, **ZnBuBPDC** and **ZnPeBPDC**.

Powder XRD measurements of **ZnAcBPDC** indicated that the structure contains two different phases. PXRD patterns of **ZnPrBPDC**, **ZnBuBPDC** and **ZnPeBPDC** revealed non-interpenetrated structures which were further proved by single crystal X-ray measurements. The chemical structure of the MOF materials was further confirmed by X-ray spectroscopy, solid state NMR and IR measurements.

N₂ Adsorption measurements of the MOF structures were carried out using different activation methods. While **ZnBuBPDC** and **ZnPeBPDC** showed porosity for acetone exchanged and evacuated samples, **ZnPrBPDC** showed porosity after supercritical CO₂ activation. **ZnAcBPDC** conserved its structure against both activation methods and showed porosity. For all four MOFs, Type I isotherms were obtained. For **ZnPrBPDC** a large hysteresis was observed in the isotherm. **ZnAcBPDC** showed the highest BET surface area.

Table 4.2 Summary of the N₂ adsorption measurements of **ZnAcBPDC**, **ZnPrBPDC**, **ZnBuBPDC** and **ZnPeBPDC**.

	A_{BET} (m ² /g) ^a	A_{BET} (m ² /g) ^b	V_p (cm ³ /g) ^a	V_p (cm ³ /g) ^b
ZnAcBPDC	920	1588	0.50	0.73
ZnPrBPDC	--	325	--	0.15
ZnBuBPDC	850	--	0.43	--
ZnPeBPDC	1100	--	0.60	--

Acronyms: A_{BET} ; BET surface area, V_p ; measured pore volume. ^a the sample exchanged with acetone and evacuated at 80°C for 24h. ^b the super critical CO₂ activated samples.

TGA measurements of the as-synthesized samples proved that their thermal stability is up to 350 °C. Elemental analysis data possessed great compatibility with TGA measurements and also confirmed the composition of the materials.

ZnAcBPDC and **ZnBuBPDC** were tested for alkane and alkene adsorptions at three different temperatures (273 K, 293 K and 313 K). For this study pure alkanes (CH_4 , C_2H_6 , C_3H_8 , and $n\text{-C}_4\text{H}_{10}$) and alkenes (C_2H_4 , C_3H_6 and C_4H_8) were used. For all sorbates, maximum uptakes were observed for **ZnAcBPDC** at all temperatures.

ZnAcBPDC and **ZnBuBPDC** were further tested for their CO_2 adsorption capabilities at 273 K, 293 K and 313 K. Both of the adsorbents showed high affinities for CO_2 . Maximum loadings were observed for **ZnAcBPDC** at all temperatures.

In the second part of the work, surface modification of three different metal oxides, ZrO_2 , TiO_2 and Al_2O_3 was performed. For this purpose firstly three different phosphonate derivatives containing thiophene units were synthesized from their halo derivatives in a four step synthesis and then used as coupling molecules for the surface modification. Nine different surfaces were obtained (**38@TiO₂**, **39@TiO₂**, **40@TiO₂**, **38@Al₂O₃**, **39@Al₂O₃**, **40@Al₂O₃**, **38@ZrO₂**, **39@ZrO₂**, **40@ZrO₂**).

All three modified metal oxide surfaces were characterized using elemental analysis, solid state NMR and IR spectroscopy. The BET surface areas of the materials were determined by N_2 adsorption measurements. TGA was used to determine the stability of the surfaces. Maximum loadings were obtained for ZrO_2 surfaces.

Due to the strong luminescence of the coupling molecules, the modified surfaces were checked for their light emission. All ZrO_2 and Al_2O_3 surfaces showed fluorescence except of **40@Al₂O₃**. On the other hand, for the modified TiO_2 surfaces, no fluorescence could be observed.

5. Experimental

5.1 Materials

Reagents were purchased from ACROS, Sigma Aldrich, Fluka, ABCR, Merck, Alfa Aesar and Evonik and used without further purification unless otherwise noted.

5.2 Instrumental Analysis

NMR Spectroscopy

Liquid phase ^1H and ^{13}C NMR spectra were recorded on Bruker Spectrospin DPX-400 and Avance 600 devices at resonance frequencies of 400 MHz or 600 MHz for ^1H nuclei and 101 MHz or 151 MHz ^{13}C nuclei.

Infrared (IR) Spectroscopy

The infrared spectra with a resolution of $\pm 2\text{ cm}^{-1}$ were recorded using a PerkinElmer FT-ATR-IR 1000 spectrometer containing a diamond coated ZnSe-window.

Elemental Analysis

Elemental analyses were determined on a CHNS vario Microcube elemental analyzer (Elementar).

Powder XRD Measurements

Powder X-Ray diffraction was measured on a Siemens D5005 with $\text{CuK}\alpha$ radiation ($\lambda = 0.15418\text{ nm}$) to confirm the phase purity and crystallinity of the synthesized samples.

X-ray Absorption Spectroscopy

X-ray absorption spectroscopy measurements were performed at the XAS beamline at the Ångströmquelle Karlsruhe (ANKA) under ambient conditions at 20 °C. The synchrotron beam current was between 80 – 140 mA at 2.5 GeV storage ring energy. A Si(111) double crystal monochromator was used for measurements at the Zn K-edge (9.696 keV). The second monochromator crystal was tilted for optimal harmonic rejection. The spectra were recorded in fluorescence mode with a hyperpure 7-element Ge-detector. Energy calibration

was performed with a zinc metal foil. To avoid mistakes in the XANES region due to small changes in the energy calibration between two measurements, all spectra were corrected to the theoretical edge energy of iron foil, which was measured before every scan. For the determination of the smooth parts of the spectra, corrected for pre-edge absorption, a piece-wise polynomial was used. It was adjusted in such a way that the low-R components of the resulting Fourier transform were minimal.^{145,146} After division of the background-subtracted spectrum by its smooth part, the photon energy was converted to photo-electron wave numbers k . The resulting $\chi(k)$ -function was weighted with k^3 . Data analysis was performed in k -space according to the curved wave formalism of the EXCURV98 program with XALPHA phase and amplitude functions.¹⁴⁷ The mean free path of the scattered electrons was calculated from the imaginary part of the potential (VPI set to -4.00).

N₂ Adsorption Measurements

Nitrogen adsorption/desorption measurements were performed on a Quantachrome Autosorb-1 at a temperature of 77 K. The samples were activated at a pressure of $< 1 \cdot 10^{-5}$ mbar and at a temperature of 353 K overnight. The specific surface areas were calculated by means of the Brunauer–Emmett–Teller (BET) equation in the low relative pressure interval (< 0.3) and the pore size distribution curves were analyzed with the adsorption branch by the BJH method. The micropore volume was evaluated with the t-plot method.

Thermogravimetric analyses (TGA)

Thermogravimetric analyses were performed on a Setaram Setsys 16/18 with a heating range of 5 K/min.

Scanning Electron Microscope (SEM) Pictures

The crystallinity and morphology of the synthesized samples were examined on a JEOL JSM-6490LA scanning electron microscope with a tungsten cathode at accelerating voltages of 5 – 25 kV and a working distance of 10 mm.

Gas Adsorption Measurements

The adsorbent was activated over night at a pressure of $< 10^{-5}$ mbar and 298 K. The isotherms were measured in a thermostated system. A separation valve H12 was placed between the dosing valve H11 and the adsorption vessel. The desired pressure was adjusted and valve H12 was rapidly opened. The adsorbed amounts were determined by the pressure changes in the system compared with the calibration measurement. The volumes of the different parts of the apparatus and the weight of the sorbent have been taken into account. The pressure change in the sorption vessel was measured with a high-accuracy piezo-membrane transmitter of type Ceravac CTR100 (Oerlikon Leybold Vacuum).

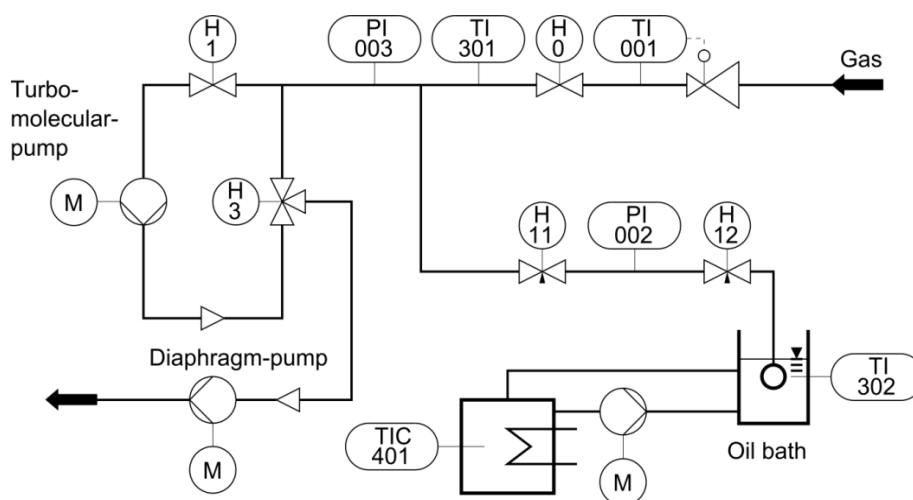


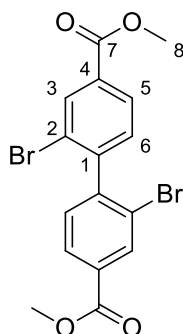
Figure 5.1 Scheme of the adsorption apparatus.

Solid State Fluorescence Data

Solid state fluorescence data was recorded on a Perkin-Elmer LS55 with a step width of 0.5 nm. The thin film powder samples were prepared from a DCM suspension or solution by evaporation of the solvent on a glass substrate.

5.3 Synthesis of the Linkers

5.3.1 Synthesis of Dimethyl-2,2'-dibromo-(1,1'-biphenyl)-4,4'-dicarboxylate (**2**)



20.00 mmol (5.40 g) of dimethyl-(1,1'-biphenyl)-4,4'-dicarboxylate (**1**) were gradually added to 50.00 ml of conc. sulfuric acid with continuous stirring and then treated with 18.80 g (60.29 mmol) of silver sulfate. 2.00 ml (80.00 mmol) of bromine were added in three portions and stirred until the color disappeared. The mixture was poured on to an ice-water mixture. The recovered precipitate was extracted with ethanol in a Soxhlet apparatus for 8 h. Recrystallisation from ethanol yielded 6.76 g of **2** as colorless crystals (yield: 79 %).

¹H NMR (400 MHz, CDCl₃): δ 8.33 (d, J = 0.8 Hz, 2H, H3), 8.04 (dd, J = 8.0 Hz, 0.8 Hz, 2H, H5), 7.30 (d, J = 8.0 Hz, 2H, H6), 3.94 (s, 6H, H8) ppm.

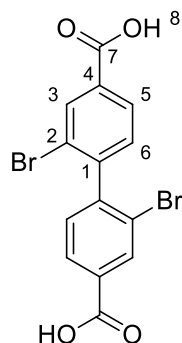
¹³C NMR (101 MHz, CDCl₃): δ 165.5 (C7), 145.7 (C1), 134.0 (C3), 131.9 (C4), 130.7 (C6), 128.4 (C5), 123.2 (C2), 52.5 (C8) ppm.

IR (ATR, cm⁻¹): ν 3006, 2952, 1715, 1289, 1119, 1048.

Elemental analysis: C₁₆H₁₂Br₂O₄ (428.07 g/mol)

Calculated	:	C: 44.89 %	H: 2.83 %
Found	:	C: 44.80 %	H: 2.92 %

5.3.2 Synthesis of 2,2'-Dibromo-(1,1'-biphenyl)-4,4'-dicarboxylic acid (3)



3.74 mmol (1.60 g) of **2** were dissolved in 20.00 ml of MeOH. In another flask, KOH (15.00 mmol, 0.84 g) were dissolved in a MeOH/water (10.00 ml/30.00 ml) mixture and then added to the former solution. The reaction mixture was refluxed for 5h. After stripping the methanol, water (10.00 ml) was added to the flask and the solution was acidified with a 10% HCl solution until pH 1.0. The resulting precipitate white was filtered and washed with water until pH 7.0 (yield: 1.20 g, 80 %).

¹H NMR (600 MHz, (CD₃)₂SO): δ 8.21 (s, 2H, H3), 8.02 (d, *J* = 7.8 Hz, 2H, H5), 7.48 (d, *J* = 7.8 Hz, 2H, H6) ppm.

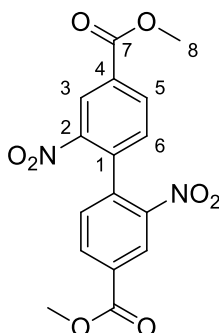
¹³C NMR (151 MHz, (CD₃)₂SO): δ 165.8 (C7), 145.0 (C1), 133.0 (C3), 132.8 (C4), 131.3 (C6), 128.7 (C5), 122.6 (C2) ppm.

IR (ATR, cm⁻¹): ν 3068, 2972, 1685, 1047, 898.

Elemental analysis: C₁₄H₈Br₂O₈ (400.02 g/mol)

Calculated	:	C: 42.04 %	H: 2.02 %
Found	:	C: 42.18 %	H: 2.19 %

5.3.3 Synthesis of Dimethyl-2,2'-dinitro-(1,1'-biphenyl)-4,4'-dicarboxylate (4)



5.00 ml of HNO_3 and 7.00 ml of H_2SO_4 were mixed and in a flask in a water-ice bath to keep the temperature of the solution between 5-10 °C. 25.00 mmol (6.76 g) of dimethyl-(1,1'-biphenyl)-4,4'-dicarboxylate (**1**) were added in small portions and the mixture was stirred over night to yield a yellow-orange solution. The solution was poured onto ice-water. The resulting precipitate was filtered off and washed with water. Recrystallisation from methanol yielded a pale yellow solid (yield: 6.64 g, 98 %).

^1H NMR (600 MHz, $(\text{CD}_3)_2\text{SO}$): δ 8.69 (d, J = 1.2 Hz, 2H, H3), 8.37 (dd, J = 8.0 Hz, 1.2 Hz, 2 H, H5), 7.71 (d, J = 8.0 Hz, 2 H, H6), 3.96 (s, 6H, H8) ppm.

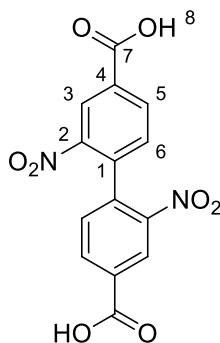
^{13}C NMR (151 MHz, $(\text{CD}_3)_2\text{SO}$): δ 164.2 (C7), 146.6 (C2), 137.0 (C4), 134.1 (C5), 132.0 (C1), 131.2 (C6), 125.0 (C3), 53.0 (C8) ppm.

IR (ATR, cm^{-1}): ν 3094, 2957, 1722, 1343, 1286.

Elemental analysis: $\text{C}_{16}\text{H}_{12}\text{N}_2\text{O}_8$ (360.28 g/mol)

Calculated	:	C: 53.34 %	H: 3.36 %	N: 7.78 %
Found	:	C: 53.39 %	H: 3.49 %	N: 7.49 %

5.3.4 Synthesis of 2,2'-Dinitro-(1,1'-biphenyl)-4,4'-dicarboxylic acid (5)



8.33 mmol (3.00 g) of **4** were dissolved in 30.00 ml of methanol. In another flask, KOH (33.31 mmol, 1.87 g) was dissolved in a MeOH/water (10.00 ml/40 ml) mixture and added to the former solution. The reaction mixture was refluxed for 5h. After stripping the methanol, water (10.00 ml) was added to the flask and the solution was acidified with a 10.00 % HCl solution until pH 1.0. The resulting light yellow precipitate was filtered and washed with water until pH 7.0 (yield: 2.35 g, 83%).

¹H NMR (400 MHz, (CD₃)₂SO): δ 13.84 (s, 2H, H8), 8.67 (s, 2H, H3), 8.35 (d, *J* = 8.0 Hz, 2H, H5), 7.68 (d, *J* = 8.0 Hz, 2H, H6) ppm.

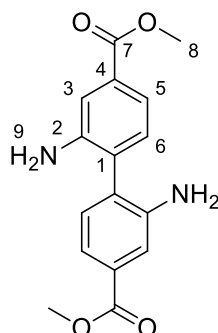
¹³C NMR (101 MHz, (CD₃)₂SO): δ 165.3 (C7), 146.7 (C2), 136.7 (C4), 134.3 (C5), 132.5 (C1), 131.9 (C6), 125.1 (C3) ppm.

IR (ATR, cm⁻¹): ν 3064, 2958, 1692, 1616, 1529, 929.

Elemental analysis: C₁₄H₈N₂O₈ (332.22 g/mol)

Calculated	:	C: 50.61 %	H: 2.43 %	N: 8.43 %
Found	:	C: 50.64 %	H: 2.42 %	N: 8.26 %

5.3.5 Synthesis of Dimethyl-2,2'-diamino-(1,1'-biphenyl)-4,4'-dicarboxylate (6)



13.89 mmol (5.00 g) of **4** were dissolved in 300.00 ml of freshly distilled methanol. 1.50 g of Pd (10% wt.)/C were added to the reaction medium under nitrogen with continuous stirring. After stirring for 5 min, 175.95 mmol (11.09 g) of NH_4HCO_2 were added under nitrogen. The reaction mixture was heated to reflux for 4 h. The resulting suspension was filtered over celite®. Methanol was stripped and a yellowish solid was obtained which was extracted with dichloromethane and water. The organic phase was dried over Na_2SO_4 . After stripping the solvent, recrystallisation of the yellow solid from methanol yielded 3.50 g (84 %) of **6**.

^1H NMR (400 MHz, $(\text{CD}_3)_2\text{SO}$): δ 7.44 (d, J = 1.2 Hz, 2H, H3), 7.23 (dd, J = 8.0 Hz, 1.2 Hz, 2H, H5), 7.08 (d, J = 8.0 Hz, 2H, H6), 5.00 (s, 4H, H9), 3.83 (s, 6H, H8) ppm.

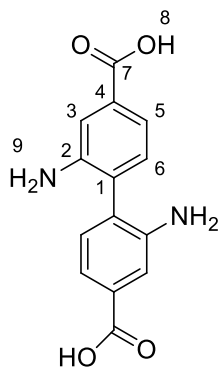
^{13}C NMR (101 MHz, $(\text{CD}_3)_2\text{SO}$): δ 166.6 (C7), 145.6 (C2), 130.8 (C6), 129.7 (C4), 127.6 (C1), 117.2 (C5), 115.8 (C3), 51.9 (C8) ppm.

IR (ATR, cm^{-1}): ν 3449, 3358, 3002, 2951, 1696, 1235.

Elemental analysis: $\text{C}_{16}\text{H}_{16}\text{N}_2\text{O}_4$ (300.31 g/mol)

Calculated	:	C: 63.99 %	H: 5.37 %	N: 9.33 %
Found	:	C: 63.95 %	H: 5.33 %	N: 9.40 %

5.3.6 Synthesis of 2,2'-Diamino-(1,1'-biphenyl)-4,4'-dicarboxylic acid (7)



Method A: 3.33 mmol (1.00 g) of **6** were dissolved in 10.00 ml of methanol. In another flask, KOH (13.32 mmol, 0.75 g) was dissolved in a MeOH/water (10.00 ml/20.00 ml) mixture and added to the former solution. The reaction mixture was refluxed for 5h. After stripping the methanol, water (10.00 ml) was added to the flask and the solution was acidified with acetic acid until pH 1.0. The resulting precipitate was filtered and washed with water until pH 7.0 (yield: 0.80 g, 78 %).

¹H NMR (400 MHz, (CD₃)₂SO): δ 7.71 (s, 2H, H3), 7.52 (d, *J* = 8.0 Hz, 2H, H5), 7.29 (d, *J* = 8.0 Hz, 2H, H6) ppm.

¹³C NMR (101 MHz, (CD₃)₂SO): δ 167.1 (C7), 140.3 (C2), 131.4 (C6), 131.3 (C4), 130.1 (C1), 121.7 (C5), 119.7 (C3) ppm.

IR (ATR, cm⁻¹): ν 3434, 3398, 3077, 1687, 1619, 932.

Elemental analysis: C₁₄H₁₂N₂O₄ (272.26 g/mol)

Calculated	:	C: 61.76 %	H: 4.44 %	N: 10.29 %
Found	:	C: 61.67 %	H: 4.68 %	N: 10.28 %

Method B: 2.78 mmol (1.00 g) of **4** were suspended in 30.00 ml of HCl (37 % v/v) solution containing 14 mmol (3.20 g) SnCl₂·2H₂O. The solution was stirred for 3 days at room temperature. The resulting pale yellow solution was poured onto an ice-water mixture. The carboxylic acid precipitation was filtered off and washed with water (yield: 0.76 g, 68 %).

¹H NMR (400 MHz, (CD₃)₂SO): δ 7.76 (s, 2H, H3), 7.60 (d, *J* = 7.6 Hz, 2H, H5), 7.34 (d, *J* = 7.6 Hz, 2H, H6) ppm.

^{13}C NMR (101 MHz, $(\text{CD}_3)_2\text{SO}$): δ 167.2 (C7), 139.2 (C1), 131.8 (C4), 131.7 (C6), 131.0 (C2), 123.0 (C3), 120.6 (C5) ppm.

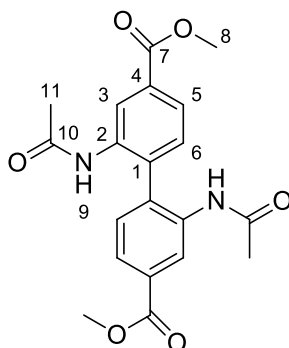
IR (ATR, cm^{-1}): ν 3312, 3077, 1698, 1622, 933.

Elemental analysis: $\text{C}_{14}\text{H}_{12}\text{N}_2\text{O}_4 \cdot \text{HCl}$ (308.72 g/mol)

Calculated : C: 54.47 % H: 4.24 % N: 9.07 %

Found : C: 54.27 % H: 4.60 % N: 8.97 %

5.3.7 Synthesis of Dimethyl-2,2'-diacetamido-(1,1'-biphenyl)-4,4'-dicarboxylate (**8**)



5.59 mmol (1.68 g) of **6** were dissolved in 30 ml chloroform. 56.00 mmol (5.72 g) of acetic anhydride were added to the solution. The reaction mixture was heated to reflux for 6 h. Chloroform was stripped off and the obtained solid was extracted with dichloromethane. The organic phase was washed with aqueous ammonia (5.00 %) and then dried over Na_2SO_4 . After stripping the solvent, recrystallisation of the yellow solid from methanol yielded 1.87 g (87%) of **8**.

^1H NMR (400 MHz, $(\text{CD}_3)_2\text{SO}$): δ 9.04 (s, 2H, H9), 8.26 (s, 2H, H3), 7.82 (d, J = 8.0 Hz, 2H, H5), 7.35 (d, J = 8.0 Hz, 2H, H6), 3.88 (s, 6H, H8), 1.85 (s, 6H, H11) ppm.

^{13}C NMR (101 MHz, $(\text{CD}_3)_2\text{SO}$): δ 168.9 (C10), 165.9 (C7), 136.2 (C41), 136.0 (C1), 131.3 (C6), 129.5 (C2), 126.5 (C3), 125.5 (C5), 52.3 (C8), 23.1 (C11) ppm.

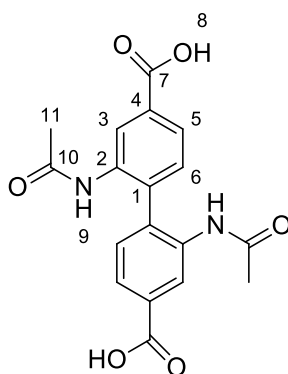
IR (ATR, cm^{-1}): ν 3345, 3006, 2955, 1691, 1250, 760.

Elemental analysis: C₂₀H₂₀N₂O₆ (384.38 g/mol)

Calculated : C: 62.49 % H: 5.24 % N: 7.29 %

Found : C: 62.33 % H: 5.38 % N: 7.28 %

5.3.8 Synthesis of 2,2'-Diacetamido-(1,1'-biphenyl)-4,4'-dicarboxylic acid (**9**)



5.58 mmol (2.30 g) of **8** were dissolved in 30 ml of methanol. In another flask, KOH (22.31 mmol, 1.25 g) was dissolved in a MeOH/water (10 ml/40 ml) mixture and added to the former solution. The reaction mixture was stirred over night at room temperature. After stripping the methanol, water (20 ml) was added to the flask and the solution was acidified with 10.00 % HCl solution until pH 1.0. The resulting precipitate light yellow was filtered off and washed with water until pH 7.0 (yield: 1.75 g, 81 %).

¹H NMR (400 MHz, (CD₃)₂SO): δ 8.99 (s, 2H, H₉), 8.22 (s, 2H, H₃), 7.80 (dd, *J* = 8.0 Hz, 1.6 Hz, 2H, H₅), 7.31 (d, *J* = 8.0 Hz, 2H, H₆), 1.84 (s, 6H, H₁₁) ppm.

¹³C NMR (101 MHz, (CD₃)₂SO): δ 168.9 (C₁₀), 167.0 (C₇), 136.0 (C₄), 135.9 (C₁), 131.1 (C₆), 130.7 (C₂), 126.3 (C₃), 125.7 (C₅), 23.1 (C₁₁) ppm.

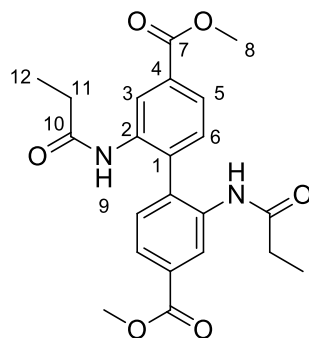
IR (ATR, cm⁻¹): ν 3303, 3007, 1698, 1665, 1534, 763.

Elemental analysis: C₁₈H₁₆N₂O₆ (356.33 g/mol)

Calculated : C: 60.67 % H: 4.53 % N: 7.86 %

Found : C: 59.40 % H: 4.80 % N: 7.32 %

5.3.9 Synthesis of Dimethyl-2,2'-dipropionamido-(1,1'-biphenyl)-4,4'-dicarboxylate (**10**)



8.32 mmol (2.50 g) of **6** were dissolved in 40 ml chloroform. 50 mmol (6.50 g) of propanoic anhydride were added to the solution. The reaction mixture was heated to reflux for 6 h. Chloroform was removed and the obtained solid was extracted with dichloromethane. The organic phase was washed with aqueous ammonia (5.00 %) and then dried over Na_2SO_4 . After stripping the solvent, recrystallisation of the yellow solid from methanol yielded 1.87 g (87 %) of **10**.

^1H NMR (400 MHz, $(\text{CD}_3)_2\text{SO}$): δ 8.90 (s, 2H, H9), 8.29 (d, J = 1.8 Hz, 2H, H3), 7.81 (dd, J = 8.0 Hz, 1.8 Hz, 2H, H5), 7.33 (d, J = 8.0 Hz, 2H, H6), 3.88 (s, 6H, H8), 2.15-2.08 (m, 4H, H11), 0.92 (t, J = 8.0 Hz, 6H, H12) ppm.

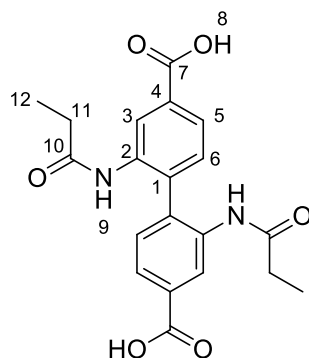
^{13}C NMR (101 MHz, $(\text{CD}_3)_2\text{SO}$): δ 172.5 (C10), 166.0 (C7), 136.2 (C4), 136.1 (C1), 131.2 (C6), 129.6 (C2), 125.8 (C3), 125.4 (C5), 52.3 (C8), 28.7 (C11), 9.3 (C12) ppm.

IR (ATR, cm^{-1}): ν 3280, 2952, 1717, 1662, 1532, 1266, 755.

Elemental analysis: $\text{C}_{22}\text{H}_{24}\text{N}_2\text{O}_6$ (412.44 g/mol)

Calculated	:	C: 64.07 %	H: 5.87 %	N: 6.79 %
Found	:	C: 63.31 %	H: 6.01 %	N: 6.73 %

5.3.10 Synthesis of 2,2'-Dipropionamido-(1,1'-biphenyl)-4,4'-dicarboxylic acid (**11**)



7.03 mmol (2.90 g) of **10** were dissolved in 30.00 ml of methanol. In another flask, KOH (28.00 mmol, 1.58 g) was dissolved in a MeOH/water (10.00 ml/40.00 ml) mixture and added to the former solution. The reaction mixture was stirred over night at room temperature. After stripping the methanol, water (20 ml) was added to the flask and the solution was acidified with a 10.00 % HCl solution until pH 1.0. The resulting precipitate was filtered off and washed with water until pH 7.0 (yield: 2.70 g, 79 %).

¹H NMR (400 MHz, (CD₃)₂SO): δ 13.09 (s, 2H, H8), 8.80 (s, 2H, H9), 8.24 (s, 2H, H3), 7.79 (d, *J* = 8.0 Hz, 2H, H5), 7.29 (d, *J* = 8.0 Hz, 2H, H6), 2.14 – 2.07 (m, 4H, H11), 0.91 (t, *J* = 8.0 Hz, 6H, H12) ppm.

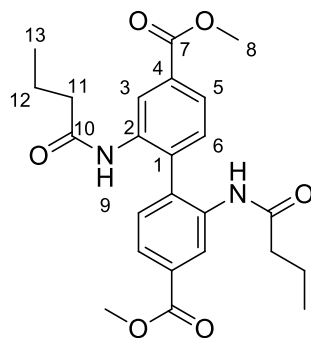
¹³C NMR (101 MHz, (CD₃)₂SO): δ 172.5 (C10), 167.0 (C7), 136.2 (C4), 135.9 (C1), 131.0 (C6), 130.9 (C2), 126.2 (C3), 125.7 (C5), 28.7 (C11), 9.4 (C12) ppm.

IR (ATR, cm⁻¹): ν 3328, 2980, 1662, 1532, 1232, 768.

Elemental analysis for C₂₀H₂₀N₂O₆:

Calculated	:	C: 62.49 %	H: 5.24 %	N: 7.29 %
Found	:	C: 63.31 %	H: 6.01 %	N: 6.73 %

5.3.11 Synthesis of Dimethyl-2,2'-dibutyramido-(1,1'-biphenyl)-4,4'-dicarboxylate (**12**)



10.00 mmol (3.16 g) of **6** were dissolved in 50 ml CHCl_3 . 82.50 mmol (13.05 g) of butyric anhydride were added to the solution. The reaction mixture was heated to reflux for 6 h. CHCl_3 was stripped off and the obtained solid was extracted with dichloromethane. The organic phase was washed with aqueous ammonia (5.00 %) and then dried over Na_2SO_4 . After stripping the solvent, recrystallisation of the yellowish solid from methanol yielded 3.69 g (90 %) of **12**.

^1H NMR (600 MHz, $(\text{CD}_3)_2\text{SO}$): δ 8.93 (s, 2H, H9), 8.26 (d, J = 1.8 Hz, 2H, H3), 7.81 (dd, J = 8.0 Hz, 1.8 Hz, 2H, H5), 7.30 (d, J = 8.0 Hz, 2H, H6), 3.88 (s, 6H, H8), 2.11 – 2.06 (m, H11), 1.48 – 1.41 (m, 2H, H12), 0.77 (t, 6H, J = 7.4 Hz, H13) ppm.

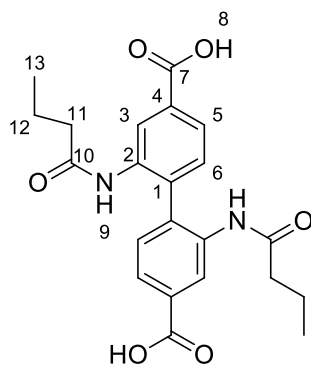
^{13}C NMR (151 MHz, $(\text{CD}_3)_2\text{SO}$): δ 171.7 (C10), 165.9 (C7), 136.5 (C4), 136.1 (C1), 131.0 (C6), 129.6 (C2), 125.9 (C3), 125.5 (C5), 52.3 (C8), 37.4 (C11), 18.3 (C12), 13.5 (C13) ppm.

IR (ATR, cm^{-1}): ν 3279, 2962, 1721, 1664, 1526, 1289, 763.

Elemental analysis: $\text{C}_{24}\text{H}_{28}\text{N}_2\text{O}_6$ (440.49 g/mol)

Calculated	:	C: 65.44 %	H: 6.41 %	N: 6.36 %
Found	:	C: 64.80 %	H: 6.51 %	N: 6.36 %

5.3.12 Synthesis of 2,2'-Dibutyramido-(1,1'-biphenyl)-4,4'-dicarboxylic acid (**13**)



6.81 mmol (3.00 g) of **12** were dissolved in 30.00 ml of methanol. In another flask, KOH (27.24 mmol, 1.53 g) was dissolved in a MeOH/water (10.00 ml/40.00 ml) mixture and added to the former solution. The reaction mixture was stirred over night at room temperature. After stripping the methanol, water (20.00 ml) was added to the flask and the solution was acidified with a 10.00 % HCl solution until pH 1.0. The resulting precipitate was filtered off and washed with water until pH 7.0 (yield: 2.81 g, 84 %).

¹H NMR (400 MHz, (CD₃)₂SO): δ 13.11 (s, 2H, H8), 8.90 (s, 2H, H9), 8.22 (s, 2H, H3), 7.79 (dd, *J* = 7.8, 1.6 Hz, 2H, H5), 7.27 (d, *J* = 8.0 Hz, 2H, H6), 2.10 – 2.06 (m, 4H, H11), δ 1.48 – 1.39 (m, 4H, H12), 0.77 (t, *J* = 7.4 Hz, 6H, H13) ppm.

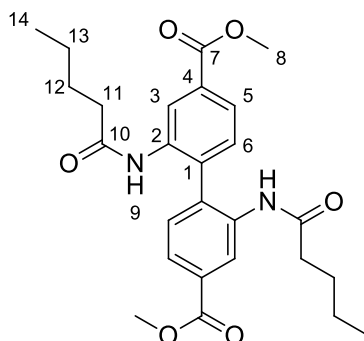
¹³C NMR (101 MHz, (CD₃)₂SO): δ 171.7 (C10), 167.0 (C7), 136.5 (C4), 136.0 (C1), 130.8 (C6), 130.8 (C2), 126.3 (C3), 125.7 (C5), 37.5 (C11), 18.3 (C12), 13.5 (C13) ppm.

IR (ATR, cm⁻¹): ν 3300, 2961, 1707, 1643, 1527, 1187.

Elemental analysis: C₂₂H₂₄N₂O₆ (412.44 g/mol)

Calculated	:	C: 64.07 %	H: 5.87 %	N: 6.79 %
Found	:	C: 64.22 %	H: 6.48 %	N: 6.36 %

5.3.13 Synthesis of Dimethyl-2,2'-dipentanamido-(1,1'-biphenyl)-4,4'-dicarboxylate (**14**)



11.00 mmol (3.42 g) of **6** were dissolved in 40 ml CHCl_3 . 68.00 mmol (12.73 g) of pentanoic anhydride were added to the solution. The reaction mixture was heated to reflux for 6h. CHCl_3 was stripped off and the obtained solid was extracted with dichloromethane. The organic phase was washed with aqueous ammonia (5.00 %) and then dried over Na_2SO_4 . After stripping the solvent, recrystallisation of the yellowish solid from methanol yielded 4.35 g (84 %) of **14**.

^1H NMR (600 MHz, $(\text{CD}_3)_2\text{SO}$): δ 8.92 (s, 2H, H9), 8.24 (d, J = 1.8 Hz, 2H, H3), 7.81 (dd, J = 8.0 Hz, 1.8 Hz, 2H, H5), 7.30 (d, J = 8.0 Hz, 2H, H6), 3.88 (s, 6H, H8), 2.14 – 2.07 (m, 4H, H11), 1.40 – 1.37 (m, 4H, H12), 1.17 – 1.11 (m, 4H, H13), 0.78 (t, 6H, J = 7.8 Hz, H14) ppm.

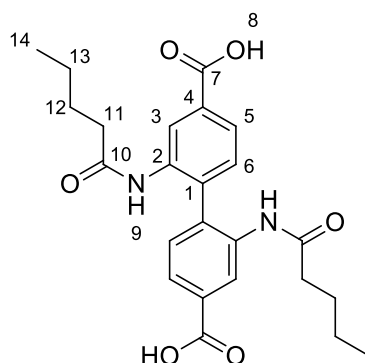
^{13}C NMR (151 MHz, $(\text{CD}_3)_2\text{SO}$): δ 171.8 (C10), 165.9 (C7), 136.7 (C4), 136.1 (C1), 131.0 (C6), 129.6 (C2), 126.0 (C3), 125.5 (C5), 52.3 (C8), 35.2 (C11), 26.9 (C12), 21.6 (C13), 13.7 (C14) ppm.

IR (ATR, cm^{-1}): ν 3284, 2954, 2874, 1723, 1663, 1292, 754.

Elemental analysis: $\text{C}_{26}\text{H}_{32}\text{N}_2\text{O}_6$ (468.54 g/mol)

Calculated	:	C: 66.65 %	H: 6.88 %	N: 5.98 %
Found	:	C: 66.21 %	H: 6.80 %	N: 5.94 %

5.3.14 Synthesis of 2,2'-Dipentanamido-(1,1'-biphenyl)-4,4'-dicarboxylic acid (15)



2.13 mmol (1.00 g) of **14** were dissolved in 10.00 ml of methanol. In another flask, KOH (8.54 mmol, 0.48 g) was dissolved in a MeOH/water (10.00 ml/20.00 ml) mixture and added to the former solution. The reaction mixture was stirred over night at room temperature. After stripping the methanol, water (10.00 ml) was added to the flask and the solution was acidified with a 10.00 % HCl solution until pH 1.0. The resulting precipitate was filtered off and washed with water until pH 7.0 (yield: 0.75 g, 85 %).

¹H NMR (400 MHz, (CD₃)₂SO): δ 13.09 (s, 2H, H8), 8.90 (s, 2H, H9), 8.19 (s, 2H, H3), 8.19 (dd, *J* = 8.0 Hz, 1.6 Hz, 2H, H5), 7.26 (d, *J* = 8.0 Hz, 2H, H6), 2.12 – 2.08 (m, 4H, H11), 1.41 – 1.35 (m, 4H, H12), 1.17 – 1.08 (m, 4H, H13), 0.78 (t, 6H, *J* = 7.6 Hz, H14) ppm.

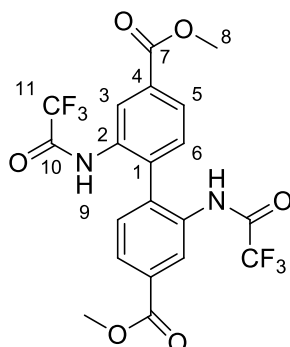
¹³C NMR (101 MHz, (CD₃)₂SO): δ 171.8 (C10), 167.0 (C7), 136.7 (C4), 136.0 (C1), 130.8 (C6), 130.8 (C2), 126.4 (C3), 125.8 (C5), 35.2 (C11), 27.0 (C12), 21.6 (C13), 13.7 (C14) ppm.

IR (ATR, cm⁻¹): ν 3345, 3199, 2956, 2964, 1717, 1657, 1235, 769.

Elemental analysis: C₂₄H₂₈N₂O₆ (440.49 g/mol)

Calculated	:	C: 65.44 %	H: 6.41 %	N: 6.36 %
Found	:	C: 63.25 %	H: 5.88 %	N: 6.71 %

5.3.15 Synthesis of Dimethyl-2,2'-bis(2,2,2-trifluoroacetamido)-(1,1'-biphenyl)-4,4'-dicarboxylate (16)



10.00 mmol (3.00 g) of **6** were dissolved in 50 ml CHCl_3 . 80.00 mmol (16.78 g) of trifluoroacetic anhydride were added to the solution. The reaction mixture was heated to reflux for 6 h. CHCl_3 was stripped off and the obtained solid was extracted with dichloromethane. The organic phase was washed with aqueous ammonia (5.00 %) and then dried over Na_2SO_4 . After stripping the solvent, a yellowish solid was obtained (yield: 3.61 g, 94 %).

^1H NMR (400 MHz, $(\text{CD}_3)_2\text{SO}$): δ 10.69 (s, 2H, H9), 8.10 (d, $J = 1.4$ Hz, 2H, H3), 8.00 (dd, $J = 8.0$ Hz, 1.4 Hz, 2H, H5), 7.47 (d, $J = 8.0$ Hz, 2H, H6), 3.90 (s, 6H, H8) ppm.

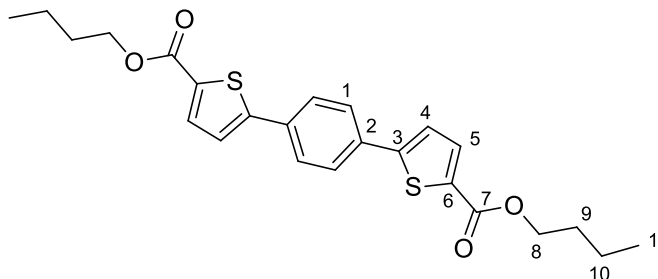
^{13}C NMR (101 MHz, $(\text{CD}_3)_2\text{SO}$): δ 165.4 (C7), 155.4 (d, $^2J_{\text{FC}} = 77.0$ Hz, C10), 138.4 (C2), 133.1 (C4), 131.6 (C1), 130.4 (C6), 127.8 (C3), 127.2 (C5), 115.7 (d, $^1J_{\text{FC}} = 288.4$ Hz, C11), 52.5 (C8) ppm.

IR (ATR, cm^{-1}): ν 3300, 3028, 2960, 1706, 1533, 1438, 1150.

Elemental analysis: $\text{C}_{20}\text{H}_{14}\text{F}_6\text{N}_2\text{O}_6$ (492.33 g/mol)

Calculated	:	C: 46.57 %	H: 2.17 %	N: 6.03 %
Found	:	C: 49.45 %	H: 3.35 %	N: 5.83 %

5.3.16 Synthesis of Dibutyl-5,5'-(1,4-phenylene)bis(thiophene-2-carboxylate) (**20**)



1,4-Bis(5-iodothiophen-2-yl)benzene (**17**) (1.00 g, 2.02 mmol) was suspended in anhydrous DMF (10.00 ml) under a nitrogen atmosphere. PPh_3 (0.05 g, 0.17 mmol), anhydrous *n*-butanol (10.00 ml) and Et_3N (1.50 ml) were added to the mixture. After adding $\text{Pd}(\text{OAc})_2$ (0.01 g, 0.06 mmol) the autoclave was closed and pressurized with 15 bar of CO until. The reaction was stirred at 100 °C for 30 h. After releasing the CO pressure, the reaction mixture was filtered over celite®. Water was added to the filtrate to precipitate the product. The resulting crystals were collected by filtration (yield 0.72 g, 81 %).

^1H NMR (400 MHz, CDCl_3): δ 7.76 (d, J = 4.0 Hz, 2H, H5), 7.65 (s, 4H, H1), 7.31 (d, J = 4.0 Hz, 2H, H4), 4.31 (t, J = 6.8 Hz, 4H, H8), 1.78 – 1.71 (m, 4H, H9), 1.52 – 1.43 (m, 4H, H10), 0.98 (t, J = 7.2 Hz, 6H, H11) ppm.

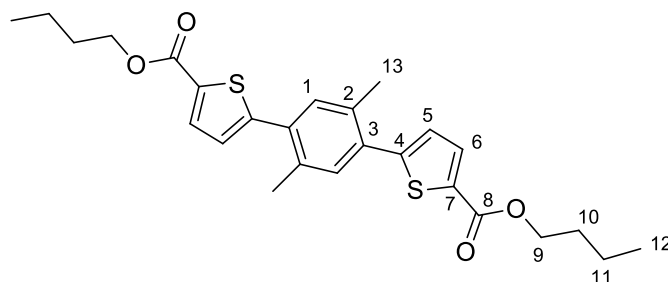
^{13}C NMR (101 MHz, CDCl_3): δ 162.3 (C7), 150.0 (C3), 134.3 (C5), 133.8 (C6), 133.1 (C2), 126.8 (C1), 124.0 (C4), 65.2 (C8), 31.0 (C9), 19.3 (C10), 13.4 (C11) ppm.

IR (ATR, cm^{-1}): ν 2960, 2934, 2875, 1689, 1478, 1441.

Elemental analysis: $\text{C}_{24}\text{H}_{26}\text{O}_4\text{S}_2$ (442.59 g/mol)

Calculated	:	C: 65.13 %	H: 5.92 %	S: 14.49 %
Found	:	C: 64.87 %	H: 5.67 %	S: 14.79 %

5.3.17 Synthesis of Dibutyl-5,5'-(2,5-dimethyl-1,4-phenylene)bis(thiophene-2-carboxylate) (21)



5,5'-(2,5-Dimethyl-1,4-phenylene)bis(2-iodothiophene) (**18**) (3.00 g, 5.74 mmol) was suspended in anhydrous DMF (30.00 ml) under a nitrogen atmosphere. PPh_3 (0.10 g, 0.40 mmol), anhydrous *n*-butanol (30.00 ml) and Et_3N (3.00 ml) were added to the mixture. After adding $\text{Pd}(\text{OAc})_2$ (0.03 g, 0.13 mmol) the autoclave was closed and pressurized with 15 bar of CO. The reaction was stirred at 100 °C for 30 h. The reaction mixture was filtered over celite. Water was added to the filtrate to precipitate the product. The resulting crystals were collected by filtration (yield: 2.20 g, 81 %).

^1H NMR (400 MHz, CDCl_3): δ 7.78 (d, J = 3.7 Hz, 2H, H6), 7.34 (s, 2H, H1), 7.09 (d, J = 3.7 Hz, 2H, H5), 4.32 (t, J = 6.6 Hz, 4H, H9), 2.43 (s, 6H, H13), 1.78 – 1.71 (m, 4H, H10), 1.52 – 1.43 (m, 4H, H11), 0.98 (t, J = 7.4 Hz, 6H, H12) ppm.

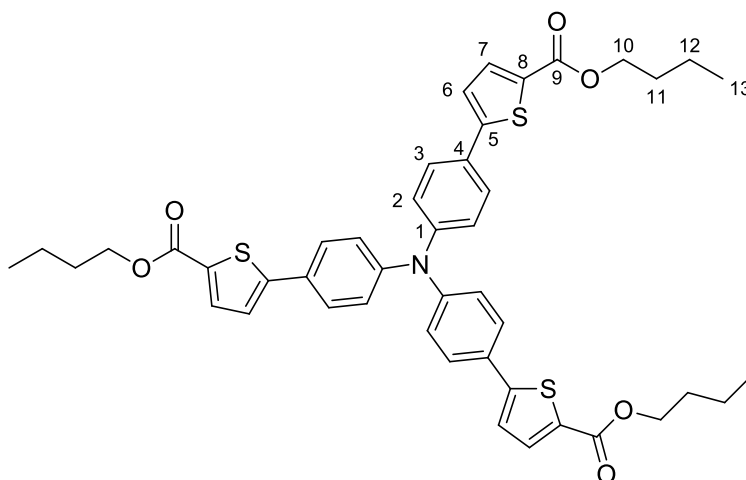
^{13}C NMR (101 MHz, CDCl_3): δ 162.5 (C8), 149.5 (C4), 133.8, 133.6, 133.6 (C7, C3, C2), 133.5 (C6), 132.9 (C1), 127.4 (C5) 65.2 (C9), 30.9 (C10), 20.7 (C13), 19.3 (C11), 13.9 (C12) ppm.

IR (ATR, cm^{-1}): ν 2959, 2935, 2873, 1697, 1541, 1506, 1450, 1327, 1318, 1254, 1231, 1092.

Elemental analysis: $\text{C}_{26}\text{H}_{30}\text{O}_4\text{S}_2$ (470.64 g/mol)

Calculated	:	C: 66.35 %	H: 6.42 %	S: 13.63 %
Found	:	C: 66.28 %	H: 6.45 %	S: 13.89 %

5.3.18 Synthesis of Tributyl 5,5',5''-(nitrilotris(benzene-4,1-diyl))tris(thiophene-2-carboxylate) (22)



Tris (4-(5-iodothiophen-2-yl)phenyl)amine (**19**) (2.00 g, 2.30 mmol) was suspended in anhydrous DMF (30.00 ml) under a nitrogen atmosphere. PPh_3 (0.10 g, 0.35 mmol), anhydrous *n*-butanol (30.00 ml) and Et_3N (3.00 ml) were added to the mixture. After adding $\text{Pd}(\text{OAc})_2$ (0.02 g, 0.12 mmol) the autoclave was closed and pressurized with 15 bar of CO until. The reaction was stirred at 100 °C for 30 h. The reaction mixture was filtered over celite. Water was added to the filtrate to precipitate the product. The resulting crystals were collected by filtration (yield: 1.50 g, 82 %).

^1H NMR (400 MHz, CDCl_3): δ 7.75 (d, J = 3.9 Hz, 3H, H7), 7.56 (d, J = 8.6 Hz, 6H, H2), 7.23 (d, J = 3.9 Hz, 3H, H6), 7.16 (d, J = 8.6 Hz, 6H, H3), 4.31 (t, J = 6.6 Hz, 6H, H10), 1.78 – 1.71 (m, 6H, H11), 1.52 – 1.43 (m, 6H, H12), 0.98 (t, J = 7.4 Hz, 9H, H13) ppm.

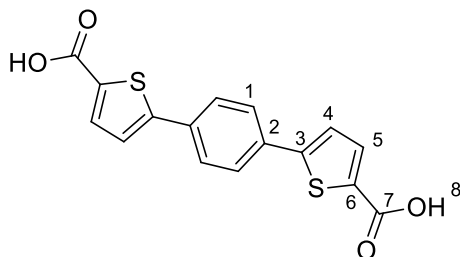
^{13}C NMR (101 MHz, CDCl_3): δ 162.5 (C9), 150.7 (C5), 147.3 (C1), 134.4 (C7), 132.1 (C8), 128.8 (C4), 127.4 (C3), 124.7 (C2), 123.2 (C6), 65.2 (C10), 30.9 (C11), 19.4 (C12), 13.9 (C13) ppm.

IR (ATR, cm^{-1}): ν 2959, 2934, 2873, 1698, 1443, 1261, 1090, 745, 660.

Elemental analysis: $\text{C}_{45}\text{H}_{45}\text{NO}_6\text{S}_3$ (792.04 g/mol)

Calculated	:	C: 68.24 %	H: 5.73 %	N: 1.77 %	S: 12.15 %
Found	:	C: 68.14 %	H: 5.67 %	N: 1.74 %	S: 12.34 %

5.3.19 Synthesis of 5,5'-(1,4-Phenylene)bis(thiophene-2-carboxylic acid) (23)



20 (0.70 g, 1.58 mmol) was dissolved in 50.00 ml of a EtOH/water (1:1) mixture. KOH (0.20 g, 3.62 mmol) was added to the solution which then was refluxed for 5 h. After cooling to room temperature, EtOH was stripped. The remaining solution was acidified with HCl (10.00 %), the resulting precipitate was filtered and washed with water and CHCl_3 (yield: 0.50 g, 96 %).

^1H NMR (400 MHz, $(\text{CD}_3)_2\text{SO}$): δ 7.82 (s, 4H, H1), 7.74 (d, J = 3.6 Hz, 2H, H5), 7.65 (d, J = 3.6 Hz, 2H, H4) ppm.

^{13}C NMR (101 MHz, $(\text{CD}_3)_2\text{SO}$): δ 162.8 (C7), 148.8 (C3), 134.4 (C5), 133.8 (C6), 133.1 (C2), 126.6 (C1), 125.1 (C4) ppm.

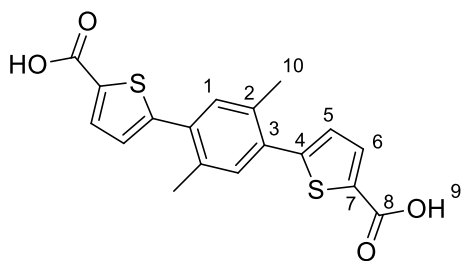
IR (ATR, cm^{-1}): ν 2972, 1659, 1446, 1267, 1235, 800, 672.

Elemental analysis: $\text{C}_{16}\text{H}_{10}\text{O}_4\text{S}_2$ (330.38 g/mol)

Calculated : C: 58.17 % H: 3.05 % S: 19.41 %

Found : C: 56.06 % H: 3.21 % S: 18.23 %

5.3.20 Synthesis of 5,5'-(2,5-Dimethyl-1,4-phenylene)bis(thiophene-2-carboxylic acid) (24)



21 (2.13 g, 4.53 mmol) was dissolved in a 100.00 ml EtOH/water (1:1) mixture. KOH (5.08 g, 91.00 mmol) was added to the solution which then was refluxed for 5 h. After cooling to

room temperature, EtOH was stripped off. The remaining solution was acidified with HCl (10.00 %), the resulting precipitate was filtered and washed with water and CHCl_3 (yield: 1.59 g, 98 %).

^1H NMR (400 MHz, $(\text{CD}_3)_2\text{SO}$): δ 7.74 (d, J = 3.8 Hz, 2H, H6), 7.43 (s, 2H, H1), 7.30 (d, J = 3.8 Hz, 2H, H5), 2.40 (s, 6H, H10) ppm.

^{13}C NMR (101 MHz, $(\text{CD}_3)_2\text{SO}$): δ 162.8 (C8), 148.2 (C4), 134.2 (C7), 133.5 (C6), 133.4 (C2), 132.9 (C3), 132.4 (C1), 128.1 (C5), 20.2 (C10) ppm.

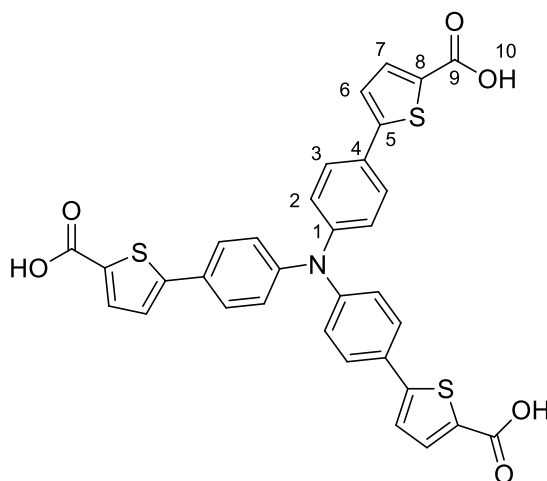
IR (ATR, cm^{-1}): ν 2956, 2923, 2859, 2654, 2536, 1655, 1537, 1501, 1450, 1315, 1275, 1237, 1114.

Elemental analysis: $\text{C}_{18}\text{H}_{14}\text{O}_4\text{S}_2$ (358.43 g/mol)

Calculated : C: 60.32 % H: 3.94 % S: 17.89 %

Found : C: 60.27 % H: 4.18 % S: 17.63 %

5.3.21 Synthesis of 5,5',5''-(Nitrilotris(benzene-4,1-diyl))tris(thiophene-2-carboxylic acid) (25)



22 (1.00 g, 1.26 mmol) was dissolved in 100 ml of a water/EtOH (1:1) mixture. KOH (2.12 g, 37.87 mmol) was added to the solution which then was refluxed over night. After cooling to room temperature, EtOH was stripped off. The remaining solution was acidified with acetic acid, the resulting precipitate was filtered and washed with water and CHCl_3 (yield: 0.65 g, 82 %).

^1H NMR (400 MHz, $(\text{CD}_3)_2\text{SO}$): δ 7.69 (d, J = 8.6 Hz, 6H, H2), 7.60 (d, J = 3.8 Hz, 3H, H7), 7.44 (d, J = 3.8 Hz, 3H, H6), 7.12 (d, J = 8.6 Hz, 6H, H3) ppm.

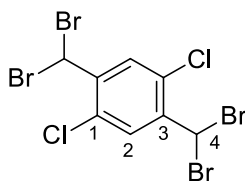
^{13}C NMR (101 MHz, $(\text{CD}_3)_2\text{SO}$): δ 163.2 (C9), 148.5 (C5), 146.6 (C1), 135.1 (C7), 133.4 (C8), 128.2 (C4), 127.2 (C3), 124.4 (C2), 123.8 (C6) ppm.

IR (ATR, cm^{-1}): ν 2958, 2541, 1658, 1533, 1441, 1263, 734.

Elemental analysis: $\text{C}_{33}\text{H}_{21}\text{NO}_6\text{S}_3$ (623.72 g/mol)

Calculated	:	C: 63.55 %	H: 3.39 %	N: 2.25 %	S: 15.42 %
Found	:	C: 61.33 %	H: 3.92 %	N: 2.14 %	S: 14.74 %

5.3.22 Synthesis of 1,4-Dichloro-2,5-bis(dibromomethyl)benzene (27)



25.0 g (0.14 mol) of $\text{C}_6\text{H}_8\text{Cl}_2$ were heated up to 120 °C in a flask connected to a condenser. Under radiation with visible light using a 350 Watt daylight lamp, the temperature was raised slowly to 180 °C over a period of 4.5h with a continuous drop wise addition of 92.0 g (4.00 mol) Br_2 . After keeping the reaction medium at 180 °C for 1.5h, the temperature was further raised to 210 °C. The reaction medium cooled down to room temperature and extracted with chloroform. Recrystallisation of the white solid from chloroform yielded 32.75 g (47 %) of **27**.

^1H NMR (600 MHz, CDCl_3): δ 7.96 (s, 2H, H2), 6.97 (s, 2H, H4) ppm.

^{13}C NMR (151 MHz, CDCl_3): δ 141.3 (C3), 131.8 (C1), 129.3 (C2), 34.4 (C4) ppm.

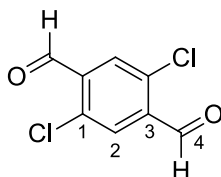
IR (ATR, cm^{-1}): ν 3016, 2922, 1468, 1369, 1154, 1078, 894, 704.

Elemental analysis: C₈H₄Br₄Cl₂ (490.64 g/mol)

Calculated : C: 19.58 % H: 0.82 %

Found : C: 18.84 % H: 1.08 %

5.3.23 Synthesis of 2,5-Dichloroterephthalaldehyde (**28**)



1.99 g (4.06 mmol) of **27** and 10.00 ml of H₂SO₄ were mixed in a flask, heated up to 125°C and stirred for 2 h under vacuum. Afterwards the suspension was stirred for additional 2.5 h at 125-130 °C. Then the reaction medium was cooled-down to room temperature and poured onto an ice-water mixture and washed with dichloromethane. The organic phase was further washed with brine. After stripping off the solvent, the obtained yellow precipitate was washed with pentane (yield: 0.45g, 54 %).

¹H NMR (600 MHz, CDCl₃): δ 10.47 (s, 2H, H₄), 8.00 (s, 2H, H₂) ppm.

¹³C NMR (151 MHz, CDCl₃): δ 188.1 (C₃), 136.4, 136.3 (C₃, C₁), 131.6 (C₂) ppm.

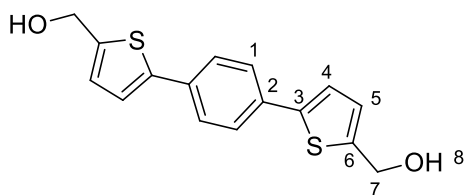
IR (ATR, cm⁻¹): ν 3082, 2917, 1684, 1357, 1154, 1078, 900, 802.

Elemental analysis: C₈H₄Cl₂O₂ (201.96 g/mol)

Calculated : C: 47.33 % H: 1.99 %

Found : C: 46.81 % H: 2.20 %

5.3.24 Synthesis of 5,5'-(1,4-Phenylene)bis(thiophene-5,2-diyl))dimethanol (**32**)



LiAlH₄ (10.20 mmol, 0.38 g) was put into a flask under a nitrogen atmosphere and 15 ml of freshly distilled THF were. In another flask 2.40 g (5.10 mmol) of **20** were dissolved in 50 ml freshly distilled THF and then added to the LiAlH₄ suspension. The reaction mixture was refluxed over night. After cooling to room temperature, water (20 ml) was added and the mixture was poured onto a 10 % HCl solution (65 ml) and which then was stirred for 5 h. The resulting yellow precipitate was filtered off, washed with CHCl₃ and dried under ambient conditions (yield: 1.43 g, 93 %).

¹H NMR (600 MHz, (CD₃)₂SO): δ 7.64 (s, 4H, H1), 7.37 (d, *J*= 6.0 Hz, 2H, H4), 6.95 (d, *J*= 6.0 Hz, 2H, H5), 4.64 (s, 4H, H7) ppm.

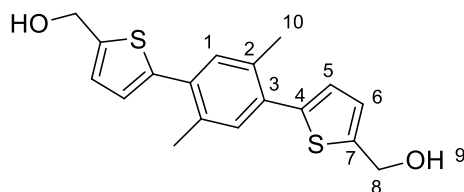
¹³C NMR (151 MHz, (CD₃)₂SO): δ 146.3 (C6), 141.6 (C3), 132.9 (C2), 125.6 (C1), 125.4 (C5), 123.2 (C4), 58.5 (C7) ppm.

IR (ATR, cm⁻¹): ν 3280, 2952, 2870, 1717, 1286, 1109, 768.

Elemental analysis: C₁₆H₁₄O₂S₂ (302.41 g/mol)

Calculated	:	C: 63.55 %	H: 4.67 %	S: 21.21 %
Found	:	C: 63.31 %	H: 4.62 %	S: 21.01 %

5.3.25 Synthesis of 5,5'-(2,5-Dimethyl-1,4-phenylene)bis(thiophene-5,2-diyl))dimethanol (33)



LiAlH₄ (11.06 mmol, 0.41 g) was put into a flask under nitrogen atmosphere and 15.00 ml of freshly distilled THF were added. In another flask 2.60 g (5.53 mmol) of **21** were dissolved in 50.00 ml of anhydrous THF and then added to the LiAlH₄ suspension. The reaction mixture was refluxed over night. After cooling to room temperature, water (20.00 ml) was added and the mixture was poured onto a 10.00 % HCl solution (65.00 ml) and stirred for 5h. Aqueous mixture was extracted with dichloromethane. After stripping off the dichloromethane, obtained oily substance washed with pentane, leading to a yellow precipitate which was filtered off and dried under ambient conditions (yield: 1.63 g, 89 %).

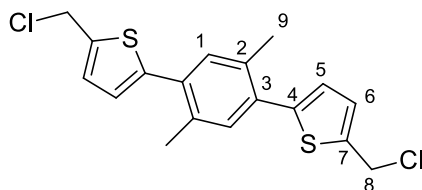
¹H NMR (400 MHz, CDCl₃): δ 7.30 (s, 2H, H1), 7.00 (d, *J* = 4.0 Hz, 2H, H5), 6.95 (d, *J* = 4.0 Hz, 2H, H6), 4.84 (s, 4H, H8), 2.41 (s, 6H, H10), 2.25 (s, 2H, H9) ppm.

¹³C NMR (101 MHz, CDCl₃): δ 143.8 (C7), 143.1 (C4), 133.6 (C2), 133.4 (C3), 132.7 (C1), 126.4 (C6), 125.8 (C5), 60.2 (C8), 20.7 (C10) ppm.

IR (ATR, cm⁻¹): ν 3264, 2922, 2861, 1002, 811, 734.

Elemental analysis: C₁₈H₁₈O₂S₂ (330.46 g/mol)

Calculated	:	C: 65.42 %	H: 5.49 %	S: 19.41 %
Found	:	C: 65.61 %	H: 5.64 %	S: 18.75 %

5.3.28 Synthesis of 5,5'-(2,5-Dimethyl-1,4-phenylene)bis(2-(chloromethyl)thiophene) (36)

Oxalyl chloride (35.00 mmol, 4.52 g) was added to 75.00 ml of anhydrous THF, the reaction medium was cooled down to 0 °C and DMF (35.00 mmol, 2.56 g) was added to the solution drop wise. The reaction mixture was warmed up slowly and stirred at room temperature for additional 15 min. The reaction mixture was again cooled down to 0 °C. **33** (4.45 mmol, 1.47 g) was added and the solution was stirred over night. After stripping off the volatiles, water was added. The resulting yellow precipitate was filtered and washed with water. (yield: 1.38 g, 84 %).

¹H NMR (600 MHz, CDCl₃): δ 7.35 (s, 2H, H1), 7.23 (d, *J* = 3.8 Hz, 2H, H5), 7.10 (d, *J* = 3.8 Hz, 2H, H6), 5.07 (s, 4H, H8), 2.38 (s, 6H, H9) ppm.

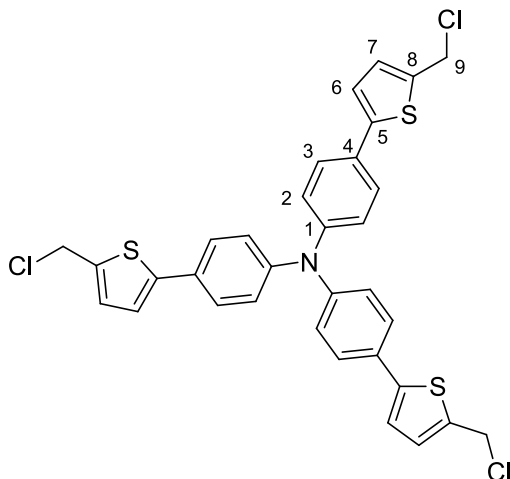
¹³C NMR (151 MHz, CDCl₃): δ 143.2 (C7), 140.2 (C4), 132.9 (C2), 132.7 (C3), 132.2 (C1), 128.9 (C6), 126.7 (C5), 40.8 (C8), 20.3 (C9) ppm.

IR (ATR, cm⁻¹): ν 2954, 2922, 2853, 1664, 1450, 1227, 802, 669.

Elemental analysis: C₁₈H₁₆Cl₂S₂ (367.36 g/mol)

Calculated	:	C: 58.85 %	H: 4.39 %	S: 17.46 %
Found	:	C: 59.57 %	H: 4.70 %	S: 16.04 %

5.3.29 Synthesis of Tris(4-(5-(chloromethyl)thiophen-2-yl)phenyl)amine (37)



Oxalyl chloride (10.31 mmol, 1.31 g) was added to 30.00 ml of freshly distilled THF, the solution was cooled down to 0 °C and DMF (10.31 mmol, 0.75 g) was drop wise. The reaction mixture was warmed up slowly and stirred at room temperature for additional 15 min. The reaction mixture was again cooled down to 0 °C. **34** (0.50 g, 0.86 mmol) was added and the mixture was stirred over night. After stripping off the volatiles, water was added. The resulting dark red precipitate was filtered and washed with water. (yield: 0.45 g, 81 %).

¹H NMR (400 MHz, (CD₃)₂SO): δ 7.57 (d, *J* = 7.6 Hz, 6H, H₂), 7.28 (s, 3H, H₆), 7.17 (s, 3H, H₇), 7.06 (d, *J* = 7.6 Hz, 6H, H₃), 5.03 (s, 6H, H₉) ppm.

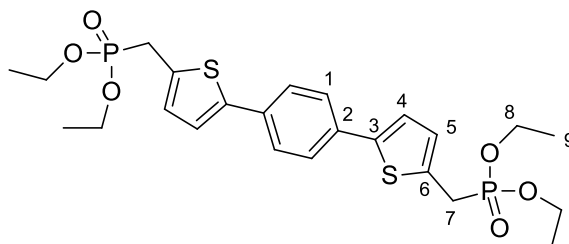
¹³C NMR (101 MHz, (CD₃)₂SO): δ 146.1 (C₁), 144.6 (C₈), 139.0 (C₅), 129.8 (C₇), 128.4 (C₄), 126.7 (C₃), 124.2 (C₂), 122.7 (C₆), 41.1 (C₉) ppm.

IR (ATR, cm⁻¹): ν 3027, 2924, 1507, 1255, 796, 657.

Elemental analysis: C₃₃H₂₄Cl₃NS₃ (637.10 g/mol)

Calculated	:	C: 62.21 %	H: 3.80 %	N: 2.20 %	S: 15.10 %
Found	:	C: 61.78 %	H: 4.24 %	N: 2.01 %	S: 15.21 %

5.3.30 Synthesis of Tetraethyl-((5,5'-(1,4-phenylene)bis(thiophene-5,2-diyl))bis(methylene))bis(phosphonate) (**38**)



0.50 g (1.47 mmol) of **35** were placed in a Schlenk tube, 7.58 g (44.10 mmol) of triethyl phosphite were added and the reaction medium was heated to 120 °C for 72 h under continuous stirring. Then all volatiles were removed under vacuum. The remaining yellow solid was washed several times with pentane and dried at ambient conditions (yield: 0.43 g, 54 %).

¹H NMR (400 MHz, (CD₃)₂SO): δ 7.63 (s, 4H, H1), 7.40 (d, *J* = 3.6 Hz, 2H, H4), 6.97 (t, *J* = 3.6 Hz, 2H, H5), 4.02 (dq, ³*J*_{PH} = 14.0 Hz, ³*J*_{HH} = 7.0 Hz, 8H, H8), 3.52 (d, ²*J*_{PH} = 20.8 Hz, 4H, H7), 1.22 (t, *J* = 7.0 Hz, 12H, H9) ppm.

¹³C NMR (101 MHz, (CD₃)₂SO): δ 141.7 (d, ⁵*J*_{PC} = 4.2 Hz, C3), 133.3 (d, ²*J*_{PC} = 10.8 Hz, C6), 132.7 (s, C2), 128.8 (d, ³*J*_{PC} = 9.1 Hz, C5), 125.6 (s, C1), 123.5 (d, ⁴*J*_{PC} = 3.4 Hz, C4), 61.7 (d, ²*J*_{PC} = 6.5 Hz, C8), 27.1 (d, ¹*J*_{PC} = 139.9 Hz, C7), 16.2 (d, ³*J*_{PC} = 5.6 Hz, C9) ppm.

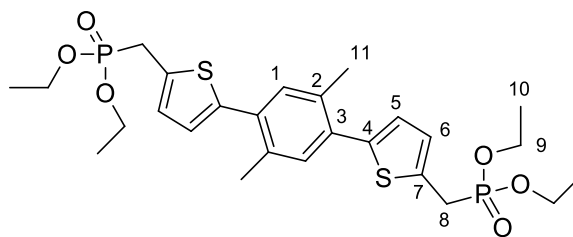
³¹P NMR (162 MHz, (CD₃)₂SO): δ 24.35 ppm.

IR (ATR, cm⁻¹): ν 3069, 2931, 1443, 1163, 1021, 952, 712.

Elemental analysis: C₂₄H₃₂O₆P₂S₂ (542.58 g/mol)

Calculated	:	C: 53.13 %	H: 5.94 %	S: 11.82 %
Found	:	C: 54.53 %	H: 5.47 %	S: 12.97 %

5.3.31 Synthesis of Tetraethyl-((5,5'-(2,5-dimethyl-1,4-phenylene)bis(thiophene-5,2-diyl))bis(methylene))bis(phosphonate) (39)



0.50 g (1.36 mmol) **36** were placed in a Schlenk tube, 6.81 g (41.00 mmol) of triethyl phosphite were added and the reaction mixture was heated to 120 °C for 72 h under continuous stirring. Then all volatiles were removed under vacuum. The remaining yellow solid was washed several times with pentane and dried at ambient conditions (yield: 0.40 g, 51 %).

¹H NMR (400 MHz, (CD₃)₂SO): δ 7.31 (s, 2H, H1), 7.09 (d, *J* = 3.6 Hz, 2H, H5), 6.99 (t, *J* = 3.6 Hz, 2H, H6), 4.02 (dq, ³*J*_{PH} = 14.1, ²*J*_{HH} = 7.1 Hz, 8H, H9), 3.52 (d, ²*J*_{PH} = 20.8 Hz, 4H, H8), 2.38 (s, 6H, H11), 1.22 (t, *J* = 7.0 Hz, 12H, H10) ppm.

¹³C NMR (151 MHz, (CD₃)₂SO): δ 140.7 (d, ⁵*J*_{PC} = 3.5 Hz, C4), 133.5 (d, ²*J*_{PC} = 10.2 Hz, C7), 132.7 (s, C2), 132.7 (s, C3), 132.0 (s, C1), 127.8 (d, ³*J*_{PC} = 9.0 Hz, C6), 126.6 (d, ⁴*J*_{PC} = 2.3 Hz, C5), 61.7 (d, ²*J*_{PC} = 6.2 Hz, C9), 26.8 (d, ¹*J*_{PC} = 135.9 Hz, C8), 20.4 (s, C11), 16.2 (d, ³*J*_{PC} = 5.7 Hz, C10) ppm.

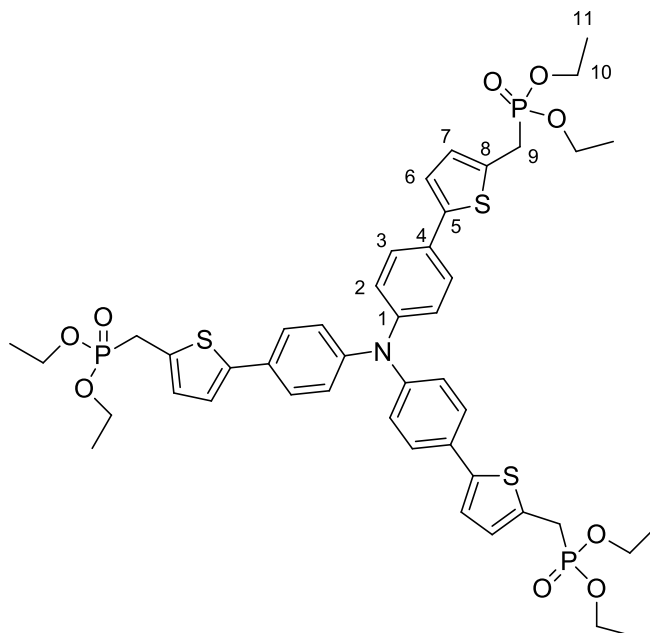
³¹P NMR (162 MHz, (CD₃)₂SO): δ 24.48 ppm.

IR (ATR, cm⁻¹): ν 3062, 2905, 1436, 1246, 1182, 1151, 1019, 959, 699.

Elemental analysis: C₂₆H₃₆O₆P₂S₂ (570.64 g/mol)

Calculated	:	C: 54.72 %	H: 6.36 %	S: 11.24 %
Found	:	C: 54.62 %	H: 6.25 %	S: 11.23 %

5.3.32 Synthesis of Hexaethyl ((5,5',5''-(nitrilotris(benzene-4,1-diyl))tris(thiophene-5,2-diyl))tris(methylene)tris(phosphonate) (40)



0.20 g (0.31 mmol) of **37** were placed in a Schlenk tube, 3.39 g (13.95 mmol) of triethyl phosphite were added and the reaction medium was heated to 120 °C for 72 h under continuous stirring. Then all volatiles were removed under vacuum. The remaining yellow solid was washed several times with pentane and dried under vacuum (yield: 0.16 g, 55 %).

¹H NMR (400 MHz, (CD₃)₂SO): δ 7.55 (d, *J* = 8.5 Hz, 6H, H2), 7.27 (d, *J* = 3.4 Hz, 3H, H6), 7.07 (d, *J* = 8.5 Hz, 6H, H3), 6.95 – 6.93 (m, 3H, H7), 4.04 – 3.96 (m, 12H, H10), 3.50 (d, ²*J*_{PH} = 20.8 Hz, 6H, H9), 1.21 (t, *J* = 7.1 Hz, 18H, H11) ppm.

¹³C NMR (101 MHz, (CD₃)₂SO): δ 145.8 (C1), 142.0 (C8), 136.8 (C5), 132.6 (C5), 128.7 (C4), 126.3 (C3), 124.2 (C2), 122.7 (C6), 61.7 (d, ²*J*_{PC} = 6.4 Hz, C10), 27.0 (d, ¹*J*_{PC} = 139.6 Hz, C9), 16.3 (d, ³*J*_{PC} = 5.6 Hz, C11) ppm.

IR (ATR, cm⁻¹): ν 2958, 2541, 1658, 1533, 1441, 1263, 734.

Elemental analysis: C₄₅H₅₄NO₉P₃S₃ (942.03 g/mol)

Calculated	:	C: 57.37 %	H: 5.78 %	N: 1.49 %	S: 10.21 %
Found	:	C: 58.96 %	H: 4.91 %	N: 1.80 %	S: 12.09 %

5.4 Synthesis of the MOFs

5.4.1 Synthesis of ZnBrBPDC

0.48 g (1.20 mmol) of **2** and 1.80 g (6.90 mmol) of $\text{Zn}(\text{NO}_3)_2 \cdot (\text{H}_2\text{O})_4$ were dissolved in a 125 ml-PP-bottle containing 100.00 ml of DMF and the mixture was stirred for 30 min. Then the bottle was closed tightly and placed for 36 h in an oven at a temperature of 100 °C yielding cubic crystals. After cooling to room temperature, the crystals were filtered off and washed three times with anhydrous acetone. Due to the instability of this MOF under ambient conditions, the crystals were soaked and kept in DMF.

Elemental analysis: $\text{C}_{42}\text{H}_{18}\text{Br}_6\text{O}_{13}\text{Zn}_4 \cdot (\text{DMF})_{6.30} \cdot (\text{H}_2\text{O})_{0.30} \cdot (\text{C}_{14}\text{H}_6\text{Br}_2\text{O}_4)_{0.70}$

Calculated	:	C: 38.30 %	H: 3.10 %	N: 3.98 %
-------------------	---	-------------------	------------------	------------------

Found	:	C: 38.75 %	H: 3.56 %	N: 3.53 %
--------------	---	-------------------	------------------	------------------

5.4.2 Synthesis of ZnNO₂BPDC

0.41 g (1.23 mmol) of **4** and 0.90 g (3.45 mmol) of $\text{Zn}(\text{NO}_3)_2 \cdot (\text{H}_2\text{O})_4$ were dissolved in a 60 ml-PP-bottle containing 35.00 ml of DMF and the mixture was stirred for 30 min. Then the bottle was closed tightly and placed for 48 h in an oven at a temperature of 100 °C yielding cubic crystals. During the synthesis, the bottle had to be shaken periodically. After cooling to room temperature, the crystals were filtered off and washed three times with anhydrous acetone. Due to the instability of this MOF under ambient conditions, the crystals were soaked and kept in DMF.

Elemental analysis: $\text{C}_{42}\text{H}_{18}\text{N}_6\text{O}_{25}\text{Zn}_4 \cdot (\text{DMF})_{0.80} \cdot (\text{H}_2\text{O})_{1.20}$

Calculated	:	C: 39.55 %	H: 1.94 %	N: 7.06 %
-------------------	---	-------------------	------------------	------------------

Found	:	C: 39.56 %	H: 1.95 %	N: 7.04 %
--------------	---	-------------------	------------------	------------------

5.4.3 Synthesis of ZnNH₂BPDC

0.34 g (1.23 mmol) of **6** and 0.90 g (3.45 mmol) of Zn(NO₃)₂·(H₂O)₄ were dissolved in a 60 ml-PP-bottle containing 35.00 ml of DMF and the mixture was stirred for 30 min. Then the bottle was closed tightly and placed for 48 h in an oven at a temperature of 100 °C yielding cubic crystals. During the synthesis, the bottle had to be shaken periodically. After cooling to room temperature, the crystals were filtered off and washed three times with anhydrous acetone. Due to the instability of this MOF under ambient conditions, the crystals were soaked and kept in DMF.

Elemental analysis: C₄₂H₃₀N₆O₁₃Zn₄·(DMF)_{1.00}·(H₂O)_{0.35}·(C₁₄H₁₂N₂O₄)_{0.15}

Calculated	:	C: 46.35 %	H: 2.78 %	N: 7.72 %
-------------------	---	-------------------	------------------	------------------

Found	:	C: 47.04 %	H: 3.49 %	N: 8.26 %
--------------	---	-------------------	------------------	------------------

5.4.4 Synthesis of ZnAcBPDC

0.02 g (0.056 mmol) of **8** and 0.125 g (0.48 mmol) of Zn(NO₃)₂·(H₂O)₄ were dissolved in a 15 ml glass vial containing 4.00 ml of DMF and the mixture was stirred for 10 min. Then the vial was closed tightly and placed for 24 h in an oven at a temperature of 100 °C yielding colorless cubic crystals. After cooling to room temperature, the crystals were filtered off and washed three times with anhydrous acetone. Due to the instability of this MOF under ambient conditions, the crystals were soaked and kept in DMF.

Elemental analysis: C₅₄H₄₂N₆O₁₉Zn₄·(DMF)_{15.7}·(H₂O)_{4.40}

Calculated	:	C: 47.30 %	H: 6.31 %	N: 11.84 %
-------------------	---	-------------------	------------------	-------------------

Found	:	C: 47.21 %	H: 6.22 %	N: 11.93 %
--------------	---	-------------------	------------------	-------------------

5.4.5 Synthesis of ZnPrBPDC

0.02 g (0.052 mmol) of **10** and 0.149 g (0.52 mmol) of Zn(NO₃)₂·(H₂O)₄ were dissolved in a 15 ml glass vial containing 4.00 ml DMF and the mixture was stirred for 10 min. Then the vial

was closed tightly and placed for 48 h in an oven at a temperature of 100 °C yielding colorless cubic crystals. After cooling to room temperature, the crystals were filtered off and washed three times with anhydrous acetone. Due to the instability of this MOF under ambient conditions, the crystals were soaked and kept in DMF.

Elemental analysis: $\text{C}_{60}\text{H}_{54}\text{N}_6\text{O}_{19}\text{Zn}_4 \cdot (\text{DMF})_{26.00} \cdot (\text{H}_2\text{O})_{9.20}$

Calculated : C: 47.48 % H: 7.35 % N: 12.84 %

Found : C: 47.59 % H: 7.46 % N: 12.73 %

5.4.6 Synthesis of ZnBuBPDC

0.02 g (0.048 mmol) of **12** and 0.125 g (0.48 mmol) of $\text{Zn}(\text{NO}_3)_2 \cdot (\text{H}_2\text{O})_4$ were dissolved in a 15 ml glass vial containing 4.00 ml of DMF and the mixture was stirred for 10 min. Then the vial was closed tightly and placed for 24 h in an oven at a temperature of 100 °C yielding colorless cubic crystals. After cooling to room temperature, the crystals were filtered off and washed three times with anhydrous acetone. Due to the instability of this MOF under ambient conditions, the crystals were soaked and kept in DMF.

Elemental analysis: $\text{C}_{66}\text{H}_{66}\text{N}_6\text{O}_{19}\text{Zn}_4 \cdot (\text{DMF})_{24.25} \cdot (\text{H}_2\text{O})_{4.15}$

Calculated : C: 49.66 % H: 7.33 % N: 12.62 %

Found : C: 49.77 % H: 7.45 % N: 12.51 %

5.4.7 Synthesis of ZnPeBPDC

0.02 g (0.045 mmol) of **14** and 0.153 g (0.58 mmol) of $\text{Zn}(\text{NO}_3)_2 \cdot (\text{H}_2\text{O})_4$ were dissolved in a 15 ml glass vial containing 4.00 ml of DMF and the mixture was stirred for 10 min. Then the vial was closed tightly and placed for 48 h in an oven at a temperature of 100 °C yielding colorless cubic crystals. After cooling to room temperature, the crystals were filtered off and washed three times with anhydrous acetone. Due to the instability of this MOF under ambient conditions, the crystals were soaked and kept in DMF.

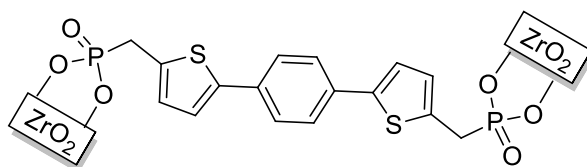
Elemental analysis: $\text{C}_{72}\text{H}_{78}\text{N}_6\text{O}_{19}\text{Zn}_4 \cdot (\text{DMF})_{23.10} \cdot (\text{H}_2\text{O})_{9.70}$

Calculated	:	C: 49.10 %	H: 7.56 %	N: 11.79 %
Found	:	C: 49.03 %	H: 7.48 %	N: 11.87 %

5.5 Immobilization of Phosphonate Derivatives on ZrO_2 , TiO_2 and Al_2O_3

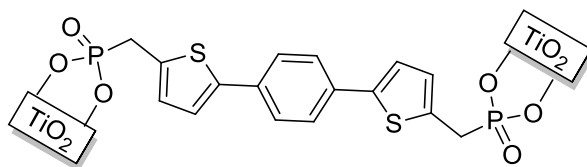
5.5.1 General Procedure for the immobilization of 38 and 39

160.00 mg of the phosphonate derivative and 1.00 g of carrier were mixed in a Schlenk tube containing 45 ml of dichloromethane. The reaction mixture was stirred for 24 h at room temperature. The resulting solid was filtered off and washed with dichloromethane, methanol and diethyl ether. All materials were dried for 10 h at 50°C.



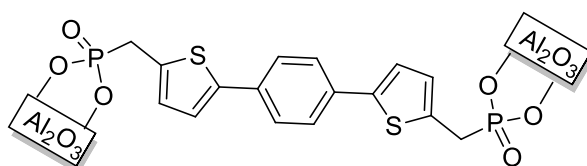
Elemental analysis: $\text{C}_{24}\text{H}_{32}\text{O}_6\text{P}_2\text{S}_2$ (542.58 g/mol) on ZrO_2

Found	:	C: 1.01 %	H: 0.60 %	S: 0.76 %
--------------	---	------------------	------------------	------------------



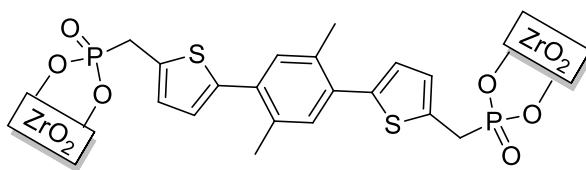
Elemental analysis: $\text{C}_{24}\text{H}_{32}\text{O}_6\text{P}_2\text{S}_2$ (542.58 g/mol) on TiO_2

Found	:	C: 0.79 %	H: 0.39 %	S: 0.42 %
--------------	---	------------------	------------------	------------------



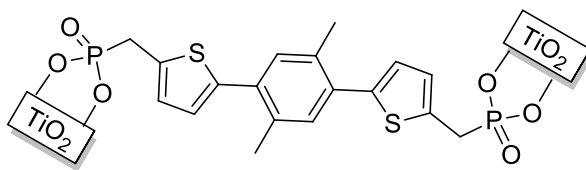
Elemental analysis: $\text{C}_{24}\text{H}_{32}\text{O}_6\text{P}_2\text{S}_2$ (542.58 g/mol) on Al_2O_3

Found	:	C: 1.04 %	H: 0.75 %	S: 0.37 %
--------------	---	------------------	------------------	------------------



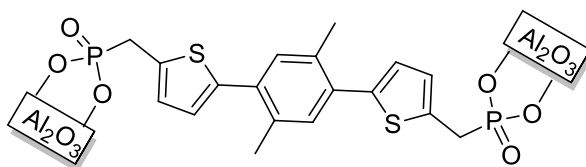
Elemental Analysis: $C_{26}H_{36}O_6P_2S_2$ (570.64 g/mol) on ZrO_2

Found : C: 1.09 % H: 0.48 % S: 0.45 %



Elemental Analysis: $C_{26}H_{36}O_6P_2S_2$ (570.64 g/mol) on TiO_2

Found : C: 1.03 % H: 0.39 % S: 0.38 %

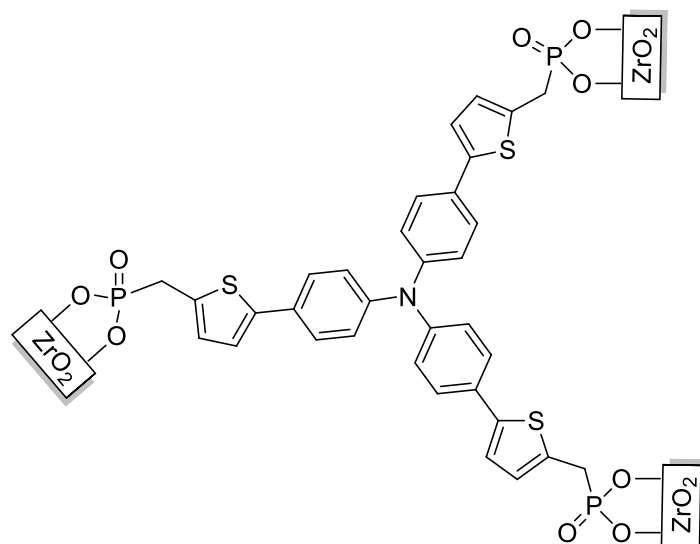


Elemental Analysis: $C_{26}H_{36}O_6P_2S_2$ (570.64 g/mol) on Al_2O_3

Found : C: 1.18 % H: 0.85 % S: 0.31 %

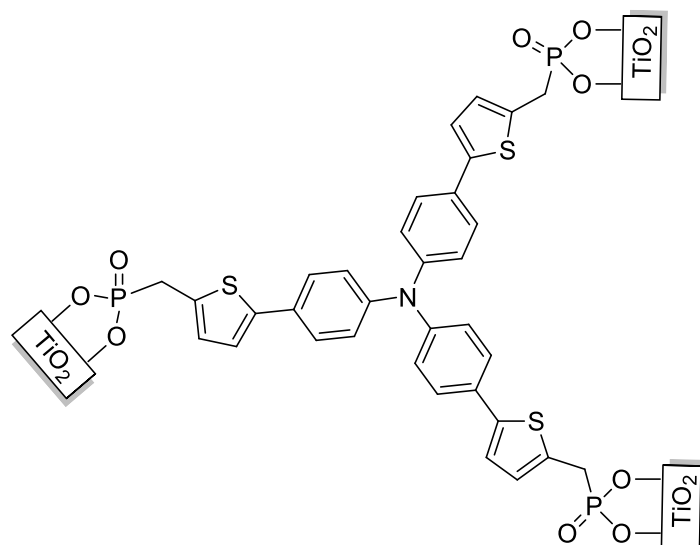
5.5.2 General Procedure for the immobilization of **40**

80.00 mg of **40** and 1.00 g of the carrier were mixed in a Schlenk tube containing 45 ml dichloromethane. The reaction mixture was stirred for 24 h at room temperature. The resulting solid was filtered off, washed with dichloromethane, methanol and diethyl ether and dried for 10 h at 50°C.



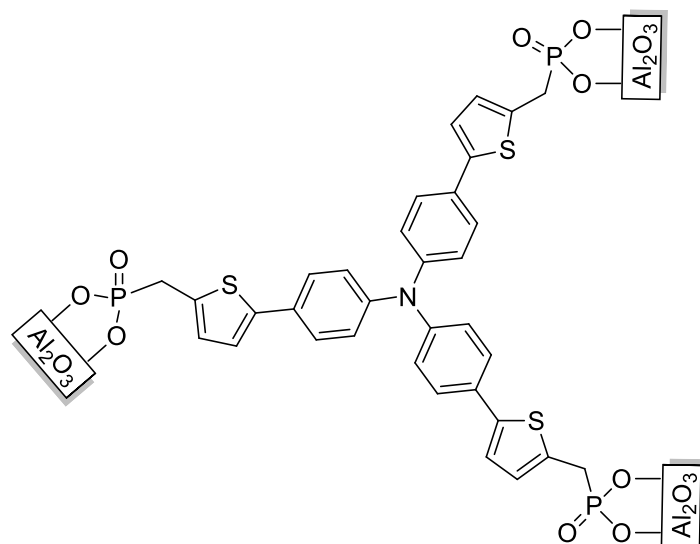
Elemental analysis: $C_{45}H_{54}NO_9P_3S_3$ (942.03 g/mol) on ZrO_2

Found : **C:** 1.60 % **H:** 0.56 % **N:** 0.11 % **S:** 0.75 %



Elemental analysis: $C_{45}H_{54}NO_9P_3S_3$ (942.03 g/mol) on TiO_2

Found : **C:** 1.31 % **H:** 0.56 % **N:** 0.12 % **S:** 0.33 %



Elemental analysis: $C_{45}H_{54}NO_9P_3S_3$ (942.03 g/mol) on Al_2O_3

Found : **C:** 1.67 % **H:** 0.76 % **N:** 0.24 % **S:** 0.35 %

6. References

1. Stein, A.; Melde, B. J.; Schroden, R. C., Hybrid Inorganic–Organic Mesoporous Silicates—Nanoscopic Reactors Coming of Age. *Adv. Mater.*, **2000**, *12*, 1403-1419.
2. Arkles B.; Commercial applications of sol gel derived hybrid materials. *MRS Bulletin.*, **2001**, *26*, 402-408.
3. Beck, J. S.; Vartuli, J. C.; Roth, W. J.; Leonowicz, M. E.; Kresge, C. T.; Schmitt, K. D.; Chu, C. T. W.; Olson, D. H.; Sheppard, E. W., A new family of mesoporous molecular sieves prepared with liquid crystal templates. *J. Am. Chem. Soc.*, **1992**, *114*, 10834-10843.
4. Zhao, D.; Feng, J.; Huo, Q.; Melosh, N.; Fredrickson, G. H.; Chmelka, B. F.; Stucky, G. D., Triblock copolymer syntheses of mesoporous silica with periodic 50 to 300 Angstrom pores. *Science*, **1998**, *279*, 548-552.
5. Goltner, C. G.; Antonietti, M., Mesoporous materials by templating of liquid crystalline phases. *Adv. Mater.*, **1997**, *9*, 431-436.
6. Li, H.; Eddaoudi, M.; O'Keeffe, M.; Yaghi, O. M., Design and synthesis of an exceptionally stable and highly porous metal-organic framework. *Nature*, **1999**, *402*, 276-279.
7. Yaghi, O. M.; Li, G.; Li, H., Selective binding and removal of guests in a microporous metal-organic framework. *Nature*, **1995**, *378*, 703-706.
8. Sanchez, C.; Belleville, P.; Popall, M.; Nicole, L., Applications of advanced hybrid organic-inorganic nanomaterials: from laboratory to market. *Chem. Soc. Rev.*, **2011**, *40*, 696-753.
9. Sanchez, C.; Rozes, L.; Ribot, F.; Laberty-Robert, C.; Grosso, D.; Sassoie, C.; Boissiere, C.; Nicole, L., "Chimie douce": A land of opportunities for the designed construction of functional inorganic and hybrid organic-inorganic nanomaterials. *Comptes Rendus Chimie*, **2010**, *13*, 3-39.
10. Livage, J.; Henry, M.; Sanchez, C., Sol-gel chemistry of transition metal oxides. *Prog. Solid State Chem.*, **1988**, *18*, 259-341.
11. Gómez-Romero, P.; Sanchez, C., Hybrid materials, functional applications. An introduction in functional hybrid materials, *Wiley*, **2005**, 1-14.
12. Sanchez, C.; Ribot, F.; Lebeau, B., Molecular design of hybrid organic-inorganic nanocomposites synthesized via sol-gel chemistry. *J. Mater. Chem.*, **1999**, *9*, 35-44.
13. Judeinstein, P.; Sanchez, C., Hybrid organic-inorganic materials: A land of multidisciplinary. *J. Mater. Chem.*, **1996**, *6*, 511-525.
14. Sanchez, C.; Ribot F., *New J. Chem.*, **1994**, *18*, 1007-1047.
15. Shulman, G. P.; Trusty, M.; Vickers, J. H., Thermal decomposition of aluminum alkoxides. *J. Org. Chem.*, **1963**, *28*, 907-910.
16. Acosta, S.; Corriu, R. J. P.; Leclercq, D.; Lefèvre, P.; Mutin, P. H.; Vioux, A., Preparation of alumina gels by a non-hydrolytic sol-gel processing method. *J. Non-Cryst. Solids*, **1994**, *170*, 234-242.

17. Gerrard, W.; Woodhead, A. H., 110. Interaction of alcohols with silicon tetrachloride. *J. Chem. Soc.*, **1951**, 519-522.
18. Corriu, R. J. P.; Leclercq, D.; Lefèvre, P.; Mutin, P. H.; Vioux, A., Preparation of monolithic gels from silicon halides by a non-hydrolytic sol-gel process. *J. Non-Cryst. Solids*, **1992**, *146*, 301-303.
19. Arnal, P.; Corriu, R. J. P.; Leclercq, D.; Mutin, P. H.; Vioux, A., Preparation of anatase, brookite and rutile at low temperature by non-hydrolytic sol-gel methods. *J. Mater. Chem*, **1996**, *6*, 1925-1932.
20. Goel, S. C.; Chiang, M. Y.; Gibbons, P. C.; Buhro, W. E., New chemistry for the sol-gel process: Acetone as a new condensation reagent. *Mater. Res. Soc. Symp. Proc.*, **1992**, *271*, 3-13.
21. Sur, G. S.; Mark, J. E., Elastomeric networks cross-linked by silica or titania fillers. *Eur. Polym. J.*, **1985**, *21*, 1051-1052.
22. Avnir, D.; Levy, D.; Reisfeld, R., The nature of the silica cage as reflected by spectral changes and enhanced photostability of trapped Rhodamine 6G. *J. Phys. Chem.*, **1984**, *88*, 5956-5959.
23. Novak, B. M., Hybrid nanocomposite materials—between inorganic glasses and organic polymers. *Adv. Mater.*, **1993**, *5*, 422-433.
24. Schubert, U.; Huesing, N.; Lorenz, A., Hybrid inorganic-organic materials by sol-gel processing of organofunctional metal alkoxides. *Chem. Mater.*, **1995**, *7*, 2010-2027.
25. Schubert, U., New materials by sol-gel processing: Design at the molecular level. *J. Chem. Soc., Dalton Trans.*, **1996**, 3343-3348.
26. Corriu, R. J. P.; Leclercq, D., Recent developments of molecular chemistry for sol-gel processes. *Angew. Chem. Int.Ed.*, **1996**, *35*, 1420-1436.
27. Ribot, F.; Sanchez, C., Organically functionalized metallic oxo-clusters: Structurally well-defined nanobuilding blocks for the design of hybrid organic-inorganic materials. *Comments Inorg. Chem.*, **1999**, *20*, 327-371.
28. Stupp, S. I.; Braun, P. V., Molecular manipulation of microstructures: Biomaterials, ceramics, and semiconductors. *Science*, **1997**, *277*, 1242-1248.
29. Corriu, R., A new trend in metal-alkoxide chemistry: the elaboration of monophasic organic-inorganic hybrid materials. *Polyhedron*, **1998**, *17*, 925-934.
30. Philipp, G.; Schmidt, H., New materials for contact lenses prepared from Si- and Ti-alkoxides by the sol-gel process. *J. Non-Cryst. Solids*, **1984**, *63*, 283-292.
31. Rozes, L.; Steunou, N.; Fornasieri, G.; Sanchez, C., Titanium-Oxo Clusters, versatile nanobuilding blocks for the design of advanced hybrid materials. *Monats. Chem.*, **2006**, *137*, 501-528.
32. Sanchez, C.; Julian, B.; Belleville, P.; Popall, M., Applications of hybrid organic-inorganic nanocomposites. *J. Mater. Chem.*, **2005**, *15*, 3559-3592.
33. Dang, D.; Wu, P.; He, C.; Xie, Z.; Duan, C., Homochiral metal-organic frameworks for heterogeneous asymmetric catalysis. *J. Am. Chem. Soc.*, **2010**, *132*, 14321-14323.

34. Kinoshita, Y.; Matsubara, I.; Higuchi, T.; Saito, Y., The crystal structure of Bis(adiponitrilo)copper(I) nitrate. *Bull. Chem. Soc. Jpn.*, **1959**, 32, 1221-1226.
35. Aleksandr, A. B.; Matveeva, N. G., Polymeric chelate compounds. *Russ. Chem. Rev.*, **1960**, 29, 119.
36. Sowerby, D. B.; Audrieth, L. F., Inorganic polymerization reactions III. Coordination polymerization. *J. Chem. Educ.*, **1960**, 37, 134.
37. Sing, K. S. W.; Everett, D. H.; Haul, R. A.; Moscou, W. L.; Pierotti, R. A.; Rouquérol, J.; Siemieniewska, T., Reporting physisorption data for gas/solid systems with special reference to the determination of surface area and porosity. *Pure & Appl. Chem.*, **1985**, 57, 603.
38. Perez-Ramirez, J.; Christensen, C. H.; Egeblad, K.; Christensen, C. H.; Groen, J. C., Hierarchical zeolites: Enhanced utilisation of microporous crystals in catalysis by advances in materials design. *Chem. Soc. Rev.*, **2008**, 37, 2530-2542.
39. Cundy, C. S.; Cox, P. A., The hydrothermal synthesis of zeolites: History and development from the earliest days to the present time. *Chem. Rev.*, **2003**, 103, 663-702.
40. Corma, A., State of the art and future challenges of zeolites as catalysts. *J. Catal.*, **2003**, 216, 298-312.
41. Kitagawa, S.; Kitaura, R.; Noro, S.-i., Functional porous coordination polymers. *Angew. Chem. Int. Ed.*, **2004**, 43, 2334-2375.
42. Rowsell, J. L. C.; Yaghi, O. M., Metal-organic frameworks: A new class of porous materials. *Microporous Mesoporous Mater.*, **2004**, 73, 3-14.
43. Corma, A.; García, H.; Llabrés i Xamena, F. X., Engineering metal organic frameworks for heterogeneous catalysis. *Chem. Rev.*, **2010**, 110, 4606-4655.
44. Dan Z.; Timmons D.J.; Yuan, D.; Zhou H.C., Tuning the topology and functionality of metal-organic frameworks by ligand design. *Acc. Chem. Res.*, **2011**, 44, 123-33.
45. Hafizovic, J.; Bjørgen, M.; Olsbye, U.; Dietzel, P. D. C.; Bordiga, S.; Prestipino, C.; Lamberti, C.; Lillerud, K. P., The inconsistency in adsorption properties and powder XRD data of MOF-5 is rationalized by framework interpenetration and the presence of organic and inorganic species in the nanocavities. *J. Am. Chem. Soc.*, **2007**, 129, 3612-3620.
46. Sun, D.; Ma, S.; Ke, Y.; Petersen, T. M.; Zhou, H.C., Synthesis, characterization, and photoluminescence of isostructural Mn, Co, and Zn MOFs having a diamondoid structure with large tetrahedral cages and high thermal stability. *Chem. Commun.*, **2005**, 2663-2665.
47. Jeong, K. S.; Go, Y. B.; Shin, S. M.; Lee, S. J.; Kim, J.; Yaghi, O. M.; Jeong, N., Asymmetric catalytic reactions by NbO-type chiral metal-organic frameworks. *Chem. Sci.*, **2011**, 2, 877-882.
48. Forster, P. M.; Thomas, P. M.; Cheetham, A. K., Biphasic solvothermal synthesis: A new approach for hybrid inorganic-organic materials. *Chem. Mater.*, **2001**, 14, 17-20.
49. Mueller, U.; Schubert, M.; Teich, F.; Puetter, H.; Schierle-Arndt, K.; Pastre, J., Metal-organic frameworks-prospective industrial applications. *J. Mater. Chem.*, **2006**, 16, 626-636.

50. Ni, Z.; Masel, R. I., Rapid production of metal–organic frameworks via microwave-assisted solvothermal synthesis. *J. Am. Chem. Soc.*, **2006**, *128*, 12394-12395.
51. Yeh, C.T.; Lin, W.C.; Lo, S.H.; Kao, C.C.; Lin, C.H.; Yang, C.C., Microwave synthesis and gas sorption of calcium and strontium metal-organic frameworks with high thermal stability. *Cryst. Eng. Comm.*, **2012**, *14*, 1219-1222.
52. Klinowski, J.; Almeida Paz, F. A.; Silva, P.; Rocha, J., Microwave-assisted synthesis of metal-organic frameworks. *Dalton Trans.*, **2011**, *40*, 321-330.
53. Yaghi, O. M.; O'Keeffe, M.; Ockwig, N. W.; Chae, H. K.; Eddaoudi, M.; Kim, J., Reticular synthesis and the design of new materials. *Nature*, **2003**, *423*, 705-714.
54. Stein, A.; Keller, S. W.; Mallouk, T. E., Turning down the heat: Design and mechanism in solid-state synthesis. *Science*, **1993**, *259*, 1558-1564.
55. Yaghi, O. M.; O'Keeffe, M.; Kanatzidis, M., Design of solids from molecular building blocks: golden opportunities for solid state chemistry. *J. Solid State Chem.*, **2000**, *152*, 1-2.
56. Lin, X.; Blake, A. J.; Wilson, C.; Sun, X. Z.; Champness, N. R.; George, M. W.; Hubberstey, P.; Mokaya, R.; Schröder, M., A Porous framework polymer based on a Zinc(II) 4,4'-Bipyridine-2,6,2',6'-tetracarboxylate: Synthesis, structure, and "Zeolite-Like" behaviors. *J. Am. Chem. Soc.*, **2006**, *128*, 10745-10753.
57. Wong-Foy, A. G.; Lebel, O.; Matzger, A. J., Porous crystal derived from a tricarboxylate linker with two distinct binding motifs. *J. Am. Chem. Soc.*, **2007**, *129*, 15740-15741.
58. Guo, Z.; Li, G.; Zhou, L.; Su, S.; Lei, Y.; Dang, S.; Zhang, H., Magnesium-based 3D metal–organic framework exhibiting hydrogen-sorption hysteresis. *Inorg. Chem.*, **2009**, *48*, 8069-8071.
59. Wang, X.S.; Ma, S.; Rauch, K.; Simmons, J. M.; Yuan, D.; Wang, X.; Yildirim, T.; Cole, W. C.; López, J. J.; Meijere, A. d.; Zhou, H.C., Metal–organic frameworks based on double-bond-coupled Di-isophthalate linkers with high hydrogen and methane uptakes. *Chem. Mater.*, **2008**, *20*, 3145-3152.
60. Eddaoudi, M.; Kim, J.; Rosi, N.; Vodak, D.; Wachter, J.; O'Keeffe, M.; Yaghi, O. M., Systematic design of pore size and functionality in isorecticular MOFs and their application in methane storage. *Science*, **2002**, *295*, 469-472.
61. Farha, O. K.; Yazaydin Ö, A.; Eryazici, I.; Malliakas, C. D.; Hauser, B. G.; Kanatzidis, M. G.; Nguyen, S. T.; Snurr, R. Q.; Hupp, J. T., De novo synthesis of a metal–organic framework material featuring ultrahigh surface area and gas storage capacities. *Nat. Chem.*, **2010**, *2*, 944-948.
62. Plabst, M.; Bein, T., 1,4-Phenylenebis(methyldiyne)tetrakis(phosphonic acid): A new building block in metal organic framework synthesis. *Inorg. Chem.*, **2009**, *48*, 4331-4341.
63. Groves, J. A.; Wright, P. A.; Lightfoot, P., Two closely related lanthanum phosphonate frameworks formed by anion-directed linking of inorganic chains. *Inorg. Chem.*, **2005**, *44*, 1736-1739.

64. Mowat, J. P. S.; Groves, J. A.; Wharmby, M. T.; Miller, S. R.; Li, Y.; Lightfoot, P.; Wright, P. A., Lanthanide N,N'-piperazine-bis(methylenephosphonates) (Ln=La, Ce, Nd) that display flexible frameworks, reversible hydration and cation exchange. *J. Solid State Chem.*, **2009**, *182*, 2769-2778.
65. Vasylyev, M. V.; Wachtel, E. J.; Popovitz-Biro, R.; Neumann, R., Titanium phosphonate porous materials constructed from dendritic tetraphosphonates. *Chem. Eur. J.*, **2006**, *12*, 3507-3514.
66. Evans, O. R.; Ngo, H. L.; Lin, W., Chiral Porous Solids Based on Lamellar Lanthanide Phosphonates. *J. Am. Chem. Soc.*, **2001**, *123*, 10395-10396.
67. Evans, O. R.; Manke, D. R.; Lin, W., Homochiral metal-organic frameworks based on transition metal bisphosphonates. *Chem. Mater.*, **2002**, *14*, 3866-3874.
68. Iremonger, S. S.; Liang, J.; Vaidhyanathan, R.; Martens, I.; Shimizu, G. K. H.; Daff, T. D.; Aghaji, M. Z.; Yeganegi, S.; Woo, T. K., Phosphonate monoesters as carboxylate-like linkers for metal organic frameworks. *J. Am. Chem. Soc.*, **2011**, *133*, 20048-20051.
69. Choi, H. J.; Dincă, M.; Long, J. R., Broadly hysteretic H₂ adsorption in the microporous metal-organic framework Co(1,4-benzenedipyrazolate). *J. Am. Chem. Soc.*, **2008**, *130*, 7848-7850.
70. Pachfule, P.; Das, R.; Poddar, P.; Banerjee, R., Structural, magnetic, and gas adsorption study of a two-dimensional tetrazole-pyrimidine based metal-organic framework. *Cryst. Growth Des.*, **2010**, *10*, 2475-2478.
71. Takashima, Y.; Martínez, V. M.; Furukawa, S.; Kondo, M.; Shimomura, S.; Uehara, H.; Nakahama, M.; Sugimoto, K.; Kitagawa, S., Molecular decoding using luminescence from an entangled porous framework. *Nat. Commun.*, **2011**, *2*, 168.
72. Hasegawa, S.; Horike, S.; Matsuda, R.; Furukawa, S.; Mochizuki, K.; Kinoshita, Y.; Kitagawa, S., Three-dimensional porous coordination polymer functionalized with amide groups based on tridentate ligand: selective sorption and catalysis. *J. Am. Chem. Soc.*, **2007**, *129*, 2607-2614.
73. Shimomura, S.; Matsuda, R.; Tsujino, T.; Kawamura, T.; Kitagawa, S., TCNQ Dianion-based coordination polymer whose open framework shows charge-transfer type guest inclusion. *J. Am. Chem. Soc.*, **2006**, *128*, 16416-16417.
74. Seo, J. S.; Whang, D.; Lee, H.; Jun, S. I.; Oh, J.; Jeon, Y. J.; Kim, K., A homochiral metal-organic porous material for enantioselective separation and catalysis. *Nature*, **2000**, *404*, 982-986.
75. Yaghi, O. M.; Li, Q., Reticular chemistry and metal-organic frameworks for clean energy. *MRS Bull.*, **2009**, *34*, 682-690.
76. Almeida Paz, F. A.; Klinowski, J.; Vilela, S. M. F.; Tome, J. P. C.; Cavaleiro, J. A. S.; Rocha, J., Ligand design for functional metal-organic frameworks. *Chem. Soc. Rev.*, **2012**, *41*, 1088-1110.
77. Millange, F.; Guillou, N.; Medina, M. E.; Férey, G. r.; Carlin-Sinclair, A.; Golden, K. M.; Walton, R. I., Selective sorption of organic molecules by the flexible porous hybrid metal-organic framework MIL-53(Fe) controlled by various host-guest interactions. *Chem. Mater.*, **2010**, *22*, 4237-4245.
78. Chang, N.; Gu, Z.-Y.; Wang, H.-F.; Yan, X.-P., Metal-organic-framework based tandem molecular sieves as a dual platform for selective microextraction and high-resolution gas chromatographic separation of *n*-alkanes in complex matrixes. *Anal. Chem.*, **2011**, *83*, 7094-7101.

79. Liu, X.; Oh, M.; Lah, M. S., Size and shape selective isostructural microporous metal–organic frameworks with different effective aperture sizes. *Inorg. Chem.*, **2011**, *50*, 5044-5053.
80. Férey, G.; Mellot-Draznieks, C.; Serre, C.; Millange, F.; Dutour, J.; Surblé, S.; Margiolaki, I., A Chromium terephthalate-based solid with unusually large pore volumes and surface area. *Science*, **2005**, *309*, 2040-2042.
81. Wang, X.-S.; Ma, S.; Sun, D.; Parkin, S.; Zhou, H.-C., A mesoporous metal–organic framework with permanent porosity. *J. Am. Chem. Soc.*, **2006**, *128*, 16474-16475.
82. Park, Y. K.; Choi, S. B.; Kim, H.; Kim, K.; Won, B.H.; Choi, K.; Choi, J.S.; Ahn, W.S.; Won, N.; Kim, S.; Jung, D. H.; Choi, S.H.; Kim, G.H.; Cha, S.S.; Jhon, Y. H.; Yang, J. K.; Kim, J., Crystal structure and guest uptake of a mesoporous metal–organic framework containing cages of 3.9 and 4.7 nm in diameter. *Angew. Chem. Int. Ed.*, **2007**, *46*, 8230-8233.
83. Koh, K.; Wong-Foy, A. G.; Matzger, A. J., A crystalline mesoporous coordination copolymer with high microporosity. *Angew. Chem. Int. Ed.*, **2008**, *47*, 677-680.
84. An, J.; Farha, O. K.; Hupp, J. T.; Pohl, E.; Yeh, J. I.; Rosi, N. L., Metal-adeninate vertices for the construction of an exceptionally porous metal-organic framework. *Nat. Commun.*, **2012**, *604*, 1-6.
85. Klein, N.; Senkovska, I.; Gedrich, K.; Stoeck, U.; Henschel, A.; Mueller, U.; Kaskel, S., A mesoporous metal–organic framework. *Angew. Chem. Int. Ed.*, **2009**, *48*, 9954-9957.
86. Yan, Y.; Telepeni, I.; Yang, S.; Lin, X.; Kockelmann, W.; Dailly, A.; Blake, A. J.; Lewis, W.; Walker, G. S.; Allan, D. R.; Barnett, S. A.; Champness, N. R.; Schröder, M., Metal–organic polyhedral frameworks: High H₂ adsorption capacities and neutron powder diffraction studies. *J. Am. Chem. Soc.*, **2010**, *132*, 4092-4094.
87. Yuan, D.; Zhao, D.; Sun, D.; Zhou, H.C., An isorecticular series of metal–organic frameworks with dendritic hexacarboxylate ligands and exceptionally high gas-uptake capacity. *Angew. Chem. Int. Ed.*, **2010**, *49*, 5357-5361.
88. Furukawa, H.; Ko, N.; Go, Y. B.; Aratani, N.; Choi, S. B.; Choi, E.; Yazaydin, A. Ö.; Snurr, R. Q.; O’Keeffe, M.; Kim, J.; Yaghi, O. M., Ultrahigh porosity in metal-organic frameworks. *Science*, **2010**, *329*, 424-428.
89. Shekhah, O.; Wang, H.; Paradinas, M.; Ocal, C.; Schupbach, B.; Terfort, A.; Zacher, D.; Fischer, R. A.; Woll, C., Controlling interpenetration in metal-organic frameworks by liquid-phase epitaxy. *Nat. Mater.*, **2009**, *8*, 481-484.
90. Zhang, J.; Wojtas, L.; Larsen, R. W.; Eddaoudi, M.; Zaworotko, M. J., Temperature and concentration Control over interpenetration in a metal–organic material. *J. Am. Chem. Soc.*, **2009**, *131*, 17040-17041.
91. Farha, O. K.; Malliakas, C. D.; Kanatzidis, M. G.; Hupp, J. T., Control over catenation in metal–organic frameworks via rational design of the organic building block. *J. Am. Chem. Soc.*, **2009**, *132*, 950-952.

92. Reineke, T. M.; Eddaoudi, M.; Moler, D.; O'Keeffe, M.; Yaghi, O. M., Large free volume in maximally interpenetrating networks: The role of secondary building units exemplified by $\text{Tb}_2(\text{ADB})_3[(\text{CH}_3)_2\text{SO}]_4 \cdot 16[(\text{CH}_3)_2\text{SO}]$. *J. Am. Chem. Soc.*, **2000**, *122*, 4843-4844.
93. Vodak, D. T.; Braun, M. E.; Kim, J.; Eddaoudi, M.; Yaghi, O. M., Metal-organic frameworks constructed from pentagonal antiprismatic and cuboctahedral secondary building units. *Chem. Commun.*, **2001**, 2534-2535.
94. Férey, G., Building Units Design and Scale Chemistry. *J. Solid State Chem.*, **2000**, *152*, 37-48.
95. Yang, S. Y.; Long, L. S.; Huang, R. B.; Zheng, L. S., $[\text{Zn}_8(\text{SiO}_4)(\text{C}_8\text{H}_4\text{O}_4)_6]$: the firstborn of a metallosilicate-organic hybrid material family ($\text{C}_8\text{H}_4\text{O}_4$ = isophthalate). *Chem. Commun.*, **2002**, 472-473.
96. Dolbecq, A.; Mellot-Draznieks, C.; Mialane, P.; Marrot, J.; Férey, G.; Sécheresse, F., Hybrid 2D and 3D Frameworks Based on ϵ -Keggin Polyoxometallates: Experiment and Simulation. *Eur. J. Inorg. Chem.*, **2005**, *2005*, 3009-3018.
97. Li, Y.; Yang, R. T., Gas Adsorption and storage in metal-organic framework MOF-177. *Langmuir*, **2007**, *23*, 12937-12944.
98. Arstad, B.; Fjellvåg, H.; Kongshaug, K.; Swang, O.; Blom, R., Amine functionalised metal organic frameworks (MOFs) as adsorbents for carbon dioxide. *Adsorption*, **2008**, *14*, 755-762.
99. Zhang, J.; Sun, L.; Xu, F.; Li, F.; Zhou, H.Y.; Liu, Y.L.; Gabelica, Z.; Schick, C., H_2 storage and CO_2 capture on a nanoscale metal organic framework with high thermal stability. *Chem. Commun.*, **2012**, *48*, 759-761.
100. Xue, Y.S.; He, Y.; Ren, S.B.; Yue, Y.; Zhou, L.; Li, Y.Z.; Du, H.-B.; You, X.Z.; Chen, B., A robust microporous metal-organic framework constructed from a flexible organic linker for acetylene storage at ambient temperature. *J. Mater. Chem.*, **2012**, *22*, 10195-10199.
101. Wu, H.; Gong, Q.; Olson, D. H.; Li, J., Commensurate adsorption of hydrocarbons and alcohols in microporous metal organic frameworks. *Chem. Rev.*, **2012**, *112*, 836-68.
102. Yuan, B.; Ma, D.; Wang, X.; Li, Z.; Li, Y.; Liu, H.; He, D., A microporous, moisture-stable, and amine-functionalized metal-organic framework for highly selective separation of CO_2 from CH_4 . *Chem. Commun.*, **2012**, *48*, 1135-1137.
103. Llabrés i Xamena, F. X.; Casanova, O.; Galiasso Tailleur, R.; Garcia, H.; Corma, A., Metal organic frameworks (MOFs) as catalysts: A combination of Cu^{2+} and Co^{2+} MOFs as an efficient catalyst for tetralin oxidation. *J. Catal.*, **2008**, *255*, 220-227.
104. Isaeva, V.; Kustov, L., The application of metal-organic frameworks in catalysis (Review). *Pet. Chem.*, **2010**, *50*, 167-180.
105. Horcajada, P.; Chalati, T.; Serre, C.; Gillet, B.; Sebric, C.; Baati, T.; Eubank, J. F.; Heurtaux, D.; Clayette, P.; Kreuz, C.; Chang, J.S.; Hwang, Y. K.; Marsaud, V.; Bories, P.N.; Cynober, L.; Gil, S.; Férey, G.; Couvreur, P.; Gref, R., Porous metal-organic-framework nanoscale carriers as a potential platform for drug delivery and imaging. *Nat. Mater.*, **2010**, *9*, 172-178.
106. Czaja, A. U.; Trukhan, N.; Muller, U., Industrial applications of metal-organic frameworks. *Chem. Soc. Rev.*, **2009**, *38*, 1284-1293.

107. Horcajada, P.; Serre, C.; Maurin, G.; Ramsahye, N. A.; Balas, F.; Vallet-Regí, M. A.; Sebban, M.; Taulelle, F.; Férey, G. R., Flexible porous metal-organic frameworks for a controlled drug delivery. *J. Am. Chem. Soc.*, **2008**, *130*, 6774-6780.
108. Harris, M. M.; Mitchell, R. K., Activation energy and entropy in the racemisation of 2,2[prime or minute]-dibromobiphenyl-4,4[prime or minute]-dicarboxylic acid. *J. Chem. Soc.*, **1960**, 1905-1908.
109. Holleman, A. F., Some factors influencing substitution in the benzene ring. *Chem. Rev.*, **1924**, *1*, 187-230.
110. Andrievsky A. M., G. M. V., Bromination of deactivated aromatic compounds. *Russ. Chem. Rev.*, **2011**, *5*, 421-428.
111. Derbyshire, D. H.; Waters, W. A., The significance of the bromine cation in aromatic substitution. Part II. Preparative applicability. *J. Chem. Soc.*, **1950**, 573-577.
112. Komm D.; Sagur J.B., m-nitrobenzoic acid. *Org. Syn. Coll.*, **1941**, *3*, 71-72.
113. Komm D.; Sagur J.B., Methyl m-nitrobenzoate. *Org. Syn. Coll.*, **1941**, *1*, 372-373.
114. Solomons, T. W. G.; Fryhle, C. B., *Organic chemistry*. Wiley, 2008.
115. Doxsee, K. M.; Feigel, M.; Stewart, K. D.; Canary, J. W.; Knobler, C. B.; Cram, D. J., Host-guest complexation. 42. Preorganization strongly enhances the tendency of hemispherands to form hemispheraplexes. *J. Am. Chem. Soc.*, **1987**, *109*, 3098-3107.
116. Pogorelić, I.; Filipan-Litvić, M.; Merkaš, S.; Ljubić, G.; Cepanec, I.; Litvić, M., Rapid, efficient and selective reduction of aromatic nitro compounds with sodium borohydride and Raney nickel. *J. Mol. Catal. A: Chem.*, **2007**, *274*, 202-207.
117. Gowda, S.; Kempe Gowda, B. K.; Channe Gowda, D., Hydrazinium monoformate: A new hydrogen donor selective reduction of nitrocompounds catalyzed by commercial zinc dust. *Synth. Commun.*, **2003**, *33*, 281-289.
118. Liu, Y.; Lu, Y.; Prashad, M.; Repič, O.; Blacklock, T. J., A practical and chemoselective reduction of nitroarenes to anilines using activated iron. *Adv. Synth. Catal.*, **2005**, *347*, 217-219.
119. Nagaraja, D.; Pasha, M. A., Reduction of aryl nitro compounds with aluminium NH₄Cl: effect of ultrasound on the rate of the reaction. *Tetrahedron Lett.*, **1999**, *40*, 7855-7856.
120. Ohashi, M.; Kapoor, M. P.; Inagaki, S., Chemical modification of crystal-like mesoporous phenylene-silica with amino group. *Chem. Commun.*, **2008**, 841-843.
121. Khurana, J. M.; Chauhan, S.; Bansal, G., Facile Hydrolysis of Esters with KOH-Methanol at Ambient Temperature. *Monatsh.Chem.*, **2004**, *135*, 83-87.
122. Ram, S.; Ehrenkauf, R. E., A general procedure for mild and rapid reduction of aliphatic and aromatic nitro compounds using ammonium formate as a catalytic hydrogen transfer agent. *Tetrahedron Lett.*, **1984**, *25*, 3415-3418.

123. Rowsell, J. L. C.; Yaghi, O. M., Effects of functionalization, catenation, and variation of the metal oxide and organic linking units on the low-pressure hydrogen adsorption properties of metal–organic frameworks. *J. Am. Chem. Soc.*, **2006**, *128*, 1304-1315.
124. Batten, S. R., Topology of interpenetration. *Cryst. Eng. Comm.* **2001**, *3*, 67-72.
125. Eddaoudi, M.; Moler, D. B.; Li, H.; Chen, B.; Reineke, T. M.; O'Keeffe, M.; Yaghi, O. M., Modular chemistry: secondary building units as a basis for the design of highly porous and robust metal–organic carboxylate frameworks. *Acc. Chem. Res.*, **2001**, *34*, 319-330.
126. Bae, Y.-S.; Dubbeldam, D.; Nelson, A.; Walton, K. S.; Hupp, J. T.; Snurr, R. Q., Strategies for characterization of large-pore metal-organic frameworks by combined experimental and computational methods. *Chem. Mater.*, **2009**, *21*, 4768-4777.
127. Deshpande, R. K.; Minnaar, J. L.; Telfer, S. G., Thermolabile groups in metal–organic frameworks: Suppression of network interpenetration, post-synthetic cavity expansion, and protection of reactive functional groups. *Angew. Chem. Int. Ed.*, **2010**, *49*, 4598-4602.
128. Liu, X.; Park, M.; Hong, S.; Oh, M.; Yoon, J. W.; Chang, J.-S.; Lah, M. S., A twofold interpenetrating porous metal–organic framework with high hydrothermal stability: structure and gas sorption behavior. *Inorg. Chem.*, **2009**, *48*, 11507-11509.
129. Tanaka, D.; Higuchi, M.; Horike, S.; Matsuda, R.; Kinoshita, Y.; Yanai, N.; Kitagawa, S., Storage and sorption properties of acetylene in jungle-gym-like open frameworks. *Chem. Asian J.*, **2008**, *3*, 1343-1349.
130. Getman, R. B.; Bae, Y. S.; Wilmer, C. E.; Snurr, R. Q., Review and analysis of molecular simulations of methane, hydrogen, and acetylene storage in metal-organic frameworks. *Chem. Rev.*, **2012**, *112*, 703-23.
131. Gassensmith, J. J.; Furukawa, H.; Smaldone, R. A.; Forgan, R. S.; Botros, Y. Y.; Yaghi, O. M.; Stoddart, J. F., Strong and reversible binding of carbon dioxide in a green metal–organic framework. *J. Am. Chem. Soc.*, **2011**, *133*, 15312-15315.
132. Park, J.; Yuan, D.; Pham, K. T.; Li, J. R.; Yakovenko, A.; Zhou, H. C., Reversible alteration of CO₂ adsorption upon photochemical or thermal treatment in a metal-organic framework. *J. Am. Chem. Soc.*, **2012**, *134*, 99-102.
133. Liu, J.; Thallapally, P. K.; McGrail, B. P.; Brown, D. R., Progress in adsorption-based CO₂ capture by metal-organic frameworks. *Chem. Soc. Rev.*, **2012**, *41*, 2308-22.
134. Zhao, X.; Xiao, B.; Fletcher, A. J.; Thomas, K. M.; Bradshaw, D.; Rosseinsky, M. J., Hysteretic adsorption and desorption of hydrogen by nanoporous metal-organic frameworks. *Science*, **2004**, *306*, 1012-1015.
135. Lin, X.; Champness, N.; Schröder, M., Hydrogen, methane and carbon dioxide adsorption in metal-organic framework materials functional metal-organic frameworks: Gas storage, separation and catalysis. *Springer*, **2010**, 293, 35-76.
136. Suh, M. P.; Park, H. J.; Prasad, T. K.; Lim, D.W., Hydrogen storage in metal–organic frameworks. *Chem. Rev.*, **2011**, *112*, 782-835.

137. Zhang, L.; Wang, Q.; Wu, T.; Liu, Y.C., Understanding adsorption and interactions of alkane isomer mixtures in isorecticular metal–organic frameworks. *Chem. Eur. J.*, **2007**, *13*, 6387-6396.
138. Düren, T.; Snurr, R. Q., Assessment of isorecticular metal–organic frameworks for adsorption separations: A molecular simulation study of methane/n-butane mixtures. *J. Phys. Chem. B*, **2004**, *108*, 15703-15708.
139. Mason, J. A.; Sumida, K.; Herm, Z. R.; Krishna, R.; Long, J. R., Evaluating metal-organic frameworks for post-combustion carbon dioxide capture via temperature swing adsorption. *Energy Environ. Sci.*, **2011**, *4*, 3030-3040.
140. Smith, M. B.; March, J., March's Advanced Organic Chemistry - Reactions, Mechanisms, and Structure (6th Edition), *John Wiley & Sons*, **2007**, 1429.
141. Kluger, R.; Hunt, J. C., Circumventive catalysis: contrasting reaction patterns of tertiary and primary amines with cyclic anhydrides and the avoidance of intermediates. *J. Am. Chem. Soc.*, **1989**, *111*, 3325-3328.
142. Mitchell, W., The acetylation of d-[small psi]-ephedrine and l-ephedrine. *J. Chem. Soc.*, **1940**, 1153-1155.
143. Vagin, S.; Ott, A.; Weiss, H.-C.; Karbach, A.; Volkmer, D.; Rieger, B., Metal-organic frameworks (MOFs) composed of (Triptycenedicarboxylato)zinc. *Eur. J. Inorg. Chem.*, **2008**, *2008*, 2601-2609.
144. Valente, C.; Choi, E.; Belowich, M. E.; Doonan, C. J.; Li, Q.; Gasa, T. B.; Botros, Y. Y.; Yaghi, O. M.; Stoddart, J. F., Metal-organic frameworks with designed chiral recognition sites. *Chem. Commun.*, **2010**, *46*, 4911-4913.
145. Ertel, T. S.; Bertagnolli, H.; ckmann, S.; Kolb, U.; Peter, D., XAFS spectroscopy of liquid and amorphous systems: Presentation and verification of a newly developed program package. *Appl. Spectrosc.*, **1992**, *46*, 690-698.
146. Newville, M.; Liviņš, P.; Yacoby, Y.; Rehr, J. J.; Stern, E. A., Near-edge x-ray-absorption fine structure of Pb: A comparison of theory and experiment. *Phys. Rev. B*, **1993**, *47*, 14126-14131.
147. Binsted, N.; Hasnain, S. S., State-of-the-art analysis of whole X-ray absorption spectra. *J. Synchrotron Rad.*, **1996**, *3*, 185-196.
148. Henke, S.; Schmid, R.; Grunwaldt, J.-D.; Fischer, R. A., Flexibility and Sorption Selectivity in Rigid Metal–Organic Frameworks: The Impact of Ether-Functionalised Linkers. *Chem. Eur. J.*, **2010**, *16*, 14296-14306.
149. Vishnyakov, A.; Ravikovitch, P. I.; Neimark, A. V.; Bülow, M.; Wang, Q. M., Nanopore structure and sorption properties of Cu–BTC metal–organic framework. *Nano Lett.*, **2003**, *3*, 713-718.
150. Lee, J.; Li, J.; Jagiello, J., Gas sorption properties of microporous metal organic frameworks. *J. Solid State Chem.*, **2005**, *178*, 2527-2532.
151. Huang, L.; Wang, H.; Chen, J.; Wang, Z.; Sun, J.; Zhao, D.; Yan, Y., Synthesis, morphology control, and properties of porous metal–organic coordination polymers. *Microporous Mesoporous Mater.*, **2003**, *58*, 105-114.

152. Panella, B.; Hirscher, M., Hydrogen physisorption in metal–organic porous crystals. *Adv. Mater.*, **2005**, *17*, 538-541.
153. Rowsell, J. L. C.; Millward, A. R.; Park, K. S.; Yaghi, O. M., Hydrogen sorption in functionalized metal–organic frameworks. *J. Am. Chem. Soc.*, **2004**, *126*, 5666-5667.
154. Kaye, S. S.; Dailly, A.; Yaghi, O. M.; Long, J. R., Impact of preparation and handling on the hydrogen storage properties of $\text{Zn}_4\text{O}(\text{1,4-benzenedicarboxylate})_3$ (MOF-5). *J. Am. Chem. Soc.*, **2007**, *129*, 14176-14177.
155. Metz, B.; Davidson, O.; De Coninck, H.; Change, I.P.C.C. 2005 Carbon dioxide capture and storage. *Cambridge University Press*, **2005**, 431.
156. Key Tables from OECD, *CO₂ emissions from fuel combustion 2011*.
157. Klara, S. M.; Srivastava, R. D.; McIlvried, H. G., Integrated collaborative technology development program for CO₂ sequestration in geologic formations—United States Department of Energy R&D. *Energy Convers. Manage.*, **2003**, *44*, 2699-2712.
158. Rochelle, G. T., Amine scrubbing for CO₂ Capture. *Science*, **2009**, *325*, 1652-1654.
159. Mu, B.; Li, F.; Huang, Y.; Walton, K. S., Breathing effects of CO₂ adsorption on a flexible 3D lanthanide metal-organic framework. *J. Mater. Chem.*, **2012**, *22*, 10172-10178.
160. Hemgesberg, M.; Ohlmann, D. M.; Schmitt, Y.; Wolfe, M. R.; Müller, M. K.; Erb, B.; Sun, Y.; Gooßen, L. J.; Gerhards, M.; Thiel, W. R., Simple access to sol–gel precursors bearing fluorescent aromatic core units. *Eur. J. Org. Chem.*, **2012**, *11*, 2142-2151.
161. Lee, J. H.; Kang, S.; Jaworski, J.; Kwon, K.-Y.; Seo, M. L.; Lee, J. Y.; Jung, J. H., Fluorescent composite hydrogels of metal–organic frameworks and functionalized graphene oxide. *Chem. Eur. J.*, **2012**, *18*, 765-769.
162. Schoenberg, A.; Bartoletti, I.; Heck, R. F., Palladium-catalyzed carboalkoxylation of aryl, benzyl, and vinylic halides. *J. Org. Chem.*, **1974**, *39*, 3318-3326.
163. Ozawa, F.; Kawasaki, N.; Okamoto, H.; Yamamoto, T.; Yamamoto, A., Mechanisms of double and single carbonylation reactions of aryl iodides catalyzed by palladium complexes to give .alpha.-keto esters and esters. *Organometallics*, **1987**, *6*, 1640-1651.
164. Sun, D.; Ke, Y.; Collins, D. J.; Lorigan, G. A.; Zhou, H.-C., Construction of robust open metal–organic frameworks with chiral channels and permanent porosity. *Inorg. Chem.*, **2007**, *46*, 2725-2734.
165. Tsuruoka, T.; Furukawa, S.; Takashima, Y.; Yoshida, K.; Isoda, S.; Kitagawa, S., Nanoporous nanorods fabricated by coordination modulation and oriented attachment growth. *Angew. Chem.*, **2009**, *121*, 4833-4837.
166. Diring, S. P.; Furukawa, S.; Takashima, Y.; Tsuruoka, T.; Kitagawa, S., Controlled multiscale synthesis of porous coordination polymer in nano/micro regimes. *Chem. Mater.*, **2010**, *22*, 4531-4538.

167. Schaate, A.; Roy, P.; Godt, A.; Lippke, J.; Waltz, F.; Wiebcke, M.; Behrens, P., Modulated Synthesis of Zr-Based Metal–Organic Frameworks: From Nano to Single Crystals. *Chem.Eur. J.*, **2011**, *17*, 6643-6651.
168. Ruggli, P.; Brandt, F., Über ein neues lineares Benzo-dipicolin, das 2, 6-Dimethyl-1, 5-anthrazolin. *Helv. Chim. Acta*, **1944**, *27*, 274-291.
169. Ferey, G., Hybrid porous solids: past, present, future. *Chem. Soc. Rev.*, **2008**, *37*, 191-214.
170. Cavka, J. H.; Jakobsen, S.; Olsbye, U.; Guillou, N.; Lamberti, C.; Bordiga, S.; Lillerud, K. P., A New tirconium inorganic building brick forming metal organic frameworks with exceptional stability. *J. Am. Chem. Soc.*, **2008**, *130*, 13850-13851.
171. Loiseau, T.; Serre, C.; Huguenard, C.; Fink, G.; Taulelle, F.; Henry, M.; Bataille, T.; Férey, G., A rationale for the large breathing of the porous aluminum terephthalate (MIL-53) upon hydration. *Chem. Eur. J.*, **2004**, *10*, 1373-1382.
172. Gao, W.; Dickinson, L.; Grozinger, C.; Morin, F. G.; Reven, L., Self-assembled monolayers of alkylphosphonic acids on metal oxides. *Langmuir*, **1996**, *12*, 6429-6435.
173. Randon, J.; Paterson, R., Preliminary studies on the potential for gas separation by mesoporous ceramic oxide membranes surface modified by alkyl phosphonic acids. *J.Memb. Sci.*, **1997**, *134*, 219-223.
174. Caro, J.; Noack, M.; Kölsch, P., Chemically modified ceramic membranes. *Microporous Mesoporous Mater.*, **1998**, *22*, 321-332.
175. Zakeeruddin, S. M.; Nazeeruddin, M. K.; Pechy, P.; Rotzinger, F. P.; Humphry-Baker, R.; Kalyanasundaram, K.; Grätzel, M.; Shklover, V.; Haibach, T., Molecular engineering of photosensitizers for nanocrystalline solar cells: Synthesis and characterization of Ru dyes based on phosphonated terpyridines. *Inorg. Chem.*, **1997**, *36*, 5937-5946.
176. Bonhôte, P.; Moser, J.E.; Humphry-Baker, R.; Vlachopoulos, N.; Zakeeruddin, S. M.; Walder, L.; Grätzel, M., Long-lived photoinduced charge separation and redox-type photochromism on mesoporous oxide films sensitized by molecular dyads. *J. Am. Chem. Soc.*, **1999**, *121*, 1324-1336.
177. Laiti, E.; Öhman, L.-O., Acid/base properties and phenylphosphonic acid complexation at the boehmite/water interface. *J. Colloid Interface Sci.*, **1996**, *183*, 441-452.
178. Laiti, E.; Öhman, L.O.; Nordin, J.; Sjöberg, S., Acid/base properties and phenylphosphonic acid complexation at the aged γ -Al₂O₃/water interface. *J. Colloid Interface Sci.*, **1995**, *175*, 230-238.
179. Laiti, E.; Persson, P.; Öhman, L.O., Surface complexation and precipitation at the H⁺-Orthophosphate-Aged γ -Al₂O₃/water interface. *Langmuir*, **1996**, *12*, 2969-2975.
180. Vioux, A.; Le Bideau, J.; Mutin, P. H.; Leclercq, D., New Aspects in Phosphorus Chemistry IV. *Springer*, **2004**, 232, 145-174.
181. Andrianainarivelo, M.; Corriu, R.; Leclercq, D.; Mutin, P. H.; Vioux, A., Mixed oxides SiO₂-ZrO₂ and SiO₂-TiO₂ by a non-hydrolytic sol-gel route. *J. Mater. Chem.*, **1996**, *6*, 1665-1671.
182. Mutin, P. H.; Guerrero, G.; Vioux, A., Hybrid materials from organophosphorus coupling molecules. *J. Mater. Chem.*, **2005**, *15*, 3761-3768.

183. Mutin, P. H.; Guerrero, G.; Vioux, A., Organic–inorganic hybrid materials based on organophosphorus coupling molecules: from metal phosphonates to surface modification of oxides. *Compt. Rendus Chimie*, **2003**, *6*, 1153-1164.
184. Impens, N. R. E. N.; van der Voort, P.; Vansant, E. F., Silylation of micro-, meso- and non-porous oxides: a review. *Microporous Mesoporous Mater.*, **1999**, *28*, 217-232.
185. Krysztafkiewicz, A.; Rager, B.; Maik, M., Surface modification of highly dispersed rubber fillers and pigments by titanate proadhesive and hydrophobic compounds. *Colloid & Polymer Science*, **1994**, *272*, 1547-1559.
186. Guerrero, G.; Mutin, P. H.; Vioux, A., Anchoring of phosphonate and phosphinate coupling molecules on titania particles. *Chem. Mater.*, **2001**, *13*, 4367-4373.
187. Van Alsten, J. G., Self-assembled monolayers on engineering metals: Structure, derivatization, and utility. *Langmuir*, **1999**, *15*, 7605-7614.
188. Gawalt, E. S.; Avaltroni, M. J.; Koch, N.; Schwartz, J., Self-assembly and bonding of alkanephosphonic acids on the native oxide surface of titanium. *Langmuir*, **2001**, *17*, 5736-5738.
189. Guerrero, G.; Mutin, P. H.; Vioux, A., Organically modified aluminas by grafting and sol-gel processes involving phosphonate derivatives. *J. Mater. Chem.*, **2001**, *11*, 3161-3165.
190. Villemin, D.; Moreau, B.; Simeon, F.; Maheut, G.; Fernandez, C.; Montouillout, V.; Caignaert, V.; Jaffres, P.A., A one step process for grafting organic pendants on alumina the reaction of alumina and phosphonate under microwave irradiation. *Chem. Commun.*, **2001**, 2060-2061.
191. Magano, J.; Dunetz, J. R., Large-scale carbonyl reductions in the pharmaceutical industry. *Org. Process Rev. Dev.*, **2012**, *16*, 1156-1184.
192. Chari, R. V. J.; Kozarich, J. W., Synthesis and properties of halohydroxyacetones and halomethylglyoxals. *J. Organic Chem.*, **1982**, *47*, 2355-2358.
193. Bänziger, M.; Cercus, J.; Hirt, H.; Laumen, K.; Malan, C.; Spindler, F.; Struber, F.; Troxler, T., The development of a practical synthesis of the potent and selective somatostatin sst3 receptor antagonist [4-(3,4-difluoro-phenyl)-piperazine-1-yl]-{(4S,4aS,8aR)-2[(S)-3-(6-methoxy-pyridin-3-yl)-2-methyl-propyl]-decahydroisoquinoline-4-yl}-methanone (NVP-ACQ090). *Tetrahedron: Asymmetry*, **2003**, *14*, 3469-3477.
194. F. Mironov, A.; D. Rumyantseva, V.; N. Ponamoreva, O., A porphyrin chlorination reaction. *Mendeleev Commun.*, **1998**, *8*, 187-188.
195. Lipshutz, B. H.; Kim, S.K.; Mollard, P.; Blomgren, P. A.; Stevens, K. L., Nickel(0)-catalyzed couplings of vinyl- alanes & - zirconocenes with chloromethylated heteroaromatics: A route to E-allylated heterocycles. *Tetrahedron*, **1998**, *54*, 6999-7012.
196. Daughenbaugh, P. J.; Allison, J. B., The action of thionyl chloride upon cholesterol and certain other alcohols *J. Am. Chem. Soc.*, **1929**, *51*, 3665-3667.

197. Collins, J. E.; Lamba, J. J.; Love, J. C.; McAlvin, J. E.; Ng, C.; Peters, B. P.; Wu, X.; Fraser, C. L., Ruthenium(II) alpha-diimine complexes with one, two, and three 4,4'-Bis(hydroxymethyl)-2,2'-bipyridine and 4,4'-Bis(chloromethyl)-2,2'-bipyridine ligands: Useful starting materials for further derivatization. *Inorg. Chem.*, **1999**, *38*, 2020-2024.
198. Serieys, A.; Botuha, C.; Chemla, F.; Ferreira, F.; Pérez-Luna, A., Zinc(0)/dimethylformamide-mediated synthesis of symmetrical carboxylic anhydrides from acid chlorides. *Tetrahedron Lett.*, **2008**, *49*, 5322-5323.
199. Lunelli, B., New, optimized preparation of 1,2-dichlorocyclobuten-3,4-dione (C₄O₂Cl₂) from squaric acid and oxalyl chloride. *Tetrahedron Lett.*, **2007**, *48*, 3595-3597.
200. Taylor, S. D.; Kotoris, C. C.; Dinaut, A. N.; Chen, M.-J., Synthesis of aryl(difluoromethylenephosphonates) via electrophilic fluorination of α-carbanions of benzylic phosphonates with N-fluorobenzenesulfonimide. *Tetrahedron*, **1998**, *54*, 1691-1714.
201. Sing, K. S. W.; Everett, D. H.; Haul, R. A. W.; Moscou, L.; Pierotti, R. A.; Rouquerol, J.; Siemieniowska, T., Reporting physisorption data for gas/solid systems. In *Handbook of Heterogeneous Catalysis*, Wiley, **2008**.
202. Pawsey, S.; Yach, K.; Reven, L., Self-Assembly of Carboxyalkylphosphonic Acids on metal oxide powders. *Langmuir*, **2002**, *18*, 5205-5212.

Appendix**Crystal Structure of 2**

Empirical formula	$C_{16}H_{12}Br_2O_4$	
Formula weight	428.08	
Crystal colour and habit	colorless prism	
Crystal size (mm)	0.14 x 0.08 x 0.07	
Temperature (K)	150(2)	
Wavelength (Å)	1.54184	
Crystal system	Monoclinic	
Space group	C2/c	
Unit cell dimensions	$a = 14.6387(2) \text{ Å}$	$\alpha = 90^\circ$
	$b = 7.8118(1) \text{ Å}$	$\beta = 91.772(1)^\circ$
	$c = 13.5267(2) \text{ Å}$	$\gamma = 90^\circ$
Volume (Å ³)	1546.10(4)	
Z	4	
Calculated density (Mg/m ³)	1.839	
Absorption coefficient (mm ⁻¹)	6.794	
F(000)	840	
θ -range for data collection (°)	6.05/62.57	
Index ranges	$-16 \leq h \leq 16, -8 \leq k \leq 8, -14 \leq l \leq 15$	
Reflections collected	6714	
Independent reflections	1231 ($R_{int} = 0.0339$)	
Completeness to $\theta = 62.57^\circ$	99.7 %	
Absorption correction	Semi-empirical from equivalents (Multiscan)	
Max. and min. transmission	1.00000 and 0.21673	
Refinement method	Full-matrix least-squares on F^2	
Data/restraints/parameters	1231/0/101	
Goodness-of-fit on F^2	1.087	
Final R indices [$I > 2\sigma(I)$]	$R_1 = 0.0244, wR_2 = 0.0649$	
R indices (all data)	$R_1 = 0.0280, wR_2 = 0.0654$	
Largest diff. Peak and hole (e·Å ⁻³)	0.479/-0.478	

Crystal Structure of 4

Empirical formula	$C_{16}H_{12}N_2O_8$	
Formula weight	360.28	
Crystal colour and habit	yellow prism	
Crystal size (mm)	0.31 x 0.13 x 0.04	
Temperature (K)	150(2)	
Wavelength (Å)	1.54184	
Crystal system	Triclinic	
Space group	P-1	
Unit cell dimensions	$a = 8.0903(5) \text{ Å}$	$\alpha = 107.890(7)^\circ$
	$b = 10.5348(7) \text{ Å}$	$\beta = 112.174(7)^\circ$
	$c = 10.6123(9) \text{ Å}$	$\gamma = 95.514(5)^\circ$

Volume (Å ³)	773.68(12)
Z	2
Calculated density (Mg/m ³)	1.547
Absorption coefficient (mm ⁻¹)	1.092
F(000)	372
Θ-range for data collection (°)	4.54/62.58
Index ranges	-7 ≤ h ≤ 9, -12 ≤ k ≤ 11, -12 ≤ l ≤ 11
Reflections collected	4366
Independent reflections	2450 (<i>R</i> _{int} = 0.0168)
Completeness to Θ = 62.58°	99.1 %
Absorption correction	Semi-empirical from equivalents (Multiscan)
Max. and min. transmission	1.00000 and 0.80092
Refinement method	Full-matrix least-squares on F ²
Data/restraints/parameters	2450/0/237
Goodness-of-fit on F ²	1.073
Final <i>R</i> indices [<i>I</i> > 2Θ (<i>I</i>)]	<i>R</i> ₁ = 0.0363, <i>wR</i> ₂ = 0.1004
<i>R</i> indices (all data)	<i>R</i> ₁ = 0.0421, <i>wR</i> ₂ = 0.1041
Largest diff. peak and hole (e·Å ⁻³)	0.231/-0.296

Crystal Structure of 6

Empirical formula	C ₁₆ H ₁₆ N ₂ O ₄
Formula weight	300.31
Temperature	150(2) K
Wavelength	1.54184 Å
Crystal system	Monoclinic
Space group	C2/c
Unit cell dimensions	a = 17.6766(22) Å α = 90°. b = 10.2098(9) Å β = 111.115(14)°. c = 8.4922(11) Å γ = 90°.
Volume	1429.7(3) Å ³
Z	4
Density (calculated)	1.395 Mg/ m ³
Absorption coefficient	0.842 mm ⁻¹
F(000)	632
Crystal colour and habit	colorless needle
Crystal size	0.23 x 0.08 x 0.07 m m ³
Θ range for data collection	5.10 to 62.63°.
Index ranges	-14 ≤ h ≤ 20, -11 ≤ k ≤ 11, -9 ≤ l ≤ 9
Reflections collected	4508
Independent reflections	1150 [<i>R</i> (int) = 0.0242]
Completeness to Θ = 62.63°	99.8 %
Max. and min. transmission	1.00000 and 0.85065
Refinement method	Full-matrix least-squares on F ²
Data / restraints / parameters	1150 / 2 / 107
Goodness-of-fit on F ²	1.116
Final <i>R</i> indices [<i>I</i> > 2Θ(<i>I</i>)]	<i>R</i> ₁ = 0.0550, <i>wR</i> ₂ = 0.1720
<i>R</i> indices (all data)	<i>R</i> ₁ = 0.0604, <i>wR</i> ₂ = 0.1778

Largest diff. peak and hole

0.608 and -0.285 e.Å⁻³**Crystal Structure of 8**

Empirical formula

C₂₀H₂₀N₂O₆

Formula weight

384.38

Temperature

150(2) K

Wavelength

1.54184 Å

Crystal system

Triclinic

Space group

P-1

Unit cell dimensions

 $a = 9.1530(3) \text{ Å}$ $\alpha = 99.765(3)^\circ$.
 $b = 10.5911(4) \text{ Å}$ $\beta = 90.142(3)^\circ$.
 $c = 19.6888(7) \text{ Å}$ $\gamma = 100.019(3)^\circ$.

Volume

1851.29(11) Å³

Z

4

Density (calculated)

1.379 Mg/m³

Absorption coefficient

0.860 mm⁻¹

F(000)

808

Crystal colour and habit

colorless prism

Crystal size

0.27 x 0.23 x 0.18 mm³

θ range for data collection

4.30 to 62.69°.

Index ranges

-10 ≤ h ≤ 10, -12 ≤ k ≤ 12, -22 ≤ l ≤ 17

Reflections collected

12958

Independent reflections

5908 [R(int) = 0.0180]

Completeness to θ = 62.69°

99.4 %

Absorption correction

Semi-empirical from equivalents (Multiscan)

Max. and min. transmission

1.00000 and 0.84757

Refinement method

Full-matrix least-squares on F²

Data / restraints / parameters

5908 / 0 / 514

Goodness-of-fit on F²

1.077

Final R indices [I > 2θ(I)]

R1 = 0.0415, wR2 = 0.1173

R indices (all data)

R1 = 0.0468, wR2 = 0.1210

Extinction coefficient

0.0037(3)

Largest diff. peak and hole

0.447 and -0.439 e. Å⁻³**Crystal Structure of 10**

Identification code

11243o

Empirical formula

C₂₂H₂₄N₂O₆

Formula weight

412.43

Temperature

150(2) K

Wavelength

1.54184 Å

Crystal system

Monoclinic

Space group

P2₁/n

Unit cell dimensions

 $a = 11.6994(2) \text{ Å}$ $\alpha = 90^\circ$.
 $b = 9.6891(1) \text{ Å}$ $\beta = 104.427(2)^\circ$.
 $c = 19.3321(3) \text{ Å}$ $\gamma = 90^\circ$.

Volume

2122.32(5) Å³

Z

4

Density (calculated)	1.291 Mg/ m ³
Absorption coefficient	0.785 mm ⁻¹
F(000)	872
Crystal colour and habit	Colorless prism
Crystal size	0.29 x 0.22 x 0.17 mm ³
Θ range for data collection	4.72 to 62.66°.
Index ranges	-13<=h<=13, -11<=k<=10, -22<=l<=22
Reflections collected	14466
Independent reflections	3387 [R(int) = 0.0253]
Completeness to Θ = 62.66°	99.5 %
Absorption correction	Semi-empirical from equivalents (Multiscan)
Max. and min. transmission	1.00000 and 0.70532
Refinement method	Full-matrix least-squares on F ²
Data / restraints / parameters	3387 / 0 / 275
Goodness-of-fit on F ²	1.064
Final R indices [I>2Θ(I)]	R1 = 0.0375, wR2 = 0.1025
R indices (all data)	R1 = 0.0413, wR2 = 0.1048
Largest diff. peak and hole	0.199 and -0.244 e. Å ⁻³

Crystal Structure of 20

Identification code	1179o
Empirical formula	C ₂₄ H ₂₆ O ₄ S ₂
Formula weight	442.57
Temperature	150(2) K
Wavelength	1.54184 Å
Crystal system	Triclinic
Space group	P-1
Unit cell dimensions	a = 8.5601(5) Å α = 110.052(6)°. b = 11.8606(9) Å β = 90.591(5)°. c = 12.1527(6) Å γ = 108.776(6)°.
Volume	1087.22(14) Å ³
Z	2
Density (calculated)	1.352 Mg/ m ³
Absorption coefficient	2.452 mm ⁻¹
F(000)	468
Crystal colour and habit	Yellow plate
Crystal size	0.31 x 0.12 x 0.06 mm ³
Θ range for data collection	3.91 to 62.65°.
Index ranges	-9<=h<=7, -13<=k<=13, -9<=l<=13
Reflections collected	6517
Independent reflections	3424 [R(int) = 0.0226]
Completeness to Θ = 62.65°	98.7 %
Absorption correction	Semi-empirical from equivalents (Multiscan)
Max. and min. transmission	1.00000 and 0.65446
Refinement method	Full-matrix least-squares on F ²
Data / restraints / parameters	3424 / 0 / 273

Goodness-of-fit on F^2	1.069
Final R indices [$I > 2\sigma(I)$]	$R1 = 0.0362$, $wR2 = 0.1044$
R indices (all data)	$R1 = 0.0416$, $wR2 = 0.1073$
Largest diff. peak and hole	0.350 and -0.178 e. \AA^{-3}

Crystal Structure of 21

Identification code	1143o
Empirical formula	$\text{C}_{26}\text{H}_{30}\text{O}_4\text{S}_2$
Formula weight	470.62
Temperature	150(2) K
Wavelength	1.54184 \AA
Crystal system	Monoclinic
Space group	$P2_1/n$
Unit cell dimensions	$a = 12.8645(3) \text{\AA}$ $\alpha = 90^\circ$. $b = 6.0509(1) \text{\AA}$ $\beta = 96.708(2)^\circ$. $c = 15.8520(4) \text{\AA}$ $\gamma = 90^\circ$.
Volume	1225.50(5) \AA^3
Z	2
Density (calculated)	1.275 Mg/m^3
Absorption coefficient	2.205 mm^{-1}
$F(000)$	500
Crystal colour and habit	yellow prism
Crystal size	0.14 x 0.08 x 0.07 mm^3
θ range for data collection	4.19 to 62.62°.
Index ranges	-10 $\leq h \leq$ 14, -6 $\leq k \leq$ 6, -18 $\leq l \leq$ 17
Reflections collected	7561
Independent reflections	1949 [$R(\text{int}) = 0.0221$]
Completeness to $\theta = 62.62^\circ$	99.8 %
Absorption correction	Semi-empirical from equivalents (Multiscan)
Max. and min. transmission	1.00000 and 0.38429
Refinement method	Full-matrix least-squares on F^2
Data / restraints / parameters	1949 / 120 / 186
Goodness-of-fit on F^2	1.059
Final R indices [$I > 2\sigma(I)$]	$R1 = 0.0263$, $wR2 = 0.0732$
R indices (all data)	$R1 = 0.0309$, $wR2 = 0.0745$
Extinction coefficient	0.0023(3)
Largest diff. peak and hole	0.264 and -0.192 e. \AA^{-3}

Acknowledgement

It was 2006 when I decided to do my PhD. I achieved one of my biggest desires in 2008. Now I am writing my favorite part of my dissertation but I should admit that this is the most difficult part by means of writing, since I am not sure that I can express my feelings which have to be limited in words and sentences. Let me try...

Firstly I would like to express my sincere gratitude to Prof. Dr. Werner R. Thiel for his great support, supervision and understanding throughout this study. I am really grateful to you for giving me the greatest opportunity of my life by accepting me for the PhD study. I learned a lot from you, whenever I needed help or I had questions, you always had time for me, but also you showed great patience for my interesting questions and the mistakes that I made. It was a great honor and pleasure for me to work with you and get to know such a nice, friendly professor. Thank you very much for everything.

I would like to thank Jun.-Prof. Dr. Matthias Bauer for the X-ray spectroscopy measurements of MOFs. With your help and discussions, my thesis became much more valuable.

I would like to thank Dr. Yu Sun for the crystal structures of the linkers.

I would like to thank Dr. Harald Kelm not only for the great NMR discussions but also giving the best two ovens of the department ☺.

I would like to thank Christiane Müller for the NMR measurements. I guess you measured nearly 1000 samples for me which were sometimes suitable for solid state NMR. I am really grateful for your patience.

I would like to thank Prof Dr. Stefan Kaskel for giving me the chance of working in his group and using their equipment. I am really grateful to Dr Vyladymir Bon for the crystal structures of the MOFs.

I would like to thank Ronny Grunker for enlightening me about MOFs and doing lots of measurements. A million times thanks to you Ronny for your great contributions, helps, friendship and patience (especially to my never ending questions via e-mails which can make a book chapter).

I would like to thank Prof. Dr. Behrens and Philip Zerner from TU Hannover for the great collaboration on Zr-MOFs. Thank you very much for your interest in my linkers and sharing all the results with me very quickly that I could insert them into my thesis.

My first lab mates Andreas Reis, Anett Schubert and Saskia Oswald... The first days were very difficult for me since I had no idea about the department, but with your help everything became easier. You not only taught me how the things work at the department and in the laboratory but you also made a nice working atmosphere in lab 678. Thanks for everything.

Former group members... I would like to thank to Claudia May, Thomas Jozak, Christoph Seubert, Zhou Zhou,. whenever I need help you were always with me. I really miss the days that we had great fun in the coffee room. Thomas, thank you very much for taking care of my schlenk line and pump whenever it was broken...

I would like to thank to Saeid Farsadpoor for taking care of the small troubles (!) in my hood..

I would like to thank Keven Müller for always being very nice and helpful to me. You helped me a lot but the greatest help was showing me how to fight with the autoclave which was a monster for me when I first met with it. Moreover, I will never forget our great MeOH drying sessions, thanks for reaching the top of the distillation apparatus which I could not see even when I stood on a footstool. We were a great distillation team, no one can do that faster than us ☺.

Katrin Roth... I am grateful to you from the first day of my life in Germany. I do not know how to express my feelings and again it is a point that saying "thank you" is not enough, but all I can do is say THANK YOU. You were always with me whenever I was struggling with the bureaucracy, but I always felt strong when you were with me and dealing with everything ☺. Thank you very much my dear friend...

Isabel Munstein... You were the second person who was taking care of my works which needed German language. Thank you very much for the telephone calls you made for me and also for the course "Introduction to German Language I"...

"Ezgi, you can do it, do not worry I believe you, I trust you, I am proud of you" Thank you Maximilian Hemgesberg... Whenever I was disappointed or hopeless, your encouragement made me feel better... Your way of thinking, your talks, your driving skills or problem solving style always surprised me. It was a really great pleasure for me to work with you and travel to the conferences, seminars, driving 7 h to Magdeburg ☺.

My first and last FP, Christian Kerner... I do not have to thank to you, since you had done the things that you had to do ☺. But... You are my dearest FP, one of my best friends in Germany that I could share everything. Now I can admit that you were the best FP ever, "off yaaaaa!!!" ☺ I will always miss our "fresh air" sessions and discussions on the aerial ladder... Lastly I am grateful for your helps...

And the members of AK Thiel... Thank you very much for the great working atmosphere, for your caring, never ending help and encouragement during this study...

Merve Çayır and Murat Küçükdişli... Merve, I am really happy that we worked in the same laboratory and shared everything. During the writing time you were my best supporter, you worked like a printing office for me or a delivery company. No doubt, the most valuable things were your encouragement and friendship. Thanks for listening to me and trying to keep me calm... Murat, I am grateful for the perfect contributions about my thesis. Thank you very much for great NMR and organic chemistry discussions, you helped me a lot...

Serap Yapar and Uğur Kaya.. You opened the doors of your sweet home to me.. It was a great feeling that there is a place that I feel like I am at home, It has not been such a long time, but I do not know why I feel that you were always with me and I always feel safe whenever I am with you.. Thank you very much for your patience and friendship whenever I am disappointed and sometimes unbearable especially during the writing time.

My first friends in Germany Selen Elyürek and Neslihan Hacıoğlu who became the best friends in a short time. It was August 2008 when we met, since then we were always together. When you left Ktown, the life became boring and sometimes unbearable... but just a phone call with you was enough to get some energy and hope, especially during the writing time. I am sure that there are lots of adventures waiting for us and we will be always together in the future... you are my family in Germany and I am looking forward to the new countries that we will discover together...

Işıl Biçer... I will never forget our drafts and never ending telephone calls which were lasting for hours. Thank you very much for being my “life couch” during four years, for your great solutions to my strange problems and for your great friendship. We shared a lot and for sure we will...

Dr. Seda Cantekin... As you mentioned in your dissertation, we started the Chemistry Adventure together and shared a lot since 1999... You were the person who inspired me for doing a PhD in a foreign country. I am really grateful for your help when I was trying to give such a difficult decision. My dear Seda, thank you very much for your great friendship.

Işıl-Erdinç Erçil... Thank you very much for your great friendship, your support, our telephone calls and being with my parents whenever they need help...

The last but not the least, my parents, my brother Öncü and his wife Sanem... There were kilometers between us, but you were always with me. Sometimes we could not see each other more than one year and I really felt guilty for leaving you alone and not being with you when you needed me, but you were always patient and considered. Thank you very much for your understanding, support, care and love during the four years which we were away from each other....

Curriculum Vitae

Ezgi Keceli

Education

- 09.2008 – 09.2012 **Technical University of Kaiserslautern, Kaiserslautern, Germany**
PhD at Department of Chemistry
- 09.2004 – 05.2006 **Middle East Technical University, Ankara, Turkey**
MS at Department of Chemistry
- 09.1999 – 06.2004 **Middle East Technical University, Ankara, Turkey**
BS at Department of Chemistry
- 09.1996 – 06.1999 **Ari High School of Science, Ankara, Turkey**

Publications:

- 02.2008 Ruthenium(III) Acetylacetonate; A Homogeneous Catalyst in The Hydrolysis of Sodium Borohydride (***Journal of Molecular Catalysis A***)
- Efficient Conversion of Arylene Precursors into Photoluminescent Phosphonates for Surface Modification of Transition Metal Oxides. (***Accepted manuscript, Dalton Transactions***)
- Three Functionalized Metal-Organic Frameworks Possessing IRMOF-9 Topology and Their Behaviour in Alkane Adsorption. (***Manuscript in preparation***)

Selbstständigkeitserklärung

Hiermit versichere ich, dass ich die vorliegende Dissertation mit dem Titel „New Linkers for Organic-Inorganic Hybrid Materials“ gemäß der Promotionsordnung des Fachbereichs Chemie der Technischen Universität Kaiserslautern selbstständig und nur unter Verwendung der angegebenen Quellen und Hilfsmittel angefertigt habe. Ich erkläre außerdem, dass diese Arbeit weder in gleicher noch in ähnlicher Form bereits in einem anderen Prüfungsverfahren vorgelegen hat.

Kaiserslautern, den August 2012

Ezgi Keceli